Towards Real-Time Terahertz Passive Imaging in Silicon Technologies

Thesis submitted for the degree of
Doktor der Ingenieurwissenschaften (Dr.-Ing.)

at the
University of Wuppertal, Germany
School of Electrical, Information and Media Engineering

by
Marcel Andree
from Wuppertal, Germany

September 2023

Contents

List of Figures

List of Tables

List of Abbreviations

2D	Two-dimensional
3D	Three-dimensional
AC	Alternating current
ADC	Analog to digital converter
A_e	Emitter area
BJT	Bipolar junction transistor
B/BW	Bandwidth
BB	Black body
BE	Base-emitter
BEOL	Back-end-of-line
B_{eq}	Equivalent bandwidth
BC	Base-collector
BiCMOS	Bipolar and CMOS
CB	Common-base
C_{bc}	Base-collector capacitance
$C_{bc,i}$	Internal base-collector capacitance
$C_{bc,x}$	External base-collector capacitance
C_{be}	Base-emitter capacitance
$C_{be,i}$	Internal base-emitter capacitance
$C_{be,x}$	External base-emitter capacitance
CC	Cascode
C_{cs}	Collector-substrate capacitance
C_{diff}	Diffusion capacitance
CE	Common-emitter

CM	Common-mode
CMOS	Complementary metal-oxide-semiconductor
CW	Continuous wave
DC	Direct current
DFG	Deutsche Forschungsgemeinschaft
DRC	Design rule check
EM	Electromagnetic
ENBW	Equivalent noise bandwidth
F	Noise factor
FFT	Fast Fourier Transformation
f_{max}	Maximum oscillation frequency
FPA	Focal plane array
FOM	Figure of merit
fps	Frames per second
f_t	Transition frequency
G_{AC}	Available gain circles
G_{eq}	Equivalent gain
$G_{m,be}$	Base-emitter diode transconductance
$G_{m,bc}$	Base-collector diode transconductance
G_{max}	Maximum available gain
G_{min}	Minimum noise reflection coefficient
G_{PC}	Power gain circles
GR	Generation recombination
HBT	Heterojunction bipolar transistor
HiCUM	High current model
$i_{b,2nd}$	Second-harmonic base current
I_c	Collector current
$i_{c,2nd}$	Second-harmonic collector current
$i_{c,dc}$	Rectified DC collector current
$I_{c,f}$	Forward collector current
$I_{c,r}$	Reverse collector current
IHCT	Institute for High Frequency & Communication Technology

IR	Infrared
J_c	Collector current density
LFN	Low-frequency noise
LNA	Low-noise amplifier
LSB	Load stability circles
M1-M5	Metal1 - Metal5
MIM	Metal-insulator-Metal
mmWave	Millimeter wave
MOSFET	Metal oxide semiconductor field effect transistor
NEP	Noise equivalent power
NEP_{eq}	Equivalent noise equivalent power
NETD	Noise equivalent temperature difference
NF	Noise figure
Q	Quality factor
P_{Ant}	Antenna input power
PCB	Printed circuit board
P_{DC}	DC power
R_b	Base resistance
$R_{b,i}$	Internal base resistance
$R_{b,x}$	External base resistance
R_c	Collector resistance
R_e	Emitter resistance
RF	Radio frequency
R_i	Current responsivity
R_L	Load resistance
R_S	Source resistance
RTS	Random telegraph signal
RX	Receiver
R_v	Voltage responsivity
$R_v(T)$	Thermal voltage responsivity
R_π	Dynamic base-emitter resistance
S_{IB}	Base current noise spectral density

SSB	Source stability circles
SiGe	Silicon germanium
SNR	Signal-to-noise-ratio
TDS	Time-domain spectroscopy
THz	Terahertz
$\boldsymbol{T_{LNA}}$	LNA noise temperature
TM1	Topmetal1
TM2	Topmetal2
TRL	Through-reflect-line
TX	Transmitter
UV	Ultraviolet
$\boldsymbol{v_{be}}$	Base-emitter RF voltage
$\boldsymbol{v_{be,i}}$	Internal base-emitter RF voltage
$\boldsymbol{v_{be,x}}$	External base-emitter RF voltage
$\boldsymbol{V_{be}}$	Base-emitter DC voltage
$\boldsymbol{V_{be,i}}$	Internal base-emitter DC voltage
$\boldsymbol{V_{be,x}}$	External base-emitter DC voltage
$\boldsymbol{v_{bc}}$	Base-collector DC voltage
$\boldsymbol{v_{bc,i}}$	Internal base-collector DC voltage
$\boldsymbol{v_{bc,x}}$	External base-collector DC voltage
$\boldsymbol{V_{bc}}$	Base-collector DC voltage
$\boldsymbol{V_{bc,i}}$	Internal base-collector DC voltage
$\boldsymbol{V_{bc,x}}$	External base-collector DC voltage
$\boldsymbol{v_n}$	Noise voltage spectral density
VNA	Vector network analyzer
x1	Device size 1
x2	Device size 2
$\boldsymbol{Z_{Det}}$	Detector input impedance
$\boldsymbol{Z_{In}}$	Input impedance
$\boldsymbol{Z_{Out}}$	Output impedance
$\boldsymbol{\beta}$	DC current gain
$\boldsymbol{\eta_{Ant}}$	Antenna radiation efficiency

$\boldsymbol{\eta_{filt}}$	Filter efficiency
$\boldsymbol{\eta_{match}}$	Matching efficiency

Declaration

I, Marcel Andree, herewith declare that I have produced this thesis without the prohibited assistance of third parties and without making use of aids other than those specified; notions taken over directly or indirectly from other sources have been identified as such. This work has not previously been presented in identical or similar form to any other German or foreign examination board.

The thesis work was conducted from 2017 to 2023 under the supervision of Prof. Dr. rer. nat. Ullrich R. Pfeiffer at the Institute for High-Frequency and Communication Technology (IHCT), University of Wuppertal, Germany. This work was partially funded by the German Research Foundation (DFG) under the collaborative research center MARIE, Project-ID 287022738 TRR 196 for project C08.

Acknowledgements

Firstly, I would like to express my appreciation toward my Ph.D. advisor, Prof. Ullrich Pfeiffer. He gave me the opportunity to pursue my doctoral thesis at the Institute for High-Frequency and Communication Technology (IHCT), with one of the best-equipped THz research labs all over the world. This research would not have been possible without his excellent guidance and the fundamental knowledge he shared with me during the last few years.

I am particularly impressed by the surgical accuracy of Dr. Janusz Grzyb, who taught me the fundamentals of precise engineering, scrutinizing both my design and publication work in the last years and making me think like a scientist. Furthermore, I would like to thank my associate advisor Prof. Dr. Daniel Neumaier, from the University of Wuppertal, for co-examining this thesis. I am also thankful to the German Research Foundation (Deutsche Forschungsgemeinschaft, DFG) for providing this research's financial support and the tremendous scientific opportunities within the MARIE Transregio 196 collaborative research center.

I would like to thank all the other colleagues and former members of the IHCT group. These include (in no particular order) Martina Grabowski, Dr. Pedro Rodríguez Vazquez, Eamal Ashna, Utpal Kalita, Dr. Dominika Warmowska, Dr. Vishal S. Jagtap, Dr. Laven Mavarani, Marc Hannapel, Wolfgang Förster, Hamadi Sadkaoui, Abdulraouf Kutaish, Dr. Nada Badraoui, Ehsan Hamzeh, and Dr. Richard Al Hadi. Many of them have contributed directly or indirectly to my Ph.D. work. Special thanks to Thomas Bücher, Arjith Chandra Prabhu and Hans M. Keller who spent their valuable time in proofreading this work. Further, Dr. Phillip Hillger and Dr. Stefan Malz supported me from the beginning by teaching me all the required RF design tools.

My major gratefulness is dedicated to my parents for their support during my education and my wonderful wife, Yvi, for understanding the large effort of this thesis and standing by my side the whole time. Even though I could rarely show it during the last few years, she and my daughter Ophelia are the center of my world.

Publications

Journal Publications

1. J. Grzyb, **M. Andree**, R. Jain, B. Heinemann and U. R. Pfeiffer, "A Lens-Coupled On-Chip Antenna for Dual-Polarization SiGe HBT THz Direct Detector," in IEEE Antennas and Wireless Propagation Letters, vol. 18, no. 11, pp. 2404-2408, Nov. 2019, doi: 10.1109/LAWP.2019.2927300

2. P. Hillger, M. van Delden, U. S. M. Thanthrige, A. M. Ahmed, J. Wittemeier, K. Arzi, **M. Andree**, B. Sievert, W. Prost, A. Rennings, D. Erni, T. Musch, N. Weimann, A. Sezgin, N. Pohl, U. R. Pfeiffer, "Toward mobile integrated electronic systems at THz frequencies", J. Infr. Millim. THz Waves, vol. 41, no. 7, pp. 846-869, 2020

3. A. Hemmetter, X. Yang, Z. Wang, M. Otto, B. Uzlu, **M. Andree**, U. Pfeiffer, A. Vorobiev, J. Stake, M.C. Lemme, D. Neumaier, "Terahertz Rectennas on Flexible Substrates Based on One-Dimensional Metal–Insulator–Graphene Diodes", ACS Appl. Electron. Mater. 2021,3, 3747–3753

4. J. Grzyb, P. Rodríguez-Vázquez, S. Malz, **M. Andree** and U. R. Pfeiffer, "A SiGe HBT 215–240 GHz DCA IQ TX/RX Chipset With Built-In Test of USB/LSB RF Asymmetry for 100+ Gb/s Data Rates," in IEEE Transactions on Microwave Theory and Techniques, vol. 70, no. 3, pp. 1696-1714, March 2022, doi: 10.1109/TMTT.2021.3127897

5. **M. Andree**, J. Grzyb, R. Jain, B. Heinemann and U. R. Pfeiffer, "Broadband Modeling, Analysis, and Characterization of SiGe HBT Terahertz Direct Detectors," in IEEE Transactions on Microwave Theory and Techniques, vol. 70, no. 2, pp. 1314-1333, Feb. 2022, doi: 10.1109/TMTT.2021.3134646.

Conference Publications

1. **M. Andree**, J. Grzyb, R. Jain, B. Heinemann and U. R. Pfeiffer, "A Broadband Dual-Polarized Terahertz Direct Detector in a 0.13-µm SiGe HBT Technology," 2019 IEEE MTT-S International Microwave Symposium (IMS), Boston, MA, USA, 2019, pp. 500-503, doi: 10.1109/MWSYM.2019.8700871
2. **M. Andree**, J. Grzyb, R. Jain, B. Heinemann and U. R. Pfeiffer, "A Broadband Antenna-Coupled Terahertz Direct Detector in a 0.13-µm SiGe HBT Technology," 2019 14th European Microwave Integrated Circuits Conference (EuMIC), Paris, France, 2019, pp. 168-171, doi: 10.23919/EuMIC.2019.8909399
3. J. Grzyb, **M. Andree**, R. Jain, B. Heinemann and U. R. Pfeiffer, "Low-NEP Room-Temperature Broadband THz Direct Detection with a 0.13-µm SiGe HBT Device," 2020 45th International Conference on Infrared, Millimeter, and Terahertz Waves (IRMMW-THz), Buffalo, NY, USA, 2020, pp. 1-2, doi: 10.1109/IRMMW-THz46771.2020.9370542.
4. **M. Andree**, J. Grzyb, B. Heinemann and U. Pfeiffer, "A D-Band to J-Band Low-Noise Amplifier with High Gain-Bandwidth Product in an Advanced 130 nm SiGe BiCMOS Technology," 2023 IEEE Radio Frequency Integrated Circuits Symposium (RFIC), San Diego, CA, USA, 2023, pp. 137-140, doi: 10.1109/RFIC54547.2023.10186116.
5. J. Grzyb, **M. Andree**, P. Hillger, T. Bücher and U. R. Pfeiffer, "A Balun-Integrated On-Chip Differential Pad for Full/Multi-Band mmWave/THz Measurements," 2023 IEEE/MTT-S International Microwave Symposium - IMS 2023, San Diego, CA, USA, 2023, pp. 186-189, doi: 10.1109/IMS37964.2023.10187952.
6. **M. Andree**, V. Jagtap, J. Grzyb and U. Pfeiffer, "A Broadband Dual-Polarized Low-NEP SiGe HBT Terahertz Direct Detector for Polarization-Sensitive Imaging," 2023 48th IRMMW-THz, Montreal, QC, Canada, 2023, pp. 1-2, doi: 10.1109/IRMMW-THz57677.2023.10298942.
7. J. Grzyb, **M. Andree**, B. Heinemann, H. Rücker and U. R. Pfeiffer, "On Cold Operation of an SiGe HBT as a Broadband Low-NEP THz Direct Detector," 2023 48th IRMMW-THz, Montreal, QC, Canada, 2023, pp. 1-2, doi: 10.1109/IRMMW-THz57677.2023.10299102.
8. **M. Andree**, V. Jagtap, J. Grzyb, and U. Pfeiffer, "Enabling Fast Polarization THz Imaging using Broadband Dual-polarization SiGe HBT Detectors," Proc. SPIE 12740, Emerging Imaging and Sensing Technologies for Security and Defence VIII, 127400J, Amsterdam, Netherlands, 2023, doi: 10.1117/12.2678549

Contribution of Others

This work was conducted at the Institute for High-Frequency and Communication Technology, (IHCT) led by Prof. Dr. rer. nat. Ullrich R. Pfeiffer at the University of Wuppertal. This work would not be possible without the contributions of other group members. Some circuit blocks, passives, and antennas in this thesis are designed by IHCT group members. These other contributions are listed below. The research not included in the following list has been conducted by myself.

Chapter 3: This chapter presents the modeling and design of broadband THz direct detectors coupled to three different antenna versions. These antennas have been designed by Dr. Janusz Grzyb, partly based on circuit simulations conducted by myself. The investigated nonlinear equivalent device model has been further reviewed and validated in extensive discussions with Dr. Janusz Grzyb.

Chapter 4: This chapter provides broadband measurement results and an analysis of the sensitivity of five different direct detectors (detector 1 - 5). Dr. Ritesh Jain has implemented detectors 1, 2, and 4.

Chapter 5: This chapter presents a transformer-based LNA design and the analysis of its measured results. The input-matching transformer design, as well as a transistor core model for another device size, was provided by Dr. Janusz Grzyb.

Chapter 6: This chapter introduces a broadband dual-polarized total power radiometer. The antenna was initially implemented by Dr. Konstantin Statnikov and re-designed and slightly modified by myself. Dr. Janusz Grzyb designed the output transformer of the second polarization path. The measurements have been conducted in close discussion with Dr. Janusz Grzyb.

Abstract

Passive imaging describes the image construction by measuring a scene or an object's naturally occurring heat radiation and is often applied in radio astronomy or security screening. The sensitivity of such a passive imaging system is expressed as noise equivalent temperature difference (NETD), the minimum resolvable object temperature difference. Well-known systems are already commercially available in the infrared (IR) and millimeter wave (mmWave) frequency range, but either lack a sub-millimeter resolution or sufficient penetration depth into common materials. By providing both, Terahertz (THz) waves defined in the frequency range from 100 GHz to 10 THz, known for their 'see-through' capability through many common materials, are a perfect candidate for passive imaging. Due to the challenging demands in sensitivity and bandwidth, most THz passive imaging systems require cryogenic cooling or are bulky III-V-based split-block assemblies. These drawbacks can be overcome by silicon technologies, which offer low-cost, miniaturized integrated circuits (ICs) and a high yield.

For this purpose, this thesis presents the fundamental requirements for passive imaging in the THz frequency range based on the most important system parameters such as bandwidth, noise equivalent power (NEP), and integration time. Further, the realization and analysis of the fundamental limitations of passive imaging systems operating in the THz frequency range with uncooled, incoherent, silicon-integrated silicon-germanium (SiGe) heterojunction bipolar transistor (HBT) receiver circuits are studied.

The central contributions of this work can be divided into two technology-dependent parts. In the first part, the frequency range close to and above the technology's maximum oscillation frequency f_{max} where only the transistors' nonlinearity can be used for signal detection is investigated. Here, a comprehensive analysis of THz direct detectors based on a developed nonlinear equivalent model and an accurate antenna-detector co-design paved the way for new detector designs operating in the 200 GHz to 1 THz frequency band with a state-of-the-art sensitivity in terms of NEP down to 1.9 pW/$\sqrt{Hz}$ at 300 GHz. Together with a large equivalent operation bandwidth of

500 GHz and based on measurements with a broadband black body source, NETD values down to 0.64 K in a 1 Hz readout bandwidth are demonstrated, which is well below the value of 1 K commonly cited as the threshold for effective detection of concealed objects in security screening.

In the second part below $f_{max}/2$, where transistors provide sufficient gain, the focus is on developing a low-noise amplifier (LNA) for integration in a total power radiometer. The LNA exploits coupled-line transformer matching and cascode stages implemented based on accurate core modeling and passive co-design. A gain of 34.6 dB, a minimum Noise Figure of 8.4 dB and a 3 dB bandwidth of 146 GHz at a center frequency of 201.5 GHz are presented. Co-designed and combined with a dual-polarized antenna at the input and a direct detector at the output, a total power radiometer is shown, offering an equivalent bandwidth of up to 147 GHz and a minimum NEP of 22 fW/$\sqrt{Hz}$. This enables a minimum NETD of 102 mK that was measured and calculated for real-time acquisition of 40 frames per second (fps) in a single polarization path.

This thesis finally demonstrates passive imaging with SiGe HBT THz direct detectors by raster-scanning a 100 °C hot resistor in a 500 ms integration time and a real-time passive imaging capability of the designed total power radiometer by raster-scanning a human finger applying a 65 ms integration time. Based on a comparison to conventionally recorded IR images, the unique ability of THz waves to detect hidden hot spots is impressively presented.

Zusammenfassung

Passive Bildgebung beschreibt die Bildkonstruktion durch Messung der natürlichen Wärmestrahlung einer Szene oder eines Objekts und wird häufig in der Radioastronomie oder bei Sicherheitsüberprüfungen eingesetzt. Die Empfindlichkeit eines passiven Bildgebungssystems wird als rauschäquivalente Temperaturdifferenz (NETD) ausgedrückt, welche der minimal auflösbaren Temperaturdifferenz entspricht. Im Infrarotbereich (IR) und Millimeterwellenbereich (mmWave) sind bereits kommerziell vermarktete Systeme erhältlich. Diese verfügen allerdings nicht über eine Auflösung im Submillimeterbereich oder eine ausreichende Eindringtiefe in gängige Materialien. Terahertz-Wellen (THz) im Frequenzbereich von 100 GHz bis 10 THz, die bekannt dafür sind verschiedene Materialen zu durchdringen, bieten beides. Daher sind sie ein perfekter Kandidat für die passive Bildgebung. Aufgrund der hohen Anforderungen an Empfindlichkeit und Bandbreite benötigen die meisten passiven THz Bildgebungssysteme eine kryogene Kühlung oder basieren auf vergleichsweise großen III-V Schaltungen integriert in Split-Block Wellenleitern. Diese Nachteile können durch Siliziumtechnologien überwunden werden, da sie kostengünstige, miniaturisierte integrierte Schaltungen (ICs) und eine hohe Ausbeute bieten.

Zu diesem Zweck werden in dieser Arbeit die grundlegenden Anforderungen an die passive Bildgebung im THz-Frequenzbereich anhand der wichtigsten Systemparameter wie Bandbreite, rauschäquivalente Leistung (NEP) und Integrationszeit untersucht. Weitergehend wird die Realisierung und Analyse der grundsätzlichen Grenzen von passiven bildgebenden Systemen im THz-Frequenzbereich mit ungekühlten, inkohärenten, siliziumintegrierten Silizium-Germanium (SiGe) Heteroübergangs - Bipolartransistor (HBT) Empfängerschaltungen untersucht. Die zentralen Beiträge dieser Dissertation lassen sich in zwei technologieabhängige Teile gliedern.

Im ersten Teil wird der Frequenzbereich nahe und oberhalb der maximalen Oszillationsfrequenz f_{max} der Technologie untersucht, in dem nur die Nichtlinearität der Transistoren zur Signaldetektion genutzt werden kann. Eine umfassende Analyse von THz-Direktdetektoren auf der Grundlage eines entwickelten nichtlinearen Transistormodells und eines präzisen Antennen-Detektor-Co-Designs ebnete den Weg für neue Detektordesigns, die im Frequenzband von 200 GHz bis 1 THz mit einem NEP auf dem Stand der Technik von bis zu 1,9 pW/$\sqrt{Hz}$ bei 300 GHz arbeiten. Zusammen mit einer großen äquivalenten Bandbreite von 500 GHz und auf der Grundlage von Messungen mit einer breitbandigen Schwarzkörperquelle werden NETD-Werte von bis zu 0,64 K in einer Auslesebandbreite von 1 Hz nachgewiesen, die deutlich unter dem Wert von 1 K liegen, der gemeinhin als Schwellenwert für die wirksame Erkennung verborgener Objekte bei Sicherheitsüberprüfungen genannt wird.

Im zweiten Teil unterhalb von $f_{max}/2$, in dem Transistoren eine ausreichende Verstärkung bieten, liegt der Schwerpunkt auf der Entwicklung eines rauscharmen Verstärkers (LNA) zur Integration in ein Radiometer. Der LNA nutzt die Anpassung von Transformatoren mit gekoppelten Leitungen und Kaskodenstufen, die auf der Grundlage einer genauen Transistor-Kernmodellierung und eines passiven Co-Designs implementiert wurden. Es werden eine Verstärkung von 34,6 dB, eine minimale Rauschzahl von 8,4 dB und eine 3 dB-Bandbreite von 146 GHz bei einer Mittenfrequenz von 201,5 GHz präsentiert. Das Radiometer, welches aus einer Kombination des LNAs mit einer dualpolarisierten Antenne am Eingang und einem Direktdetektor am Ausgang besteht, verfügt über eine äquivalente Bandbreite von 147 GHz und ein minimales NEP von 22 fW/$\sqrt{Hz}$. Dies ermöglicht minimale NETD-Werte von 102 mK, welche für eine Echtzeit-Erfassung von 40 Frames pro Sekunde (fps) in einem einzigen Polarisationspfad berechnet wurde.

Diese Arbeit demonstriert schließlich die passive Bildgebung mit SiGe HBT THz-Direktdetektoren durch Rasterabtastung eines 100 °C heißen Widerstandes in einer Integrationszeit von 500 ms und die passive Detektion eines menschlichen Fingers mit Hilfe des entwickelten Radiometers in einer 65 ms Integrationszeit. Anhand eines Vergleichs mit konventionell aufgezeichneten IR-Bildern wird die einzigartige Fähigkeit von THz-Wellen, versteckte heiße Stellen zu erkennen, eindrucksvoll dargestellt.

Chapter 1

Introduction

The Terahertz (THz) frequency spectrum comprises electromagnetic waves within the frequency range of 100 GHz to 10 THz [1]. It is sometimes also defined as submillimeter wave (submmWave) frequency range from 300 GHz to 3 THz [2]. As shown in Figure 1.1, THz waves lie between the microwave or millimeter wave (mmWave) and infrared regions of the electromagnetic spectrum. With around 0.4 to 40 meV [3] THz radiation does not possess enough photon energy for molecular ionization contrary to well investigated X-rays [4]. THz waves have many unique properties and advantages compared to infrared (IR), mmWave, and X-ray radiation, which are used in diverse applications across various fields and are briefly summarized below.

- **Communication**: THz waves offer the potential for extremely high data rates higher than 100 Gbps in wireless communications [own1] and build the fundament of the next generations of wireless communication systems (6G) [5] due to their large fractional bandwidth compared to mmWaves [6].

- **Imaging**: THz waves can penetrate certain materials without the harmful ionizing effects associated with X-rays, making them suitable for medical imaging [7] and active and passive security screening [8] and allow a better (submmWave) resolution compared to mmWaves.

- **Spectroscopy**: THz waves interact with molecular vibrations and rotations, enabling THz spectroscopy to provide information about molecular structures and chemical compositions [9], i.e., for the chemical recognition of gases and gas mixtures [10]. In more detail, THz spectroscopy systems make use of the emission or absorption lines for the rotational and vibrational excitations of

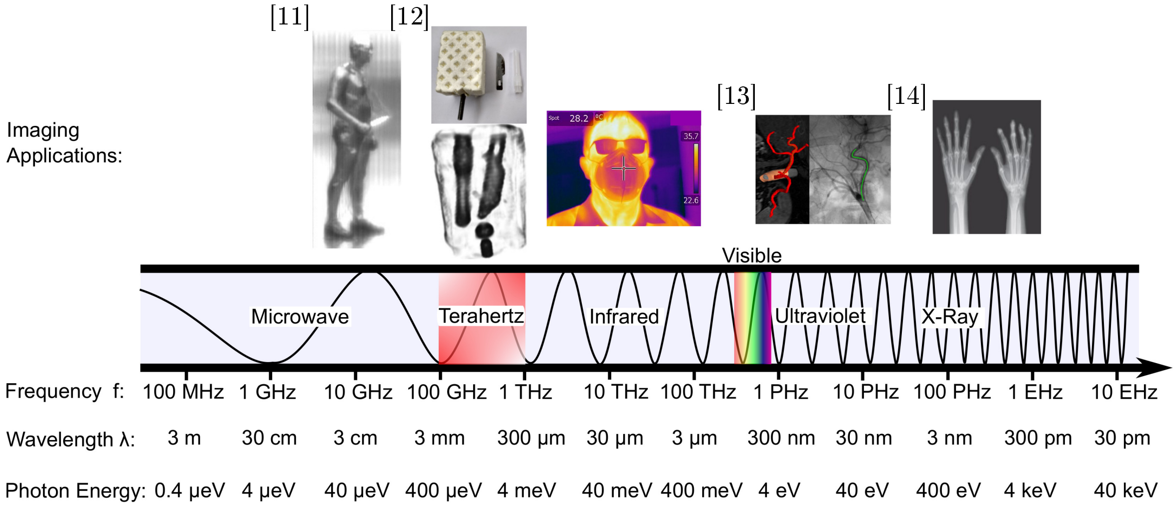

Figure 1.1: Electromagnetic spectrum from microwaves to X-rays, including imaging examples. Images after [11] ©2007 IEEE, [12] ©2019 IHCT, [13] ©2023 IEEE, [14] ©2023 IEEE.

lighter molecules. The strength of these lines often peaks in the THz frequency range, thus resulting in a strong natural sensitivity and advantages against the mmWave frequency range [2].

- **Radar Sensing**: Radar systems benefit from the large achievable bandwidths leading to range resolutions in the millimeter and submillimeter range [15], [16].

Providing all these unique properties, the small THz wavelengths (see Figure 1.1) allow monolithic integration of complete electronic systems, including active circuits and passive structures such as transmission lines, couplers, or antennas on a single silicon chip.

The investigations in this dissertation are funded by the mentioned inherent advances of the THz frequency range and focus on the development of silicon-integrated circuits for passive imaging applications. Therefore, the following sections present an extended overview of the challenges and applications of active and passive THz imaging. In the latter case, a comparison to conventional passive imaging in the IR frequency range is introduced to motivate the development of new silicon-integrated sensors in the field of THz passive imaging. At the end of this chapter, the central research questions of the thesis are formulated and the original contributions, as well as the thesis structure are introduced.

1.1 Active Terahertz Imaging

Up to now, the unique properties of electromagnetic (EM) waves emitted at THz frequencies, such as transparency of many common materials like plastic or cardbox [own2], [17] and its low non-ionizing electron power levels paved the way to many imaging applications in several research and industry relevant fields [18]. A particular interest in the THz frequency range exists for medical imaging applications in microscopy for cell identification [19], skin and breast cancer monitoring [7], [20], spectroscopy analysis of several tissues [21], radio astronomy [22], and quality inspection in non-destructive testing [23] where several advanced techniques such as polarization sensitive imaging can be applied [24] [own3],[own4]. Unfortunately, many systems for THz power generation, including time-domain spectroscopy (TDS) systems [25], or vector network analyzer (VNA) extender modules relying on split block hollow waveguide connections are mostly bulky or not able to generate sufficient power. Due to the latter fact, the THz frequency range is often referred to as the THz gap, where both electronic and photonic components cannot efficiently convert electrical power into electromagnetic radiation due to the small carrier velocities and the lack of appropriate bandgaps [26], [27] making THz power generation extremely challenging.

To accommodate these issues, silicon technologies are a perfect choice, not only due to their high yield, small feature size and good integration capabilities but also due to the latest development in the semiconductor industry resulting in SiGe HBTs with f_t/f_{max} of 505/700 GHz [28]. Despite significant advances, silicon is still lacking the performance of III-V semiconductors, currently reaching f_{max} above 1 THz [29] and f_t/f_{max} of up to 0.61/1.5 THz [30]. However, several high-performance, silicon-integrated THz imaging chips have been implemented in recent years. Starting from fully integrated THz video cameras with more than 1000 pixels [31], [32], heterodyne systems [33], [34], THz sources [35] and source arrays [36]. Further nearfield arrays [37] were presented, and experiments focusing on 3D CT imaging [38] entirely based on silicon ICs were introduced.

1.2 Passive Terahertz Imaging

Despite these tremendous advances in silicon technologies, passive imaging funded in measuring an object's THz radiation due to its specific heat is rarely demonstrated in uncooled systems, as the natural ambient THz radiation is weak [2]. This request is almost exclusively done with III-V semiconductor front-ends [39], micro-bolometers [40], [41] or in the IR frequency range from 10 THz to 430 THz, benefitting from the approximately 100 times higher photon energy and an image resolution of several µm exceeding the resolution of THz imaging systems by up to two orders of magnitude [42].

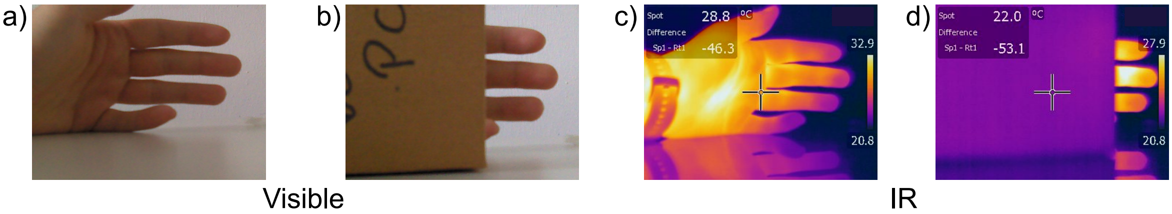

Figure 1.2: Images of a human hand.
a)-b) Visible images with and without cardbox covering (0.4 mm thickness).
c)-d) Corresponding IR images.

The uncooled signal detection for passive imaging in the IR region relies on devices such as barrier infrared detectors [43], pyroelectric detectors [44] or bolometers [45]. It is further already exploited in many commercially available IR cameras [46], [47]. However, the main drawback of passive IR sensing is the low penetration depth of the emitted radiation through many materials. This drawback of passive imaging in the IR frequency range is emphasized in Figure 1.2. Here, visible and IR images of a cardbox-covered human hand recorded with a commercially available FLIR T450sc IR camera operating in a spectral range from 40 to 23 THz (7.5 to 13 µm) are compared. Most important to note is that already a 0.4 mm thick cardbox entirely blocks the human hand's IR radiation in this spectral range and makes IR an inappropriate option for see-through security screening. To overcome this effect, THz and mmWaves are suitable candidates.

In the THz frequency range, complete passive imaging systems have been developed, but they mostly rely on bulky [48], waveguide-based [49] or (cryogenically) cooled III-V sensor architectures or scenes [50]–[52]. In the mmWave frequency range, where amplifiers usually are developed operating around $f_{max}/2$ [53], also silicon-integrated pre-amplified incoherent circuits as well as coherent implementations for radiometry have been presented in the literature. Based on sufficient gain available, these systems were focusing on operating ranges around 100 GHz [54]–[57]. However, even reaching good minimum resolvable temperature differences, passive images recorded with uncooled silicon-integrated detection circuits above 200 GHz have rarely been published.

First images were recorded with THz direct detectors [58], [59]. Despite their reduced sensitivity, passive imaging can be achieved with large detection bandwidths of several hundred GHz [60], as the emitted power described by Planck's law is integrated among the entire frequency range [61]. Nevertheless, currently recorded passive images with uncooled silicon-integrated THz direct detectors lack the sensitivity for concealed weapon detection in security screening or require large pixel integration times of several minutes. Therefore, the main research questions in this thesis will address the design and development of real-time passive imaging receivers within silicon technologies.

1.3 This Dissertation

In the preceding introduction, preliminary knowledge about active and passive THz imaging and their corresponding applications was built up. A brief review of the current state-of-the-art in THz imaging was given and it was pointed out that silicon-integrated, room-temperature-operated THz detection circuits for passive imaging applications rarely exist at frequencies above 100 GHz. Associated with this fact, the subject matter of this dissertation will be discussed based on the following research questions.

1.3.1 Primary Research Questions

The investigations in this thesis are based on the following central research question.

Central Research Question

How to build silicon-integrated, room-temperature operated detection circuits sensitive enough for passive imaging in the THz frequency band?

Different direct detection receivers are proposed as the answer to the above problem. The sensitivity, bandwidth and integration time trade-offs will be investigated for two operation regions (**I** and **II**) of silicon-integrated SiGe HBT-based circuits.

I: Below f_{max} where transistors can provide gain.

II: Close to and above f_{max} where only the devices' nonlinearity can be exploited.

In region **I**, pre-amplified direct detection architectures comprise an LNA that highly enhances the radiometer's sensitivity. Contrary to this, standalone direct detectors exploited in region **II** require a very high bandwidth for passive imaging in the sub-mmWave and THz frequency range. Further, the sensitivity, bandwidth and integration time directly influence the typical figure of merit for passive imaging systems: The noise equivalent temperature difference (NETD). This, in other words, is the smallest temperature resolution such a system can resolve and should be as small as possible. In the literature, NETDs of 1 K are commonly cited as acceptable thresholds for effective concealed object detections [62], [63], wherein commercially available infrared cameras achieve typical values of around 40 mK in real-time operation. Efforts focused on enhancing the NETD for both operation ranges, resulting in derived research questions that are also strongly related to the primary research question.

Derived Research Questions

- Can a compact LNA-based radiometer be designed with enough sensitivity to detect buried objects without active illumination in the frequency range from 100 GHz to 300 GHz, providing a NETD less than 0.5 K for real-time passive imaging?
- How far can the sensitivity and bandwidth of silicon-integrated SiGe HBT direct detectors be improved towards THz passive imaging at room temperature?
- Can THz passive imaging be demonstrated in a (real-time) imaging system?

1.3.2 Original Contributions

The primary contribution of this thesis towards real-time THz passive imaging in silicon technologies is the development and analysis of several uncooled, fully-packaged, antenna-coupled direct detection circuits implemented in advanced 130 nm silicon-germanium (SiGe) heterojunction bipolar transistor (HBT) technologies [own5]–[own9]. On the one hand, the thesis provides the (co-)design challenges and optimum operating conditions for antenna-coupled THz direct detectors. It analyses the internal device rectification process with an equivalent nonlinear device model. This way, it evaluates the influence of each parasitic device component on the maximum device sensitivity and its limitations for further device technologies.

On the other hand, this thesis presents the broadband design, implementation and measurement challenges of high-gain LNAs. A broadband LNA is implemented after a precise transistor core EM co-design with passive transformer-based matching structures in a detector-coupled radiometer chipset. To the best of the author's knowledge, the presented LNA is the world's first silicon-integrated LNA operating above 200 GHz with more than 100 GHz bandwidth and more than 30 dB gain [own10]. Finally, this thesis demonstrates NEP, responsivity and NETD measurements of packaged direct detectors and radiometer circuits in a broad frequency range from 200 GHz to 1 THz. Here, a state-of-the-art NETD smaller than 1 K is highlighted for a detector with an equivalent bandwidth of 500 GHz, an integration time of 500 ms, and a radiometer operating from 150 GHz to 280 GHz in real-time with 40 ms signal integration. Moreover, the thesis presents the first passively recorded images of several hot objects with SiGe HBTs in a frequency range above 200 GHz.

1.3.3 Structure

This dissertation is divided into seven chapters and organized as follows.

Chapter 1: Introduction. The motivation, scientific background, and state-of-the-art of THz passive imaging with room-temperature-operated, silicon-integrated THz detection circuits are presented in Chapter 1.

Chapter 2: Fundamentals of Passive Imaging. Chapter 2 provides the theoretical background for passive imaging in the THz frequency domain. Based on Planck's law and the Rayleigh-Jeans approximation in the THz frequency range, the most crucial figures of merit of direct detection circuits for passive imaging are derived.

Chapter 3: Modeling and Design of Broadband SiGe HBT THz Direct Detectors. Chapter 3 presents the development of a nonlinear equivalent model for SiGe HBT direct detectors that helps to understand the device-limiting parasitics' influence on the detector sensitivity in the THz frequency range. Further, the detector-antenna co-design approach based on constant responsivity contours is briefly introduced and the optimum device biasing conditions are derived.

Chapter 4: Detector Characterization and Measurements. In Chapter 4, the experimental characterization of various developed direct detector circuits in terms of NEP and NETD is described.

Chapter 5: Broadband Low Noise Amplifier Design and Measurements. Chapter 5 provides the information required for a broadband high-gain, low-noise amplifier design and its characterization across an operation range of more than 100 GHz.

Chapter 6: Radiometer Design and Measurements. Chapter 6 focuses on the radiometer design. It gives insights into several aspects, such as antenna implementation and antenna detector matching, and provides a general analysis of the radiometer performance. Further, the experimental characterization of the NEP and NETD is exploited and a real-time passive imaging setup is described.

Chapter 7: Conclusions and Outlook In Chapter 7, the dissertation's work is summarized and suggestions for future research toward real-time passive imaging THz cameras with in-pixel integrated readout circuits are given.

Chapter 2

Fundamentals of Passive Imaging

The theoretical fundamentals serving as the basis to understand the operating principle and design trade-offs of the developed receiver circuits in the submmWave and THz frequency range for passive imaging are based on the investigations of Max Planck on heat radiation starting around 1896 [61].

2.1 Planck's Law

In 1900, Max Planck published an equation correctly describing thermal black body radiation across the whole frequency spectrum for the first time [64]. With Planck's law, the spectral radiance B of an ideal black body source of area A, radiating over a solid angle Ω_s, at a temperature T can be described as

$$B(f,T) = \frac{2 \cdot h \cdot f^3}{c^2} \cdot \frac{1}{e^{\frac{hf}{k_B T}} - 1}, \tag{2.1}$$

where h is the Planck constant ($6.62 \cdot 10^{-34}$ Js), c the speed of light ($2.99 \cdot 10^{8}$ m/s) and k_B the Boltzmann constant $1.38 \cdot 10^{-23} m^2 kg s^{-1} K^{-1}$. The spectral radiance B is described in $[W \cdot m^{-2} \cdot Hz^{-1} \cdot sr^{-1}]$. In the THz frequency range, Equation 2.1 can be replaced by the Rayleigh-Jeans law where the exponent is approximated by a two-term Taylor Series [65] in the form

$$B_{RJ}(f,T) = \frac{2 \cdot f^2}{c^2} \cdot k_B T. \tag{2.2}$$

An integral across a frequency range from 100 GHz to 2 THz across the spectral radiance defined by the Rayleigh-Jeans approximation results in a maximum deviation of 13 % in comparison to a direct calculation of the integral based on Planck's law.

The feasibility of passive imaging depends on the fact that each object, depending on its temperature, emits electromagnetic radiation, described by Planck's law. The spectral radiance of natural objects is less than that of an ideal black body. Hence, Equation 2.1 needs to be multiplied with a material-specific spectral emissivity $\epsilon_r(f,T) < 1$ [66] that for the following considerations is assumed to be equal to 1. The challenges of passive imaging in the THz frequency range can be directly derived when calculating the radiant exitance M_e, the total emitted power by a surface per unit area [W/m^2]. An expression for M_e can be derived by integrating Equation 2.1 across the hemisphere and the investigated bandwidth assuming diffuse radiation emission

$$M_e(T) = \int_{BW} \int_{\Omega_s} B(f,T) d\Omega_s df \tag{2.3}$$

$$= \int_{f_1}^{f_2} \int_0^{2\pi} \int_0^{\pi/2} \frac{2 \cdot h \cdot f^3}{c^2} \cdot \frac{1}{e^{\frac{hf}{k_B T}} - 1} \sin\Theta \cos\Theta d\Theta d\Phi df \tag{2.4}$$

$$= \int_{f_1}^{f_2} \frac{2 \cdot h \cdot f^3}{c^2} \cdot \frac{\pi}{e^{\frac{hf}{k_B T}} - 1} df = \int_{f_1}^{f_2} \pi B(f,T) df, \tag{2.5}$$

including $d\Omega_s$ as $\sin\Theta d\Theta d\Phi$. The factor $\cos\Theta$ is present as each black body radiator behaves as a Lambert radiator. An integral of Equation 2.3 across the whole frequency range results in the Stefan Boltzmann law [67] describing the total radiated power of an ideal black body with area A as

$$P = M_e(T) \cdot A = \sigma \cdot T^4, \tag{2.6}$$

where σ equals $5.670 \cdot 10^{-8}$ $[W/(m^2 \cdot K^4)]$. Important to note is that the total emitted black body power only depends on the body's temperature. The spectral radiance of an ideal black body source is illustrated in Figure 2.1, assuming an arbitrarily chosen object with a uniformly distributed surface temperature of 293 K (approximately 20 °C). The radiated power per m^2 ($M_{e,THz}$ - blue) in the investigated THz frequency range (100 GHz to 2 THz) is more than two orders of magnitude smaller than $M_{e,IR}$ (red) in the longwave infrared region (≈ 20 to 37.5 THz), in which most commercially available IR cameras operate.

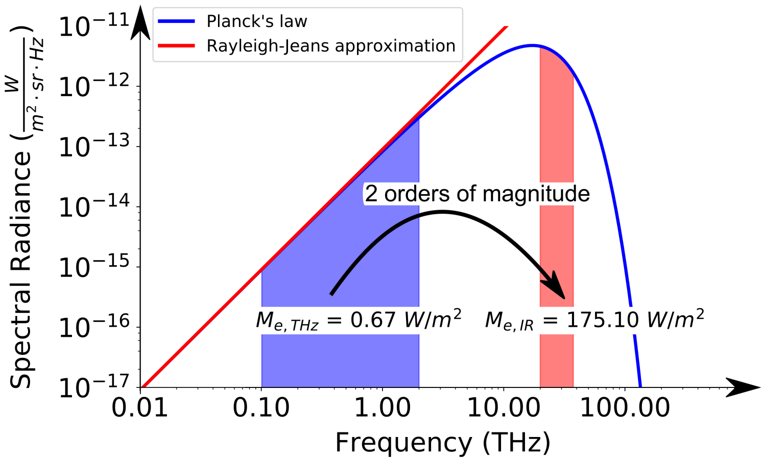

Figure 2.1: Spectral radiance of an ideal black body with T = 293 K and calculated radiant exitance M_e in a portion of the THz (100 GHz to 2.0 THz) and IR (20 to 37.5 THz) frequency range.

2.2 The View Factor

A view or configuration factor defines the radiation heat transfer between diffusely radiating surfaces. Thus, it is an important quantity to calculate the total power received by an antenna-coupled THz detector or radiometer circuit based on the antenna effective area A_{eff}. A view factor F_{ij} is the fraction of radiation leaving a surface A_i that is intercepted by another surface A_j [68]. A general equation of the view factor between two surfaces can be derived based on Figure 2.2 a) assuming an ideal diffuse radiation of all surfaces. Here, two ideal black surfaces, A_1 and A_2 with an isotropic heat distribution, are arbitrarily oriented in a three-dimensional room. dA_1 and dA_2 are the differential surfaces separated by distance d under an angle Θ_1 and Θ_2 to the surface normals n_1 and n_2, respectively. In this case, the view factor F_{12} can be expressed as

$$F_{12} = \frac{P_{12}}{M_{e1}(T) \cdot A_1}, \tag{2.7}$$

with P_{12} as power emitted by A_1 and received by A_2. To calculate P_{12} first the differential power emitted by dA_1 and received by dA_2 (dP_{12}) needs to be considered. It can be expressed based on Equation 2.1 as

$$dP_{12} = \int_{f_1}^{f_2} B(f,T) \cdot \cos\Theta_1 dA_1 d\omega_{21} df, \tag{2.8}$$

where ω_{21} is the solid angle subtended by dA_2 from the perspective of dA_1, which is $\cos\Theta_2 dA_2/d^2$ and indicated in Figure 2.2 a). With Equation 2.5 it follows

$$dP_{12} = M_{e1}(T)\frac{\cos\Theta_1 cos\Theta_2}{\pi d^2}dA_1 dA_2. \tag{2.9}$$

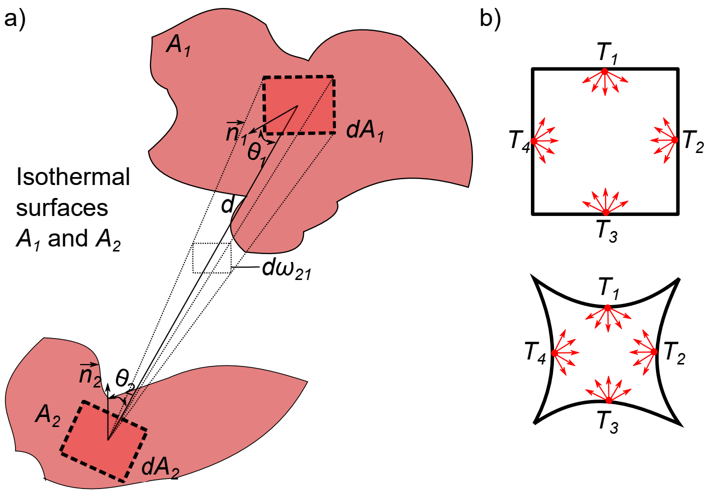

Figure 2.2: a) Illustration of isothermal surfaces for view factor calculation.
b) Radiation exchange in plane and convex enclosures resulting in $F_{ii} = 0$.

The total power emitted by surface A_1 and received by A_2 is then defined by integrating Equation 2.9 across both surfaces, resulting in

$$P_{12} = M_{e1}(T) \int_{A2} \int_{A1} \frac{\cos \Theta_1 cos\Theta_2}{\pi d^2} dA_1 dA_2, \tag{2.10}$$

under the assumption of a uniform M_{e1}(T) across A_1. Substituting Equation 2.10 into Equation 2.7 results in the general view factor integral

$$F_{12} = \frac{1}{A_1} \int_{A2} \int_{A1} \frac{cos\Theta_1 cos\Theta_2}{\pi d^2} dA_1 dA_2. \tag{2.11}$$

With the same derivation based on the emitted radiation of surface A_2, F_{21} is obtained as

$$F_{21} = \frac{1}{A_2} \int_{A2} \int_{A1} \frac{cos\Theta_1 cos\Theta_2}{\pi d^2} dA_1 dA_2. \tag{2.12}$$

2.2.1 Important View Factor Rules

Many view factor calculations can be completed without the complex solution of the integral shown in Equation 2.11 but with simple view factor relations known as view factor algebra that is derived in the following [67], [68].

2.2.1.1 Reciprocity

The total radiation leaving A_1 and A_2 is $A_1 \cdot M_{e1}(T)$ and $A_2 \cdot M_{e2}(T)$, respectively. Thus, the power P_{12} emitted by surface A_1 and received by surface A_2 as well as P_{21}

as power emitted by surface A_2 and received by surface A_1 are defined as

$$P_{12} = M_{e1}(T) \cdot A_1 \cdot F_{12}, \tag{2.13}$$

$$P_{21} = M_{e2}(T) \cdot A_2 \cdot F_{21}. \tag{2.14}$$

If both surfaces have the same temperature, it follows $M_{e1} = M_{e2}$ and $P_{12} = P_{21}$ (no heat flow between the surfaces), which results in the reciprocity theorem that in his general form is

$$A_i \cdot F_{ij} = A_j \cdot F_{ji}. \tag{2.15}$$

2.2.1.2 Summation Rule in Enclosures

Inside an enclosed room, all radiation emitted by a surface A_i is completely intercepted by the room border (enclosure) surfaces as shown in Figure 2.2 b). In other words, the fractional power emitted by A_i and received by all enclosure surfaces adds up to 1, resulting in the enclosure rule for N enclosed surfaces

$$\sum_{j=1}^{N} = F_{ij} = 1. \tag{2.16}$$

Most commonly, the view factor relations are used in a view factor matrix form as

$$F = \begin{bmatrix} F_{11} & F_{12} & \cdots & F_{1N} \\ F_{21} & F_{22} & \cdots & F_{2N} \\ \vdots & \vdots & \vdots & \vdots \\ F_{N1} & F_{N2} & 1 & F_{NN} \end{bmatrix}. \tag{2.17}$$

With Equation 2.16, it follows that the sum of each line in the view factor matrix adds up to 1 in an enclosure.

2.2.1.3 Plane and Convex Surfaces

As indicated in Figure 2.2 b), the fraction of radiation emitted by a surface A_i and intercepted by the same surface A_i is 0 for plane and convex surfaces, resulting in

$$F_{ii} = 0. \tag{2.18}$$

The in this chapter derived equations are important for later discussions and NETD calculations in Section 4.2.

2.3 CW Signal Detection with THz Direct Detectors

THz direct or square law detectors consist of antenna-coupled nonlinear devices such as Schottky diodes [69], (SiGe) HBTs [70] or MOSFETs [71], where the antenna couples all incident radiation power $P_{Ant}(f)$ with an antenna radiation efficiency $\eta_{Ant}(f)$ to the detecting devices. Further, they convert it to a DC output signal based on their nonlinearity. This output signal is directly proportional to the coupled input power $P_{RF}(f) = P_{Ant}(f) \cdot \eta_{Ant}(f) \cdot \eta_{match}(f)$, which includes a matching-efficiency factor $\eta_{match}(f)$ accounting for the power losses due to a non-ideal antenna-device matching. In a current-mode readout, a small rectified DC current ΔI_{DC} can be measured, while in a voltage-mode readout, the detector is loaded with an output resistance resulting in a rectified DC voltage signal ΔV_{DC}. The strength of this RF to DC conversion can be quantified when the ratio of the DC output signal to the RF input power is built, corresponding to the detector current R_i [A/W] or voltage responsivity R_v [V/W] [72].

$$R_i = \frac{\Delta I_{DC}}{P_{Ant}} \qquad\qquad R_v = \frac{\Delta V_{DC}}{P_{Ant}}. \tag{2.19}$$

The responsivity is generally reported with P_{Ant} instead of P_{RF} in the denominator. Thus, the calculated detector responsivity includes all relevant loss mechanisms down to the device level ($\eta_{Ant}(f)$, $\eta_{match}(f)$), preventing an overestimation of the investigated detector circuits. The responsivity is commonly measured in a free-space setup with the input signal provided by a continuous wave radiation source.

To quantify its detection capability, the most important quantity for detector operation is the signal-to-Noise-Ratio at the output (SNR_o). For room-temperature operated detectors, the output noise is limited by the device output noise itself (mostly shot, thermal or flicker noise). The most important figure of merit for THz direct detectors is its noise equivalent power NEP [W/$\sqrt{Hz}$], as the input RF power level at the antenna, resulting in an SNR of 1 at the detector output. It is defined as ratio of the output current (i_n) or voltage (v_n) noise spectral density and the corresponding responsivity

$$NEP = \frac{i_n}{R_i} \qquad\qquad NEP = \frac{v_n}{R_v}. \tag{2.20}$$

Equation 2.20 is valid for a 1 Hz bandwidth, corresponding to a 0.5 s integration time τ_I. For other integration times, Equation 2.20 is multiplied by a factor $1/\sqrt{2 \cdot \tau_I}$ [73], as long as white noise is the dominant noise source at the detector output.

For the following considerations, a voltage-mode readout is assumed. By substituting the responsivity with Equation 2.19 and including the equation for the signal-to-noise-ratio $SNR_o = \Delta V_{DC}/v_n$ at the detector output, a relation between the NEP and the detector SNR_o is obtained

$$NEP = \frac{P_{RF}}{SNR_o}. \tag{2.21}$$

Another important system parameter is the detector noise factor F, defined as the ratio between the detector input and output SNR ($F = SNR_i/SNR_o$) that yields its Noise Figure (NF) when evaluated in dB [74]. An equation for F is obtained by including Equation 2.21 in the noise factor definition

$$F = \frac{SNR_i}{P_{RF}} \cdot NEP. \tag{2.22}$$

Under the assumption of a complex-conjugated detector-antenna power match with $\eta_{match} = 1$ and an ideal antenna radiation efficiency without Fresnel losses ($\eta_{Ant} = 1$), the SNR_i can be replaced by

$$SNR_i = \frac{V_{Ant}}{v_{n,Ant}} = \frac{\sqrt{R_{Ant} \cdot P_{Ant}}}{\sqrt{4k_B \cdot R_{Ant} \cdot T_{Ant}}}, \tag{2.23}$$

where V_{Ant} is the input voltage at the antenna output (detector input), R_{det} the real part of the detector/antenna input impedance and T_{Ant} the antenna temperature and $v_{n,Ant}$ noise spectral density at the antenna input. If Equation 2.23 and Equation 2.22 are combined, this results in a system noise factor that depends on the input power level

$$F = \frac{\sqrt{R_{Ant} \cdot P_{Ant}}}{\sqrt{4k_B \cdot R_{Ant} \cdot T_{Ant}} \cdot P_{Ant}} \cdot NEP = \frac{1}{\sqrt{4k_B \cdot T_{Ant} \cdot P_{Ant}}} \cdot NEP. \tag{2.24}$$

In other words, the noise factor F decreases with increasing input power. This effect is based on the low detector responsivity and is only valid for detector input powers smaller than -40 dBm. In this case, a rise in detector input power results in an increase in the output signal ΔV_{DC} or ΔI_{DC}, while the output noise stays constant (v_n, i_n). In this form, all equations are only valid in a small bandwidth when operated with a CW source.

2.4 Passive Signal Detection with THz Direct Detectors

In radiometry, small signal power changes due to different object temperatures are detected. As the responsivity $R_v(f)$ or $R_i(f)$ as well as an object's radiated heat power is highly frequency dependent, the temperature-dependent output signal change can only be evaluated by integrating Equation 2.5 across the full detector operation bandwidth. In the following, the maximum detectable output signal change of a single-polarized THz detector is calculated based on its responsivity, assuming a hypothetical case with its room-temperature operated antenna ($\eta_{Ant}(f), \eta_{match}(f) = 1$) located directly on top of an ideal isothermal black body surface with area A_{BB} and temperature T_{BB} as shown in Figure 2.3.

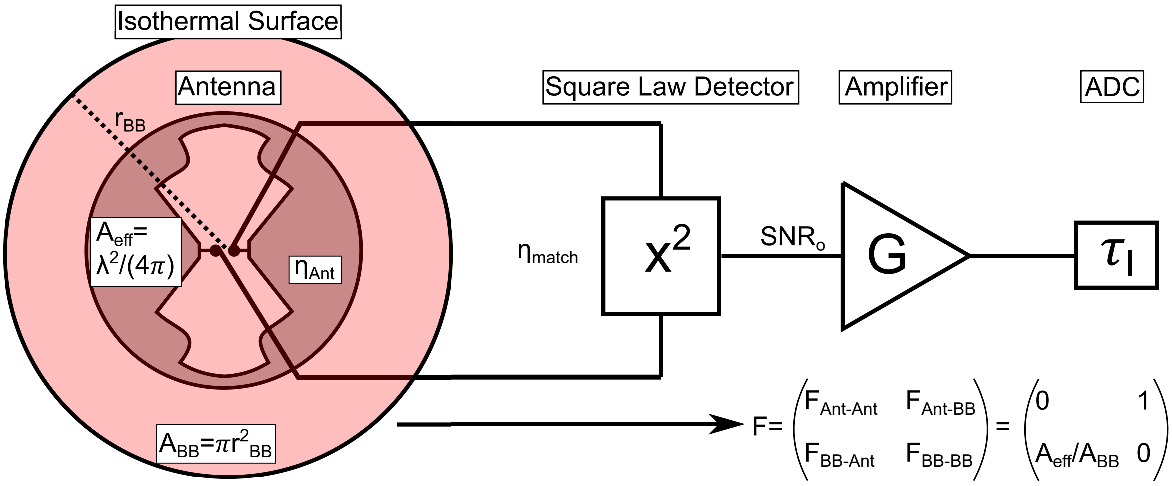

Figure 2.3: Schematic of an antenna-coupled direct detector connected to an external amplifier with gain G and an ADC with integration time τ_I. The antenna is located on top of an isothermal ideal black body surface with size A_{BB} and temperature T_{BB}.

In this case, ΔV_{DC} is obtained, when substituting P_{Ant} from Equation 2.19 by Equation 2.2 integrated across the hemisphere, which results in a factor of 2π and including the view factor relation F_{BB-Ant} from the black body surface A_{BB} to the effective antenna area A_{eff}

$$\Delta V_{DC} = \int_{f_1}^{f_2} P_{Ant}(f) \cdot R_v(f) df = 2\pi A_{BB} \int_{f_1}^{f_2} B_{RJ}(f,T) \cdot R_v(f) \cdot F_{BB-Ant}(f) df. \quad (2.25)$$

Calculating the emitted black body power of the black body surface into the hemisphere (Equation 2.25, $R_v = 1, F = 1$) results in a proportionality to f^3. Nevertheless, determining the output voltage ΔV_{DC} by Equation 2.25 requires the view factor F_{BB-Ant} to be evaluated by the view factor relations introduced in Section 2.2. By assuming a plane antenna and black body surface, where the antenna is fully enclosed by the black body surface, the 2 × 2 view factor matrix can be easily derived as indicated in Figure 2.3. Here, the view factors $F_{Ant-Ant}$ and F_{BB-BB} are equal to 0 (plane surface rule), $F_{Ant-BB} = 1$ (enclosure rule) and $F_{BB-Ant} = A_{eff}/A_{BB}$ (reciprocity rule). Inserting the view factor F_{BB-Ant} in Equation 2.25 leads to

$$\Delta V_{DC} = 2\pi \int_{f_1}^{f_2} B_{RJ}(f,T) \cdot R_v(f) \cdot A_{eff}(f) df. \quad (2.26)$$

Substituting A_{eff} by $\lambda^2/(4\pi) = c^2/(4\pi f^2)$, which is the maximum effective antenna area [75] and including the expression of the Rayleigh-Jeans approximation results in a frequency-independent power spectral density at the detector input provided by the antenna that equals to

$$P_{Ant} = k_B \cdot T_{BB}. \tag{2.27}$$

Substituting this in the previous equation gives

$$\Delta V_{DC} = k_B \cdot T_{BB} \int_{f_1}^{f_2} R_v(f) df, \tag{2.28}$$

showing that the maximum output signal is directly proportional to T_{BB}. A derivation of Equation 2.28 results in the detector's thermal sensitivity, which is the rise in output voltage per black body temperature change in Kelvin [V/K] [76]

$$R_v(T) = \frac{\partial V}{\partial T} = k_B \int_{f_1}^{f_2} R_v(f) df. \tag{2.29}$$

The most important figure-of-merit for a radiometer is the minimum detectable temperature difference (NETD) [77], defined as the ratio of the output noise spectral density and the system's thermal sensitivity

$$NETD = \frac{v_n}{\frac{\partial V}{\partial T}} = \frac{1}{k_B} \frac{v_n}{\int_{f_1}^{f_2} R_v(f) df}. \tag{2.30}$$

In other words, the NETD is the minimum black body temperature change ΔT_{BB} that results into an SNR of 1 at the detector output. The NETD for direct detectors is commonly evaluated with a constant NEP in an equivalent bandwidth B_{eq}, producing the same NETD as the integral shown in Equation 2.30. This equivalent bandwidth is calculated as [56]

$$B_{eq} = \frac{[\int_0^\infty R_v(f) df]^2}{\int_0^\infty R_v(f)^2 df}. \tag{2.31}$$

In the equivalent bandwidth, the equivalent detector responsivity $R_{v,eq}$ is defined as

$$R_{v,eq} = \frac{\int_0^\infty R_v(f)^2 df}{\int_0^\infty R_v(f) df}. \tag{2.32}$$

Now, the equivalent NEP (NEP_{eq}) can be calculated as the ratio of the output noise v_n and $R_{v,eq}$. If additionally the integration time is taken into account, the NETD is obtained as [78]

$$NETD = \frac{1}{k_B} \frac{NEP_{eq}}{B_{eq} \cdot \sqrt{2\tau_I}}, \tag{2.33}$$

where NEP$_{eq}$ is the NEP in the calculated equivalent bandwidth B_{eq}. If not specifically included in the derived equations, a τ_I of 500 ms is assumed.

In conclusion, despite increasing the integration time τ_I, there are two options to improve the NETD performance of direct detectors for passive imaging. Either increase the equivalent bandwidth B_{eq} or improve the detector responsivity. Assuming an optimum antenna-detector co-design ($\eta_{match} = 1$ and $\eta_{Ant} \approx 1$), a larger B_{eq} can only be achieved in a better device technology with less parasitic losses, while the latter one requires either an increase in device nonlinearity or a signal pre-amplification with an LNA between the detector and the antenna. As a high-gain LNA integration results in an output noise spectral density depending on the input signal, which is not the case for direct detectors without pre-amplification, it is discussed in the following section.

2.5 CW Signal Detection with THz Direct Detectors and LNA Pre-amplification

Contrary to the previous considerations for THz direct detectors, the detector output noise spectral density of a total power radiometer with LNA pre-amplification depends on the received CW input signal and the input-referred LNA noise temperature. In the case of a CW input signal, three rectified components are present at the detector output [79]. Firstly, the rectified input signal power P_{RF} multiplied by the LNA power gain G_{LNA} results in a rectified output signal ΔV_{DC} of

$$\Delta V_{DC} = R_{v,det} \cdot G_{LNA} \cdot P_{Ant}. \tag{2.34}$$

Equation 2.34 is only valid in simulations with realistic matching conditions, where the LNA output node is terminated with detector input impedance and $R_{v,det}$ is evaluated when the detector input is terminated with the LNA output impedance. The second component is the LNA input noise spectral density $P_{n,LNA} = k_B T_{LNA}$ multiplied by G_{LNA}. T_{LNA} is the LNA's input noise temperature and can be calculated from the LNA noise factor as [80]

$$T_{LNA} = T_{ref} \cdot (F - 1) = T_{ref} \cdot (10^{NF/10} - 1). \tag{2.35}$$

This results in a rectified output voltage noise spectral density component $v_{n,trans1}$ of:

$$v_{n,trans1} = R_{v,det} \cdot G_{LNA} \cdot P_{n,LNA}. \tag{2.36}$$

The third component is defined as mixing product of the input signal and the input noise. It involves a second rectified noise component $v_{n,trans2}$ that is proportional to the square root of the input signal P_{Ant}

$$v_{n,trans2} = R_{v,det} \cdot G_{LNA} \cdot \sqrt{2P_{n,LNA} \cdot P_{Ant}}. \tag{2.37}$$

In total, the full radiometer output voltage noise spectral density $v_{n,radiom}$ can be approximately defined as

$$\begin{aligned} v_{n,radiom} &= \sqrt{v_{n,det}^2 + v_{n,trans1}^2 + v_{n,trans2}^2} \\ &= \sqrt{v_{n,det}^2 + R_{v,det}^2 \cdot G_{LNA}^2 (P_{n,LNA}^2 + 2P_{n,LNA} \cdot P_{Ant})}, \end{aligned} \tag{2.38}$$

showing the dependency of the output voltage noise spectral density on the input signal and noise spectral density. For sufficiently high gain values, the third term of Equation 2.38 dominates the detector output noise spectral density in the presence of a CW input signal P_{Ant}. It defines the maximum system's dynamic range ($v_{n,det}^2 << v_{n,trans2}^2$). By rearranging Equation 2.34 the radiometer responsivity $R_{v,radiom}$ is obtained

$$R_{v,radiom} = R_{v,det} \cdot G_{LNA} = \frac{\Delta V_{DC}}{P_{Ant}}. \tag{2.39}$$

Combined with Equation 2.38, the minimum radiometer NEP is achieved as

$$NEP_{radiom} = \frac{v_{n,radiom}}{R_{v,radiom}} = \frac{\sqrt{v_{n,det}^2 + R_{v,det}^2 \cdot G_{LNA}^2 \cdot k_B^2 \cdot T_{LNA}^2}}{R_{v,det} \cdot G_{LNA}}. \tag{2.40}$$

As the influence on the output noise spectral density decreases with lower input power levels, the third term of Equation 2.38 is commonly omitted when calculating the radiometer NEP. This result assumes not only a CW tone at the radiometer input but also the presence of the input noise only at a single frequency point. Therefore, Equation 2.40 lacks general accuracy and cannot be used to calculate the radiometer NETD. For this purpose, broadband input noise spectral densities and their inherent self-mixing realized by the direct detector are analyzed in the following section.

2.6 Passive Signal Detection with THz Direct Detectors and LNA Pre-amplification

For a better understanding of the radiometer operation, Figure 2.4 shows a detailed radiometer signal chain analysis. The radiometer LNA is assumed to provide a constant NF of 10 dB and a gain of 40 dB in an ideal, rectangular 100 GHz bandwidth centered at $f_{center} = 200$ GHz. This radiometer chain is analyzed to finally derive an equation for the entire radiometer NETD to detect an object's thermal radiation in the THz frequency range based on a temperature difference ΔT to the ambient room temperature. These temperature differences are most commonly in the range of several 100 mK. For demonstration purposes, a ΔT of 1000 K was chosen for the following step-by-step signal analysis at different positions (① - ⑥) in the radiometer chain. Note that the main objective of the preceding study is to derive an expression for the overall radiometer NETD. Therefore, the focus is set on positions ⑤ and ⑥ at the radiometer output. Further, only a single frequency sideband is considered and all graphs were generated by numerical simulations in Python.

①: As shown in Section 2.4, the input signal provided by the (lossless) antenna is given by $k_B \cdot \Delta T$. Considering the LNA as noiseless, the input signal is described as $k_B \cdot (T_{sys} + \Delta T)$ with $T_{sys} = T_{ref} + T_{LNA}$. The corresponding input power spectral density is -164 dBm/Hz as the sum of the noise floor at room temperature (-174 dBm/Hz) and the NF. LNA and antenna are operated at room temperature (T_{ref}).

②-③: The detector input noise spectral density is calculated as the product of the LNA gain and input noise spectral density with the corresponding result shown in ③ and the total detector input noise power calculated as $G_{LNA} \cdot B_{LNA} \cdot (T_{sys} + \Delta T)$, where B_{LNA} is the LNA bandwidth.

④-⑤: The square law operation of the direct detector is defined as a self-multiplication of the input detector noise voltage in the time domain. This translates into a convolution of the detector input noise power spectral density in the frequency domain [81], which needs to be multiplied with the detector responsivity $R_{v,det}$ to calculate the detector output noise spectral density. The resulting rectified DC voltage noise spectral density $S_v(f)$ is then defined by the following Equation [82], [83]

$$\begin{aligned} S_v(f) = & \underbrace{k_B(T_{sys} + \Delta T) \int_{-\infty}^{\infty} G_{LNA}(f) R_{v,det}(f) df \delta(f) +}_{DC\,Peak} \\ & \underbrace{\sqrt{2} k_B (T_{sys} + \Delta T) \sqrt{\int_{-\infty}^{\infty} G_{LNA}(f) G_{LNA}(f - f') R^2_{v,det}(f) df}\,.}_{Noise\,Floor} \end{aligned} \tag{2.41}$$

The first term of Equation 2.41 corresponds to a DC peak ΔV_{DC} funded in the autocorrelation function of white noise, which is a Dirac-Delta function δ (f) [84]. In the investigated case with an ideal rectangular bandwidth, ΔV_{DC} can be calculated as

$$\Delta V_{DC} = k_B(T_{sys} + \underbrace{\Delta T}_{Wanted\,Signal}) \cdot G_{LNA} \cdot B_{LNA} \cdot R_{v,det}. \tag{2.42}$$

This is equal to Equation 2.34 with P_{Ant} expressed as $k_B(T_{sys} + \Delta T) B_{LNA}$. However, only the part of Equation 2.42 induced by ΔT corresponds to the (wanted) input signal, while the DC part funded in T_{sys} results in a DC offset at the detector output. In the investigated example, a large DC voltage difference of $\Delta V = 69$ mV is calculated based

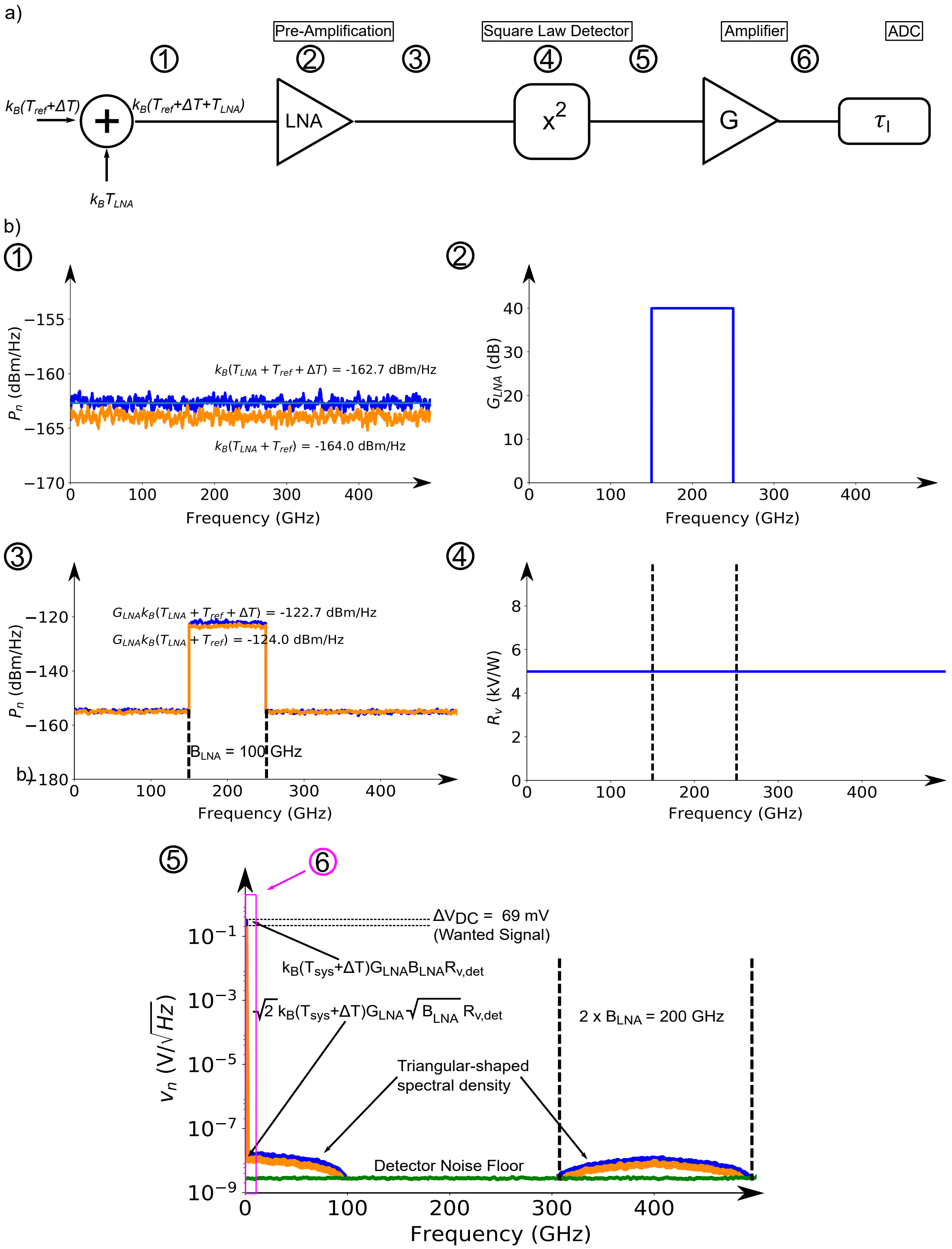

Figure 2.4: a) Schematic of a total power radiometer comprising an antenna-coupled LNA with 40 dB gain (G_{LNA}), 10 dB NF and 100 GHz bandwidth, a direct detector ($R_{v,det} = 5$ kV/W), an external buffer amplifier ($G = 1$) and an ADC (τ_I).
b) Corresponding noise spectral densities at several points in the radiometer signal chain assuming an input signal caused by a black body temperature variation of $\Delta T = 1000$ K.

on a ΔT of 1000 K. The frequency trend of the LNA gain mainly defines the second term of the input power spectral density convolution. In the case of a rectangular LNA bandwidth, the convolution results in two triangular-shaped noise spectral densities, centered around DC and the second harmonic at $2 \cdot f_{center}$ spanning over two times the LNA bandwidth. The maximum height of these noise spectral densities $S_{v,max}(f)$ is derived as [73]:

$$S_{v,max}(f) = \sqrt{2} k_B \cdot (T_{sys} + \Delta T) \cdot G_{LNA} \cdot \sqrt{B_{LNA}} \cdot R_{v,det}. \tag{2.43}$$

The detector output voltage noise spectral density is further affected by the intrinsic detector low-frequency noise voltage. If this is considered, the total radiometer output noise voltage spectral density $v_{n,radiom}$ is the square root of the sum of both mean-square noise voltages [85].

⑥: The radiometer readout bandwidth is defined either by an additional low-frequency amplifier or the speed of the data acquisition ADC, which is used to capture the measured DC voltages. In the investigated case, the amplifier is used as a buffer with a gain of 1. In an assumed readout bandwidth of 1 GHz, when the 1/f noise as well as the noise of the low-frequency amplifier are neglected, the radiometer output noise spectral density is approximately constant with a value of

$$v_{n,radiom} = \sqrt{S_{v,max}^2 + v_{n,det}^2} = \sqrt{2 k_B^2 \cdot (T_{sys} + \Delta T)^2 \cdot G_{LNA}^2 \cdot B_{LNA} \cdot R_{v,det}^2 + v_{n,det}^2}. \tag{2.44}$$

Now, the radiometer $NETD_{radiom}$ is derived with the thermal responsivity as $\partial V / \partial T$ referring to Equation 2.42 as

$$R_{v,radiom}(T) = k_B \cdot G_{LNA} \cdot B_{LNA} \cdot R_{v,det}. \tag{2.45}$$

This equation is valid with an ideal rectangular LNA bandwidth and a constant R_v. In a realistic scenario, the corresponding equivalent bandwidths according to Equations 2.31 and 2.32 need to be calculated. As ratio of the radiometer output noise voltage spectral density $v_{n,radiometer}$ (Equation 2.44) and $R_{v,radiom}$ (Equation 2.45), the integration time dependent $NETD_{radiom}$ results in

$$NETD_{radiom} = T_{sys} \sqrt{\frac{1}{B_{LNA} \cdot \tau_I} + \frac{1}{2\tau_I} \cdot \left(\frac{NEP}{k_B \cdot B_{LNA} \cdot T_{sys} \cdot G_{LNA}} \right)^2}, \tag{2.46}$$

assuming $T_{sys} >> \Delta T$. It can be easily shown that the detector output voltage noise spectral density can be neglected if the amplifier gain and bandwidth are high enough, then the last part of Equation 2.46 tends to zero.

However, in a realistic scenario, not only the input signal changes (ΔT) but also the intrinsic LNA gain fluctuations ΔG contribute to variations in the measured output signal voltage. These, furthermore, cannot be separated from an input signal. Thus, they may determine the radiometer's minimum NETD. Including gain variations, the radiometer NETD is determined as

$$NETD_{radiom} = T_{sys}\sqrt{\frac{1}{B_{LNA}\cdot\tau_I} + \frac{\Delta G^2}{G^2} + \frac{1}{2\tau_I}\cdot\left(\frac{NEP}{k_B\cdot B_{LNA}\cdot T_{sys}\cdot G_{LNA}}\right)^2}. \quad (2.47)$$

As the gain variations are usually based on the radiometer system's temperature variances, the generated radiometer DC output signal typically varies within several seconds [73]. As ΔG is dominated by, i.e., thermal variations, mechanical vibrations or power supply stability, it has to be evaluated through empirical measurements [86] and cannot be estimated in the preceding derivation of the radiometer design objectives. To overcome these drifts, many radiometer systems use a Dicke Switch in front of the amplifier that switches between the input signal and a known reference [87] but results in a NETD deterioration of at least a factor of 2 [88].

2.7 Derived Design Objectives

All previous derivations are not only intended to establish a fundamental understanding of passive imaging in the THz frequency range. Moreover, they are used to deduce design objectives for the subsequently presented silicon-integrated detector circuits. For this purpose, the final expressions for the system NETD shown in Equation 2.47 and Equation 2.33 are evaluated in the following under ideal conditions without antenna and matching losses. Two cases are investigated in Figure 2.5. For direct detectors without pre-amplification, the minimum achievable NEP in the current state-of-the-art is several $pW/\sqrt{Hz}$ [89]. Due to the low sensitivity of THz direct detectors, a sub-Kelvin NETD is only possible in a moderate integration time.

The main objective is to reach a NETD smaller than 1 K within a 1 Hz bandwidth (τ_I = 500 ms). The for this purpose required NEP and equivalent bandwidth values are indicated in Figure 2.5 a) by red color. Reaching such values is very challenging, i.e., even low NEP values of 5 pW/$\sqrt{Hz}$ require a B_{eq} of more than 400 GHz. In the second case, with LNA pre-amplification, several assumptions were made. First, the maximum LNA operation frequency is limited to approximately $f_{max}/2$, around 300 GHz for IHP's SG13G3 technology. Therefore, the targeted LNA center frequency was chosen to be around 200 GHz. A minimum detector NEP of 5 pW/$\sqrt{Hz}$ is possible in this frequency range, as already presented in the literature [89]. Furthermore, a moderate NF of 10 dB was assumed and the influence of the gain variations, which simulations cannot easily describe, was omitted. Finally, an integration time of 40 ms

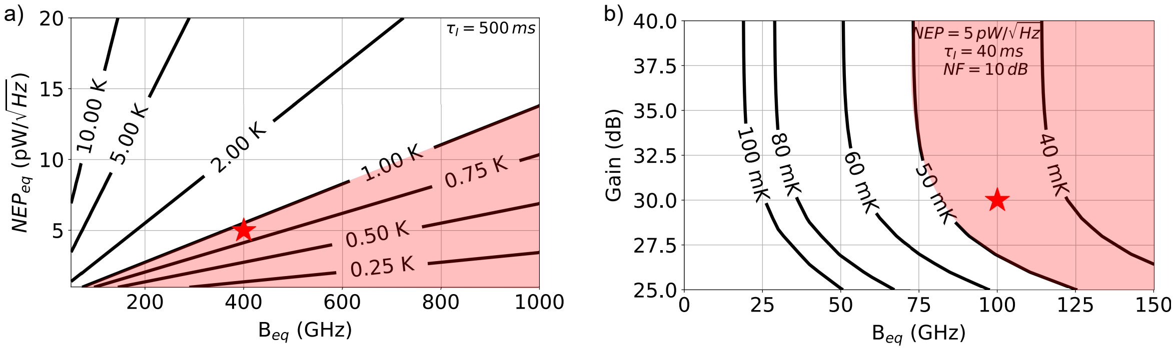

Figure 2.5: Minimum theoretically achievable NETD contours calculated based on Equations 2.33 and 2.47 for direct detectors without (a) and with LNA pre-amplification (b). The design objectives (NETD < 1 K and NETD < 50 mK) are indicated in red.

was considered for real-time passive imaging. In this configuration, a minimum NETD between 40 mK and 50 mK is desirable as it is comparable to most commercially available IR cameras. To achieve these values, the necessary gain and B_{eq} values are indicated in red in Figure 2.5 b). Here, exemplarily, a combination of G $=$ 30 dB and $B_{eq} = 100$ GHz was highlighted, resulting in a NETD of 45 mK.

2.8 Summary and Conclusion

This chapter reviews the theoretical fundamentals for passive imaging in the THz frequency range based on antenna-coupled direct detectors with and without LNA pre-amplification, starting from the Rayleigh-Jeans approximation of Planck's law. A crucial observation is that the input power spectral density at the detector input is frequency-independent and equals $k_B T_{BB}$ for ideal black body radiation in the THz frequency range due to the antenna's solid angle of view that decreases towards higher frequencies. Furthermore, the most important detector parameters, such as noise equivalent power NEP, voltage responsivity R_v, thermal voltage responsivity $R_v(T)$ and noise equivalent temperature difference NETD, were mathematically determined.

The derived equations were applied to define the research objectives, allowing a concealed object detection (NETD $\leq$ 1 K) with THz direct detectors (without pre-amplification) in 500 ms integration time (1 Hz readout bandwidth). For THz direct detectors with LNA pre-amplification, a real-time operation (40 ms integration time) is targeted with a NETD of 50 mK comparable to a commercially available IR camera. In total, THz direct detectors need to provide an equivalent bandwidth of at least 400 GHz and a NEP of 5 pW/$\sqrt{Hz}$, while in radiometer systems with pre-amplification several assumptions (detector NEP 5 pW/$\sqrt{Hz}$, LNA NF 10 dB) result in the necessity of at least 100 GHz bandwidth and an LNA gain of 30 dB to achieve these challenging objectives.

Chapter 3

Modeling and Design of Broadband SiGe HBT THz Direct Detectors

A broadband direct detector design with minimum NEP operation requires an extensive analysis of the THz rectification process that is introduced in [own5] for contemporary high-speed SiGe HBT transistors with f_t/f_{max} of 350/550 GHz, named SG13D5 in the following. In this work, the detailed analysis of internal device parasitics' influence on the maximum achievable responsivity is extended with a focus on different transistor sizes, a comparison between two advanced SiGe HBT technologies and an analysis of their fundamental potential for high-sensitivity, low power THz direct detectors. An understanding of all critical design and operation aspects for SiGe HBT THz direct detectors in forward-active and saturation is developed in the frequency range from 100 GHz to 1 THz. This way, the inherent device limitations for passive imaging with SiGe HBTs at THz frequencies are emphasized. This analysis is based on a self-developed device behavioral model defined by the devices' HiCUM model [90]. With the help of this model, the fundamentals of the device rectification process are linked to the internal device parasitics for the forward-active and saturation regions. Thus, a prediction of possible responsivity improvements by future device technologies can be conducted. Furthermore, bias/readout schemes (load conditions) for minimum low-frequency noise (LFN) operation and the required antenna design space for maximum detector responsivity are analyzed. A particular focus is set on the saturation region, which enables low power, zero bias operation and is especially important for large scale THz cameras.

3.1 Direct Detection Fundamentals

Direct power detection (from THz to DC) of classical HBTs operating in the forward-active region is explained by the rectification process incorporated with the device base-emitter diode nonlinearity. This is expressed by the well-known Shockley equation [91], which is included in the traditional Gummel-Poon model [92] by modeling the collector current I_{ce} as

$$I_{ce} = I_s \cdot (e^{\frac{qV_{be}}{k_B T} - 1}), \tag{3.1}$$

where q is the elementary charge ($1.6 \cdot 10^{-19}$ C) and I_s the reverse saturation current. With the help of the Taylor expansion evaluated at the point a = 0, Equation 3.1 can be expressed as

$$I_{ce} = \frac{\partial I_{ce}(0)}{1! \cdot \partial V_{be}} \cdot V_{be} + \frac{\partial^2 I_{ce}(0)}{2! \cdot \partial V_{be}^2} \cdot V_{be}^2 + \cdots + \frac{\partial^n I_{ce}(0)}{n! \cdot \partial V_{be}^n} \cdot V_{be}^n, \tag{3.2}$$

where n is the number of evaluated Taylor polynomials. Most important for the RF to DC conversion in this static case is the second-order nonlinearity of I_{ce}

$$\frac{\partial^2 I_{ce}}{2 \cdot \partial V_{be}^2} \cdot V_{be}^2. \tag{3.3}$$

Equation 3.3 is valid across the whole biasing range. Assuming an RF input signal $V_{be} = A_{RF} \cdot \cos \omega_{RF} t$ with amplitude A_{RF}, V_{be} can be expressed by applying well-known addition theorems as

$$V_{be} = \frac{A_{RF}}{2} \cdot [1 + \cos(2\omega_{RF} t)], \tag{3.4}$$

describing a DC and a second harmonic component. The DC biasing part of V_{be} is omitted here. As the product of Equation 3.3 and the DC part of Equation 3.4, the rectified DC collector current $i_{c,dc}$ based on the device's second order nonlinearity is obtained

$$i_{c,dc} = \frac{A_{RF}^2}{4} \cdot \frac{\partial^2 I_{ce}}{\partial V_{be}^2}, \tag{3.5}$$

which is the dominant part of the rectified DC current for considerably low detector input powers smaller -30 dBm [own5]. As Equation 3.5 describes the rectification of an equivalent internal current source, a more complex HBT model needs to be evaluated to understand all static (DC) and dynamic (RF) contributions to the rectification process. In the following, the investigated detector circuit and its DC bias conditions are described. Then, a nonlinear equivalent model including all important device internal parasitics of the investigated differential common-base (CB) detector circuit are analyzed to finally evaluate the potential of the investigated detector circuits towards passive imaging.

3.2 The Differential Common-Base Detector Circuit

The differential CB circuit topology is shown in Figure 3.1 a). It is implemented with SiGe HBTs in the smallest device size, providing an emitter area A_e of $1\times$ 0.12 μm^2 denoted as x1. This topology is chosen for the following analysis with a self-developed nonlinear equivalent model, as it features optimum detector responsivity, NEP and RF bandwidth [72]. The differential CB topology further provides a virtual AC ground at the external base and collector nodes, resulting in all odd components of Equation 3.2 (fundamental RF driving signals and odd harmonics) being approximately zero. Thus, a broadband self-mixing process with inherent RF-to-DC isolation is achieved. Due to its differential configuration, the rectified output current, as introduced in Equation 3.5, will be doubled.

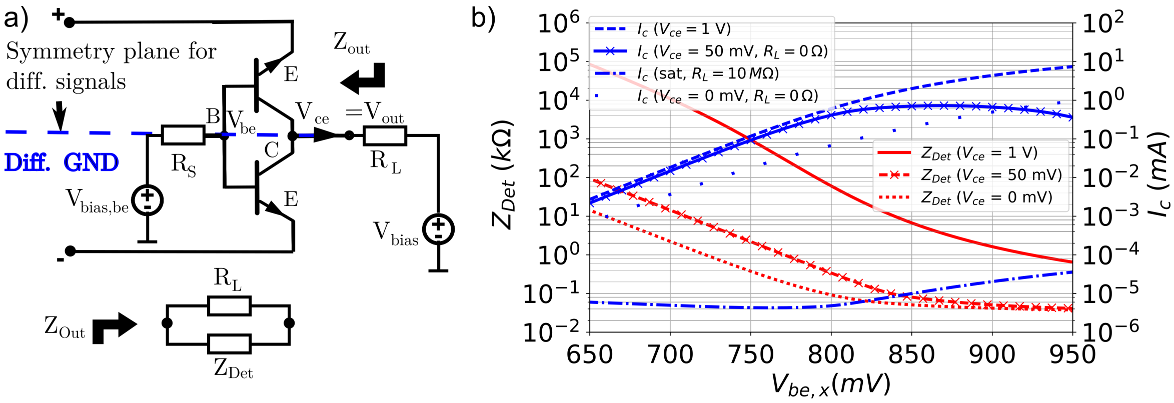

Figure 3.1: a) Investigated differential common-base detector circuit.
b) Detector bias currents I_{ce} and output impedance Z_{Det} at four bias points for device operation in the forward-active (V_{ce} = 1 V), weak saturation (V_{ce} = 50 mV) and deep saturation (sat, R_L = 10 MΩ and sat, V_{ce} = 0 mV, R_L = 0 Ω). Images after [own5] ©2022 IEEE.

In the following, the process of building up a detector voltage or current responsivity is discussed based on the CB detector circuit operated in forward-active and saturation regions. This process requires a careful analysis and is highly dependent on the detector output impedance denoted as Z_{Out}. Z_{Out} itself can be calculated by the parallel connection of the devices' output resistance Z_{Det} and the external load resistor R_L as $Z_{Out} = Z_{Det}||R_L$. The trend of Z_{Det} is further shown in Figure 3.1 a), indicating a bias-dependent, high detector DC output impedance in the forward-active region typically above 50 kΩ. In this operation region, the detector's current responsivity, R$_i$, is classically exploited with the corresponding NEP. However, with a sufficiently high external load resistance at the collector output, the voltage readout scheme can equivalently be used without penalty in NEP, as shown later in Section 3.4. In this case, the current and voltage responsivity are related by the load resistance R_L. Then, the simple relation $R_v = R_i \cdot R_L$ is valid, resulting in the same optimum device bias point for both cases.

In the saturation region, the forward-biased base-collector (BC) diode presents a bias-dependent load to the DC current rectified in the base-emitter junctions. This results in a relatively low Z_{Det} compared to the device biased in the forward-active region, which decreases for an intermediate V_{be} larger than 700 mV and low collector bias voltages. Therefore, the resulting voltage responsivity in saturation has to be calculated as $R_v = Z_{Out} \cdot R_i$. This results in an optimum operation point falling at different base voltages due to its complex dependency on Z_{Det} and R_i. To emphasize the previous analysis, the simulated output impedance with the corresponding DC collector current is shown in Figure 3.1 b). A few collector DC bias points in the forward-active and different saturation regions were selected. All curves are a function of the external base-emitter bias voltage. With the knowledge of the most important noise components and the evolution of the device output impedance, the external detector bias conditions must be investigated before analyzing the rectification process to ensure optimum bias conditions.

3.3 SiGe HBT Noise

The direct detector NEP is mainly dominated by the device's output noise spectral density, with rectified output signals embedded in the noise floor generated by LFN components. To counteract the device's LFN, the input signals are usually modulated by a square-wave modulation (chopping). Further, the chopping frequency is set above the LFN corner, usually in the kHz frequency range, to maximize the device SNR. With chopping applied, thermal and shot noise components dominate the detector output noise. A short summary of bipolar junction transistors' (BJTs) noise sources is presented in the following and a brief literature-based summary for high-speed SiGe HBTs are given for the saturation and forward-active regions.

- **Thermal Noise:** Thermal noise is based on the parasitic access resistances (R_c, R_b, R_e) and can be described as white Gaussian noise in the considered low-frequency range [93]. In the forward-active region, DC current-flow-dependent noise sources are of higher importance than access resistance-related thermal noise.

- **Shot Noise:** Shot noise results from the DC charge flow through the base-emitter p-n junction [93]. The more important shot noise at the collector output is a correlated version of the base-emitter junction's shot noise [94]. Shot noise typically dominates at frequencies above the LFN corner. The base-emitter and BC junction independently contribute to shot noise generation if operated in saturation.

- **1/f Noise:** 1/f noise (flicker noise) is commonly described by conductivity fluctuations due to mobility and number of carriers [93]. The 1/f noise spectrum either shows a linear or a square dependence based on the device DC current [94]–[97] and is typically inverse to the emitter area [96], [98].
- **GR Noise:** The Generation-Recombination (GR) noise funds in bias-current dependent carrier trapping-de-trapping processes among different energy states. It results in a release-time-dependent Lorentzian-shaped noise spectral density [97], [99]. For small SiGe HBT devices, the distribution of traps inside the devices may become non-uniform. Hence, the trapping-de-trapping processes become random, resulting in current pulses based on minor changes in the base-emitter voltage ΔV_{be} that are associated with random telegraph signal noise (RTS) [100], which is also observed for MOSFETs [101].

High-speed SiGe HBTs are highly affected by 1/f and GR noise components attributed to the device's external surface and periphery [99], [102] that is not the case for classical BJTs. At low bias currents, 1/f noise may be masked by multiple GR noise mechanisms, making it difficult to extract the individual noise spectra [97], [99]. Common for high-speed SiGe HBTs is that devices with higher device size (larger emitter area and lower perimeter) show lower GR and 1/f noise spectral densities [95], [99]. Tiny devices operated at low current densities, typically used in direct detectors, are primarily influenced by GR noise [99], [102].

The saturation operation mode, where both junctions (BE, BC) are forward biased, is only scarcely described in the literature due to the low device speed in terms of f_t and f_{max}. In [103] and [104], the LFN performance for inverse-biased SiGe HBT is reported with similar or degraded performance compared to the forward-active operation due to additional noise sources around the BC junction. An accurate analysis of the LFN, especially 1/f and GR components, requires substantial effort in the experimental characterization and is done in Chapter 4. However, the choice of the optimum detector bias point reducing its overall output noise relates to the well-defined thermal and shot noise of the external voltage or current bias and readout circuits, which are analyzed in the following to ensure optimum bias conditions.

3.4 Optimum Detector Bias and Readout Scheme

The main differences in the commonly applied current or voltage mode readout/biasing schemes are the detector load and source impedance conditions. A current mode bias scheme is applied by a high impedance current source ($R_S \to \infty\ \Omega$). A current mode readout is utilized by a low impedance amplifier ($R_L \to 0\ \Omega$). In the voltage mode, the source/load conditions are exactly opposite ($R_S \to 0\ \Omega$, $R_L \to \infty\ \Omega$). Both biasing/readout methods have advantages and disadvantages, which are analyzed in the following.

3.4.1 Voltage vs. Current Biasing Scheme

The influence of the external DC source resistance R_S at the base node on the detector noise performance is investigated based on noise simulations with the HiCUM device model. Three biasing regions, the forward-active ($V_{ce} = 1\,\mathrm{V}$), the weak ($V_{ce} = 50\,\mathrm{mV}$) and the deep ($V_{ce} \approx 0\,\mathrm{mV}$) saturation region are analyzed in a voltage mode readout. In deep saturation, the bias-dependent device output resistance mainly determines the output voltage noise spectral density v_n. Therefore, the collector is loaded with an external R_L of 1.83 $k\Omega$ only in the forward-active and weak saturation region to supply collector bias voltage. In contrast, the collector node is left floating in the deep saturation region. Here, the shot noise is assumed to be negligible due to the low collector current I_{ce} and current gain β.

Simulation results showing the detector output voltage noise spectral density v_n as a function of the external base resistance R_S are shown in Figure 3.2 a) for three different base-emitter voltages. In the forward-active region v_n shows a square dependence based on R_S for $(R_b + R_e) \ll R_S < R_\pi/2$ [94], [105], [106], where R_π is the dynamic base–emitter resistance. This dependency is related to the base current noise spectral density (S_{Ib}) transferred to the collector by the device's high current gain β. The main message is that a current biasing scheme with high external resistances (current mirror) must be applied cautiously. In this technology, R_S should be below $500\,\Omega$. For higher R_S values, the output voltage noise spectral density will increase by up to one order of magnitude. Contrary to this, the detector is insensitive to R_S in deep saturation.

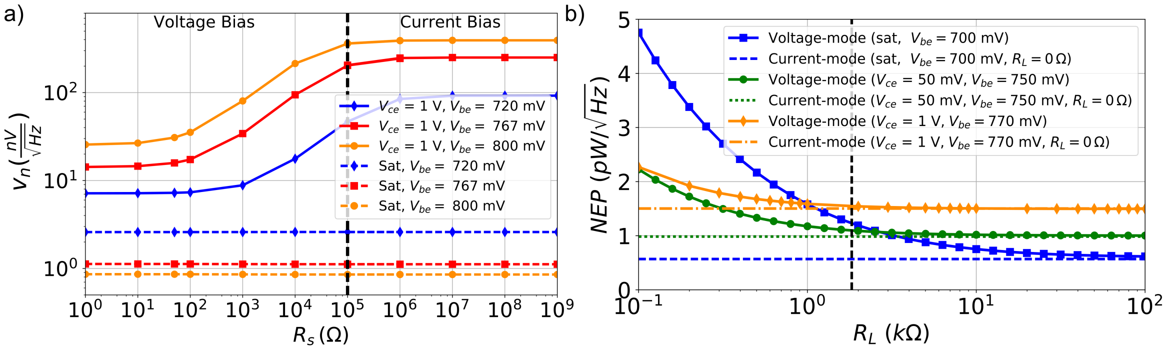

Figure 3.2: a) Simulated detector output noise spectral density vs. source resistance R_S for voltage- and current biasing schemes with shot and thermal noise present.
b) Simulated influence of the load resistance R_L on minimum detector NEP comparing a voltage- and a current mode-readout ($R_L = 0\ \Omega$) at 300 GHz.
Images after [own5] ©2022 IEEE.

3.4.2 Voltage vs. Current Readout Scheme

In a current mode readout, the amplifier's low input impedance levels are beneficial for devices requiring a MHz chopping frequency due to high LFN corners. A parasitic low-pass filter formed by the amplifier's input impedance and the peripheral cable capacitance will not affect the output signal due to device connection, which might appear in a voltage mode readout. However, if this is not the case, and only thermal and shot noise are considered, current and voltage mode readouts, in theory, result in the same minimum NEP if the output resistance is sufficiently high in a voltage mode readout. This trend is shown in the simulated NEP curve at 300 GHz for different load resistances in a voltage mode readout compared to a current mode readout with $R_L = 0\ \Omega$ in Figure 3.2 b). Nevertheless, a current-mode readout cannot be applied in the device saturation region without signal degradation, as shown in Figure 3.1 b), where the detector output impedance levels drop even below 100 Ω [own6].

Therefore, and to provide a comparison basis between devices operating in saturation and forward-active, a voltage mode readout is applied for the consecutive simulation and characterization in Chapter 4. Under ideal conditions (not limited by input-referred amplifier noise), a voltage and current mode readout for devices operated in the forward-active region result in the same minimum NEP. Thus, the corresponding simulations in this chapter mainly focus on the rectified output current $i_{c,dc}$.

3.5 Broadband Modeling of THz Direct Detectors

The main idea of developing a nonlinear equivalent device model is to get a detailed insight into the detector rectification process at THz frequencies and to directly link it with the internal device parasitics. All relevant model parameters were extracted from the corresponding HiCUM Level-2 device model (device parameters extracted from the DC operating point) for devices operated in forward-active and saturation regions. Further, they were polynomially fitted and re-imported to the simulation tool as lumped components implemented in a Verilog-A code as indicated in Figure 3.3 a).

Contrary to the purely numerical HiCUM model, the equivalent model provides access to the internal device nodes. The evolution of the internal diodes' driving voltage is crucial for analyzing many circuits relying on rectification or harmonic generation, such as direct detectors, frequency doublers, or triplers. For the detector analysis, first, the forward-active region is investigated as it is the classical operation range for SiGe HBT THz direct detectors and provides the highest device speed in terms of f_t/f_{max} even if this is not directly related to the device rectification process. It is assumed that all device parasitics depend only on the internal base-emitter DC voltage $V_{be,i}$, valid for a

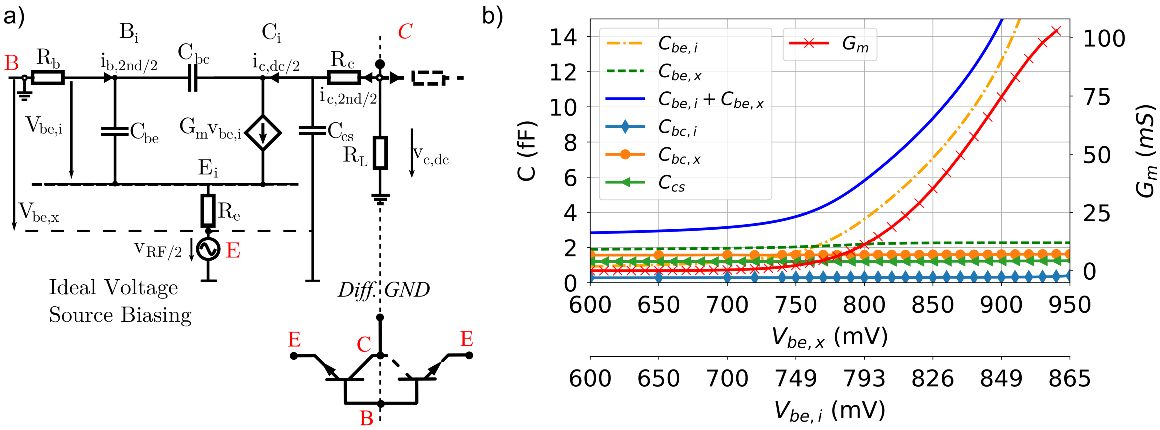

Figure 3.3: a) Nonlinear equivalent circuit model of the differential common-base detector circuit in forward-active region ($V_{ce} = 1$ V). A differential AC ground is present at the external base and collector nodes due to its differential emitter drive.
b) Corresponding device model parameters for a x1 device as a function of the relevant external ($V_{be,x}$) and internal ($V_{be,i}$) DC base–emitter voltages.
Images after [own5] ©2022 IEEE.

low detector input power smaller than $-30\ dBm$, where the rectified detector output voltage $v_{c,dc}$ does not significantly affect the DC collector bias voltage ($v_{c,dc} << V_{ce}$). To omit power matching effects, the detector model is initially driven by an ideal RF voltage source between the emitter nodes of two devices in CB configuration, which complies with the basic Shockley equation (Equation 3.1).

The frequency-dependent detector performance funded in the rectified collector voltage is studied in the following. As previously described, the AC ground at the external base and collector nodes is absent for even harmonics and may become detrimental to the detector rectification process with sufficient input power. However, in THz imaging applications and especially for passive imaging, there are typically very low power levels, preventing a 2nd-harmonic voltage built-up ($v_{c,2nd}$) at the collector output node. Therefore, 2nd-harmonic effects at the internal collector are disregarded in the analysis.

3.5.1 Detector Model for the Forward-Active Region

In the following, the most important detector model parameters shown for the forward-active operation region in Figure 3.3 a) are briefly introduced.

- **Nonlinear Voltage-Controlled Current Source:** $G_{m,be} = \partial I_{ce}/\partial V_{be,i}$ is the frequency-independent derivation of the large-signal device output current I_{ce} defined by the internal BE voltage [92]. As shown in Equation 3.5, the second order current nonlinearity or $\partial G_m/\partial V_{be,i}$ is the main source of THz rectification.

- **Parasitic Device Access Resistances:** The emitter resistance R_e, collector resistance R_c and base resistance R_b are assumed to be constant across the detector biasing range. The latter is further divided into an intrinsic, R_{bi}, and an extrinsic part, R_{bx}, which relates to the base-link region [107]. To model the forward-active region, R_{bi} and R_{bx} can be combined into a single component without a noticeable difference in the simulated detector responsivity compared to the full HiCUM model. Access resistance values for a x1 device are shown below in Table 3.1.

Table 3.1: Access resistance values for x1 devices in SG13D5

R_{bi}	R_{bx}	R_e	R_c
57 Ω	41 Ω	24 Ω	40 Ω

- **Base-Emitter Capacitance:** The nonlinear BE capacitance C_{be} includes intrinsic $C_{be,i}$ contributions from the depletion as well as the diffusion capacitance C_{diff}. Together with extrinsic $C_{be,x}$ contributions based on the device periphery, it follows $C_{be} = C_{be,i} + C_{be,x}$. In the forward-active region, the latter is mainly linear and has no significant influence on the rectification process at THz frequencies. The internal component $C_{be,i}$ is originated in the storage of locally compensated minority carriers during forward transistor operation of the BE junction and exploits a very nonlinear, roughly exponential behavior depending on $V_{be,i}$ [107]. Due to this capacitive nonlinearity, G_m is not the only contributor to the rectification process at THz frequencies. For low bias currents in the forward-active region, C_{be} shows a weak dependency on the base-collector voltage. Thus, it is assumed to be independent of V_{ce}. Nevertheless, for operation in the saturation region, V_{ce} needs to be taken into account, as it strongly affects C_{be}.

- **Base-Collector Capacitance:** C_{bc} is also divided into an intrinsic, $C_{bc,i}$ and an extrinsic part, $C_{bc,x}$. In the forward-active region, C_{bc} is defined by the constant parasitic inter-electrode BC capacitance resulting from the shallow trench isolation and metallization [108]. In saturation, the increasing influence of the peripheral depletion capacitance C_{jcx} results in a very nonlinear behavior.

- **Collector Substrate Capacitance:** C_{cs} includes the depletion charge of the large collector-substrate region and is approximated as linear. At THz frequencies, it causes a low collector node impedance.

Please note that the dynamic base–emitter resistance R_π is omitted here, as it is considered as an open-circuit at THz frequencies.

The bias-dependent values of all significant internal device capacitances for a detector implemented in ×1 transistor size are shown in Figure 3.3 b) together with the relevant values of G_m. The bias voltages at the internal ($V_{be,i}$) and external ($V_{be,x}$) base-emitter nodes are additionally depicted. Their difference increases for larger collector currents (corresponding to $V_{be,x} \geq 800$ mV) due to the linearizing emitter resistance R_e, which prevents an effective growth of $V_{be,x}$ independently from the operating frequency. For the bias-independent capacitances, the following values were assumed: $C_{bc,i}$= 0.3 fF, $C_{bc,x} = 1.6$ fF, $C_{be,x} = 2$ fF and $C_{cs} = 2$ fF. However, $C_{be,i}$ and G_m are very nonlinear, thus potentially influencing the rectification process for higher harmonics.

In the following model analysis, a 10 mV RF voltage source (fundamental v_{RF}) is applied differentially between the emitter nodes of both devices as indicated in Figure 3.3 a). Such an input RF voltage value is equivalent to an input power of $P_{In} = -30$ dBm for a 100 Ω reference impedance Z_{In}. The model validity range was further verified to be around a maximum input power of -10 dBm without any noticeable difference in the rectified voltage compared to HiCUM simulations, which serve as a reference basis. The influence of each device parasitic on the rectification process is investigated between 100 GHz to 1 THz. For this purpose, the rectified output collector current, $i_{c,dc}$, is studied as a function of the fundamental RF voltages $v_{be,x}$ and $v_{be,i}$.

3.5.2 Simplified Detector Models

Four model types of different complexity help to separate the various static and dynamic frequency effects influencing the rectification process.

Model I: Only a voltage-controlled current source with $I_{ce} \approx G_{m,be} \cdot V_{be,i}$ and C_{be} are present, as shown in Figure 3.4.

Model II: The emitter contact resistance, R_e, is included in Model I see Figure 3.5.

Model III: Same as Model II but R_b is included instead of R_e indicated in Figure 3.6.

Model IV: Full simplified model including all parasitics as shown in Figure 3.3.

In the following, the rectification potential of each model is investigated individually.

3.5.2.1 Model I: G_m, C_{be}

The model shown in Figure 3.4 a) contains the two most important nonlinear components: $G_{m,be} = \partial I_{ce}/\partial V_{be,i}$ and $C_{be} = C_{be,i} + C_{be,x}$. With an ideal RF voltage source drive, the rectified DC and the second-harmonic collector current are fully defined by

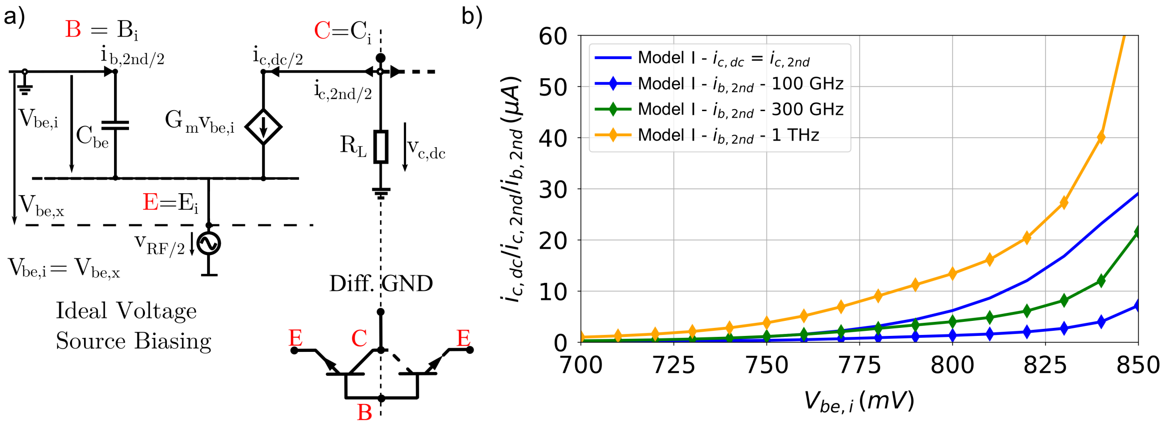

Figure 3.4: a) Model I with $G_{m,be}$ and C_{be}.
b) Simulated rectified DC ($i_{c,dc}$) and second-harmonic currents at the collector ($i_{c,2nd}$) and base nodes ($i_{b,2nd}$) for different RF input frequencies.
Images after [own5] ©2022 IEEE.

G_m and can be approximated by the frequency-independent 2nd-order Taylor polynomial expansion of the Shockley equation as derived in Equation 3.5

$$|i_{c,2nd}| = |i_{c,dc}| = \frac{\partial^2 I_c}{\partial V_{be,i}^2} \cdot \frac{A_{be,i}^2}{2}. \tag{3.6}$$

$A_{be,i}$ denotes the peak amplitude of the fundamental RF drive voltage $v_{be,i}$ at the internal base-emitter nodes. In this simple model configuration, the RF driving voltage can be expressed as $v_{be,i} = A_{be,i} \cdot \cos(\omega t)$. $V_{be,i}$ refers to the internal DC voltage at the base-emitter diode and I_c to the DC collector current, respectively. The internal and external base and collector voltages refer to the same nodes on AC ground. Thus, including C_{bc} does not affect the model results as the feedback through C_{bc} is shorted.

As shown in Figure 3.4, the detector rectified current improves with bias voltage, approaching around $29\,\mu A$ for the maximum simulated $V_{be,i}$ of 850 mV. This is based on its linear dependency on the diode static nonlinearity $\partial G_m / \partial V_{be,i}$. Further, by exploiting the 2nd-order Taylor polynomial expansion of its current/voltage relation, it is worth mentioning that also the strongly nonlinear capacitance C_{be} generates 2nd-order harmonic currents, as given by the following equation

$$|i_{b,2nd}| = \omega \frac{\partial C_{be}}{\partial V_{be,i}} \cdot A_{be,i}^2. \tag{3.7}$$

At 1 THz, the 2nd-harmonic base current $i_{b,2nd}$ exceeds the maximum $i_{c,dc}$ two times.

3.5.2.2 Model II: G_m, C_{be}, R_e

In Model II, shown in Figure 3.5 a), the emitter contact resistance R_e is included. R_e provides a series DC feedback path. This path is critical for the detector rectification process. It creates a voltage division network between the internal and the external BE DC bias ($V_{be,i} \leq V_{be,x}$) and RF driving voltages ($v_{be,i} \leq v_{be,x}$) and further linearizes the inherent junction nonlinearity independently from the operating frequency. The static influence of this linearization on the rectified current $i_{c,dc}$ can be quantified as

$$|i_{c,dc}|= \frac{\partial^2 I_c}{\partial V_{be,i}^2} \cdot \frac{A_{be,i}^2}{2} \cdot \frac{1}{1+G_m \cdot R_e}. \tag{3.8}$$

Further, with R_e present, an AC transfer function between $v_{be,x}$ and $v_{be,i}$ is defined. This manifests in the dynamic low-pass voltage division network

$$v_{be,i} = v_{be,x} \cdot \frac{Z_{Cbe}||\frac{1}{G_m}}{Z_{Cbe}||\frac{1}{G_m} + R_e}. \tag{3.9}$$

Combining static and dynamic non-idealities, a complete formulation for the rectified collector current in this model case can be formulated

$$|i_{c,dc}|= \frac{1}{2} \cdot \frac{\partial^2 I_c}{\partial V_{be,i}^2} \cdot \frac{A_{be,x}^2}{1+G_m \cdot R_e} \cdot \left| \left(\frac{1}{1+(G_m + j\omega C_{be}) \cdot R_e} \right)^2 \right|. \tag{3.10}$$

This equation highlights the importance of a low emitter resistance for a strong rectification process. Now, the second order collector current nonlinearity ($\partial^2 I_c / \partial V_{be,i}^2$), which improves the rectification process with increasing DC BE emitter voltage, is counteracted by the series feedback path. At low operation frequencies towards DC (f → 0 Hz), its impact is already very strong and reduces $i_{c,dc}$ by a factor of $1/(1+G_m \cdot R_e)^3$. Therefore, the optimum bias point is shifted to lower $V_{be,i}$ around 810 mV. Further, the maximum rectified collector current is reduced by almost a factor of 10 compared to the ideal case (Model I) depicted in Figure 3.4.

The dynamic voltage division network between $v_{be,i}$ and $v_{be,x}$, as indicated in Figure 3.5 b), shows only a weak frequency dependence with a cut-off frequency above 1 THz when biased with a $V_{be,i}$ of 810 mV. The 2nd-order harmonic base current $i_{b,2nd}$ scales down even stronger than $i_{c,dc}$. With the help of Figure 3.5 b), the influence of scaling R_e is indicated. A 50 % reduction in R_e leads to a doubled detector responsivity that even improves toward higher operating frequencies (1 THz). In other words, to minimize the influence of R_e on the rectification process, the device should either provide a small R_e or an optimum nonlinearity appearing at low bias currents.

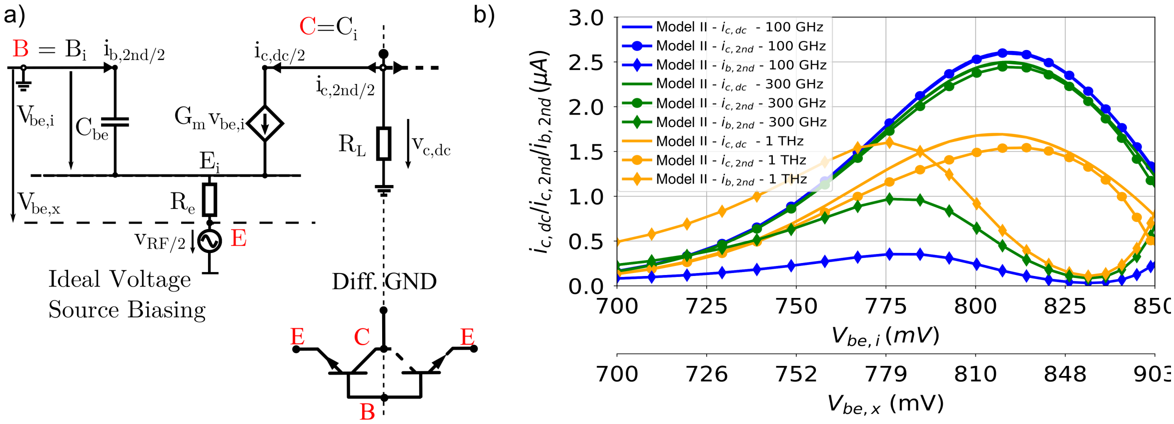

Figure 3.5: a) Model II with $G_{m,be}$, C_{be} and R_e.
b) Simulated rectified DC ($i_{c,dc}$) and second-harmonic currents at the collector ($i_{c,2nd}$) and base nodes ($i_{b,2nd}$) for different RF input frequencies.
Images after [own5] ©2022 IEEE.

3.5.2.3 Model III: G_m, C_{be}, R_b

In this model configuration, Model I is extended with the base-emitter resistance R_b as shown in Figure 3.6 a). R_b combined with C_{be} creates another time constant degrading the device's dynamic rectification process. Without R_e and omitting the low influence of R_π at THz frequencies, there is only a voltage division between the internal and external AC signals $v_{be,i}$ and $v_{be,x}$ (DC: $V_{be,i} = V_{be,x}$). Now, the rectified collector current shows a low-pass behavior with the following frequency roll-off

$$|i_{c,dc}| = 2 \cdot \frac{\partial^2 I_c}{\partial V_{be,i}^2} \cdot \frac{A_{be,x}^2}{4} \cdot \left| \left(\frac{1}{1 + j\omega R_b C_{be}} \right)^2 \right| . \tag{3.11}$$

By comparing simulations of Model I and III, the optimum device bias points resulting in a maximum detector response still come close together due to the absence of a static linearization effect by R_e. In total, the R_b/C_{be} induced low-pass filter results in a quick $i_{c,dc}$ drop with frequency increase as indicated in Figure 3.6 b). Due to the inherent C_{be} nonlinearity increasing with $V_{be,i}$, the low-pass cut-off frequency f_c is a strong function of the bias point. f_c varies between 900 GHz and 182 GHz for $V_{be,i}$ of 700 mV and 850 mV and, thus, is considerably lower than for Model II. Hence, the rectification at lower frequencies <100 GHz is unaffected. The loss in rectification efficiency toward 1 THz is at least 40 % higher than in Model II with R_e. The most important outcome for the rectified DC current based on this model configuration is that a possible down-scaling of R_b improves the detector performance only at higher RF towards 1 THz. Due to its strong influence, a halving of R_b results in a quadrupled $i_{c,dc}$.

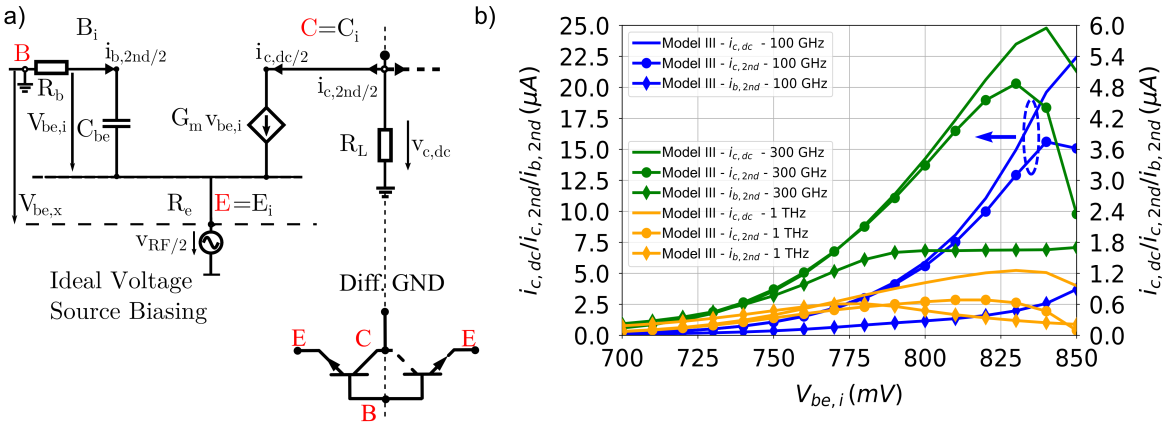

Figure 3.6: a) Model III with $G_{m,be}$, C_{be} and R_b.
b) Simulated rectified DC ($i_{c,dc}$) and second-harmonic currents at the collector ($i_{c,2nd}$) and base nodes ($i_{b,2nd}$) for different RF input frequencies.
Images after [own5] ©2022 IEEE.

The following transfer function can be applied to describe the generation of $i_{b,2nd}$

$$|i_{b,2nd}| = \omega \frac{\partial C_{be}}{\partial V_{be,i}} \cdot A_{be,i}^2 \cdot \left| \frac{Z_{Cbe,2nd}}{Z_{Cbe,2nd} + R_b} \right| . \tag{3.12}$$

Now, the second term ($A_{be,i}^2$) is further influenced by the voltage division network at fundamental RF, defined as

$$A_{be,i} = A_{be,x} \cdot \frac{Z_{Cbe}}{Z_{Cbe} + R_b} . \tag{3.13}$$

The last component of Equation 3.12 represents the voltage division network of the 2nd-harmonic current source based on C_{be} and R_b. The predicted 2nd-harmonic current values peak at around 300 GHz. This is in contrast to the inherent potential of the 2nd-harmonic current generation in the base, which improves with frequency and is presented in Model I. Here, the cascaded influence of two low-pass networks, one acting at the fundamental and the second operating at the 2nd-harmonic, results in a significantly reduced $i_{b,2nd}$. With R_b present, there is no virtual AC ground at the internal base nodes. Then, C_{bc} may affect the rectification process. This effect was ignored for simplicity.

3.5.2.4 Model IV: $G_m, C_{be}, C_{bc}, R_b, R_e, R_c$

The influence of all device parasitics shown in Figure 3.3 is included in this model configuration. Now, the virtual AC ground at the internal base and the internal collector node are prevented by R_b and R_e. Therefore, the capacitance C_{bc} may influence the detector responsivity by providing an RF feedback path. Further, both time constants introduced in Model II and III are included with their effects demonstrated in Figure 3.7 a). Their influence on the internal voltage divider at the base nodes can be

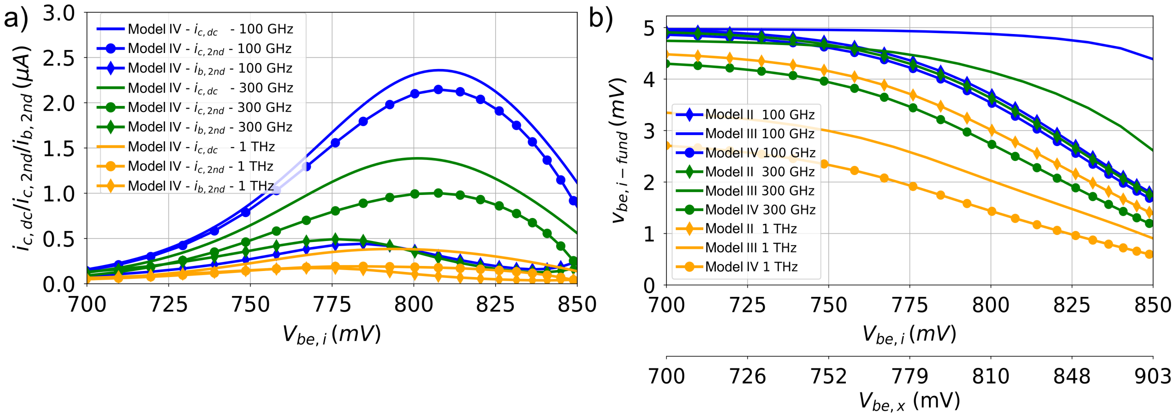

Figure 3.7: a) Model IV, including all device parasitics shown in Figure 3.3.
a) Simulated rectified DC ($i_{c,dc}$) and 2nd-harmonic currents at the collector ($i_{c,2nd}$) and base nodes ($i_{b,2nd}$) for different RF input frequencies.
b) Simulated evolution of fundamental $v_{be,i}$ across DC base-emitter voltage ($V_{be,i}$) for different frequencies and model variants.
Images after [own5] ©2022 IEEE.

approximated with the following transfer function

$$v_{be,i} = v_{be,x} \cdot \frac{(Z_{Cbe} + R_b)||\frac{1}{G_m}}{(Z_{Cbe} + R_b)||\frac{1}{G_m} + R_e} \cdot \frac{Z_{Cbe}}{Z_{Cbe} + R_b}. \tag{3.14}$$

As here the influence of C_{bc} is not included, its impact was verified by simulations and added in Figure 3.7 a). To distinguish between the impact of C_{bc} and the influence of the voltage transfer functions derived from the previous model cases and combined in Equation 3.14. The C_{bc} feedback path leads to further deterioration of the rectified current compared to the joint influence of Models II and III. Still, it needs to compete against the low-pass transfer function from Equation 3.14. Therefore, the drop in $i_{c,dc}$ changes non-monotonically in frequency. As the rectified collector currents at 1 THz for Model IV and a combination of Model II and Model III are approximately the same, a low impact of C_{bc} is indicated. In summary, the influence of C_{bc} is masked by the dominant low-pass networks introduced by C_{be}, R_b and R_e, which shunt the internal base-emitter voltage.

The evolution of the internal $v_{be,i}$ RF voltage driving the base-emitter diode is shown in Figure 3.7 b) depending on the base bias point. Additionally to the $v_{be,i}$ trends, another key fact is that the internal RF base-collector voltage towards 1 THz already exceeds the internal base-emitter voltage. This may result in a deterioration of the detector rectification if the base-collector diode bias condition changes from the reverse-bias to saturation, as explained in more detail in Section 3.5.3. The trend of $v_{bc,i} > v_{be,i}$ increases with the base bias voltage and is based on the high base-emitter diffusion capacitance, which shunts the internal emitter and base nodes. To conclude, the assumption of an ideal virtual AC ground at the inner base and collector nodes, which are typically not handeled in the literature, is unrealistic for a detector operation at THz frequencies.

The complete model predicts a substantial reduction of the feasible rectification efficiency, especially compared to the ideal rectification shown for Model I. This reduction is based on static and dynamic effects. In the static case, the emitter resistance R_e moves the optimum bias point to lower base-emitter voltages and drastically limits the detector response independently from the operating frequency by at least one order of magnitude. In the dynamic case, the primary influence of R_b and C_{be} increases with frequency and is around 1 THz even stronger than the influence of R_e. Due to all parasitic phenomena, the maximum possible device responsivity calculated based on the DC nonlinearity shown in Figure 3.4 b) is reduced by at least two orders of magnitude.

3.5.2.5 Detector Thermal and Shot Noise

The foundry-provided HiCUM model does not include any 1/f or GR noise components. Therefore, only thermal and shot noise components were investigated within the model analysis as a comparison basis. An overview of the output voltage noise for all model versions with an ideal voltage-mode biasing is depicted in Figure 3.8. Based on Figure 3.8, the influence of the parasitic access resistances on the output voltage noise can be evaluated. Due to the emitter resistance R_e, present in Model II, the base-emitter diode junction is linearized, resulting in less collector-emitter current flow for the same base-emitter voltage and thus in reduced shot noise at the output, especially for higher bias points with $V_{be,x}$ larger 770 mV. Hence, the noise of Model I is larger than the noise of Model II with R_e. Most critical for the output current noise is the size of the base-emitter resistance R_b included in Model III as its noise is transferred with respect to the device current gain β from the base node to the collector node. For this purpose, the simulated noise of Model III exceeds the noise in all other model types. Model IV includes effects induced by R_b and R_e, resulting in an intermediate noise curve. For lower bias points smaller than 730 mV, the output noise is dominated by thermal noise of the external 1.83 kΩ load resistance, which is around 5.5 nV/$\sqrt{Hz}$.

The influence of the device parasitics on the noise performance at low frequencies close to DC is relatively low compared to their impact on the rectification process towards THz frequencies. Here, the maximum rectified current reduces by roughly a factor of 10 if the emitter resistance is included in the model. At the same time, the noise reduces 'only' by a factor of approximately 2. The deviation between the HiCUM model's simulated noise and the equivalent model's voltage noise is less than 2 %.

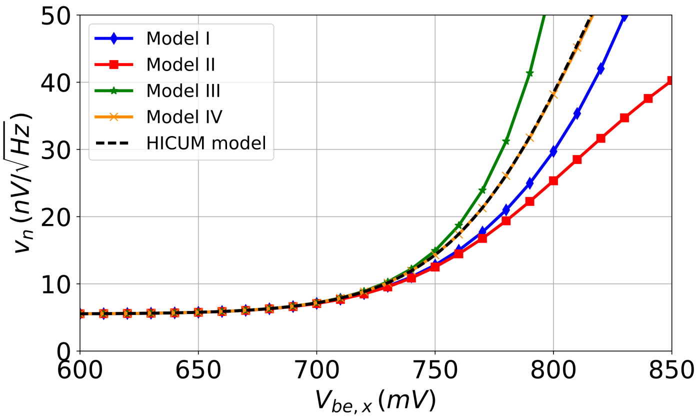

Figure 3.8: Simulated voltage noise for different types of the developed nonlinear equivalent model and the HiCUM model vs. external base-emitter voltage ($V_{be,x}$) biased in the forward-active region with $R_S = 0\ \Omega$ and $R_L = 1.83\ k\Omega$. Only thermal and shot noise are modeled.

3.5.3 Detector Model for the Saturation Region

In the saturation region, the base-emitter and base-collector diode are forward-biased, as explained in the basic Gummel Poon model [92]. An extension of Model IV for the forward-active region is crucial for accurate device modeling, especially as the base-collector diode's nonlinearity and the RF and DC driving conditions of the base-collector diode ($V_{b,ci}$, $v_{b,ci}$) can now affect the device rectification process. This extension manifests in two significant model changes, as shown in Figure 3.9 a). Firstly, the device parasitics and the base node are represented by their internal and external parts. A component splitting improves the high-frequency modeling of the base-collector node. It does not significantly affect the device responsivity in the forward-active region (≈5 %). Secondly, an additional current source denoted as $G_{m,bc}$ [92] was included based on the forward current $I_{c,r}$ of the base-collector diode relating to the internal base-collector RF voltage $v_{bc,i}$. The total DC rectification process in analogy to Model I can now be formulated with two components acting out-of-phase

$$|i_{c,dc}|= \left|\frac{\partial^2 I_{c,f}}{\partial V_{be,i}^2}\cdot\frac{v_{be,i}^2}{2}-\frac{\partial^2 I_{c,r}}{\partial V_{bc,i}^2}\cdot\frac{v_{bc,i}^2}{2}\right|. \tag{3.15}$$

$I_{c,f}$ corresponds to the base-emitter diode and $I_{c,r}$ to the base-collector diode. In the saturation region without V_{ce}, both currents nearly compensate each other, resulting in a very low total DC collector current I_c in the range of 1 μA.

In this configuration, an inherent load resistance of $1/G_{m,bc}$ is present due to the $V_{bc,i}$-driven current source. Therefore, a DC output voltage swing appears at the detector output, enabling direct measurements of the corresponding detector voltage responsivity R_v without an additional load resistance. Now, the bias-dependent voltage responsivity relates to the current responsivity of the base-emitter diode and the

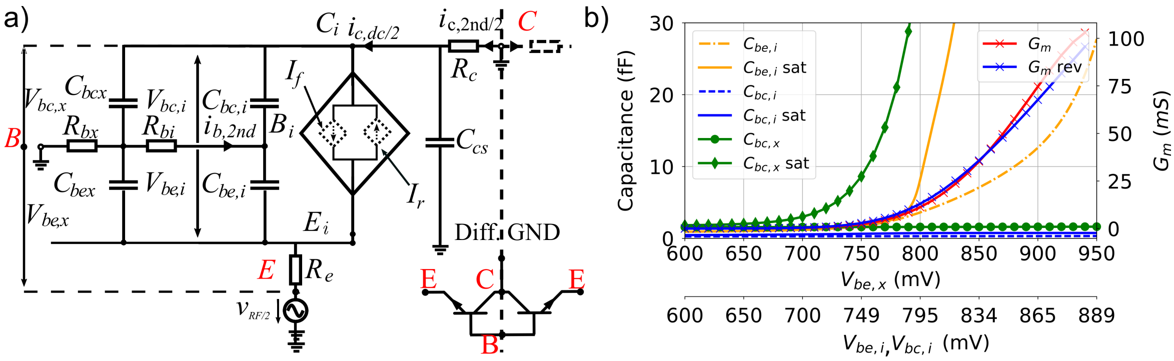

Figure 3.9: a) Model for the saturation region, including all distributed device parasitics. b) Values of the corresponding device parasitics compared to their values in the forward-active region and $G_{m,be}$ as well as $G_{m,bc}$. Images after [own5] ©2022 IEEE.

output resistance of $1/G_{m,bc}$ set by the base-collector diode. As both trends are different vs. $V_{be,i}$, R_i and R_v for a detector operating in deep saturation show other optimum bias points.

The simulated bias-dependence of the most important model parameters is depicted in Figure 3.9 b) to gather the main trends of the device responsivity in the saturation region. In comparison to the forward-active mode, C_{bc} and C_{be} grow much faster with their corresponding bias voltages $V_{be,i}$ and $V_{bc,i}$. This is related to an increase of the peripheral depletion capacitances of the external BC region and the space-charge variation associated with the BE junction and the BE depletion capacitance [108] resulting in a $V_{bc,i}$ and $V_{be,i}$ dependency. Large C_{bc} values limit the detector operation to lower base bias points below 800 mV and result in a deterioration of the detector response with frequency.

In the saturation region, $v_{bc,i}$ creates additional rectification components that are out-of-phase with those from $v_{be,i}$. At sufficiently low RF, $v_{bc,i}$ is small and has no notable contribution to the total detector's current responsivity. However, as plotted in Figure 3.10 a), a difference in the rectified current between both operation regions grows quickly with frequency, with the optimum bias point shifting toward lower base voltages. Another essential aspect of detector operation in saturation is related to the shunting action of C_{be}, which transfers the fundamental driving voltage from the input emitter nodes to the internal base/collector nodes, as shown in Figure 3.10 b).

The significance of a local minimum in the rectified collector current for higher bias points should be highlighted in the following. It was experimentally verified as non-existent with a floating collector node for the saturation region but observed in the simulation results with the full HiCUM model. In further measurements, this behavior appeared at a different bias point with a slightly reverse-biased collector node of

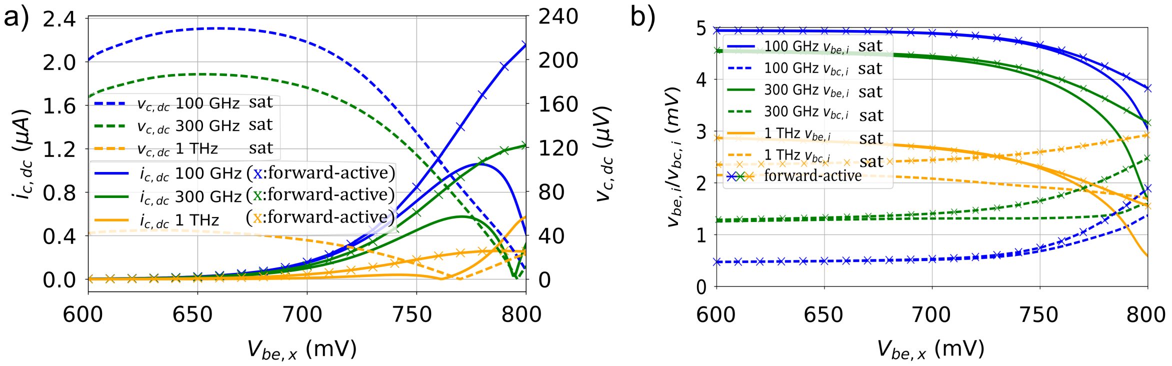

Figure 3.10: a) Rectified DC current simulated with the equivalent model in deep saturation (sat, $V_{ce} = 0$ mV) and forward-active mode ($V_{ce} = 1$ V) for different RF input frequencies (100 to 1000 GHz).
b) Corresponding internal fundamental BE ($v_{be,i}$) and BC ($v_{bc,i}$) voltages (RF Amplitude: $A_{rf} = 10$ mV).
Images after [own5] ©2022 IEEE.

$V_{ce} = -50$ mV. This effect may be attributed to two effects: First of all, C_{be} is not strictly increasing as a monotonic function of V_{be}. This may lead to some parasitic numerical divergence while calculating the relevant derivatives for the rectified currents. Secondly, under appropriate bias conditions, the rectified components of both diodes cancel each other. As this effect was seen in the measurements with a 50 mV different V_{ce}, it might indicate model uncertainties in the saturation region, which usually is not the focus of the given HiCUM model [109].

To indicate the model-based rectification limitations, R_v as a function of $V_{be,x}$ is shown in Figure 3.10. Now, the maximum R_v bias point is shifted to 700 mV and below as the voltage response also depends on the output resistance, plotted in Figure 3.1 and decreases with $V_{be,x}$. The maximum voltage responsivity corresponds to a bias point of $V_{be,x} = 680$ mV, where the detector output resistance is around $3\,\mathrm{k}\Omega$. At these bias conditions, C_{bc} and C_{be} are substantially reduced, resulting in a lower frequency dependence of the voltage responsivity compared to R_i from the conventional current-mode operation. The low output noise floor based on the detector 'cold' operation ($I_c \approx 1\,\mu$A) challenges the characterization of its NEP.

A central message found in this analysis is that the maximum responsivity, even in the saturation region, is only reduced by a factor between two and three compared to the forward-active region. This factor is nearly constant across the entire frequency range from 200 GHz to 1 THz. This trend indicates a low dependency of the detector NEP on the standard performance metrics of SiGe HBTs, namely f_t/f_{max}, which in deep saturation are in the range of several GHz.

3.5.4 Antenna-Detector Power Coupling

Contrary to the previous analysis with an ideal voltage drive, which is unrealistic at THz frequencies, the free-space power received by an antenna is first converted into an external base-emitter voltage $v_{be,x}$. The magnitude of $v_{be,x}$ is given by an impedance ratio of Z_{Ant} and Z_{Det}. For optimum detector operation, $v_{be,x}$ has to be maximized across the full operation bandwidth. This is commonly achieved by a complex-conjugate antenna-detector impedance matching. To link this standard matching technique with the necessary $v_{be,x}$ maximization, firstly, the basic equation relating the free-space power P_{Ant} available from the antenna and the input driving voltage is investigated

$$v_{be,x} = 2 \cdot \sqrt{P_{Ant} \cdot Re\{Z_{Ant}\}} \cdot \frac{Z_{Det}}{Z_{Ant} + Z_{Det}}. \tag{3.16}$$

Maximizing $v_{be,x}$, requires a large Z_{Ant} and Z_{Det} magnitude. It can be achieved by increasing either $Re\{Z_{Ant}\}$ or $Im\{Z_{Ant}\}$. Most commonly, a conjugate match with a dominant resistive part is traced. By applying the same conditions (conjugate match) with a dominant $Im\{Z_{Ant}\}$ Equation 3.16 can be rearranged as

$$v_{be,x} = \sqrt{P_{Ant}} \cdot (\sqrt{Re\{Z_{Det}\}} + \frac{j \cdot Im\{Z_{Det}\}}{\sqrt{Re\{Z_{Det}\}}}). \tag{3.17}$$

In this case, a considerably higher $|v_{be,x}|$ can be reached with a low resistive detector impedance part and a large imaginary part that is comparable to an ideal LC tank at the detector input. This fact is commonly omitted in the design process as Z_{Det} is predefined by the internal device parasitics and can only be changed under different bias conditions. Thus, the hypothetical case of $Re\{Z_{Det}\} \rightarrow 0\ \Omega$ is unrealistic but theoretically results in a maximum detector responsivity. Also, from the antenna point of view, both driving conditions are challenging, as they are either narrowband with high $Re\{Z_{Ant}\}$ [110] or accomplish low antenna radiation efficiencies and a dominant $Im\{Z_{Ant}\}$. Due to the highly reactive detector impedance at THz frequencies, a more general detector-antenna impedance search space is required to maximize $|v_{be,x}|$.

For this purpose, the detector input impedance was simulated as a function of the base bias at three different frequencies (100 GHz, 300 GHz, 1 THz) and drawn in Figure 3.11 a). The main observations are: The input impedance becomes less capacitive toward higher input frequencies and higher bias voltage $V_{be,i}$. Furthermore, at high-frequency operation, the influence of the parasitic contact resistances increases as the impedance levels drop and the bias dependency decreases. In general, the antenna needs to provide an inductive input impedance for a conjugate match. Around a bias point of $V_{be,i} = 770$ mV, the optimum reactance is nearly constant in the whole frequency range, while the resistive part drops by a factor of three.

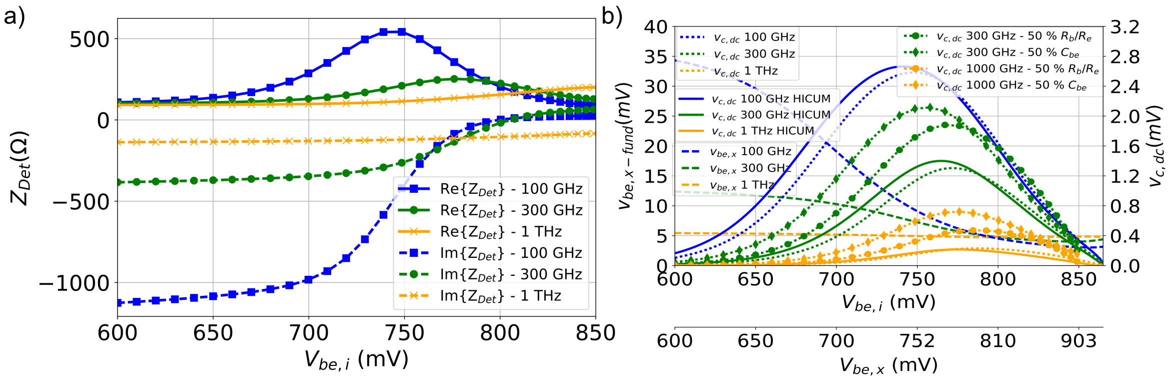

Figure 3.11: (a) Simulated real- and imaginary part of the detector input impedance Z_{Det} (HiCUM model) vs. $V_{be,i}$ for $V_{ce} = 1\ V$.
b) Fundamental external base-emitter voltage $v_{be,x}$ and rectified DC voltage $v_{c,dc}$ at different frequencies and for different model versions in the forward-active mode (Solid: HiCUM model, dashed: Equivalent model).
The detector is complex-conjugately matched at each DC operating point.
Images after [own5] ©2022 IEEE.

In Figure 3.11 b) the simulated rectified DC collector voltage across the load resistance R_L and the evolution of the external RF drive voltage, $v_{be,x}$ depending on the internal and external base-emitter voltages are shown. The detector was conjugately matched at all investigated bias points, assuming the ideal impedance values from Figure 3.11 a) and driven by an input power of -40 dBm. Simulation results are shown based on the previously introduced Model IV and the device HiCUM model to indicate the excellent modeling approach. With the help of the former analysis, it can be noted that $v_{be,x}$ increases very fast with rising detector reactance. The highest rectified collector voltage is achieved with a V_{be} of around 760 mV, as a trade-off between the previously described rectification process and the maximum drive voltage $v_{be,x}$. Further, the optimum bias point moves slightly toward higher voltage values with increased frequencies, where the detector impedance shows the highest magnitude as shown in Figure 3.11 a). If both effects are taken into account, the rectified voltage can be approximated by

$$|v_{c,dc}| = \Big|\frac{\partial^2 I_{ce}}{\partial V_{be,i}^2} \cdot P_{Ant} \cdot Re\{Z_{Ant}\} \cdot (\frac{Z_{Det}}{Z_{Ant} + Z_{Det}})^2 \cdot$$

$$(\frac{(Z_{Cbe} + R_b)||\frac{1}{G_m}}{(Z_{Cbe} + R_b)||\frac{1}{G_m} + R_e} \cdot \frac{Z_{Cbe}}{Z_{Cbe} + R_b})^2 \cdot \frac{1}{1 + G_m \cdot R_e} \cdot R_L\Big|. \tag{3.18}$$

Equation 3.18 allows a prediction of the rectification strength for devices in future technologies with reduced device parasitics or improved G_m. To visualize the influence of several reduced parasitics, a 50 % reduction in R_b, R_e and C_{be} was assumed and included in the simulations with the developed equivalent model as shown in Figure 3.11 b). One essential observation is that reducing C_{be}, which is the main contributor to $Im\{Z_{det}\}$, is the most efficient way of improving the responsivity in the 300 GHz to 1 THz frequency band. Additionally, the maximum responsivity appears at lower $V_{be,i}$, where $Im\{Z_{det}\}$ grows. Due to the lower current density in these bias points, a decrease in $C_{be,i}$ is also beneficial for the output shot noise and helps to reduce the overall detector NEP.

The optimum frequency-dependent complex drive impedances need to be generated across a near-THz bandwidth to achieve the maximum responsivity. These impedance values cannot be provided by classical matching techniques relying on transmission line networks coupled to inductors or capacitors but can further be synthesized based on the antenna structure. This is a challenging task, especially if a certain compactness of the antenna structure is requested for successive inclusion into large FPAs. Thus, the antenna impedance will also derivate from the necessary optimum impedance values at several frequency points.

It is crucial to understand to what extent the antenna impedance variations from the optimum conjugate match influence the maximum achievable detector responsivity. Therefore, before designing the antenna, first the contours of constant responsivity for the most important bias points and operation frequencies were simulated for the forward-active region as shown in Figure 3.12 a). These simulations can be seen as source pull simulations, which present the relative drop in responsivity as a function of the antenna impedance deviation from the optimum [own6], [own5]. Three different frequencies (300 GHz, 500 GHz, 1 THz) were chosen and the $V_{be,i}$ providing the optimum responsivity at the corresponding frequency point according to Figure 3.11 b), was selected as device bias. For a better comparison of forward-active and saturation regions, the current responsivity R_i was chosen, as the voltage responsivity in saturation strongly depends on the device output impedance.

The most important conclusion from this contour analysis is that the contours of constant responsivity come much closer together at lower impedance values. This effect is related to the previously mentioned decrease in the fundamental driving voltage $v_{be,i}$. Thus, low real parts should be avoided, as a small modeling error might result in a significant responsivity drop. Due to the elliptical contour shape, it can be concluded that the maximum responsivity is more sensitive to $Im\{Z_{det}\}$ for sufficiently high $Re\{Z_{det}\}$. For the antenna design, apart from the radiation efficiency, an optimum antenna impedance trajectory should preferably lie within the 90 % contour across the whole frequency range with a large real part and an inductive imaginary part favored.

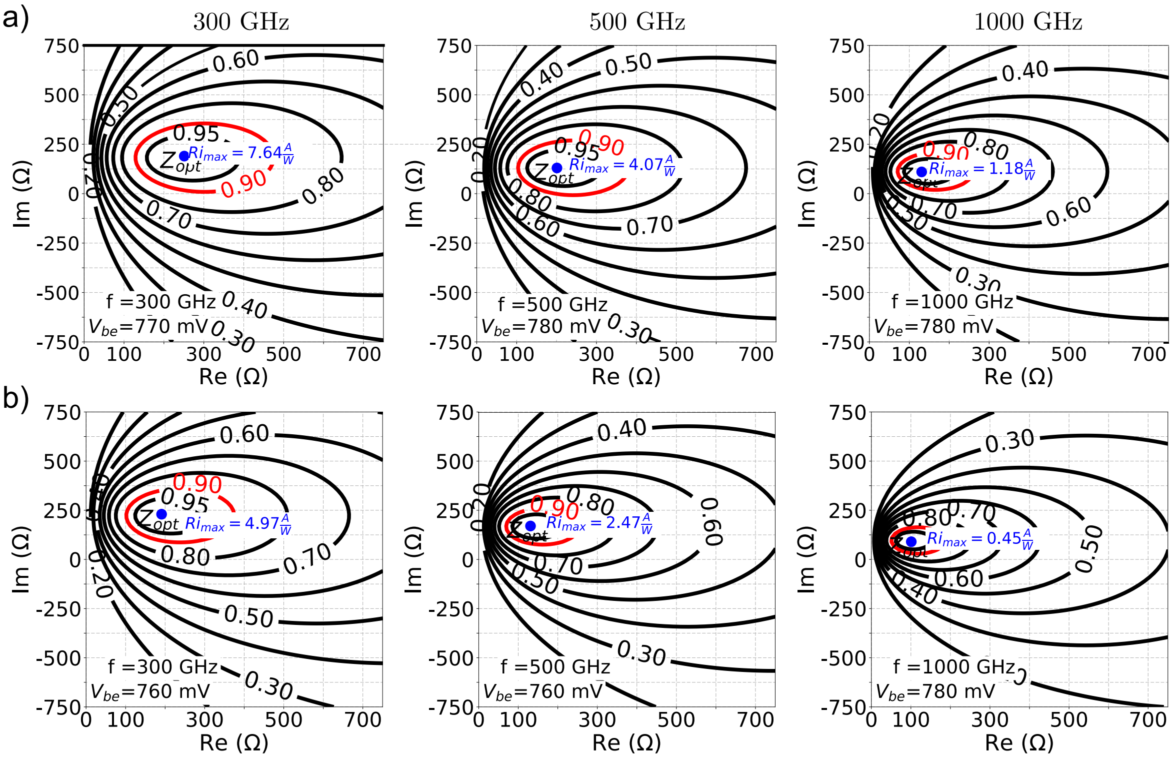

Figure 3.12: Normalized contour plots of simulated detector current responsivity R_i as a function of the antenna driving impedance Z_{Ant} at 300 GHz, 500 GHz and 1000 GHz for different bias regions.
a) Forward-active region.
b) Saturation region.
Images after [own5] ©2022 IEEE.

3.5.4.1 Device in Saturation

The contours of constant current responsivity were also simulated for the detector operated in the deep saturation region with $V_{ce} = 0$ V, as shown in Figure 3.12 b). For a better comparison between both operation modes, the same frequency points previously demonstrated for the forward-active region were chosen for the simulations corresponding to the maximum R_i bias points. Contrary to a faster responsivity drop with operation frequency in saturation, the optimum impedance levels are in the same range for both operation ranges. This is reasoned in the detector input impedance defined by the same device parameters. The difference is mainly attributed to $C_{bc,x}$ and $C_{be,i}$, which largely increase with bias voltage in saturation as shown in Figure 3.9 b). In other words, the antenna does not need to be redesigned to improve the detector performance by changing the operation region between forward active and saturation in a current mode readout. However, if the detector is operated in the voltage mode, the optimum bias voltage decreases to a V_{be} of 650 mV, as indicated in Figure 3.10 a). Thus, the detector input becomes more capacitive, resulting in the need for a higher antenna impedance imaginary part for an operation at lower frequencies, as indicated in Figure 3.11.

3.5.5 Optimum Device Size

In the investigated device technology from IHP, the transistor device size can be modified by increasing the number n of emitter fingers. Such a change in device size will affect the maximum achievable detector responsivity R_i, minimum NEP and the antenna design space. These dependencies are analyzed for SiGe HBT direct detectors biased in the forward-active and saturation regions in the following.

3.5.5.1 Responsivity and NEP vs. Device Size

It is crucial to evaluate the device parasitics' evolution among different device sizes to analyze the influence of device size on the maximum R_i. In Figure 3.13, simulations of selected model parameters, $C_{be} = C_{be,i} + C_{be,x}$, $C_{bc} = C_{bc,i} + C_{bc,x}$, R_e, R_c and G_m for different device sizes are shown for devices operated in forward-active region. Three device sizes are invesigated: x1 $= 1{\times}0.12\ \mu m^2$, x2 $= 2{\times}0.12\ \mu m^2$ and x3 $= 3{\times}0.12\ \mu m^2$. By a comparison of the graphs shown in Figure 3.13, the following trends can be noticed. If the number of emitter fingers, respectively, the device size is doubled (multiplied by a factor of x)

- The contact access resistances are divided by a factor of 2 (x), Figure 3.13 a)-b).
- Parasitic device capacitances increase by a factor of 2 (x), Figure 3.13 c).
- The transconductance G_m is multiplied by a factor of 2 (x), Figure 3.13 d).

These trends were validated by simulations of the device parasitics for devices in several device sizes until the maximum device size (x8). In total, contact access resistances and parasitic capacitances derivate by less than 5 % from the trends mentioned above.

In consequence, the corresponding input impedance is inversely proportional to the number of emitter fingers. When referring to Equation 3.18, all these effects nearly compensate each other, resulting in a constant maximum detector responsivity for different device sizes. As this equation is partly valid also in the saturation region (R_i reduced by rectified BC diode current), the same conclusion is drawn for the saturation region.

Another critical aspect of device performance is the change of detector output voltage noise for different device sizes. With chopping above the low-frequency noise corner frequency applied, shot noise is the dominating noise source that scales with the collector output current I_c. As I_c is proportional to the device size, the overall optimum detector NEP will degrade for larger device sizes.

In saturation, the trend is different. Here, the output voltage noise is mainly defined

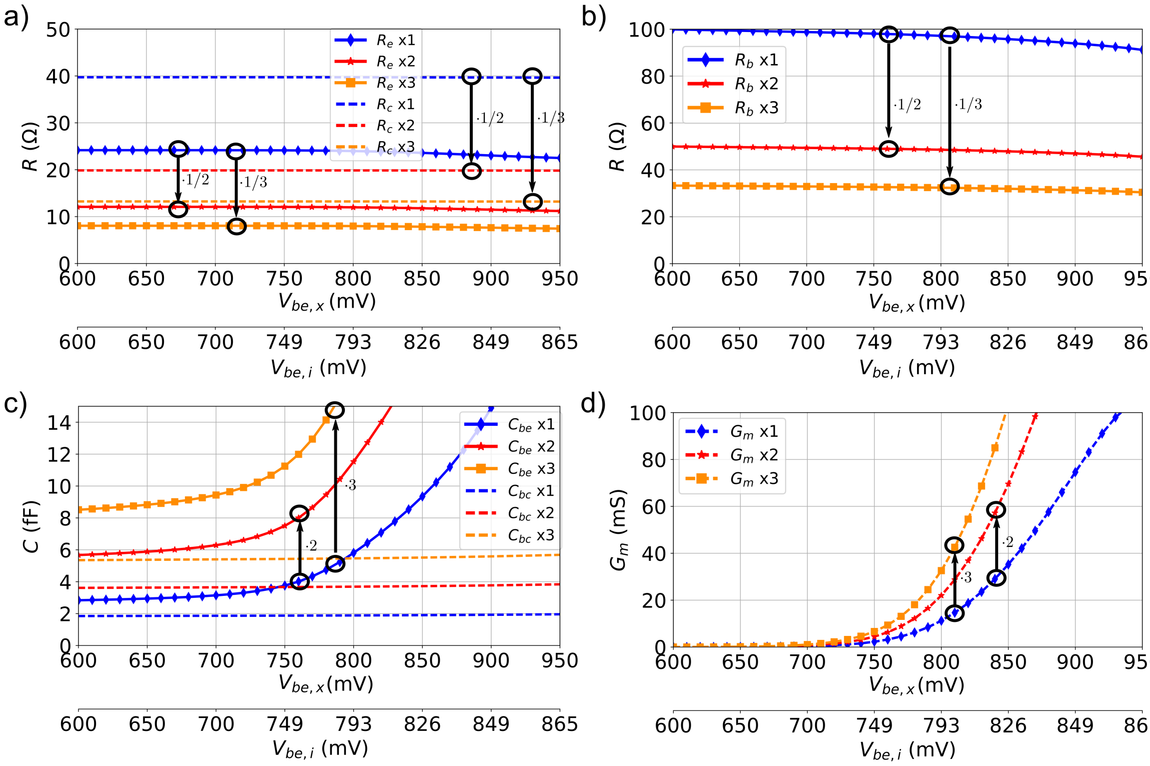

Figure 3.13: Selected model parameters vs. $V_{be,i}$ and $V_{be,x}$ for different device sizes (x1 to x3). All parasitics contain internal and external contributions.
a) Contact access resistance R_e and R_c.
b) Base resistance R_b.
c) Transconductance G_m.
d) Parasitic base-emitter C_{be} and base-collector capacitance C_{bc}.

by the thermal noise from the device output impedance. The thermal noise is expected to decrease with increasing device size as the output impedance drops. Unfortunately, the simulated output noise of the device operated in saturation may become much lower than an external amplifier's input noise for several bias points. Therefore, this effect in saturation will not be visible in the measurement Chapter 4.

3.5.5.2 Antenna Design Space vs. Device Size

The best way of analyzing the antenna design space is based on normalized detector current responsivity contours as a function of the antenna impedance Z_{Ant}. These are shown for various frequencies and different detector device sizes (x1, x2) in Figure 3.14 related to $R_{i,max}$. The nearly constant maximum current responsivity and the evolution of the detector input impedance among different device sizes are underlined. Multiplying the device size by a factor of n decreases the corresponding contour area of constant responsivity by n^2. Thus, the detector input impedance decreases proportionally to n for larger device sizes. Further, an absolute variation of the antenna input impedance from the optimum may result in lower responsivity for larger device sizes. In total, detectors with larger device sizes feature a much smaller antenna impedance

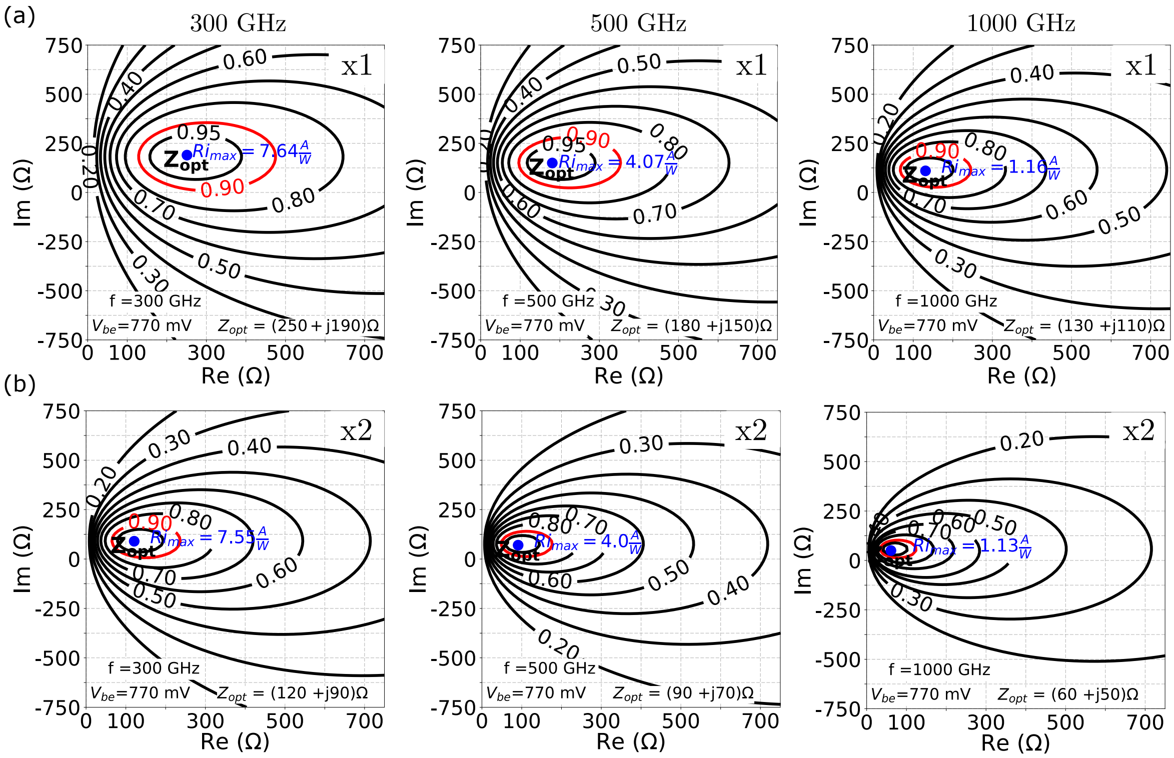

Figure 3.14: Normalized contour plots of simulated detector current responsivity R_i as a function of the antenna driving impedance Z_{Ant} at 300 GHz, 500 GHz and 1000 GHz for different detector device sizes biased in the forward-active region.
a) device size: x1: 1× 0.12 μm^2.
b) device size: x2: 2× 0.12 μm^2.

design space (scaled with $1/n^2$) as detectors implemented with devices in the minimum device size (x1). All trends are also proven to be valid in the saturation region.

3.6 Technology Comparison

The previous analysis, especially for the detector operated in the saturation region, did not indicate a direct dependency of the detector rectification process on the devices' f_t/f_{max}. During this thesis work, IHP provided access to its new high-performance technology SG13G3 with f_t/f_{max} of 470/650 GHz and the corresponding HiCUM models. Based on the challenging design requirements for passive imaging, it is of particular interest if the newest device technologies can help in improving future detector sensitivities and push their performance towards real-time passive imaging. First, the differences of SG13G3 and SG13D5, which was used for the previous detector simulations, are introduced to analyze the possible detector performance in the newest device technology. Then, the influence of static and dynamic parasitic effects limiting the detector performance similar to the previous Section 3.5.2 is briefly discussed, focusing on the forward-active region with $V_{ce} = 1$ V.

3.6.1 Major Technology Modifications

The main model changes between SG13D5 and SG13G3 concern the parasitic access resistances, device nonlinearity and BE and BC capacitances. A concise summary of the relevant changes is given below:

- **Parasitic Access Resistances:** A comparison between the access resistances in both device technologies is shown in Table 3.2, which assumes constant resistance values across the detector biasing range. The main difference in the parasitic access resistances is established with a nearly halved R_c and R_e. In particular, the reduction of R_e has a crucial influence on the static device nonlinearity due to the reduced series feedback. Furthermore, the base resistance R_b without changing its total value is differently distributed between internal and external components.

Table 3.2: Access resistances for x1 devices in SG13G3 and SG13D5

Technology	R_{bi}	R_{bx}	R_e	R_c
SG13D5	57 Ω	41 Ω	24 Ω	40 Ω
SG13G3	70 Ω	25 Ω	12.8 Ω	26 Ω

- **Device Nonlinearity $\partial^2 I_{ce}/\partial V_{be,x}^2$:** The difference in the device DC nonlinearity is shown in Figure 3.15 a). To include the linearizing influence of R_e, the derivation of I_{ce} was taken with respect to the external BE voltage $V_{be,x}$. Due to the reduced R_e and a different doping profile of the BE diode, a 2.5 times higher maximum nonlinearity is achieved within the SG13G3 process. This is beneficial for the maximum device responsivity but not necessarily for the overall device NEP due to the corresponding current density that is at least increased by a factor of 3.

- **Parasitic Device Capacitances:** As indicated in Figure 3.15 a), there is no notable difference between $C_{bc,i}$, $C_{bc,x}$ and $C_{be,x}$ in both technologies. However, $C_{be,i}$ differs significantly. Especially at lower bias points ($V_{be,i} < 780$ mV), $C_{be,i}$ in the SG13G3 technology is roughly doubled. At higher bias points, the trend changes and $C_{be,i}$ is reduced by roughly 20 % as compared to $C_{be,i}$ in the SG13D5 technology.

3.6.2 Detector Sensitivity

Concerning the previous analysis, first, the static effects on the rectification process are analyzed. Based on the increased maximum nonlinearity and the reduced R_e feedback path, the maximum responsivity should be nearly doubled as indicated in

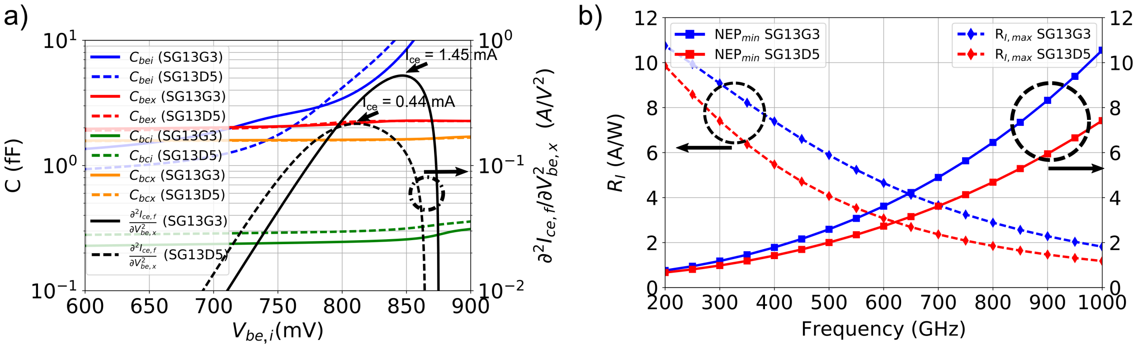

Figure 3.15: a) Simulated internal and external BE (C_{be}) and BC (C_{bc}) capacitances for x1 devices in SG13D5 and SG13G3 biased in the forward-active region.
b) Corresponding simulated minimum NEP and maximum voltage responsivity curves (1.83 kΩ load). The following bias points were chosen:
Max. R_v: $V_{be,i} = 780$ mV (SG13D5), $V_{be,i} = 810$ mV (SG13G3)
Min. NEP: $V_{be,i} = 750$ mV (SG13D5), $V_{be,i} = 770$ mV (SG13G3)

Equation 3.18. This comes along with a higher shot noise for devices implemented in SG13G3, as the peak nonlinearity is achieved with $I_{ce} = 1.45$ mA at a $V_{be,i}$ of 850 mV, as compared to $I_{ce} = 0.44$ mA at ≈ 810 mV $V_{be,i}$ (SG13D5). When now applying the following metric $\partial^2 I_{ce}/\partial V_{be,x}^2/\sqrt{I_{ce}}$, under the assumption of a dominant shot noise component in the forward-active region, the optimum bias points for a minimum NEP shift to lower $V_{be,i}$ values around 775 mV (SG13D5) and 825 mV (SG13G3). At these bias points, the ratio between the device nonlinearities in both technologies is still around 2.5.

Now, the dynamic effects introduced by the primary time constants (R_b, C_{be} and R_e, C_{be}) need to be taken into account. At 770 mV in SG13D5 and 825 mV in SG13G3, $C_{be,i}$ differs significantly in both technologies. In the SG13G3 technology, $C_{be,i}$ is around 50 fF, while for SG13D5 it is around 25 fF. For this purpose, the low-pass filter introduced by R_e and C_{be} and its cut-off frequency stays nearly the same (Model II). Nevertheless, the effect of the second low-pass filter (R_{bi}, $C_{be,i}$) becomes more pronounced and cancels the increased DC nonlinearity already at around 300 GHz. Further, this effect is enhanced due to the higher R_{bi} in SG13G3. As $C_{be,i}$ is essential for higher frequencies (see Figure 3.3), a performance deterioration is expected towards 1 THz.

The expected minimum electrical NEP and maximum voltage responsivity simulated for the differential common-base detector circuit in both technologies is shown in Figure 3.15 b) under ideal detector input matching and bias conditions. For maximum R_v, a $V_{be,i}$ of 780 mV (SG13D5) and 810 mV (SG13G3) was found, while the minimum NEP was achieved at a $V_{be,i}$ of 750 mV (SG13D5) and 770 mV (SG13G3), respectively. The following two important observations should be highlighted. Firstly, in both technologies, the maximum voltage responsivity drops by at least a factor of 5 from 200 GHz to 1 THz due to the low-pass characteristic formed by the internal device parasitics. This effect is explained in detail in Sections 3.5.2.2 and 3.5.2.3. The responsivity drop can only be avoided with access to the technology process, in particular by reducing $C_{be,i}$ and R_{bi}, but not by any circuit design technique without reducing the responsivity towards lower frequencies. Secondly, the maximum current responsivity in SG13G3 is at least 20 % higher than in SG13D5. Due to the previously explained reasons (shot noise, $C_{be,i}$), the overall minimum NEP is at least 15 % lower in SG13D5 at 300 GHz (1.2 pW/$\sqrt{Hz}$ for SG13G3, 1.0 pW/$\sqrt{Hz}$ for SG13D5). Furthermore, this deviation increases towards higher frequencies due to the increasing influence of $C_{be,i}$ towards higher frequencies resulting in a NEP of 7.5 pW/$\sqrt{Hz}$ (SG13D5) and 10.5 pW/$\sqrt{Hz}$ (SG13G3).

In summary, the simulations show a 1 dB better performance for direct detectors implemented in SG13D5. This performance improvement is on the same level as the typical measurement uncertainties in the THz frequency range of approximately 1 dB. Therefore, similar results are expected for THz direct detectors implemented in both technologies in the following measurements. An integral of the simulated responsivities shown in Figure 3.15 across frequency and a calculation of the NETD according to Equation 2.30 under the assumption of 3 dB implementation losses results in NETD values of 500 mK to 600 mK in a 1 Hz bandwidth. This underlines the feasibility of passive imaging with THz direct detectors in both technologies.

3.7 Antenna Implementations

Three antenna versions were implemented and coupled to SiGe HBT devices in different technologies. The antenna versions are denoted as A_1 to A_3 and the direct detector performance is further investigated in the following measurement sections. The antennas are shown in Figure 3.16 and their common features are discussed in the following. All antennas are embedded into a seven-metal layer back end of line (BEOL) stack. They are designed for backside illumination of a 3 mm diameter, hyper-hemispherical silicon lens with a near-elliptical extension through a lossy 150 µm thick silicon substrate (50 Ω.cm) with a 3.75 µm epi-layer (20 Ω.cm). Due to the broadband detector operation, no anti-reflection-coating at the lens interface was applied, resulting in approximately 30 % Fresnel loss at the lens-air interface. The overall size of all antennas is relatively small (110 to 160 µm).

The main antenna design goals, as discussed in the previous section 3.5.4, are the synthesis of a complex and frequency-dependent input impedance, which maximizes the detector response in a near THz bandwidth by the antenna shape and, at the same time provides a near ideal radiation efficiency in the whole frequency band. Achiev-

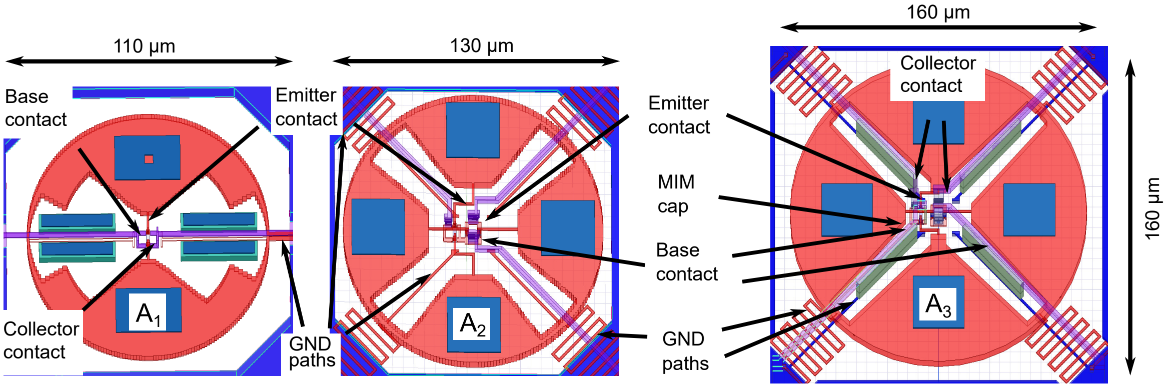

Figure 3.16: Simulation models of the investigated antenna geometries $A_1 - A_3$

ing the first objective most likely requires an inductive antenna input impedance to compensate for the capacitive detector imaginary part.

3.7.1 Single-Polarized Antenna A_1

The first version, denoted as A_1 [own5], [own6], [own8], is a single-polarized antenna that was implemented in two different advanced SiGe HBT technologies with f_t/f_{max} of 350/550 GHz (named SG13D5) and f_t/f_{max} of 470/650 GHz (SG13G3). Due to the antenna's differential operation, a DC path for the emitter nodes, as well as the low-frequency routing to contact the detector base and collector nodes, can be applied along its H-plane [111]–[113]. In this structure, the differential operation establishes a broadband RF AC ground for the fundamental input excitation at the external base and collector nodes. As only odd modes are excited, the operation bandwidth can be improved.

The antenna consists of two magnetically coupled wire semi-rings connected along with its center feed. The feed and ring shape towards the AC ground along the H-plane, starting from the antenna center, controls the self- and mutual impedance between both wire semi-rings. In this way, the overall antenna impedance profile is shaped. In more detail, the broadband impedance transformation due to the nonuniformly tapered radiator shape can be understood with the help of the transmission-line theory, where each part of the antenna can be viewed as a (coupled) transmission line section. The wideband operation is mainly funded in the center diagonally-tapered feed designed with a suitable opening angle and length. The antenna inductive behavior is further reached by choosing narrow center strip widths and lengths in the antenna center.

3.7.2 Dual-Polarized Antenna A_2

The second antenna geometry (A_2) [own5], [own7]–[own9] is a dual-polarized antenna that was implemented in SG13D5. In the dual-polarized structure, the tapered antenna feed needed to be modified. Here, the second polarization path is placed in the H-plane of the other polarization feed without space left for DC wiring. Therefore, all DC paths for detector connection are implemented on the antenna diagonal planes. A shared base bias for both polarizations, two separate collector outputs and substrate and ground contacts are included in the DC routing.

In this complex topology, the existing antenna fields at the diagonals may interact with the DC lines at higher frequencies. Such a coupling has several consequences on the antenna's broadband operation. A simple short of the antenna ring to GND would influence the overall antenna current flow. Hence, the ground path is provided by serpentine feeds. All DC line connections are within the top metal layer to reduce the line interaction further. However, the antenna is implemented in the lower metal layers. To avoid any resonances at multiple integers of quarter-wavelengths at THz frequencies, the DC lines were terminated by 50 fF Metal–insulator–metal (MIM) caps placed outside the antenna geometry, minimizing the injection of THz currents. As two pairs of transistors are now located in the antenna center, an ideal external AC ground between the base and collector can hardly be achieved due to the layout asymmetries of the required DC routing. The overall layout was carefully analyzed to reduce these asymmetries.

3.7.3 Dual-Polarized Antenna A_3

The third antenna geometry A_3 is a redesigned version of A_2 and was implemented in IHP's newest device technology SG13G3. It includes multiple layout changes to enhance the antenna radiation efficiency towards lower frequencies and combat the influence of some performance-deteriorating layout inclusions necessary to properly operate two device pairs in the antenna center. Here, four diagonal lines along the ring perimeter are used for DC biasing, such that the shared base connections are removed, enhancing the polarization separation. Furthermore, the transmission lines between the top-metal level DC lines and the corresponding bottom-metal level ground return paths were filled with a 100 fF MIM cap layer, creating a broadband short towards RF frequencies. As a result, an increased 30 to 40 dB suppression of RF signals across 200 to 1000 GHz at the external DC supply ports around the pixel periphery can be reached. Nevertheless, a perfect AC short at the device nodes cannot be provided due to the connecting distance of around 25 µm (12 µm vertical distance) to the MIM cap boundary. In total, the aperture size increased to 160 µm. The radiation efficiency could be further enhanced with the help of an ocean script, creating design rule check (DRC) compliant metal structures with a minimum feature size. This is notable when comparing the staircase-shaped antenna ring of A_2 with the geometry of A_3.

3.7.4 Antenna Radiation Efficiency and Impedance Profile

The simulated radiation efficiency η_{Ant} and input impedance of the antennas on a semi-infinite silicon substrate are shown in Figure 3.17. The complementary polarization path's efficiency and impedance values are not derivating more than 5 % by simulations. The assumed layer-dependent metal conductivity ranges from 1.98 to 2.4×10^7 S/m. Based on Figure 3.17 b), the implemented inductive imaginary part is achieved for all antenna structures with only a small exception in the dual-polarized geometries (500 to 600 GHz or 600 to 700 GHz). The large real part of A_2's input impedance at 550 GHz will not deteriorate the overall R_i as this impedance still lies within the 90 % $R_{i,max}$ contour evaluated for the implemented device technology, as shown in Figure 3.12.

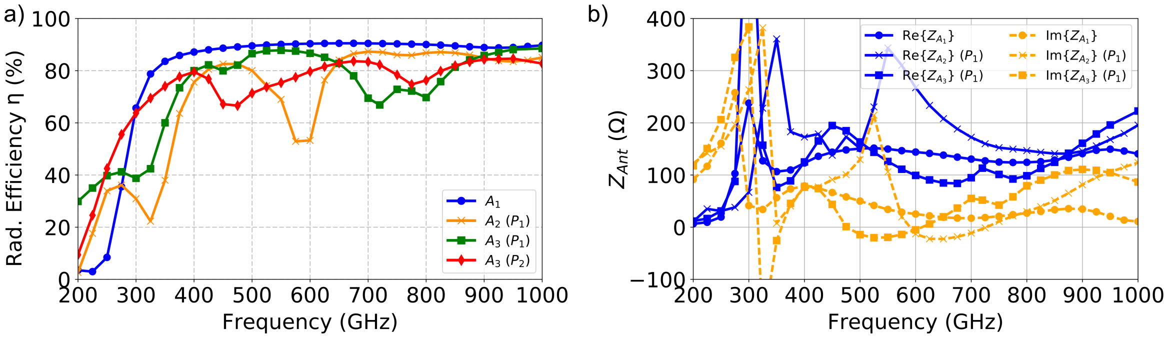

Figure 3.17: a) Simulated antenna radiation efficiencies ($A_1 - A_3$). For A_3 also the efficiency of the second polarization is plotted (P_2).
b) Real- and imaginary parts of the corresponding antenna input impedances.

The assumed implementation losses for all antenna implementations can further be estimated. With an assumed radiation efficiency around 80 %, a matching efficiency around 90 % and 30 % Fresnel losses at the lens-air interface, they are expected to be in the range of 3 dB. To estimate the performance improvement achieved with the modifications implemented in the dual-polarized antenna version A_3 as compared to A_2 for passive imaging, the metric $\int_{f_1}^{f_2} \eta_{A_3} df / \int_{f_1}^{f} {}_2\eta_{A_2} df$ was applied from 200 GHz to 1 THz, resulting in a broadband radiation efficiency improvement of 5 to 10 % (depending on the polarization). In summary, with an expected implementation loss of only 3 dB and at least 700 GHz RF bandwidth based on their radiation efficiency and inductive behavior across the entire frequency band, all implemented antenna versions fulfill the challenging requirements for passive imaging.

3.8 Summary and Conclusion

The theoretical analysis in this chapter provides the fundamentals of the internal THz rectification process for SiGe HBTs operated in the active-forward and saturation regions. Based on investigations with a HiCUM-based, nonlinear equivalent transistor model implemented in Verilog A, the maximum device responsivity of a differential common-base detector circuit was analyzed mathematically and by simulations with an advanced SiGe BiCMOS technology with f_t/f_{max} 350/550 GHz (SG13D5). The maximum responsivity depends on the static device nonlinearity and the internal base-emitter RF voltage $v_{be,i}$, which deteriorates dynamically due to the time constants introduced by internal device parasitics and the external matching circuit. The following summarizes the most significant outcomes of the equivalent model analysis.

From the static point of view, the internal emitter resistance R_e of 24.11 Ω linearizes the maximum device current and thus deteriorates the maximum device responsivity by more than a factor of ten, even at low frequencies towards DC. Furthermore, primary low-pass networks are formed by R_b, C_{be} and R_e, C_{be}, manifesting as a voltage transfer function from the external base-emitter voltage reducing $v_{be,i}$. These low-pass networks are crucial for high-frequency device rectification and result in a steadily decreasing responsivity towards THz frequencies that cannot be overcome with device matching without performance deterioration at lower frequencies. In the saturation region, the same trend was observed with responsivity values reduced by a factor of approximately three due to an out-of-phase rectification of the base-emitter diode induced by the fundamental base-collector voltage $v_{bc,i}$, which increases towards higher bias points and operation frequencies. With access to the internal nodes, a scaling of the most important device parasitics could be applied to analyze the performance of future device technologies with reduced parasitics. It was found that C_{be} is crucial for the rectification and demonstrated that a 50 % C_{be} reduction theoretically enables an at least doubled responsivity at 300 GHz.

Furthermore, the influence of the device matching on the responsivity was analyzed. A maximum external voltage drive is reached for a complex conjugate detector input match. This results in a power-to-voltage transfer function at the detector input, which shifts the maximum rectification point to lower bias points (around 790 mV) and sets the antenna design space. As a conjugate device match is impossible across a close to THz bandwidth, the antenna design space was analyzed with a detector source pull analysis, resulting in contours of constant responsivity. The primary outcome is that 90 % of the maximum responsivity can be reached within a broad impedance contour across the whole frequency range. Further, a close-to-optimum responsivity requires an inductive antenna impedance.

With this derived knowledge, three different antennas were implemented and their influence on the optimum detector operation conditions was analyzed. The simulated implementation loss is only around 3 dB. By simultaneously providing a large operation bandwidth of 700 GHz while maintaining a radiation efficiency of more than 80 %, all antenna versions are feasible options for passive imaging.

Based on the responsivity contours for different device sizes, it was further demonstrated that the maximum responsivity does not depend on the device size. For this purpose, a detector implemented in the minimum device size supports a minimum NEP operation compared to larger device size implementations if the shot noise is assumed as the dominant noise source (active-forward bias, chopping above 1/f noise corner frequency). Additionally, optimum bias conditions for minimum detector noise were investigated. A voltage bias reduces the base shot noise transferred to the collector node. A maximum output load resistance enables a minimum NEP operation in the voltage mode, which is favorable due to the low output impedance of the detector in the saturation region.

The detector performance of two different technologies (SG13G3 and SG13D5) was analyzed by simulations. It was demonstrated that detector implementations in both technologies theoretically achieve NETD values <1 K (200 GHz to 1 THz) in a 1 Hz bandwidth with ideally assumed 3 dB losses and only 20 % deviation between both technologies. This demonstrates the theoretical feasibility of THz passive imaging with detector implementations in both technologies.

Chapter 4

Detector Characterization and Measurements

For responsivity and NEP characterization, the previously described detector-coupled antennas were combined with a 3 mm diameter hyper-hemispherical silicon lens with an extension length of 0.38 mm near the elliptical position [114] and glued to a recess of a simple two-layer FR-4 board. The chip micrographs and the chip-to-lens assembly of the investigated direct detectors are shown in Figure 4.1. Five different detector antenna combinations are characterized in a free-space CW measurement setup in terms of NEP and voltage responsivity R_v to verify the previous NEP simulations and the feasibility of passive imaging. These detectors are implemented in different technologies (SG13D5 f_t/f_{max} 350/550 GHz, SG13G3 f_t/f_{max} 470/650 GHz) with different device sizes. A short list summarizing the investigated detectors, which are marked in red in Figure 4.1 a), is given below as a reference.

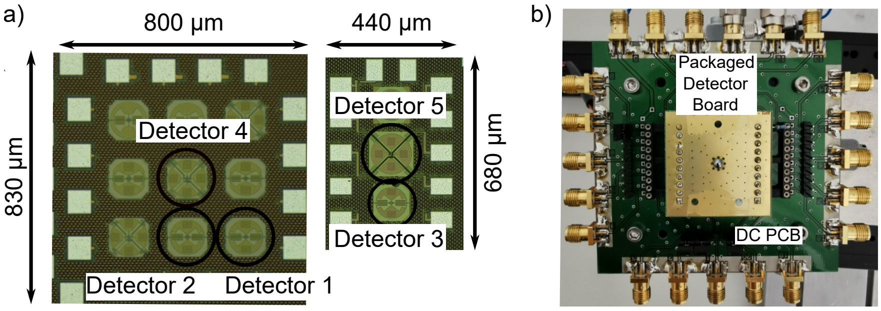

Figure 4.1: a) Chip micrographs of the investigated antenna-coupled detectors implemented in different device technologies.
b) Packaged detector board mounted on a low-frequency DC PCB.

- **Detector 1**: Antenna A_1, technology SG13D5, $A_e = 1 \times 0.12\,\mu m^2$ (x1)
- **Detector 2**: Antenna A_1, technology SG13D5, $A_e = 2 \times 0.12\,\mu m^2$ (x2)
- **Detector 3**: Antenna A_1, technology SG13G3, $A_e = 0.96 \times 0.1\,\mu m^2$ (x1)
- **Detector 4**: Antenna A_2, technology SG13D5, $A_e = 1 \times 0.12\,\mu m^2$ (x1)
- **Detector 5**: Antenna A_3, technology SG13G3, $A_e = 0.96 \times 0.1\,\mu m^2$ (x1)

Note that even though the detectors are partly implemented in different device technologies, the back end of line (BEOL) is the same. Furthermore, in the consecutive CW measurements only one polarization path of both dual-polarized detectors is evaluated, with the other one verified to derivate not more than 10 % above 300 GHz.

4.1 CW Measurement Setup

The free-space measurement setup for detector responsivity and NEP characterization is shown in Figure 4.2. The distance r between the detectors and the CW illumination source is located in the far-field zone for the investigated frequency range from 200 GHz to 1 THz, given by the Fraunhofer distance [115]. Three vector network analyzer extension (VNA) modules equipped with linearly polarized antennas were used in the characterization setup: A WR-3 module from OML operating between 220 and 320 GHz, a WR-2.2 extender from VDI (325 to 520 GHz) and a HG-wr-1.2-FB source from AB Millimeter covering the frequency range from 620 to 1000 GHz. Due to a lack of equipment, the 520 to 620 GHz band was not covered by measurements. The output power of all modules was pre-calibrated with a PM4 power meter from VDI. All modules were electronically chopped at 100 kHz to ensure a detector operation above the devices' low-frequency noise corner frequency.

The detectors were biased in a voltage-mode setup with a low-noise, low-impedance, 50 Ω B2962A power supply from Keysight, which is crucial for highly sensitive measurements minimizing the base shot noise transferred to the collector nodes. A 1.83 kΩ load resistance was used for measurements in the forward-active region. Furthermore, the detector performances were additionally evaluated in the weak saturation region with $V_{ce} \approx 50$ mV and saturation region without collector bias. The saturation region provides a low power consumption that is comparable to the commonly used zero-bias MOSFET detectors [116]. Please note that an external V_{ce} is not necessary to bias the devices in the saturation region. Therefore, the load resistance was removed in the corresponding measurements. A Femto HVA10M60F and an additional SR552 voltage amplifier from Stanford Research are used as buffers to amplify the detector output noise spectral density above the noise floor of the Keysight E4440A PSA spectrum

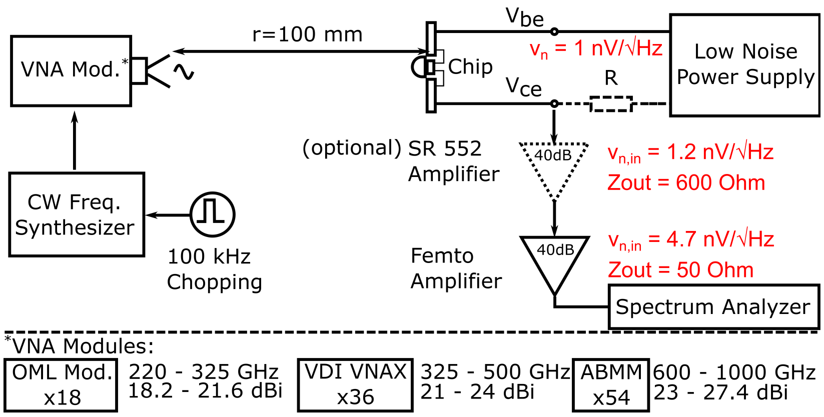

Figure 4.2: Free-space measurement setup with three different VNA extension modules operating between 220 GHz and 1 THz for detector NEP and responsivity characterization. The frequency range from 520 GHz to 630 GHz is not covered due to missing equipment.

analyzer. The voltage responsivity was calculated based on Equation 2.19 and the power $P_{received}$ at the lens surface constituted by the Friis-transmission equation [117] resulting in

$$R_v = \frac{v_{c,dc}}{P_{received}} = \frac{v_{c,dc}}{G_s P_s D_{ant}} \cdot \left(\frac{4\pi r}{\lambda}\right)^2 . \tag{4.1}$$

$v_{c,dc}$ is the rectified DC output voltage. P_s is the measured output power and G_s is the gain of the corresponding source horn antennas specified for the band center frequency. G_s was scaled with a f^2/f^2_{center} dependency for other frequencies [116].

For R_v calculation, the directivity D_{ant} of all lens-coupled antennas was characterized by radiation pattern measurements over a 100° × 100° section of the hemisphere and calculated as an integration of the measured power density patterns [75] from 200 GHz to 1 THz. Appropriate power levels for the unmeasured parts of the hemisphere were assumed based on full-wave EM simulations of the antenna structure. Then, by dividing the measured rectified output voltage by the directivity according to Equation 4.1, the magnifying influence of the lens aperture size on the detector responsivity is eliminated. That way, all relevant loss mechanisms down to the device level, such as Fresnel loss at the lens aperture, antenna radiation efficiency and antenna-detector matching conditions, are included in the measured responsivity. The measured directivity curves vs. frequency, as well as an example of full radiation patterns at 460 and 822 GHz, are shown in Figure 4.3. The slow directivity increase toward high frequencies approaching 1 THz can be attributed to three main aspects: The gradual influence of higher-order modes [118], [119], internal lens reflections due to the off-axis positions of the single-polarized antenna and the coupling between the two orthogonal tapered line sections in the dual-polarized geometries.

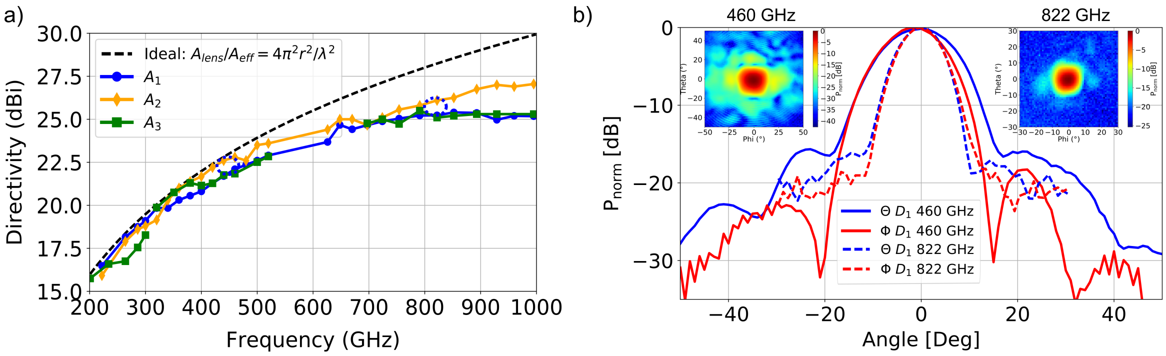

Figure 4.3: a) Measured directivity of the antenna detector combinations between 200 GHz and 1 THz and ideal directivity based on the lens aperture size.
b) Measured radiation patterns and cross-cuts at 460 and 822 GHz for detector D_1 normalized to the corresponding maximum.

4.1.1 Noise Measurements

Determining the detector NEP requires an accurate experimental characterization of the low-frequency noise components introduced in Section 3.3. This is necessary, as the device models for the SG13D5 technology only include thermal and shot noise components with a near-white frequency spectrum. Furthermore, especially in the saturation region, the device models might lack the accuracy, showing simulated output voltage noise spectral densities with values less than 1 nV/$\sqrt{Hz}$.

For this purpose, first, the measured detector output voltage noise spectral density is presented in Figure 4.4 for devices operated in the forward-active and saturation regions. A few close-to-optimum NEP bias points were selected for differently sized detectors in both device technologies. The bottom black and gray lines are the reference noise floor set by the readout amplifier with a short-circuited input. It has to be further mentioned that the 1.83 kΩ detector output load in the forward-active region additionally introduces a thermal noise voltage of 5.4 nV/$\sqrt{Hz}$ that overlays the amplifiers' output noise.

In saturation, the detector output impedance Z_{Out} changes with the device bias point due to the in general lower device output impedance Z_{Det}, indicated in Figure 3.1. Thus, the output voltage noise reduces for higher bias voltages. Therefore, all measurements in saturation were performed with the SRR552 amplifier providing a near frequency independent input referred voltage noise floor of 1.2 nV/$\sqrt{Hz}$ that is at least four times lower than the noise floor of the Femto amplifier. This central challenge of determining the detector noise in saturation is demonstrated in Figure 4.4 b). With very low bias currents smaller 1 μA, the output noise is primarily represented by thermal effects and related to the detector's output resistance values. Then, the detector NEP at higher bias voltages with $V_{be} > 750$ mV cannot be determined with the Femto

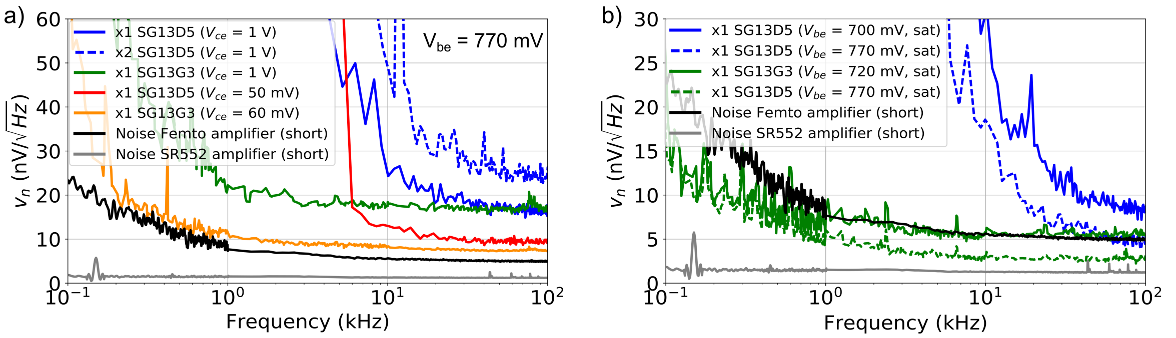

Figure 4.4: Measured low-frequency noise for several bias points and different detector sizes (x1, x2) implemented in SG13D5 and SG13G3.
a) Detector biased in the forward-active and saturation region with V_{ce} applied.
b) Detector biased in the saturation regions without V_{ce}.

amplifier due to its insufficient noise performance. Here, the blue curve (x1, SG13D5) measured with the SR552 amplifier is already below the input noise of the Femto amplifier. Due to the high output impedance at lower bias points with $V_{be} < 650$ mV, a noise frequency roll-off at higher chopping frequencies can be observed related to an increase of the effective time constant involving the cable capacitance. When comparing the measured voltage noise curve for the forward-active and the weak saturation region, it has to be pointed out that the equivalent current noise is comparable for both operation regions due to the similar bias currents, i.e., $I_c = 84$ µA vs. $\mathrm{I}_c = 65$ µA for weak saturation at $\mathrm{V}_{be} = 760$ mV implemented in SG13D5.

Significant differences can be obtained by comparing the low-frequency noise spectra for both device technologies. In the SG13D5 technology, irrespectively from the operation region and bias point, the detector noise is dominated by low-frequency noise components up to relatively high chopping frequencies, even when operated in deep saturation with negligible collector current. Only in the forward-active region, the noise floor above 50 to 100 kHz is set by collector shot noise as $\sqrt{2qI_c}$ [120], while in deep saturation this frequency range is dominated by thermal effects. Contrary to that, in SG13G3, the LFN corner frequency is drastically reduced. Here, the influence of 1/f and GR noise is already negligible above 1.5 to 2 kHz, making the implemented detectors a feasible option for imaging setups where optical chopping at low frequencies is required.

In both technologies, the noise corner frequencies scale with V_{be} in the forward-active and saturation regions. In the forward-active region, varying time constants related to GR noise components define the noise low pass behavior. In the saturation region, the corner frequency is set by the bias-dependent thermal noise components, whereas the measurements indicated roughly bias-independent LFN components. The weak saturation bias operation provides a stable voltage noise down to low chopping frequencies.

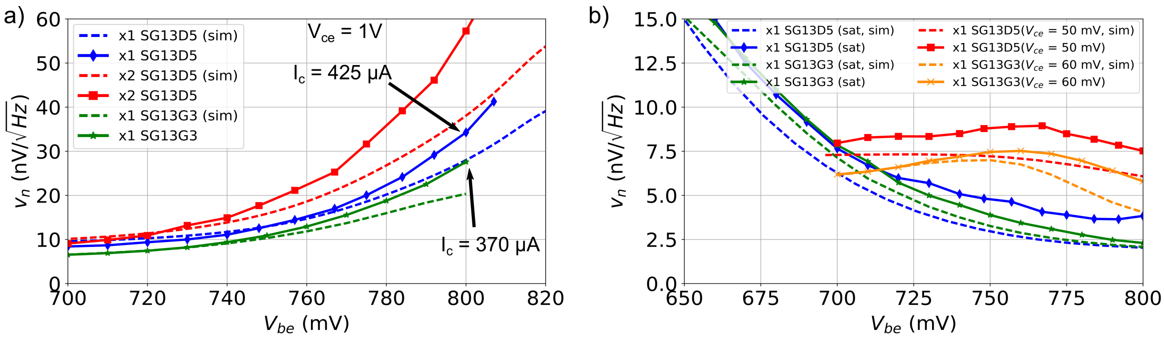

Figure 4.5: Measured and simulated detector output voltage noise spectral density vs. V_{be} at chopping frequency of 100 kHz. The detectors were implemented in two different device sizes (x1, x2) and different technologies (SG13D5, SG13G3).
a) Detector biased in the forward-active region.
b) Detector biased in the saturation regions with and without V_{ce} applied.

Furthermore, the noise scaling for increased device sizes (x2) was investigated. In the saturation region, its influence is hard to predict due to the effect of the amplifier noise floor, which changes with the detector output impedance. However, in the forward-active region, it was found that the noise scales with the expected behavior: A doubled device size provides two times higher I_c and thus the corresponding noise scales by a factor of $\sqrt{2}$. Further important observations are related to the different voltage scaling of v_n as a function of V_{be}, shown in Figure 4.5. As previously mentioned, the voltage noise spectral density is proportional to $\sqrt{I_c}$ towards higher bias points in the forward-active region. Due to a lower current density at the investigated bias points, the values measured for detectors in SG13G3 are approximately 10 to 20 % lower than for those implemented in SG13D5. In the weak saturation region, the same difference is observed, but an increase of current noise with V_{be} is counteracted by the decreasing output resistance, resulting in a lower bias-dependent v_n than for the forward-active region. In deep saturation, the trends are related to the inverse relation between output resistance and base bias voltage. Thus, v_n decreases with V_{be}.

A relatively high minimum chopping frequency of around 100 kHz was chosen for the subsequent measurements of the device responsivity to reduce the influence of the GR and 1/f noise components. Even if this is not necessary for detectors integrated within the SG13G3 technology due to corner frequencies in the low kHz range, it builds up a common comparison basis of both technologies.

4.1.2 Responsivity and NEP vs. Device Bias

Before studying the frequency-dependent NEP and responsivity trends, the optimum bias points for the detectors operated in the forward-active, weak saturation and saturation are evaluated. Therefore, the evolution of the detector responsivity and the corresponding NEP are shown in Figure 4.6 for a selected RF frequency of 430 GHz. The focus is set on detector 1 (A_1, SG13D5, x1) and detector 3 (A_1, SG13G3, x1) as they were implemented with the same antenna in two different technologies.

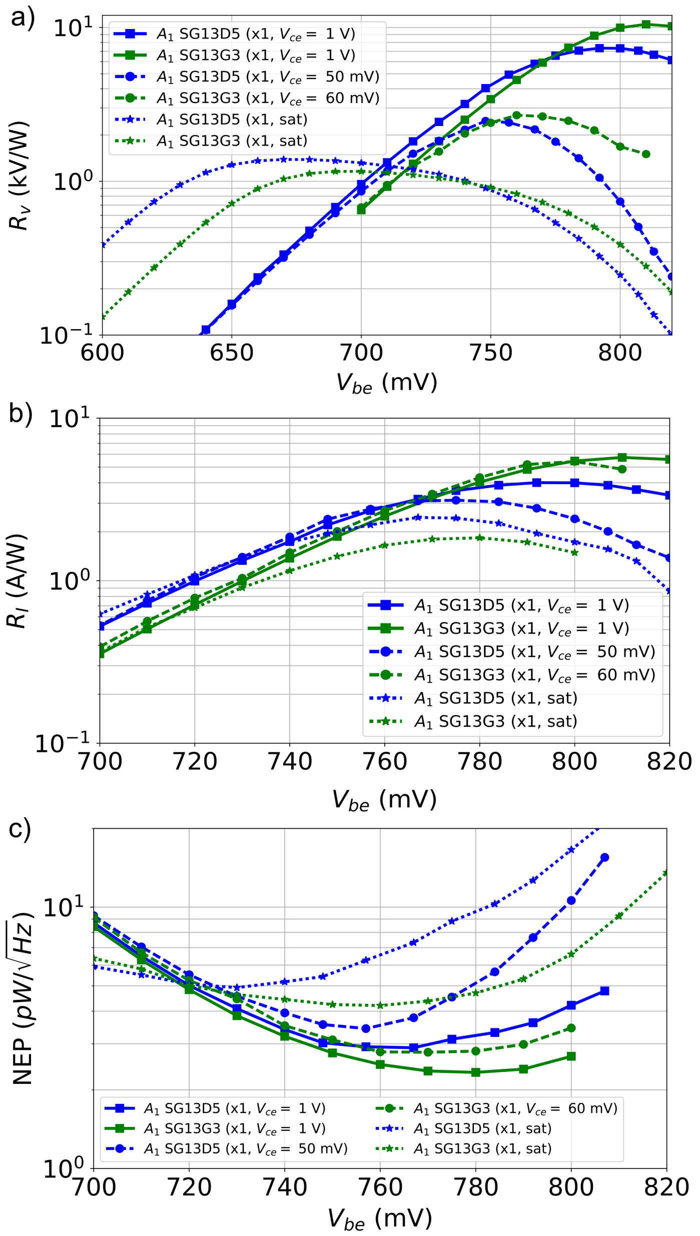

Figure 4.6: Measured a) R_v, b) R_i and c) NEP at 430 GHz vs. device bias point for the forward-active, weak saturation and saturation region.

Furthermore, it has to be mentioned that all detectors implemented in the same technology show similar trends in responsivity and NEP due to near identical antenna impedances at around 430 GHz and comparable responsivity contour levels.

It was experimentally proven that the bias dependency slightly varies across the entire frequency range, as shown in Figure 3.11, with a shift of the corresponding maximum R_v points towards higher V_{be} at higher operation frequencies. For a fair comparison between the forward-active and the saturation operation ranges, both the voltage and current responsivity are evaluated in Figure 4.6 showing the same general trends for detectors operated in both device technologies. In the case of R_v, the corresponding output resistance levels (Z_{Out}) are very different for each operation region. In the forward-active region, the 'fixed' 1.83 kΩ output load resistance R_L defined by the external load is a simple conversion factor resulting in $R_i = R_v/R_L$. In deep saturation (without R_L), Z_{Out} quickly grows towards low V_{be}, while it decreases to values $< 1\ k\Omega$ for $V_{be} > 750$ mV. This sets different optimum bias points for the evaluated voltage and current responsivities. In the forward-active region, the maximum values of 7.3 kV/W (A_1, SG13D5) at 790 mV V_{be} and 10.5 kV/W at 810 mV V_{be} (A_1, SG13G3) are reached. Here, the higher responsivity values, which are shifted towards larger V_{be} values, are based on the increased device nonlinearity and the different $C_{be,i}$ trends as shown in Figure 3.15 a). Contrary to this, in the saturation regions, the maximum voltage responsivity appears at a V_{be} of around 670 mV to 690 mV in both technologies and is around one order of magnitude lower.

The shown current responsivity trends vs. bias point avoid such a masking influence of the output impedance. Concerning the device R_i, all maximum bias points are located around a V_{be} between 770 and 810 mV. Here, a maximum R_i for the detectors implemented in SG13G3 technology is on average reached at 20 mV higher V_{be}, with a roughly doubled current density in the forward-active region ($I_c = 270$ µA, SG13D5, $V_{be} = 790$ mV, $I_c = 430$ µA, SG13G3, $V_{be} = 810$ mV). The described bias dependencies align well with the previous analysis in Chapter 3.

The rectified collector currents are similar for low bias points in all operation regions. This is mainly based on the internal base-collector RF driving voltage $v_{bc,i}$ that was analyzed in Figure 3.10, which is too low to produce sufficient rectification components with reverse orientation compared to $v_{be,i}$ at 430 GHz. According to this analysis, the difference between the rectified currents in the forward-active and saturation regions grows with frequency increase. In Figure 4.6 c), the measured NEP values are shown. The voltage spot noise at the detector output at 100 kHz was divided by the corresponding voltage responsivity to calculate the NEP. The impact of the amplifier on the measured NEP for forward-active bias operation is negligible.

Compared to [own5], an accurate de-embedding of the detector NEP was done by the use of the SR552 amplifier, preventing the output noise of the saturated devices from being below the amplifier noise floor. This leads to an improved measured detector performance in detector NEP of roughly 15 %, also seen in the consecutive frequency trends for the devices operated in the saturation region. In total, the minimum NEP values correspond to a V_{be} of around 770 mV for all detectors implemented in the SG13G3 technology. For the ones implemented in SG13D5 technology, the minimum NEP point shifts toward 760 mV. However, in the saturation region, it is around 730 mV. It is important to note that these bias points do not match those for the maximum responsivity. In total, similar minimum NEP values of around 2.4 pW/$\sqrt{Hz}$ (SG13G3) and 2.8 pW/$\sqrt{Hz}$ (SG13D5) were measured in the forward-active region. Further, a near-optimum NEP can be reached in the (weak) saturation regions with the advantage of low power consumption. The measured NEP difference in both technologies is still in the expected measurement uncertainty of the previous analysis shown in Section 3.6. A slightly better NEP is expected for detectors implemented in the SG13D5 technology.

Two main reasons can be attributed to the deviation between the simulation of the ideal detector performance in both technologies and the corresponding measured performances apart from general model inaccuracies. First, even at 100 kHz, far from the 1/f noise corner frequency, the measured noise for the detectors in the SG13D5 technology still slightly decreases with the chopping frequency. Here, a roughly 10 % improvement in NEP could be achieved with a chopping frequency of 400 kHz. Secondly, as indicated in Figure 4.1, detector 1 is located on a diagonal off-axis position at a displacement (X/R) ratio of around 0.12. This results in an additional increase in reflection loss of roughly 15 % [121].

4.1.3 Responsivity and NEP vs. Frequency

An extensive measurement and simulation effort was invested to characterize all detector implementations across the 200 GHz to 1 THz frequency band. The most important results are gathered in Figures 4.7 and 4.8, showing the frequency trends of the measured minimum NEP and maximum R_v evaluated at the optimum bias points found in Figure 4.6. Due to the model uncertainties, not all bias combinations were simulated, especially in the saturation and weak saturation regions. The responsivity simulation results are based on Harmonic Balance simulations of the detectors terminated with the antenna input impedance and include an additional 30 % Fresnel loss and the antenna radiation efficiency. The simulated NEP values imply the influence of the readout amplifier. Furthermore, to better estimate the implementation losses and the potential for improvements, another curve denoted as $R_{v,max}$ is included in Figure 4.7 a) that only contains the 30 % Fresnel loss and, thus, corresponds to the maximum achievable detector responsivity with the optimum antenna driving impedance and ideal antenna radiation efficiency. Due to the complexity of the mentioned Figures, only the most important results are briefly discussed in the following, with a focus set on a qualitative analysis of the detector performance in different device technologies, operation regimes and device sizes.

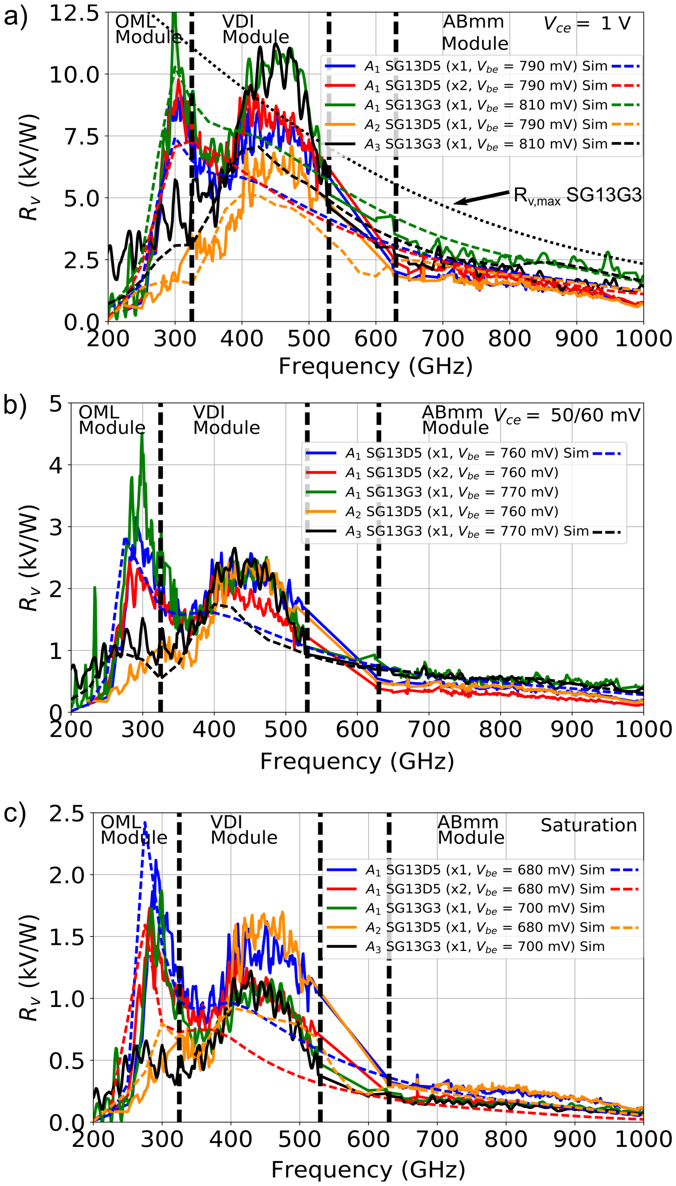

Figure 4.7: Evolution of the maximum detector R_v: a) in the forward-active region, b) in weak saturation and c) in saturation for several selected detector implementations.

4.1.3.1 Device Size Dependency

The measured voltage responsivity R_v for detectors implemented in SG13D5 with the same antenna (A_1) but different device size (x2) is highlighted at this point. It can be noticed that the response for the implementation with the x2 device size (red curve) is 10 to 20 % higher as compared to the design with the x1 device (blue curve) within 300 to 500 GHz. This, on the first view, contradicts the previous analysis shown in Section 3.5.5. However, by further research, the difference can be at least partly attributed to an improved fit between the implemented and the ideal antenna impedance. This is demonstrated in Figure 4.9 showing the constant responsivity contours for both device sizes and the implemented antenna impedance Z_{Ant}.

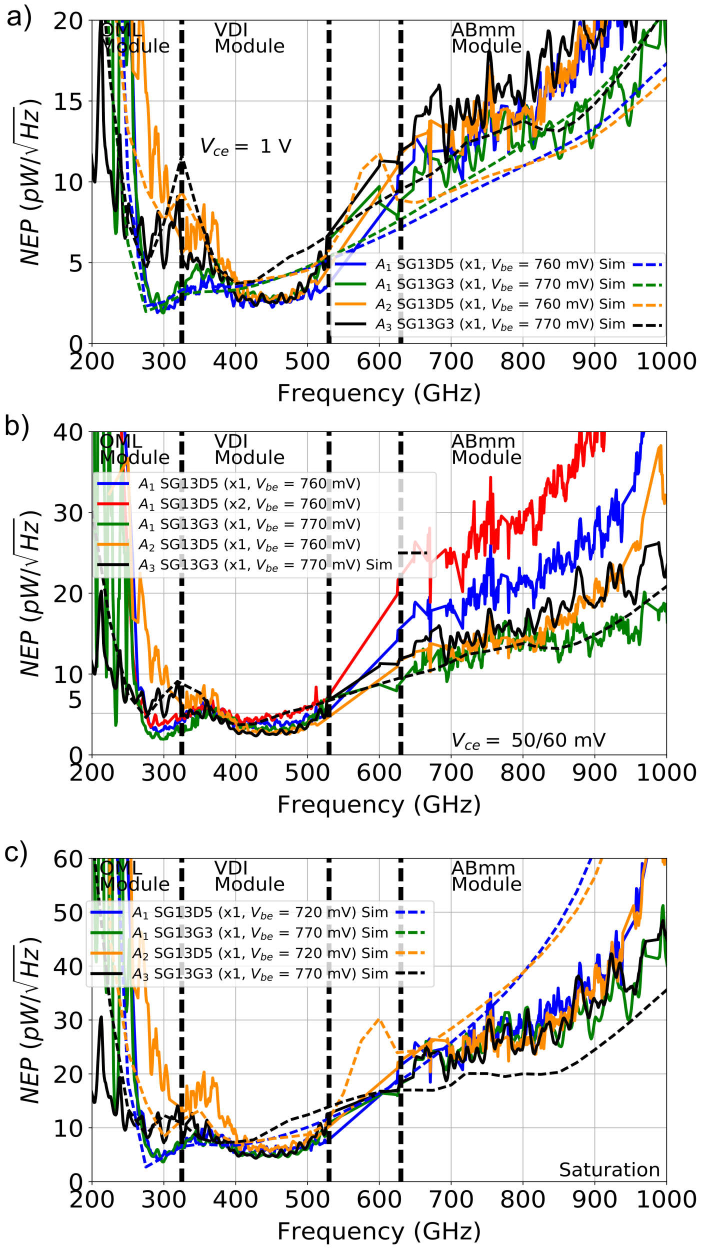

Figure 4.8: Evolution of the minimum detector NEP in the forward-active region a), in weak saturation b) and in saturation c) for several selected detector implementations.

By comparing the location of the antenna impedance within the contours for several frequencies, it becomes clear that the antenna impedance at lower frequencies, from 320 to 450 GHz, is more suitable for detectors based on x2 devices. For this purpose, the measured responsivity, i.e., shown in Figure 4.7 a), shows a clear size dependence. In other words, a modified antenna version that better fits to x1 devices could potentially improve the detector NEP by approximately 10 to 20 %. It must be further mentioned that due to the increased shot noise at the detector output, the x2-based detector does not improve the measured NEP. Here, the measured trends for both device sizes follow each other nearly one by one.

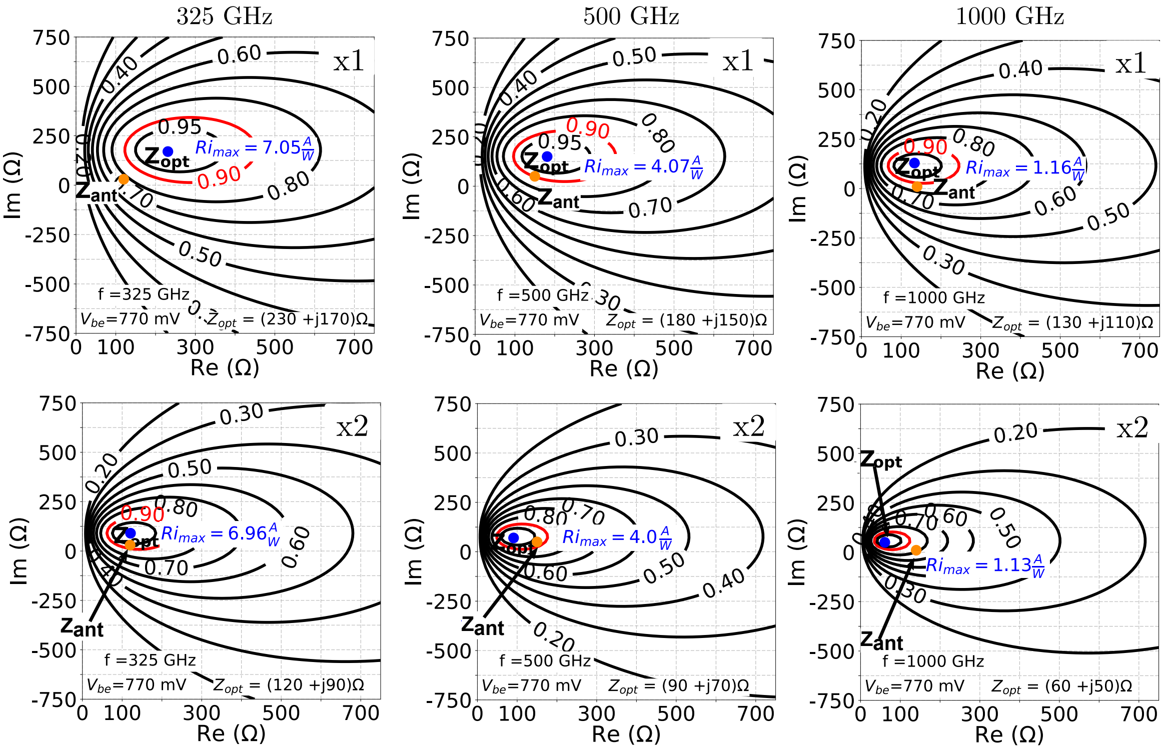

Figure 4.9: Normalized contour plots of the simulated detector current responsivity R_i as a function of the input impedance at 325 GHz, 500 GHz and 1000 GHz for detector device sizes x1 and x2 biased in the forward-active region and implemented in the SG13D5 technology. The simulated antenna impedance (A_1) is named Z_{ant}.

4.1.3.2 Technology Dependency

The main differences in the measured responsivity and NEP of detectors implemented in both device technologies can be specifically attributed to the variations in the device parasitics as discussed in Section 3.6. In the saturation region, detectors implemented in the SG13D5 technology show a higher responsivity according to Figure 4.7 c), mainly attributed to two effects. Firstly, an in general higher second-order current nonlinearity $\partial^2 I_{ce}/\partial V_{be,x}^2$ for lower bias points with a V_{be} smaller than 750 mV is provided combined with a negligible influence of the doubled R_e on the static nonlinearity due to the low collector currents in saturation $< 1\,\mu$A. Secondly, the internal base-emitter capacitance is nearly halved, thus also increasing the overall detector responsivity.

In the forward-active region, the trends are in general opposite. Here, after a crossing point, $\partial^2 I_{ce}/\partial V_{be,x}^2$ in the SG13G3 technology is nearly doubled for a V_{be} larger than 800 mV, combined with a roughly 20 % reduced $C_{be,i}$. This results in the shift of the maximum responsivity towards higher bias points with the drawback of higher shot noise at the detector output. Therefore, despite their increased maximum responsivity, the detectors implemented in the SG13G3 technology show a similar NEP vs. frequency trend to the detector implementations in the SG13D5 technology as indicated in Figure 4.8 for lower frequencies up to 600 to 800 GHz (depending on the bias region). At higher frequencies, the dynamic R_e, C_{be} low pass network becomes more pronounced, resulting in an in general degraded NEP of SG13D5 detector implementations around 1 THz.

4.1.3.3 Detector Performance Summary

An excellent model-hardware correlation could be achieved for the detector voltage responsivity and NEP when the overall measurement and simulation complexity at near-THz frequencies with multiple precise calibration and (re-)alignment steps for the three different VNA extender modules are considered. The deviation between measurement and simulations is typically within 1 dB across the 200 GHz to 1 THz frequency range for all detector implementations. It is further shown that even for the detector operated in the saturation region, the measured and simulated values still correspond well to each other in a broadband sense, validating the entire modeling approach. Compared to the forward-active region, the discrepancy between simulations and measurements is higher, with in general similar frequency trends for a detector operating in deep saturation. A performance summary of all measured detectors can be found in Table 4.1, showing the achieved minimum detector NEP and maximum R_v for each detector in the forward-active and the weak saturation region operated in the optimum bias points found in Figure 4.6. The measured NEP values for detectors biased in the weak saturation region with a V_{ce} of 50 mV are in between the values measured for the deep saturation and forward-active region but provide a roughly 20 % reduced collector current compared to the forward-active region.

Table 4.1: Measured performance of all detector implementations

Detector	Operation Region	Max. Responsivity (@ Frequency)	Min. NEP [pW/$\sqrt{Hz}$]	B_{eq} [GHz]	NEP_{eq} [pW/$\sqrt{Hz}$]	Calc. NETD [K]
Detector 1	Forward-Active	9.0 kV/W (292 GHz)	1.9	498	3.7	0.54
(A_1, SG13D5)	Saturation	2.1 kV/W (292 GHz)	4.2	513	8.0	1.12
Detector 2	Forward-Active	9.8 kV/W (304 GHz)	2.2	490	4.0	0.59
(A_1, SG13D5 x2)	Saturation	1.7 kV/W (281 GHz)	4.5	460	9.9	1.56
Detector 3	Forward-Active	13.0 kV/W (300 GHz)	2.1	582	5.0	0.62
(A_1, SG13G3)	Saturation	1.8 kV/W (300 GHz)	3.7	522	7.5	1.04
Detector 4	Forward-Active	7.0 kV/W (476 GHz)	2.7	505	4.8	0.71
($A_2{}^{\dagger}$, SG13D5)	Saturation	1.7 kV/W (476 GHz)	4.9	538	10.9	1.47
Detector 5	Forward-Active	11.2 kV/W (430 GHz)	2.3	512	4.7	0.67
($A_3{}^{\dagger}$, SG13G3)	Saturation	1.2 kV/W (430 GHz)	4.3	548	8.8	1.16

† Single Polarization

The best detector performance is shown for the forward-active device biasing without the additional influence of the BC diode. A maximum responsivity between 7 and 13 kV/W for all detector implementations and a minimum NEP from 1.9 to 2.7 pW/$\sqrt{Hz}$ are reported. In the saturation region, the measured NEP is on average 2 to 3 times higher. For both operation regions, all detector implementations show a large bandwidth with a typical NEP increase of one order of magnitude from 200 GHz to 1 THz. For a detector performance estimation towards passive imaging, a calculation of the equivalent bandwidth B_{eq} and NEP_{eq} according to Equations 2.31 and 2.32 was included into Table 4.1 and was used to calculate the corresponding, estimated detector NETD in a 1 Hz readout bandwidth.

All implemented detectors are feasible options for passive imaging, based on the calculated NETD with minimum values ranging from 0.54 K in forward-active bias to 1.56 K in saturation. For the dual-polarized detectors, the calculated NETD is expected to reduce by a factor of $\sqrt{2}$ as compared to the NETD values de-embedded from CW measurements where only one single polarization path was considered. By combining both polarizations through a single resistor, the output signal doubles, while at the same time, the shot noise increases by a factor of $\sqrt{2}$. By combining both polarizations, the dual-polarized antenna-coupled detectors provide the lowest calculated NETD approaching 0.5 K. Due to the minor LFN corner frequency around 1 to 2 kHz, easily realizable with conventional optical choppers, the following NETD measurements focus on detector 5 (A_3).

4.1.4 Contribution to the State-of-the-Art

A short state-of-the-art comparison in terms of NEP is introduced in the following, beginning with the valuable development of THz direct detectors at the Institute for High Frequency and Communication Technology (IHCT). During the last 15 years, the IHCT became one of the leading research groups in developing silicon-integrated, antenna-coupled THz direct detectors. Not only due to the continuous device scaling but further by the in this work presented complex antenna detector co-design approach and the continuous development in detector noise analysis, the NEP was pushed by two orders of magnitude starting from 400 $pW\sqrt{Hz}$ [122] to state-of-the-art values of $\leq$2 $pW/\sqrt{Hz}$ (300 to 500 GHz) [own6] as presented in this thesis and shown in Figure 4.10. Furthermore, the measurements and the analysis of the devices operated in the saturation region pave the way for the next generation of high-performance, power-efficient SiGe HBT THz direct detector arrays with only a small NEP deterioration by a factor of around 2, as compared to the forward-active region making it a good alternative to the commonly implemented 'cold' MOSFET devices. In total, the complex detector analysis and measurements within three different waveguide bands resulted in a NEP trend of all demonstrated detector versions outperforming nearly the whole state-of-the-art of SiGe HBT, MOSFET and Schottky diode-based THz direct detectors in the 200 GHz to 1 THz frequency range as shown in Figure 4.10 b).

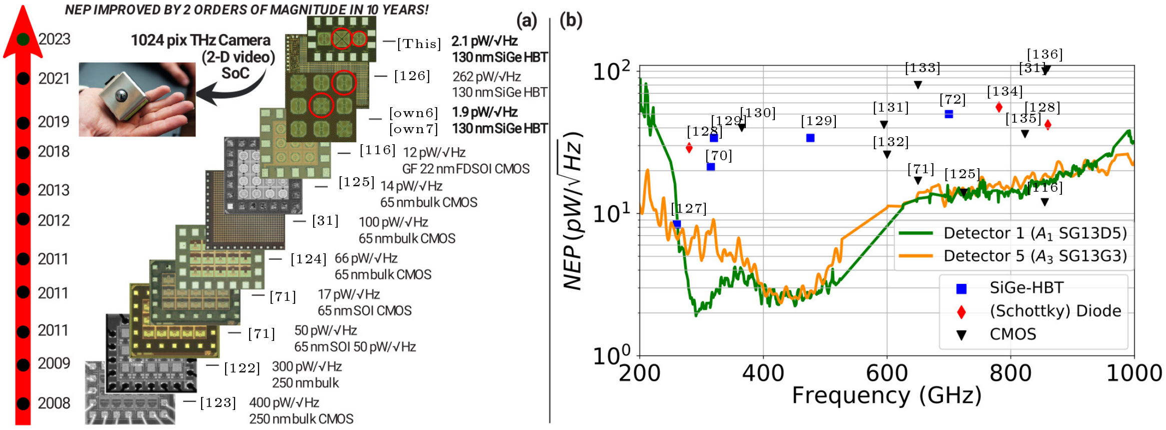

Figure 4.10: a) State-of-the-art of silicon-integrated direct detectors developed at the IHCT. b) State-of-the-art of silicon-integrated THz direct detectors (SiGe HBTs, MOSFETs, Schottky diodes) operated between 200 GHz and 1 THz.

4.2 Broadband Black Body Characterization Setup

Figure 4.11 a) shows the passive THz characterization setup. It consists of two elliptical mirrors with an 11.3 cm aperture diameter along the minor axis, a 16.3 cm diameter along the major axis and a focal length f of 18.75 cm, placed by a distance of 37.5 cm (2f). The mirrors refocus the incident power from a temperature-controlled (50 to 1200 °C) SR-200 high emissivity black body source from CI systems to the antenna aperture with minimum optical loss. An additional set of THz multi-mesh filters from QMC with an out-of-band rejection of at least 10 dB (30 dB typical) was inserted before the detector plane to limit the operation bandwidth to 1.5 THz to avoid parasitic IR coupling to the detector. The filter insertion loss η_{filt} was characterized as 85 % and then de-embedded from the consecutive measurements.

For a proper alignment, the lens-coupled detector, mounted on a dual-axis goniometer and the black body source were placed in the focal points of 2 mirrors and then manually displaced along the optical axis to maximize the receiver signal. Contrary to the previously discussed free-space detector NEP characterization detector setup, in such an optical setup, additional loss factors related to the optical coupling efficiency are present that can be defined by the beam Gaussicity. This was found to stay between 85 and 90 % from 250 to 900 GHz, resulting in negligible spillover losses from the detector side due to the low sidelobe levels. The same readout topology as in the previously described free-space measurements was used. Measurements with two combined polarizations in the forward-active region were investigated. Here, a two times higher rectified voltage is present due to the unpolarized black body radiation.

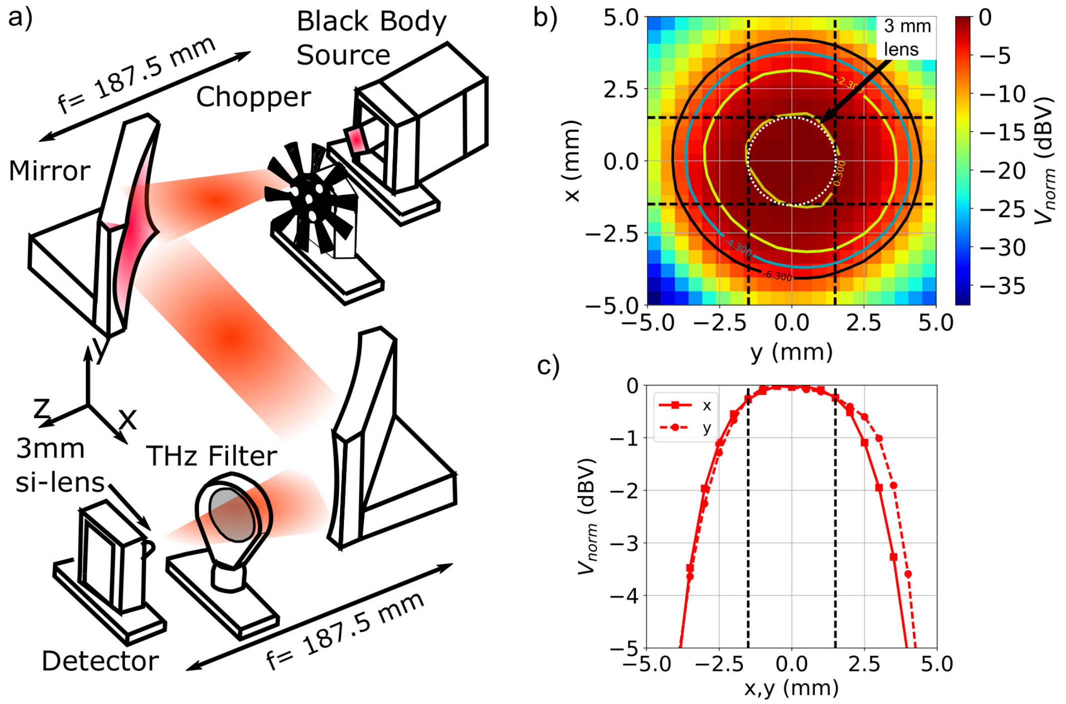

Figure 4.11: a) Black body source and mirror setup for NETD characterization.
b) Raster-scanned spot of the used black body aperture (9.5 mm) at T = 1000 °C.
c) Corresponding cross sections of the thermal spot.

4.2.1 Uniform Detector Illumination and Optimum Lens Size

A proper NETD characterization is achieved when the antenna field-of-view on the detector side, and, as such, the silicon lens is filled with black body radiation in the entire expected RF frequency band. Only then the detector thermal sensitivity can be calculated as an integral of the measured voltage responsivity multiplied by the Boltzmann constant across frequency without any spillover loss factor according to Equation 2.29 with the detector output voltage directly proportional to the input power and as such to $k_B \cdot T_{BB}$. This is achieved with the previously described elliptical mirror setup, which approximately produces a 1:1 focused image of the black body thermal spot in which the silicon lens is placed. The preceding NETD measurements can now be done with different silicon lens sizes. However, the influence of the silicon lens has, in theory, to be de-embedded to truly measure the integrated detectors' NETD without any magnifying lens influence. Therefore, in the following, the influence of different lens sizes on the thermal input power levels at the integrated antenna will be qualitatively discussed based on the presented optical setup.

For this purpose, a hypothetical case with two silicon lenses of different diameters (i.e., 3 mm and 9 mm) placed at the boundary of a 3-dimensional room heated up to a uniform temperature is considered. In this simple case, both lens surfaces are located inside the room and at the same temperature. At the same time, the detector chip coupled to the antenna is placed outside the room and operated at a lower temperature. Here, for diffuse black body radiation, the antenna coupled to the 9 mm lens accumulates the same thermal input power as the 3 mm lens (despite its larger surface area) as its field of view shrinks or its directivity increases ideally as the ratio of the lens surface area and the effective antenna area as described in more detail in Section 2.4. These two effects cancel each other and, when included in Equation 2.26, result in $P_{Ant} = k_B \cdot T_{BB}$ for detectors with different diameter sizes. The same result is accomplished when the view factor relations are considered. Nevertheless, it should be mentioned at this point that these relations differ when the lenses are illuminated by coherent (CW) radiation. Here, the measured P_{Ant} increases with the lens surface.

In the used mirror setup, different lens sizes can theoretically be used, as long as the spillover losses are negligible and the lenses are entirely filled with black body radiation resulting in the same expected detector NETD. In the following, only the implemented detectors coupled to the introduced 3 mm hyperhemispherical lens are treated. To fill the whole lens with black body radiation, the effective aperture of the lens-coupled antenna was matched with the mirror system and an appropriate circular aperture of the emitting black body unit was chosen. Here, the adjustable black body aperture was increased until the maximum detected signal saturates. A minimum aperture of 9.5 mm was required to cover a 3 mm diameter lens.

To verify the uniformity of the illumination pattern over the required spatial extension, the antenna-coupled detector illuminated by the black body source heated up to 1000 °C was scanned in 2 dimensions along the receiving plane. The acquired light intensity profile for the minimum sized aperture of 9.5 mm resulted in a uniform illumination with less than 0.25 dBV signal variation within the 3 mm lens diameter as shown in Figure 4.11 together with the corresponding cross sections for the investigated detector (A_3, SG13G3) with both polarizations connected. Considering the relationship between the antenna effective area and its directivity or, equivalently, its solid angle of view, without spillover losses, the power spectral density available at the detector is frequency-independent ($k_B T_{BB}$) according to Equation 2.29 in the limit of the Rayleigh-Jeans approximation. The thermal emission was chopped mechanically at 1.5 kHz for all measurements with an in-built mechanical blade at the black body unit. At the same time, the corresponding measured noise values were captured with a spectrum analyzer in a 1 Hz bandwidth.

4.2.2 Thermal Responsivity and Optimum Bias Point

Before characterizing the detector NETD by measurements, the optimum detector biasing for passive imaging with the optical chopping frequency of 1.5 kHz was investigated. For this purpose, an additional detector bias sweep under black body

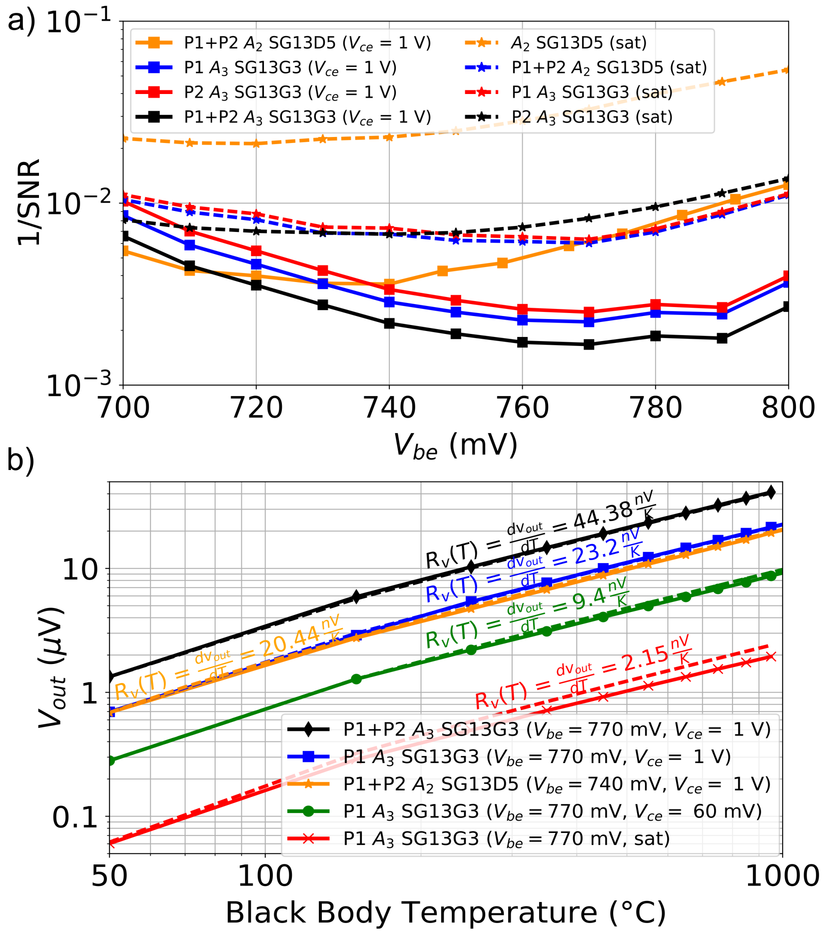

Figure 4.12: a) Measured optimum detector bias points (minimum 1/SNR) under 1000 °C hot black body illumination.
b) Measured and calculated (dotted line from previous CW measurements) thermal detector responsivity R_v(T) for three different bias points.
For comparison, measured values for detector 4 (A_2, SG13D5) are also included.

illumination at T = 1000 °C was performed and is shown in Figure 4.12 a). A V_{be} of 770 mV was found to maximize the SNR at the detector output well correlating with the optimum NEP bias points from Figure 4.6 c). However, for detector 4 (A_2, SG13D5), included as a comparison basis, the maximum SNR is at a V_{be} of 740 mV due to the high 1/f noise in the corresponding technology, which decreases for lower collector currents.

For NETD characterization, the rectified detector output voltage was measured at various black body temperatures from 50 to 1200 °C. Then, the slope $\Delta V_{Out}/\Delta T$, equivalent to the thermal voltage sensitivity R_v(T), which is the increase of the output voltage signal per Kelvin, was calculated as derived in Equation 2.29. In the measurement setup, several additional loss mechanisms need to be considered, resulting in

$$R_v(T) = \frac{\Delta V_{DC}}{\Delta T \cdot \eta_{filt}} \cdot \frac{\pi}{\sqrt{2}}, \tag{4.2}$$

where η_{filt} is the in-band filter transmission factor and $\pi/\sqrt{2}$ the chopping factor for an optical modulated square wave signal [137] that is also de-embedded for commonly used measurements with lock-in amplifiers [51]. The integration time factor $1/(\sqrt{2\tau_I})$ equals to 1 with a 1 Hz readout bandwidth. The corresponding results are shown in Figure 4.12 b) including all correction factors applied at the measured output voltage. The measured R_v(T) values range from 2.15 nV/K to 23.2 nV/K in one and 44.4 nV/K for two polarization paths. The difference between both antenna implementations (factor 2) arises due to the choice 740 mV V_{be} for the minimum NETD operation of detector 4.

4.2.3 NETD

The NETD was calculated as the ratio of the detector output spot noise v_n and the measured $R_v(T)$ based on Equation 2.30 and its variations among the black body temperature are depicted in Figure 4.13. A minimum NETD of 0.64 K for both polar-

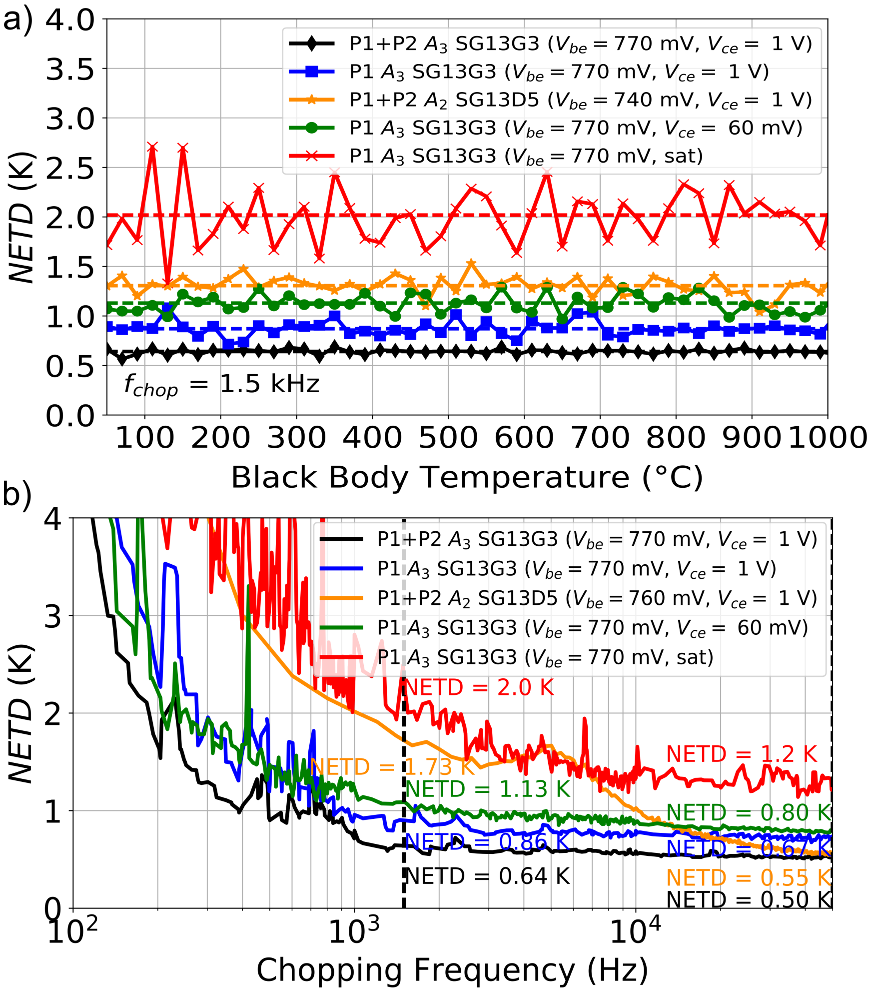

Figure 4.13: a) Measured detector NETD variations with increasing black body temperature and corresponding mean values (dashed lines).
b) Measured detector NETD evaluation vs. chopping frequency.

izations in forward-active and 0.86 K for a single polarization were measured, as well as 2 K for a single-polarization in saturation with detector 4 (A_3, SG13G3) at 1.5 kHz. Parasitic ripples exist in the measured NETD curve in the saturation region as the applied chopping frequency is within the 1/f noise corner frequency. These ripples cannot be compensated by averaging.

Essential for a comparison to the previously calculated NETD values based on the CW measurements shown in Table 4.1 is the derived frequency trend indicated in Figure 4.13 b). Due to the detectors' low-frequency noise characteristic and a stable R_v(T) in the kHz chopping frequency range verified by measurements, the NETD strongly reduces toward higher chopping frequencies above 50 kHz. NETD values as low as 0.5 K (P1+P2) and 0.67 K (P1) in forward-active and 1 K in the saturation region were calculated for chopping frequencies around 50 kHz, not supported in the optical measurement setup. Furthermore, both dual-polarized detector implementations in different device technologies show similar minimum NETD values around 0.5 K with an excellent correlation to the pre-calculated NETD from CW measurement results.

4.2.4 Passive Images

Now, with the detector NETD characterized by measurements, this dissertation's main objective is to demonstrate passive imaging with realistic scenes. To record passive images, the black body source was replaced by two different objects. A 25 × 6 mm large, 10 Ω ceramic resistor that was heated up to 100 °C and a T-shaped paper mounted on a heated aluminum plate of approximately 100 °C with a paper-surface temperature of 50 to 60 °C. Both objects were mounted on a programmable translation stage and raster-scanned in the xy-plane with a step size of 1 mm.

Passive Resistor Images

An additional image of the resistor covered by a 0.4 mm thick cardbox was recorded to show the unique properties of THz waves. The distance from the resistor to the cardbox was set to a minimum of 5 cm to avoid parasitic cardbox heating. Several images of the resistor are shown in Figure 4.14, comparing visible, IR and THz passive images of the uncovered and cardbox covered 100 °C hot resistor.

A conventional FLIR T450sc IR camera with a NETD $\leq$ 30 mK was used to record the corresponding IR images. The recorded THz images provide a sufficient SNR of 17.6 dB. Contrary to the IR images, where only the ambient temperature of the cardbox is visible, the maximum output voltage is only reduced by 50 % when the resistor is covered by the 0.4 mm thick cardbox. This clearly indicates the see-through ability of passive THz imaging. Considering the measured $R_v(T)$ of 44.38 nV/K shown in Figure 4.12 a) and including the chopping factor of $\sqrt{2}/\pi$ [137], the reduced fill factor

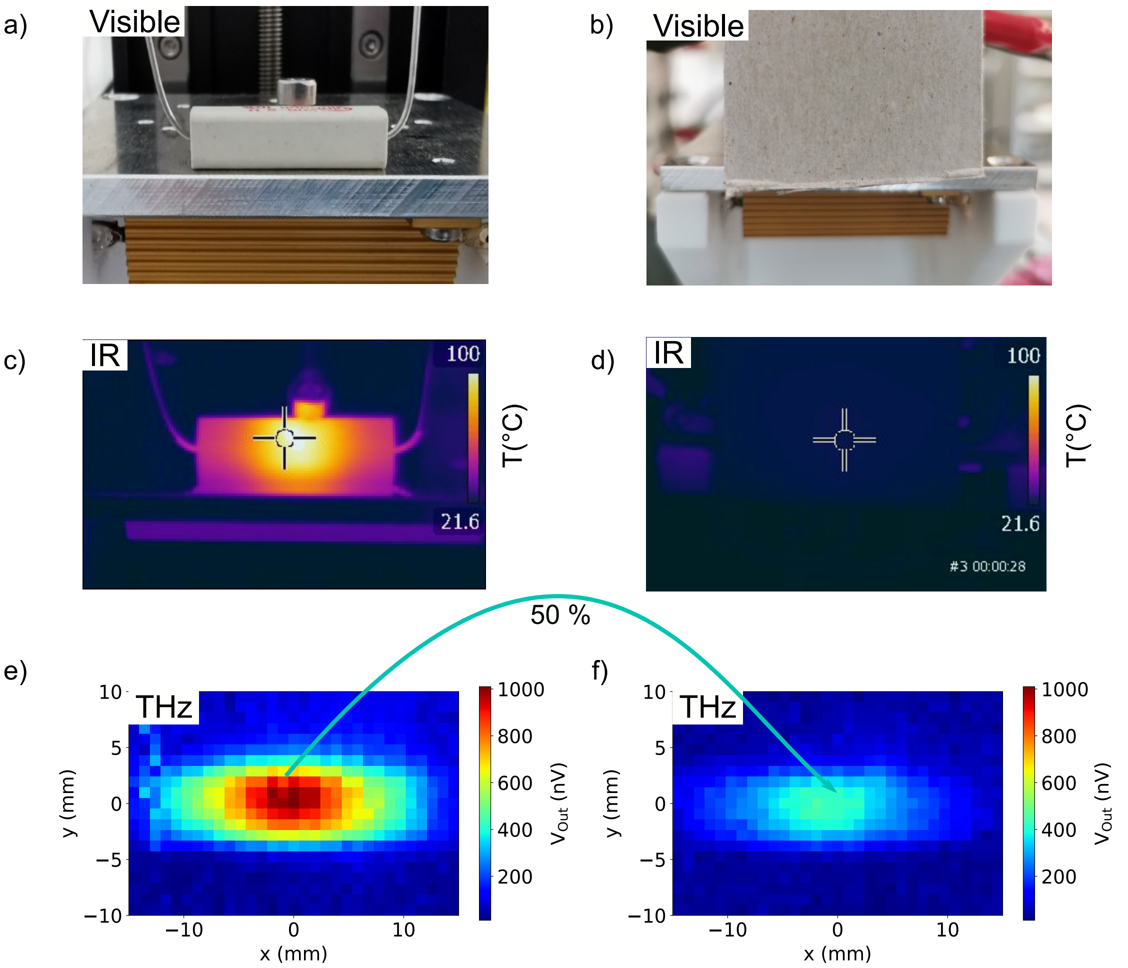

Figure 4.14: Visible, IR and THz images of the 100 °C hot resistor.
a) Visible image.
b) Visible image of the resistor covered by cardbox (0.4 mm thickness).
c) IR image.
d) IR image of the resistor covered by cardbox (0.4 mm thickness).
e) Passive THz image.
f) Passive THz image of the resistor covered by cardbox (0.4 mm thickness) showing only a 50 % signal drop.

due to the smaller resistor feature size, which is approximately 0.8 and the assumed ceramic emissivity at THz frequencies of 0.9, the estimated rectified signal due to the 100 °C hot resistor is 1.12 µV. This matches to the measured peak value of 1.01 µV and indicates an excellent correlation to the previous black body measurements.

Passive Paper-T Images

A different detector sample with an approximately 20 % degraded NEP was chosen to record the T-shaped paper images, as one of the polarization paths broke during the measurements. For the investigated sample, both polarization paths connected and biased through the same 1.83 kΩ resistor were used for image detection. In the recorded images shown in Figure 4.15, an IR detection capability of the investigated detectors is indicated in the raster-scanned images without the 1.5 THz filter shown in Figure 4.14 c).

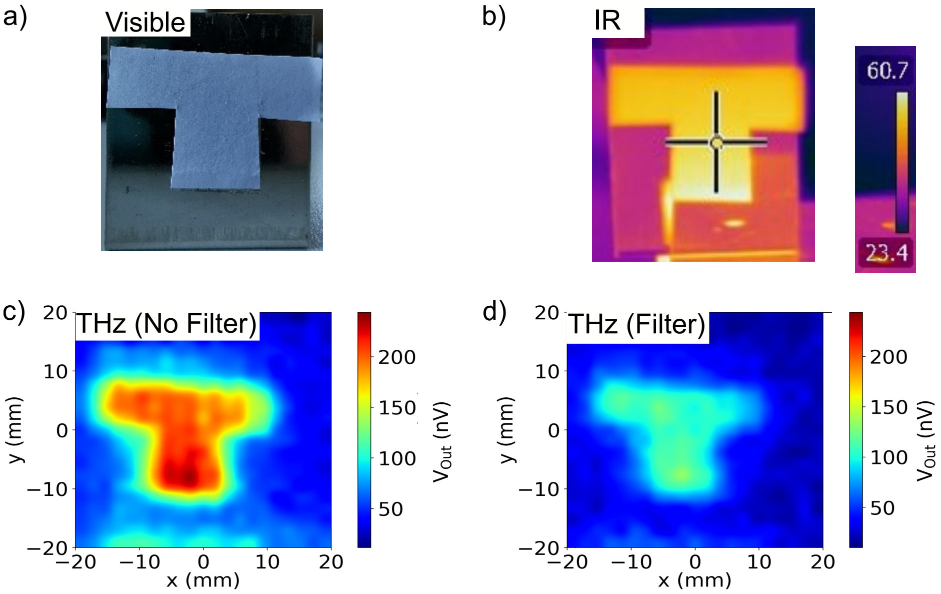

Figure 4.15: Visible, IR and THz images of a 60 °C paper T placed on a hot aluminum plate.
a) Visible image.
b) IR image.
c) Passive THz image without IR filter.
d) Passive THz image with THz filter.
A Gaussian filter was applied to enhance the contrast in the THz images.

In this configuration, the measured SNR is 13 dB. An inclusion of the THz filter results in a signal drop of 40 % indicated in Figure 4.14 d). As the measured filter losses are 15 %, the remaining signal drop of around 25 % can be assigned to the IR band lying above 3 THz. However, the exact frequency band could not be determined due to missing IR filters in this frequency range. Please note that the hot aluminum plate at the object's background is only weakly visible in the recorded IR and THz images due to the low emissivity of aluminum in the THz frequency range ($\leq$ 10 %).

4.2.5 Summary and Conclusion

The practical study presented in this chapter sets out to determine the sensitivity of five silicon-integrated THz direct detectors implemented in two advanced SiGe HBT technologies with f_t/f_{max} of 350/550 GHz (SG13D5) and 470/650 GHz (SG13G3) towards passive imaging. For this purpose, the detectors were packaged with a 3 mm hyper-hemispherical silicon lens and extensively characterized in a CW free-space measurement setup in the operating range from 200 GHz to 1 THz while operated with a low-noise voltage bias and readout. Then, the detector responsivity and NEP were calculated based on the Friis transmission equation and an accurate de-embedding of the measured directivity to avoid any lens magnifying influence.

The corresponding results show a state-of-the-art minimum NEP and maximum responsivity of all detectors in the range of 1.9 to 2.7 pW/$\sqrt{Hz}$ and 7 to 13 kV/W in the forward-active region and roughly doubled NEP values in the saturation region at a chopping frequency above the 1/f noise corner frequency. These NEP values approximately drop one order of magnitude in the frequency range from 200 GHz to 1 THz. Funded in the CW measurements, the NETD for all detectors was estimated with the equivalent NEP_{eq} and its corresponding bandwidth B_{eq} in the range of 500 GHz and 4 pW/$\sqrt{Hz}$. As a result, unprecedented NETD values reaching down to 0.5 K were calculated with the superior performance of the dual-polarized antenna implementations. With its low 1/f noise corner frequency, the calculated NETD values were verified by measurements of the dual-polarized detector (A_3, SG13G3), implemented in a broadband measurement setup with a black body source under optical chopping at 1.5 kHz. Spillover losses could be avoided as the black body radiation fully illuminated the lens surface.

To calculate the NETD, first, the detector's thermal responsivity $R_v(T)$ was measured as output voltage slope vs. black body temperature. This resulted in a detector thermal responsivity of 2.15 nV/K (saturation) to 23.2 nV/K (forward-active region) for a single polarization and 44.38 nV/K when both polarizations were connected. Then, by building the output noise voltage and thermal responsivity ratio, the corresponding NETD in a 1 Hz readout bandwidth was calculated to stay between 2 K (single polarization, saturation) and 0.64 K (dual polarization, forward-active). Furthermore, potentially possible NETD values of 0.5 K at 100 kHz chopping frequency correlate very well with the estimated values from the CW measurements. Finally, the first passive images of a 100 °C hot resistor recorded with uncooled SiGe HBT THz direct detectors were presented.

Chapter 5

Broadband Low Noise Amplifier Design and Measurements

In order to achieve a minimum real-time NETD of less than 50 mK in a total power radiometer, a low noise amplifier design with at least 30 dB gain and 100 GHz bandwidth and a low NF is required as discussed in Chapter 2. Achieving such a high gain, low NF and large bandwidth in an LNA design with a center frequency above 200 GHz is extremely challenging in silicon technologies. Most common LNA designs in the literature are based on classical transmission line matching networks [138], [139]. With this design technique, a flat high gain over 100 GHz bandwidth has not been reported yet in silicon technologies. Another disadvantage of such a design technique is the requirement for many densely tuned stages. Each stage is tuned to a different frequency. Further, all stages are staggered in the entire LNA system. This compromises the LNA NF across its bandwidth, where N_{Fmin} is only achieved in a small frequency band mainly defined by the gain/bandwidth of the first two LNA stages. Therefore, as the basis for a broadband radiometer towards real-time passive imaging, in the following, a transformer-matching based LNA design is introduced to fulfill the derived performance specifications. The main focus is on the complex modeling approach, the transistor core and the realized matching trajectories. An in-detail transformer design analysis with the development of an equivalent model for matching purposes and thus giving a detailed design recipe is not in the scope of this thesis.

5.1 Amplifier Topology

The latest silicon-integrated device technologies with f_t/f_{max} of 505/720 GHz paved the way for broadband amplifiers reaching operation frequencies above 300 GHz [28]. Towards these frequency ranges, the literature mainly focuses on the integration of common-base (CB) [140] and cascode (CC) [141], [142], [143] circuit topologies in integrated LNA and PA designs. IHP's SG13G3 technology with f_t/f_{max} of 470/650 GHz was used for the following analysis and the later integration of the proposed LNA employing an x2 device size ($A_e = 2 \times 0.96 \times 0.1\,\mu m^2$), which aims for a reduced power consumption compared to larger device sizes.

Firstly, the ideal amplifier performance for the most common differential CE, CB and CC topologies is investigated in terms of minimum noise figure NF_{min} and available gain G_A depending on the device biasing for different frequencies from 180 to 300 GHz. G_A was simulated under the assumption of a conjugately matched load impedance [144] with a broadband input noise match applied for NF_{min} operation. The corresponding constant available gain and minimum noise figure contours vs. device biasing at 300 GHz are shown in Figure 5.1. The maximum available gain for all circuit topologies is reached at a V_{be} of 900 mV with a corresponding single stage V_{cc} of 1.5 V. The ideal performance of the CE stage is poor with a maximum G_A of only 3.38 dB and the NF_{min} values corresponding to very low V_{be}. At these bias points, sufficient gain cannot be provided when 1 to 2 dB additional losses of the input and interstage matching networks are taken into account. In general, it can be observed that the gain roll-off of the CE topology vs. frequency starts earlier, making it unfeasible for amplifiers operating around 300 GHz.

Contrary to the CE stage, the CB stage provides a higher G_{max} of around 8 dB (not shown), realized under complex conjugate input and output matching conditions. However, if G_A for an ideal noise match is considered, the maximum available gain drops to 4.38 dB, which indicates a significant difference between the conjugate device input impedance and the optimum source impedance to minimize the amplifier's NF. Therefore, only the cascode topology is a feasible option as it provides a high available gain at 300 GHz (towards $f_{max}/2$). Further, the minimum noise factor F for an amplifier implementation with a number of n stages was calculated based on the following Friis Noise equation [145] for the total noise factor F_{total}

$$F_{total} = F_1 + \frac{F_2 - 1}{G_1} + \frac{F_3 - 1}{G_1 \cdot G_2} + \cdots + \frac{F_n - 1}{G_1 \cdot G_2 \cdots G_n}. \tag{5.1}$$

Especially the second term is minimized within a cascode topology by providing a G_A of more than 10 dB close to the NF_{min} bias point. Thus, in a cascode topology,

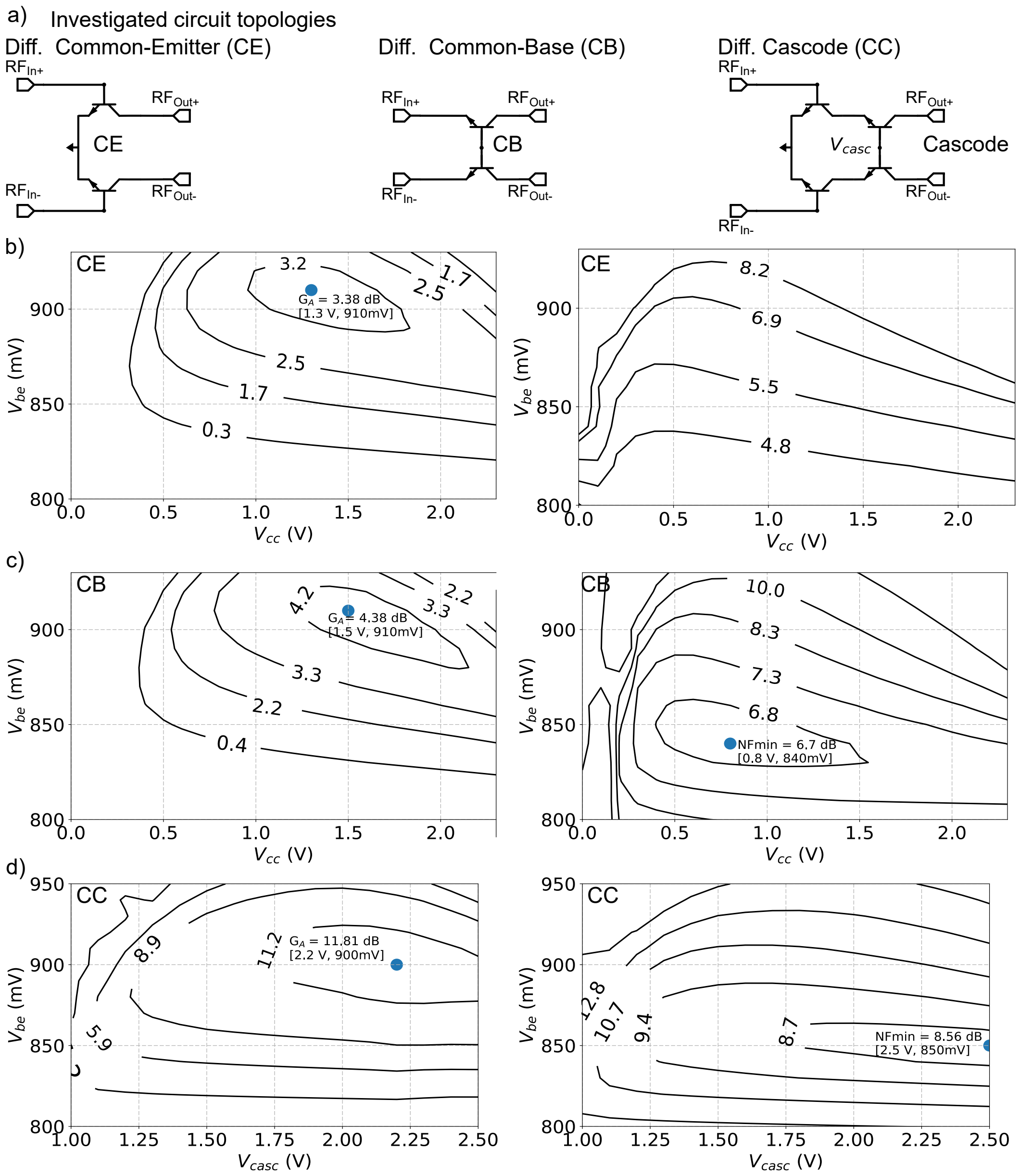

Figure 5.1: a) Schematics of the investigated ideal differential CE, CB and CC topologies.
b) G_A and NF$_{min}$ for CE topology.
c) G_A and NF$_{min}$ for CB topology.
d) G_A and NF$_{min}$ for CC topology with $V_{cc} = 3$ V.
All contours are simulated at 300 GHz.

the influence of the following stages on F_{total} is reduced. In summary, a bias point of V_{be} = 880 mV and a V_{casc} = 2.2 V was chosen for an implementation of the differential cascode topology resulting in a maximum gain of in theory 10 dB per stage at 300 GHz (NF < 9 dB, J_c = 22 mA/µm^2) without losses of the matching network included. Despite its better noise figure performance, the single-ended cascode circuit topology was not considered here as there will not be any symmetry plane for DC bias network inclusion. Hence, additional RF chokes would be necessary, which may deteriorate the overall system bandwidth.

The cascode topology typically allows higher output power levels due to larger voltage swings in the series voltage combination of two stages and higher isolation between the input and output port. Even if the former fact is commonly more relevant for power amplifiers, in LNAs with a large gain of more than 30 dB, it helps to prevent saturation and thus enlarges the LNA's dynamic range. Despite the high available cascode gain at lower frequencies between 100 and 200 GHz, broadband amplification towards 300 GHz remains challenging and is limited by the high Q-factor of the cascode's output.

Achieving the optimum values shown in the previous plots is impossible as the transistor interconnections and matching network implementation highly influence the amplifier performance. Here, in particular, optimizing the device core layout, which is not provided by the foundry, is a crucial design task as all interconnects result in degraded f_t/f_{max} for the overall amplifier stage in comparison to an ideal lumped transistor simulation. Further, the core layout initially sets the design space of the input and output matching network and is thus analyzed carefully in the following.

5.2 EM Core Analysis

A simplified schematic of the implemented cascode stage, including the DC bias paths, is shown in Figure 5.2 a). Here, the influence of the core layout analyzed in the following and shown in Figure 5.2 b) is indicated by a blue rectangle. The core layout is essential for accurate device modeling in a broad bandwidth and was done in co-simulations with the output matching network in more detail explained in Section 5.3.

5.2.1 GND Path

The first important point concerning the core layout is the patterned co-planar ground plane in between and around the transistors. Due to the short wavelength in silicon at 300 GHz ($\lambda/4 \approx 70$ µm), the surrounding ground cut-out dimensions in the cascode layout with ×2 devices ($18{\times}16\,\mu m^2$) may become non-negligible, leading to distributed ground plane effects potentially affecting the model accuracy of the s-matrix ported into a circuit simulator, which assumes an ideal ground plane for all ports. In other words, the re-imported s-matrix may change with the size and the location of the lumped ports set in the full-wave 3D EM solver (HFSS), especially at higher frequencies. This effect becomes more pronounced for cascode implementations implemented in larger device sizes and used in power amplifiers [146], [147].

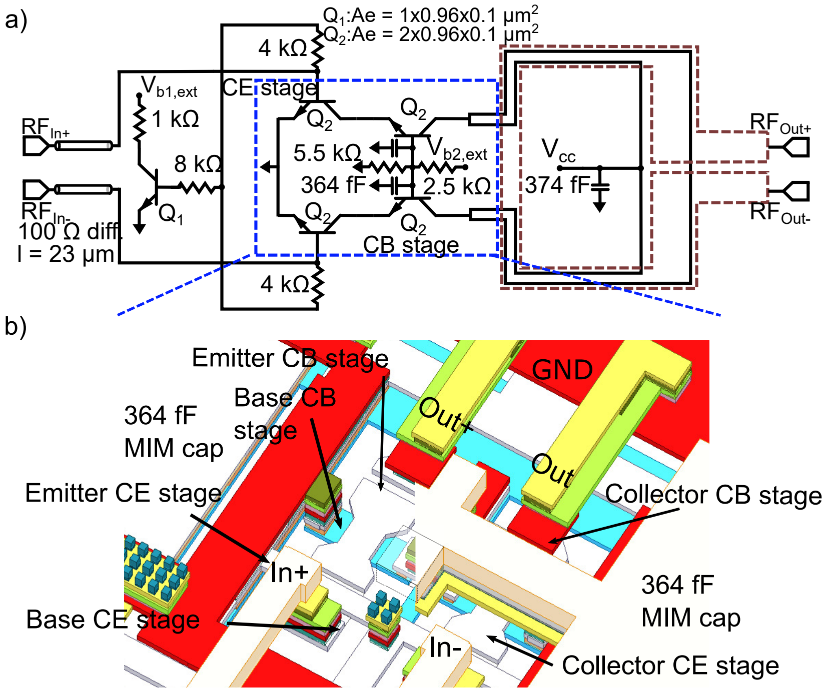

Figure 5.2: a) Schematic of a single pseudo-differential cascode stage with indicated biasing.
b) EM-model of the cascode core.
Images after [own10] ©2023 IEEE.

5.2.2 Mixed Mode Analysis

In the presence of the described co-planar ground plane, the differential and common mode signals can easily propagate, although the propagation paths may become very different, particularly with discontinuities in the ground return path. This parasitic common-mode operation at near-THz frequencies is funded in a differential to common mode conversion due to small layout asymmetries and device mismatches. Despite its relevance, i.e., causing potential instabilities, the common mode is usually not treated in detail in a differentially-driven circuit analysis due to its modeling complexity.

A unified port-definition system for the common- and differential modes was implemented to allow a mixed-mode analysis. For this purpose, an additional ground return path between the devices in both differential signal paths was implemented in the core layout on the lowest metal layers close to the cascode layout level (M1, M2), as shown in Figure 5.2 b). Several device-related ground-referring internal ports for a mixed-mode excitation scheme were established for all important device interconnects, such as CE base, CB base and CB collector, meaning all relevant device nodes are modeled as lumped ports. Additionally, coupled microstrip lines connected each cascode stage's inputs and outputs, which support differential and common-mode signaling.

5.2.3 Cascode Interconnections

Another issue causing the layout modeling uncertainty is directly linked to the cascode circuit topology and to the internal nodes between CE and CB devices as well as to the ground paths at the base nodes of the CB devices. Mainly, the via-induced inductances in the ground paths at the CB base nodes are challenging to model but very important to ensure broadband unconditional device stability. Ideally, the inductance value should be zero resulting in an ideal AC ground. This parasitic inductance can also be used for inductive peaking and gain boosting. It further leads to instability and lower bandwidth. Therefore, the optimized layout targets to reduce the CB base inductance as much as possible. Here, side-located decoupling capacitors implemented in the higher metal layers (M5 - TM1) are used as ground points of the corresponding signals. However, the crossing interconnection layer between the CE and CB stage may result in varying effective path lengths to the ground for each device finger due to the distributed via connections. To minimize the effect of the varying ground path lengths, the internal base of the CB stage is additionally AC-shorted by a distributed capacitor with a symmetric center-point contact to the global ground between both differentially-operated devices.

Different metal layers were investigated as the connection of the internal collector of the CE stage and the emitter of the CB stage. This connection is typically not modeled due to the layout complexity, although it might influence the circuit operation at 300 GHz. In this case, it was modeled as a coupled transmission-line section with corresponding differential and common mode impedances. The use of higher metal layers could not reduce the wiring parasitics due to the short distance of 5 µm between the emitter of the CB and the collector of the CE stage. However, the increased wiring distance resulted in additional coupling effects between the cascode's input and output. For this reason, the internal wiring was finally implemented using only the two lowest layers (M1 and M2).

Toward 300 GHz, the vertical interconnects cannot be seen as lumped inductors because capacitive effects co-exist, resulting in non-negligible phase shifts between the bottom and top metal layers. For the output cascode nodes, which can be approximated as a shunt RC connection, the layout was optimized to reduce the excess capacitance. That way, a deterioration of the voltage swing, the operation bandwidth and its influence on the matching structure feasibility range was minimized. Complete wiring to the topmost layer was avoided. The output connection to the following matching network was limited to M4 and M5, interconnected for current density purposes. The optimized cascode output layout was implemented with staircase-like vertical wiring as in [147], [148] to the combined M4/M5 layer with a direct connection to the transformer-based matching network, which reduces the resulting parasitics.

5.2.4 Simulated Results

The simulated input and output reflection factors of the ideal cascode and the implemented core layout (denoted as post-layout) are shown in Figure 5.3 b) under G_{max} biasing conditions ($V_{be} = 900$ mV, $V_{casc} = 2.2$ V, $V_{cc} = 3$ V, current density $J_c = 34$ mA/μm^2, $I_c = 6.6$ mA). With reference to Figure 3.15 a) and Figure 3.3 a), the input network can be modeled as a series RC connection as shown in Figure 5.3 a). Furthermore, the transistor output impedance at the collector node in the forward-active mode of operation can be simplistically approximated by a shunt connection of a capacitance and a resistance. For a better comparison, the equivalent circuit parameters of the input and output network were evaluated at the targeted LNA center frequency of 200 GHz with and without core layout included. The following equivalent model parameters were found for both layout options.

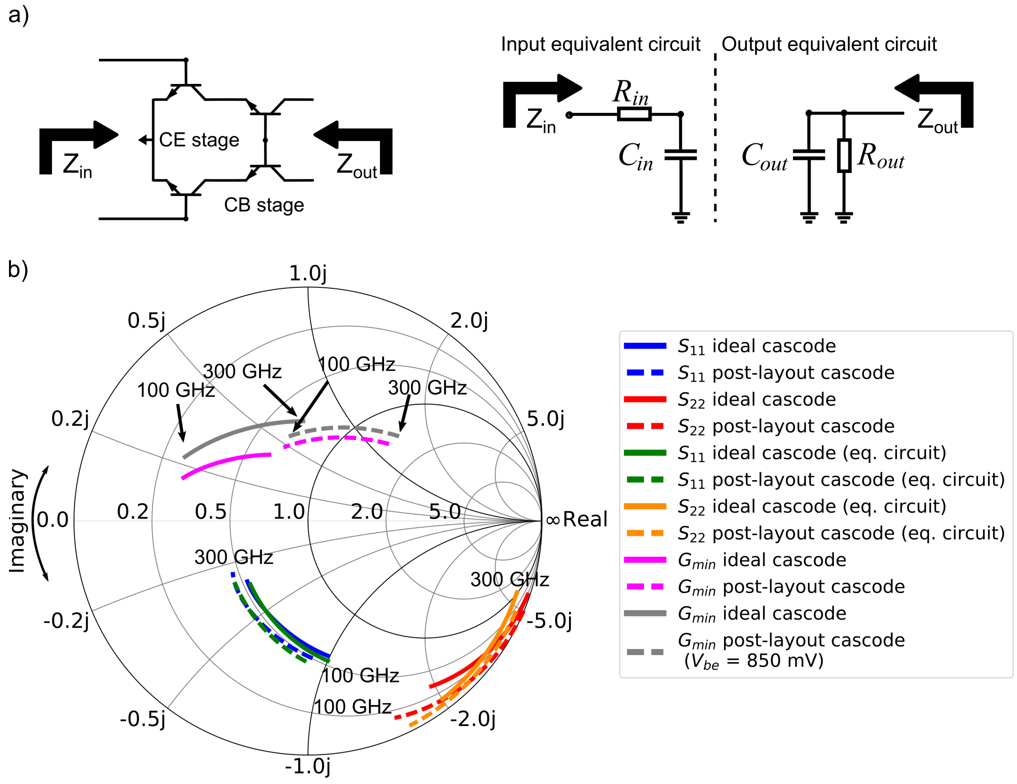

Figure 5.3: a) Schematic of a single pseudo-differential cascode stage with simplified equivalent circuits of the input and output networks evaluated in the core optimization. b) Simulated input, output and minimum noise reflection coefficients (S_{11}, S_{22}, G_{min}) of the ideal cascode and the cascode, including core layout, both implemented with x2 devices.

- Ideal cascode layout: $R_{in} = 53\,\Omega$, $C_{in} = 15.9$ fF, $R_{out} = 3.3\,k\Omega$, $C_{out} = 2.6$ fF
- Core cascode layout: $R_{in} = 46\,\Omega$, $C_{in} = 18.2$ fF, $R_{out} = 6\,k\Omega$, $C_{out} = 3.3$ fF

For comparison, the s-parameters corresponding to both equivalent model configurations are additionally shown in Figure 5.3 b). To emphasize the influence on the impedance trajectories, which are crucial for maximum gain and minimum noise matching, the values of the cascode input impedance Z_{in}, output impedance Z_{out} and minimum noise impedance $Z_{n,opt}$ close to the design band edges at 150 GHz and 300 GHz are summarized in the following.

- Ideal cascode layout (150 GHz): $Z_{in} = (55 - j66)\,\Omega$, $Z_{out} = (23 - j400)\,\Omega$, $Z_{n,opt} = (44 + j28)\,\Omega$
- Ideal cascode layout (300 GHz): $Z_{in} = (52 - j33)\,\Omega$, $Z_{out} = (30 - j195)\,\Omega$, $Z_{n,opt} = (28 + j15)\,\Omega$
- Core cascode layout (150 GHz): $Z_{in} = (47 - j59)\,\Omega$, $Z_{out} = (7 - j325)\,\Omega$, $Z_{n,opt} = (105 + j89)\,\Omega$
- Core cascode layout (300 GHz): $Z_{in} = (47 - j24)\,\Omega$, $Z_{out} = (14 - j152)\,\Omega$, $Z_{n,opt} = (67 + j47)\,\Omega$

In total, the influence of the core layout on the input impedance trajectory is minor, showing a maximum deviation of less than 20 %. However, the core layout largely influences the optimum noise impedance $Z_{n,opt}$, resulting in a roughly doubled real and a tripled imaginary part. Furthermore, the core layout-induced effects on $Z_{n,opt}$ become dominant over different device biasing points, which is indicated by another G_{min} trajectory that belongs to the NF_{min} bias point with $V_{be} = 850$ mV showing no notable difference to the G_{min} trajectory for G_{max} biasing. This again emphasizes the necessity of accurate core modeling to achieve a close-to-optimum noise match among broad bandwidths.

Another crucial issue is the output reflection coefficient S_{22} that derivates significantly with and without the core layout implemented. After calculating the corresponding equivalent model values, it was found that the resistance is nearly doubled and the output capacitance increases by 20 %. This results in a significant change of the output impedance values and is based on the transformation through the vertical metal-via connection that changes the resulting output impedance very fast, even for relatively short lengths of several µm. The resulting large values of the shunt resistor at the output node present the most complex challenge for broadband impedance matching due to the high required impedance transformation ratios.

5.3 Broadband Device Matching

Considering the maximum available gain drop vs. frequency for a conjugately-matched amplifier as shown in [146] (G_{max} of the ideal cascode drops from 27 dB at 150 GHz to 12 dB at 300 GHz), a broadband matching network for a 3 dB bandwidth of more than 100 GHz has two main tasks. Firstly, a close-to-optimum conjugate match has to be provided at the highest operation frequency to ensure sufficient gain and set the upper corner frequency. Secondly, a selective mismatch has to be introduced for a flat overall gain characteristic and to increase the cascodes stability at lower design frequencies. The gain can be distributed differently among the stages in the investigated multistage low-noise amplifier. However, the primary constraints here are inherently broadband first two stages with sufficient gain to avoid further NF deterioration based on the following stages according to Equation 5.1. Especially a commonly applied gain staggering has to be avoided towards a broadband minimum NF characteristic.

5.3.1 The Bode-Fano Criterion: Theoretical Bandwidth Limitations

Based on the equivalent models from Figure 5.3 with the simplistically approximated input and output cascode networks as series and shunt RC connection, the fundamental limits of the cascode bandwidth can be analyzed by the Bode-Fano criterion [149] under the assumption of an ideal, passive and lossless matching network. In other words, the Bode–Fano criterion defines the theoretically achievable maximum matching bandwidth concerning the resistance and capacitance combination and the reflection coefficient $\Gamma(\omega)$. A larger bandwidth can be theoretically achieved with higher reflection coefficients. Therefore, the matching bandwidth is here defined as the bandwidth, where $\Gamma(\omega)$ is below an average threshold value Γ_{avg}. The Bode-Fano criterion is evaluated for the input and output node in the following to identify the dominant bandwidth limitations.

For the input (series RC connection,) the Bode-Fano limit is expressed by the following inequation [150]

$$\int_0^\infty \frac{1}{\omega^2} ln\left(\frac{1}{|\Gamma_{in}(\omega)|}\right) d\omega < \pi\tau = \pi RC, \tag{5.2}$$

where τ is the RC time constant and $\Gamma_{in}(\omega)$ the input reflection coefficient, including the input matching network. Equation 5.2 can now be simplified by the assumption of a (desired) constant in-band reflection coefficient $\Gamma_{in,avg}$ and a total out-of-band reflection coefficient of 1. Then, the integral can be expressed as a multiplication of $ln(1/\Gamma_{in,avg})$ by the angular frequencies $(\omega_2 - \omega_1)$, which corresponds to the angular bandwidth in relation to the center frequency ω_c. After re-arranging and transforming to the frequency domain, the maximum theoretical bandwidth (BW_{max}) is given by

$$BW_{max} = \frac{2\pi^2 \cdot RC}{ln(\frac{1}{\Gamma_{in,avg}})}. \tag{5.3}$$

Important to note is that BW_{max} increases with higher operating frequencies. With the help of Equation 5.3, a theoretical maximum input matching bandwidth of 290 GHz was calculated under the assumption of $\Gamma_{in,avg} = 0.1$ (-20 dB), a center frequency of 200 GHz and the previously computed series RC input values (with and without core layout) showing a negligible influence of the input network on the maximum theoretical bandwidth of the whole cascode stage.

For the output, modeled as parallel RC connection, the following inequation was derived by Bode [151]

$$\int_0^{\infty} ln\left(\frac{1}{|\Gamma_{out}(\omega)|}\right) d\omega < \frac{\pi}{RC}. \tag{5.4}$$

If simplified as before, the maximum theoretically achievable bandwidth is

$$BW_{max} = \frac{1}{2RC \cdot ln(\frac{1}{\Gamma_{out,avg}})}. \tag{5.5}$$

In contrast to the previous case, the absolute output node limited bandwidth does not increase with the center frequency. If now evaluated for the extracted output node RC values, including the core layout at 300 GHz, with $\Gamma_{out,avg}$ =0.1 (-20 dB), BW_{max} is limited to 40 GHz, which is far below the derived design objective in Chapter 2. However, BW_{max} scales with the assumed $\Gamma_{out,avg}$. If the output reflection coefficient $\Gamma_{out,avg}$ is reduced to 0.56 (-5 dB), a bandwidth of 150 GHz is theoretically possible. In other words, a $\Gamma_{out,avg}$ (S_{22}) $\leq$ -10 dB in more than 100 GHz of bandwidth can hardly be achieved with an ideal passive lossless matching network. Another noteworthy aspect is the influence of modeling accuracy. If, i.e., the derived output capacitance derivates by only ± 1 fF, the bandwidth limit may change by 100 GHz. This underlines that accurate device (parasitics) modeling is critical for an appropriate model-hardware correlation.

In conclusion, calculations of the maximum theoretically achievable bandwidth based on the Bode-Fano criterion showed that the device input matching network will not be a limiting factor to achieve overall system bandwidths larger than 100 GHz even with sufficient $\Gamma_{in,avg}$ smaller than -20 dB. The Bode-Fano limit further underlines the challenging design task of the output-matching network and that the output RC time constant mainly limits the amplifier bandwidth. A large amplifier bandwidth above 100 GHz can only be achieved under a trade-off in the average output reflection coefficient $\Gamma_{out,avg}$ of approximately -5 dB. Despite this, the insertion loss of the accompanying matching network that compensates for the gain roll-off of the uncompensated cascode stage vs. frequency may improve the theoretically achievable bandwidth or the corresponding output reflection coefficient.

5.3.2 Transformer based Matching

Coupled transmission lines can be applied to transform the impedance between two network nodes. Symmetric transmission lines are the most straightforward matching network to be analyzed with a regular even/odd-mode calculation. The even- and odd-mode impedance differences control the impedance transformation ratio commonly applied for purely real source and load terminations. In this case, the line sections are typically in the range of a quarter wavelength. The impedance transformation scales not only with the transformation ratio but also depends on the source and load impedance. This becomes especially important for the highly reactive cascode output network and has to be accounted for in EM-circuit co-simulations.

A tight line coupling is required through a broadside line coupling and a variable line spacing applied in the 7-layer BEOL to achieve the subsequently described impedance trajectories for broadband device matching. Furthermore, as shown in [152] in a comparative study of several LNA matching network topologies in the D-Band, asymmetric coupled lines generate the highest bandwidth and gain and are well-suitable as interstage matching networks. A simple symmetry plane referring to a global ground can hardly be applied in this case. A theoretical analysis of these structures can be found in [146], relying on the normal mode impedance parameters Z_c and Z_π for the asymmetric coupled lines. The following section focuses on the top-level design in terms of the realized impedance trajectories at the cascode stages' input-, interstage- and output nodes that enable broadband device matching in more than 100 GHz bandwidth. These were realized by asymmetric broadside coupled lines forming a transformer matching network for all relevant matching nodes.

In the following, the common features of all matching transformers are discussed. All transformers are implemented as asymmetric coupled line sections between TM1 and M3. The bottom strip is mostly wider than the top strip due to a roughly four times lesser thickness compared with TM1 (2 µm thickness) to realize the required characteristic impedances. The bottom ground is removed to improve the coupling between the line sections, which now refer to the side ground. These side ground walls enclose the transformer layout and are built up throughout the complete metal stack to provide sufficient shielding from the nearby components or the subsequent stages. Due to the side ground wall's nearby location, a compact layout can be realized. Based on these common features, the most important coupled line parameters (width, length, side wall location, metal layers) were numerically optimized in full-wave EM simulations to achieve the required impedance transformations, allowing more than 100 GHz bandwidth with 30 dB gain above 200 GHz.

5.3.3 Input Matching Transformer

A 3D model of the implemented input matching transformer is shown in Figure 5.4 a) with all relevant size parameters included. The coupled lines are located on TM1 and M4 with a 1.88 µm vertical spacing.

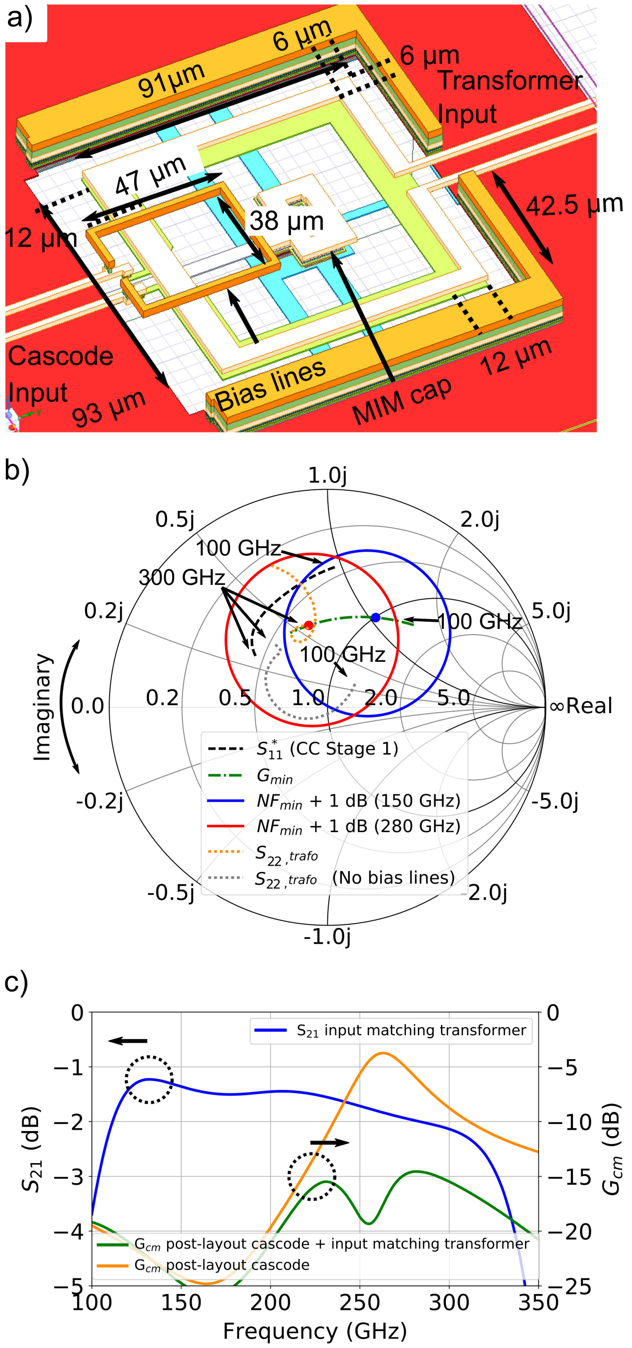

Figure 5.4: a) Input matching transformer with all relevant dimensions.
b) Simulated S_{11}^* and G_{min} of the post-layout cascode from 100 to 300 GHz and implemented S_{22} of the input matching transformer with and without DC bias lines. NF_{min}+1 dB circles are included for 150 and 280 GHz.
c) Insertion loss of the input matching transformer and common-mode gain G_{cm} of a single cascode stage with and without input matching transformer.

Additional M1 ground strips are used to reduce the aperture size of the ground opening to minimize the common mode radiation into the substrate at the cost of a slightly reduced operational bandwidth.

The most important design objective of the input matching transformer is providing an impedance trajectory close to the overall optimum noise impedance $Z_{n,opt}$ of the input cascode stage while maintaining sufficient available gain to reduce the influence of the subsequent cascode stage in the desired frequency range. Taking into account Figure 5.4 b), the corresponding optimum noise impedance $Z_{n,opt}$ varies roughly 2.5 times in real- and imaginary parts from 100 to 300 GHz. The maximum gain can only be achieved if the input is complex conjugately matched, as indicated by the complex conjugated impedance trajectory. To reach this, the coupled line transformer should provide a broadband 100 to 46 Ω real impedance conversion for differential signaling with a compensation of the capacitive imaginary part of the cascode input impedance according to the equivalent model shown in Figure 5.3 b). Reaching both design objectives simultaneously is not possible without inductive emitter degeneration, which was avoided for stability purposes.

As a trade-off, the transformer's output impedance trajectory approximates the complex conjugate of the first stage's input impedance, ranging from (40 + j80) Ω to (44 - j26) Ω at 150 and 280 GHz but lies within the 1 dB noise circles of the first stage from 150 to 300 GHz. In other words, the realized NF will only derive by less than 1 dB from the optimum NF$_{min}$. A good input match in the entire frequency range was achieved due to the inclusion of 2 shunt transmission lines at the transformer output. Three return loss minima are generated with these lines, as shown in the later measurements in Section 5.6.1. These lines are further used for device biasing and connected to 600 fF MIM capacitors in the transformer center for common-mode suppression. To emphasize this, the common mode gain of the first LNA stage with and without input transformer are shown in Figure 5.4 c). In total, the common mode gain above 200 GHz is suppressed by roughly 10 dB due to the input transformer. Furthermore, the losses of the input transformer are below 2 dB from 111 to 283 GHz.

5.3.4 Interstage Matching Transformer

A 3D simulation model with all significant dimensions for each coupled line section of the first inter-stage transformer is shown in Figure 5.5 a). The coupled lines are located on TM1 and M3 with a 2.91 µm vertical spacing. The cascodes stages' V_{cc} biasing is supplied by a center tap at the output coupled line section on M3 located in the transformer symmetry plane (differential ground). The main design objective of the inter-stage transformer is an impedance conversion from around (47 - j24) Ω

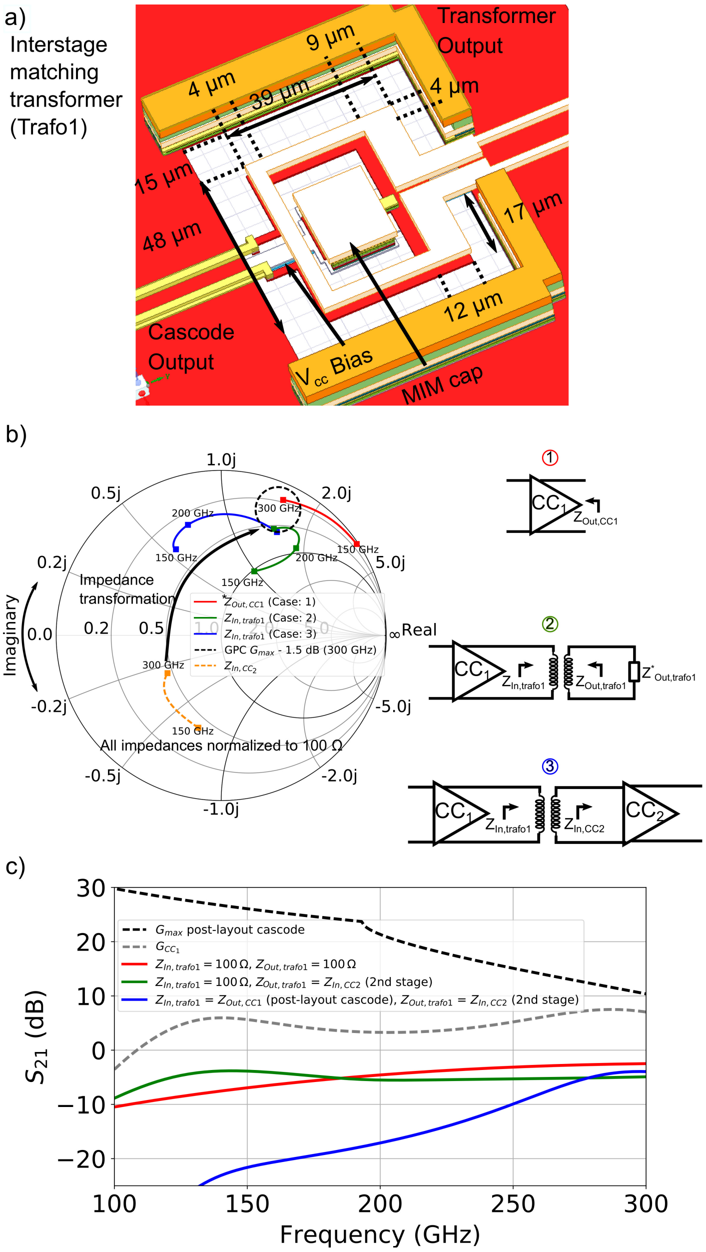

Figure 5.5: a) Interstage matching transformer of the first three stages, including dimensions.
b) In- and output reflection coefficients emphasizing the matching process. Three cases (1 to 3) are investigated. Case ①: S^*_{22} (ideal output match of the post-layout cascode). Case ②: Optimum S_{11} of the interstage transformer when the input is connected to the post-layout cascode and the transformer output is conjugately matched. Case ③: S_{11} of the interstage transformer when the output is connected to the input of the second post-layout cascode stage.
c) Source and load impedance dependent interstage transformer losses.

at the input of the consecutive stage ($Z_{In,CC2}$) to the output impedance $Z_{Out,CC1}$ (14 - j152) Ω ($R||C = 1.6k\,\Omega||3.4\,fF$) of the first cascode stage to provide a close to conjugate match at the desired upper operation frequency around 300 GHz. The previously applied transformation technique, with a near 2:1 (real) transformation ratio and minimum insertion loss cannot be used at 300 GHz. However, achieving transformation ratios of more than a factor of ten with additional compensation of the large output impedance imaginary part requires much smaller coupled line strip widths that can no longer be implemented.

An alternative approach was applied based on constant power gain circles, which span a circular area within the Smith Chart with less than the optimal gain under the assumption of a conjugate input match. First, the impact of the related strip dimensions on the transformed impedance trajectory was investigated numerically by full-wave EM simulations. Then, the corresponding transformer s-parameter file was re-imported into the circuit simulator to provide realistic impedance terminations. Finally, the impedance trajectory was optimized to provide an inductive transformed impedance value $Z_{In,CC2}$ of $(60 + \mathrm{j}150)\Omega$ at 300 GHz that allows sufficient overall gain of the first cascode stage staying within the G_{max} - 1.5 dB gain circle, which corresponds to a gain of 8.5 dB without transformer losses and is indicated in Figure 5.5 b). This ensures a close-to-optimum cascode gain at around 300 GHz but without broadband gain behavior.

The requirements on the impedance transformation to achieve a broadband LNA gain are much more challenging and differ significantly from the narrowband matching commonly applied for submmWave amplifiers. To emphasize this, first of all, the G_{max} trend of the post-layout cascode for the chosen bias point ($J_c = 22$ mA/µm^2, $V_{be} = 880$ mV) is shown in Figure 5.5 c). Taking into account the presented G_{max} characteristic of the cascode stage in the used SG13G3 technology dropping from 30 dB at 100 GHz to 10 dB at 300 GHz, it becomes clear that a broadband operation across the entire bandwidth is not feasible with an ideal output match. Instead, the matching transformer has to provide a steadily growing mismatch towards lower operating frequencies to compensate for the higher device G_{max}. In other words, the desired impedance trajectory at the output of the first stage needs to stay within similar power gain circles across the whole operation bandwidth.

For a more detailed analysis, the simulated impedance trajectories present at the output of the first stage and input of the second stage are further shown in Figure 5.5 b) for several cases, including the full-wave EM simulated interstage matching transformer. Case 1 (red curve) corresponds to the complex conjugate output impedance of the post-layout cascode, which potentially causes a G_{max} behavior across the whole bandwidth. Case 2 (green curve) expresses the impedance seen by the post-layout cascode when connected to the complex conjugately matched interstage transformer. With the optimum transformer load conditions applied, a broadband gain characteristic with an 11.5 dB gain peak at 220 GHz is achieved, which drops towards higher frequencies. Most important is the blue trajectory, as the impedance trajectory at the input of the interstage matching transformer loaded with the realistic input impedance of the second stage ($Z_{In,CC2}$). When comparing all three curves, the previously mentioned, close-to-optimum match around 300 GHz (within the G_{max}-1.5 dB circle) becomes apparent. Furthermore, the blue and green curves significantly deviate from each other at 200 GHz and come closer together at 150 GHz.

In total, this results in two gain peaks in the overall gain of the first transformer coupled cascode stage (at 150 and 300 GHz) of around 6 and 7.5 dB and a gain dip to 3.5 dB (around 200 GHz) as shown in Figure 5.5 c) with a very flat gain characteristic that stays above 3.5 dB from 120 to 325 GHz. For this purpose, it was decided to use the topology of this interstage transformer for the first three stages. It has to be further mentioned that a similar analysis as the one presented for the output of the first stage was also applied for the input of the second stage based on available gain circles G_{AC}, leading to a very similar gain performance of the first three LNA stages. Compared to the input transformer, the interstage transformer not only makes use of a much higher transformation impedance at 300 GHz but also includes a mismatch/attenuation at lower frequencies. Therefore, the lengths of the individual sections can be reduced, which leads to a more compact transformer layout. This mismatch grows towards lower frequencies and enables a broadband gain across more than 200 GHz bandwidth. That way, the large intrinsic available gain of more than 20 dB at frequencies below 200 GHz is attenuated and the device stability and enough gain to minimize the noise contribution of the consecutive stages is ensured. As indicated in Figure 5.5 c), it is essential to model the transformer losses appropriately as they highly depend on the termination impedances.

5.3.5 Output Matching Transformer

With the first three stages providing a broadband double peaking gain characteristic, the main objective of the following cascode-transformer sections is now a broadband single peak gain characteristic that fills the gain dip at around 200 GHz. Therefore, two additional stages were implemented to reach an overall gain characteristic with more than 30 dB gain. Due to its different load impedance termination compared to the previous interstage transformer, the following analysis focuses on the implemented impedance transformation of the output matching transformer whose 3D model, including relevant dimensions, is shown in Figure 5.6 a).

The output transformer was intended to fulfill the total power radiometer design requirements. As described in more detail in the subsequent radiometer chapter, it needs to allow a broadband interstage matching between the LNA and the following capacitive detector implemented in the radiometer chip-set. Furthermore, an output

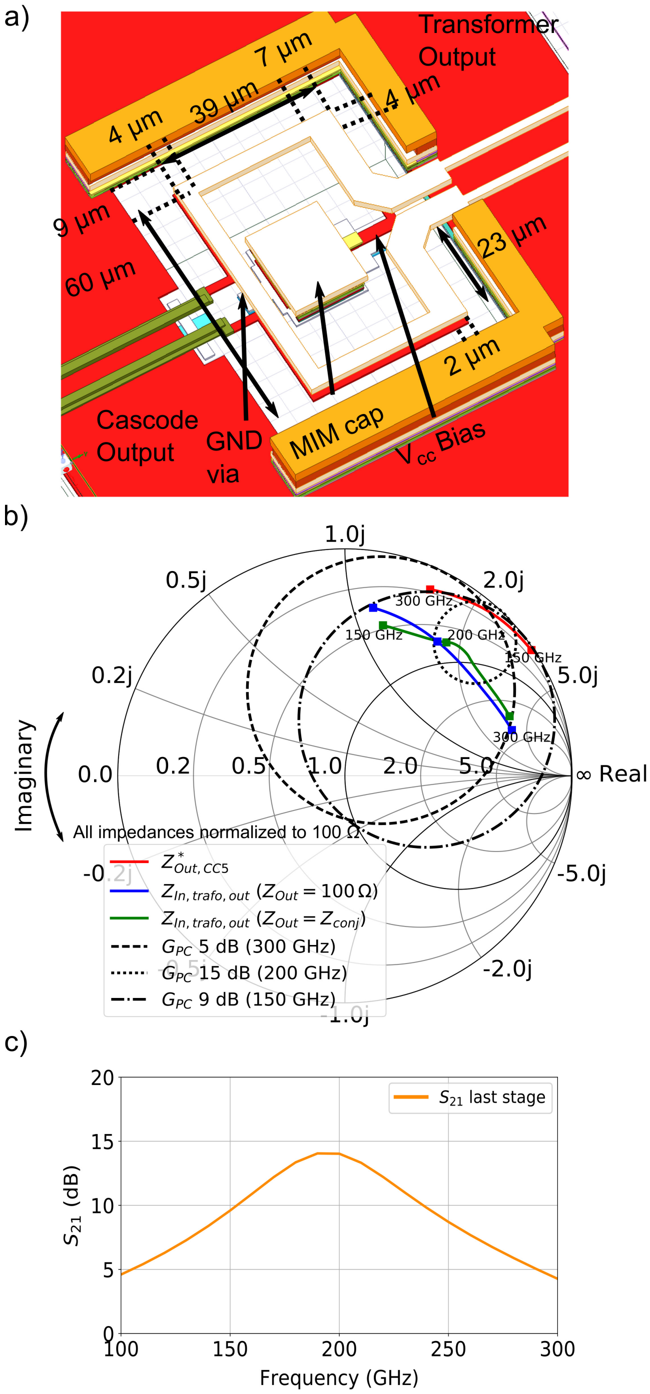

Figure 5.6: a) Output matching transformer.
b) In- and output reflection coefficients emphasizing the matching process. Power gain circles indicate the gain levels at 150 GHz, 200 GHz and 300 GHz.
c) Small-signal gain of the last stage loaded with Z_{Out} of the previous stage.

ground path for detector biasing is necessary that was implemented through a ground via connecting the transformer output TM1 layer to the overall ground plane at its symmetry plane. In the investigated breakout circuit, the 100 Ω differential output impedance has to be transformed to an adequate inductive impedance trajectory to ensure the desired gain characteristic. The large inductive impedance transformation was reached here by reducing the strip width of the bottom M3 layer to 2 µm. Similarly to the previous interstage transformer design, the necessary impedance trajectory was evaluated based on power gain circles of the post-layout cascode (last stage), that in this case, was biased with $J_c = 34$ mA/µm^2 ($I_c = 6.6$ mA) as the NF of the last stage is negligible for the overall 5-stage LNA.

After an optimization within 3D simulations, the realized impedance trajectories at the input of the output transformer (seen at the output of the post-layout cascode) are shown in Figure 5.6 b) for similar cases as described for the interstage matching transformer. The blue curve, assuming the output transformer is complex conjugately matched, does not differ significantly from the ideal curve. Most important is that the realized impedance trajectory lies within the 15 dB power gain circle G_{PC} at around 200 GHz. Further, the realized impedance trajectory separates from the ideal red curve towards 150 and 300 GHz, resulting in a single gain peak at 200 GHz. At 300 GHz, the trajectory lies within the 5 dB power gain circle. At 150 GHz it is in the 9 dB power gain circle. Thus, the slight gain difference of the dual peak gain characteristic of the previous three stages at 150 and 300 GHz is compensated. In total, the achieved gain of the last stage with the input terminated by the output impedance of the previous stage is gathered in Figure 5.6 c) showing a maximum gain of 14 dB at 200 GHz in a 3 dB bandwidth of 70 GHz (160 to 230 GHz).

5.4 5-stage LNA Simulation Results

The realized performance of the final 5-stage amplifier is analyzed in the following when loaded with ideal 100 Ω differential in- and output terminations. At this point, it should be mentioned that the stability of each stage and the stability of the 5-stage LNA implementation were investigated by source and load stability circles (SSB, LSB). SSB and LSB lie entirely outside the Smith Chart in the whole frequency range with the implemented matching transformers, indicating an unconditional stable amplifier. These simulations are based on EM co-simulations of the individual cascode core and interstage matching networks, not accurately accounting for the coupling between the consecutive stages. This can only be done with the complete 5-stage LNA layout included in the EM simulation tool, which results in a drastically increased effort and thus was omitted here.

5.4.1 Aggregate Gain and NF Curves

The simulated aggregate small-signal gain after 1 to 5 stages is shown in Figure 5.7 a), including all interstage matching and the input and output coupled line transformer sections. The aggregate gain and NF of the first two stages are critical for the total

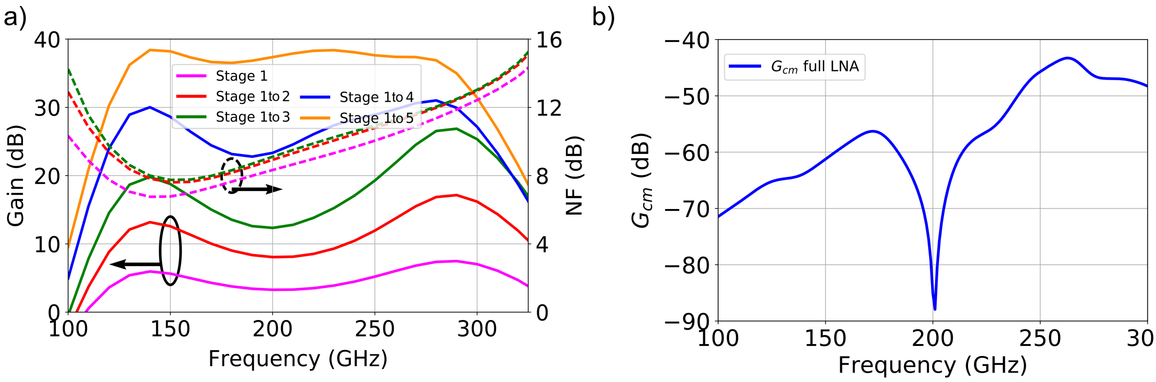

Figure 5.7: a) Simulated aggregate small-signal gain (solid) and NF (dashed) for an increasing number of LNA stages (1 to 5). All matching transformers are included with the implemented termination impedance of the following stage. Image after [own10] ©2023 IEEE.
b) Simulated common mode of the 5-stage LNA.

broadband NF and were traded against the LNA bandwidth. Here, the compensation of the gain dip induced by the first three stages in the band center that is balanced by the last two stages is visible. In total, a minimum NF of 7.8 dB at 150 GHz and 13 dB at 300 GHz was simulated with a corresponding maximum gain of 38.5 dB in a 159 GHz bandwidth (129 to 288 GHz) to provide enough headroom towards the design objectives (100 GHz bandwidth, 30 dB gain) for passive imaging in case of model uncertainties.

5.4.2 Common Mode Suppression

The previous analysis focused on the differential impedance transformation. However, the common mode will also be present in the amplifier due to non-ideal differential operation by process variations or non-symmetrical layouts and imperfect differential signal generation and potentially cause common mode oscillations. Therefore, the common mode gain was further simulated and optimized by choosing an appropriate 374 fF MIM cap placed at the center of all interstage transformers. The common mode gain is now primarily eliminated due to the MIM capacitor in the layout center providing a broadband common mode short as it is shunt on one side (M3) to the global ground. The global ground is provided on M1 with the help of a center bottom strip. The other top transformer line section on TM1 can also be connected through a respective center tap to provide a separate bias for the consecutive stage. This results in a global AC short on both center taps. It was found by simulations that only if one center tap is connected with the decoupling capacitor a global short-circuit on one side is transformed into an open-circuit on the other center tap, which improves the CM rejection ratio. Finally, the cascode output ports are DC-biased with 3 V V_{cc} through the transformer center tap. All other inputs of the cascode stages are biased by separate networks shown in Figure 5.2 a). As depicted in Figure 5.7 b), the common mode rejection of a single amplifier stage increased from maximum 20 to 60 dB for the 5-stage cascode implementation in the entire frequency band. At the same time, a minimum common mode gain of -90 dB is achieved at 200 GHz.

5.5 Implemented LNA and Balun

The simplified schematic and micrograph of the implemented LNA are shown in Figure 5.8. A Marchand balun is used to compensate for the parasitic on-chip pad capacitance and inductance for broadband on-wafer measurements. Its design is based on a coupled-line section with a non-uniform characteristic impedance profile implemented in TM1 and M3 layers. The initial balun design is based on a higher tuned version presented in [own11] that was scaled by increasing the length of both metal lines (TM1, M3) from 55 to 90 µm towards a lower frequency cut-off of 130 GHz. It is placed at the amplifier's input and output and transforms the complex single-ended pad impedance trajectories to a broadband differential 100 Ω load at its output. At frequencies below 160 GHz, the simulated pad impedance provides $L_{pad} \approx 21.5$ pH and $C_{pad} \approx 21$ fF. At higher frequencies around 300 GHz, the pad impedance drops approximately to 20 to 25 Ω. For a broadband design, both effects were compensated in the complex balun design [own11].

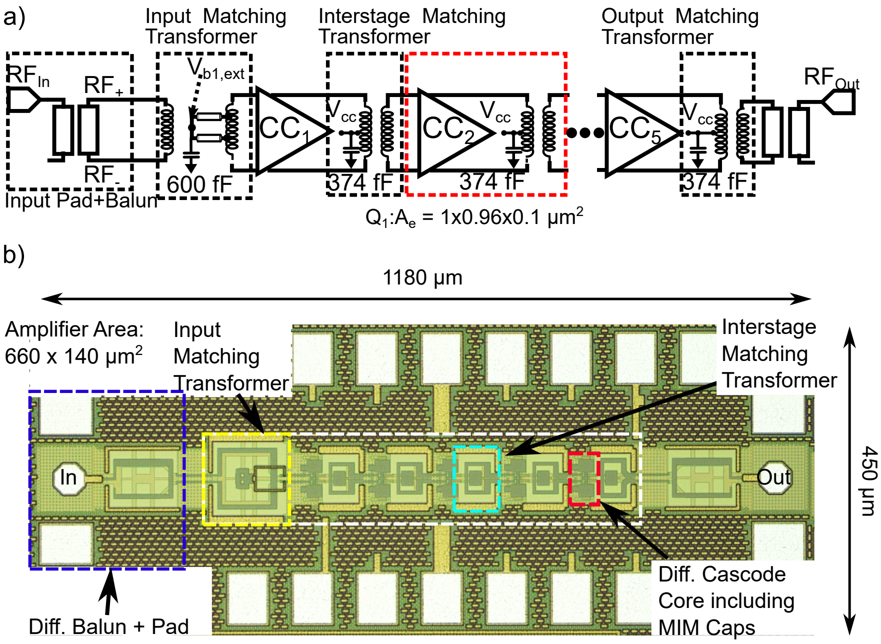

Figure 5.8: a) Schematic of the 5-stage pseudo-differential cascode LNA with indicated biasing and transformer matching blocks.
b) LNA micrograph.
Images after [own10] ©2023 IEEE.

The balun was measured separately in a set of back-to-back configurations that, together with corresponding measurement and simulation results, are indicated in Figure 5.9. A maximum insertion loss better than 1.5 dB per balun, de-embedded in the 136 to 325 GHz band, is indicated that well correlates with the simulations deviating by not more than 0.5 dB. Further, the measured S_{11} is below -10 dB between 134 and 306 GHz. The full LNA chip area is 0.53 mm^2 with baluns and pads and 0.09 mm^2 without.

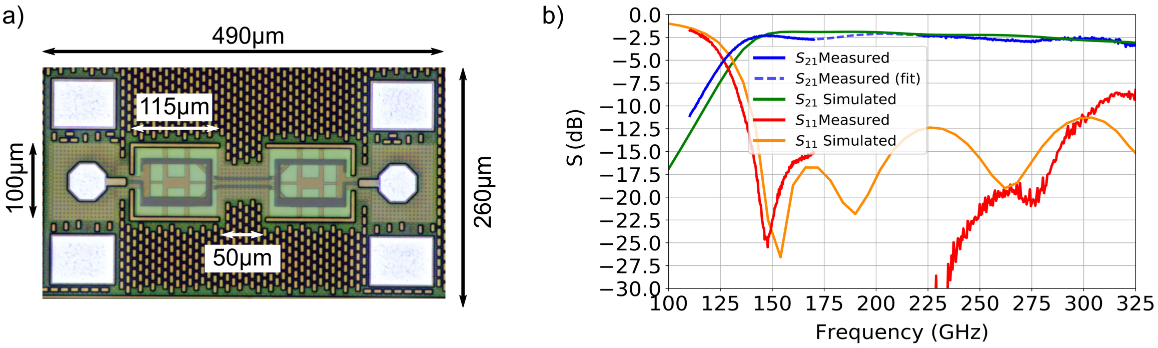

Figure 5.9: a) Micrograph of the balun in back-to-back measurement configuration. b) Corresponding measurement and simulation results.

5.6 Breakout Measurements

Two VNA extension modules were used for on-wafer measurements from 110 to 325 GHz. These were a WR-6 (110 to 170 GHz) and a WR-3 (220 to 325 GHz) module from OML as shown in the measurement setup in Figure 5.10. The modules were connected to a Keysight P8361A PNA network analyzer for small-signal measurements. Both modules were calibrated out-of-band between 110 to 185 GHz and 200 to 325 GHz as no equipment covering the whole G-Band, spanning from 140 to 220 GHz, was available.

Out-of-band, the modules still provide sufficient SNR. In total, there is a gap of 15 GHz present in the measurements. Due to the high LNA gain, all small-signal and power measurements were performed with additional waveguide attenuators at the LNA input, ensuring linear LNA and VNA extension module operation.

A standard through-reflect-line (TRL) method on a calibration substrate was used for calibration. After calibration, the insertion loss of each interconnect component in the measurement setup was measured and de-embedded as shown in Figure 5.11. In the LNA measurement, high attenuation values up to 40 dB were used, which do not permit reliable on-wafer calibrations. Therefore, the initial TRL calibration was performed with the attenuator values set to the reliable minimum. If the attenuator

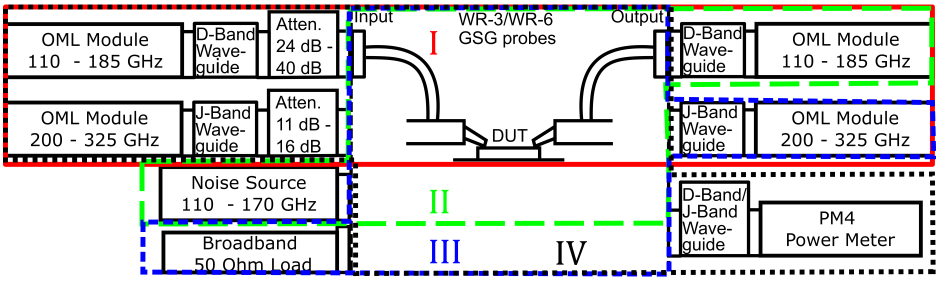

Figure 5.10: a) Different on-wafer LNA measurement setups.
I: Small-signal measurement setup.
II–III: NF measurement setup in D-Band (II) and J-Band (III).
IV: Large-signal measurement setup.
The frequency bands from 110 to 185 GHz and 200 to 325 GHz are covered by two different OML extension module pairs.

after the TRL is set to the required value for measurements, small load impedance changes are present at the attenuator output. Hence, standing waves were present in the measurements with the calibration substrate and the on-chip balun. This slight inaccuracy of the insertion loss calibration manifested as parasitic ripples of approximately 1 dB in the de-embedded small-signal gain curves. Due to the good reverse isolation, the return loss measurements could be performed with the attenuation set to the corresponding minimum when the last two LNA stages are saturated.

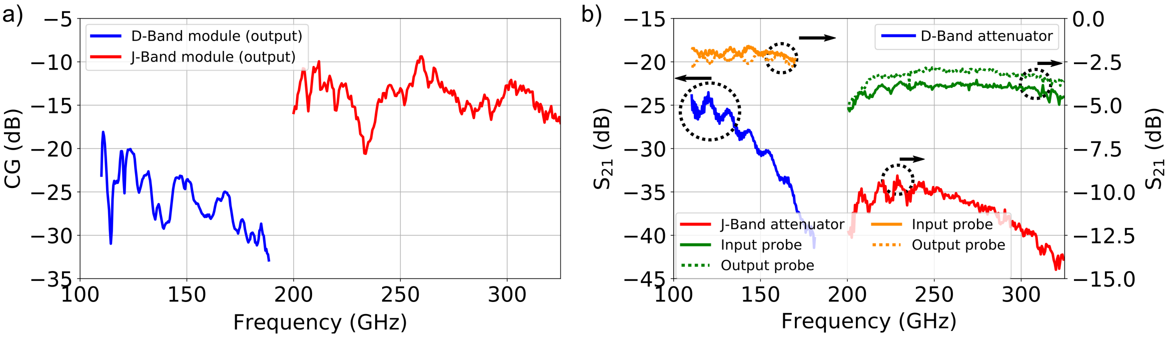

Figure 5.11: a) Measured conversion gain of the output extension modules for NF calculations.
b) Measured probe and attenuator losses.

5.6.1 Small-Signal Measurements

The measured and simulated s-parameter results are shown in Figure 5.12. S_{22} is mostly below -5 dB. This well aligns with the previously derived theoretical bandwidth limitations of the output matching network calculated with the Bode-Fano criterion. A maximum S_{21} of 34.6 dB is achieved at 160 and 235 GHz with a small-signal 3-dB bandwidth of 146 GHz spanning from 131 to 277 GHz. With the baluns de-embedded, these values increase to a peak gain of 37 dB and a BW of 155 GHz (124 to 279 GHz). The faster gain roll-off in the measurements that starts at around 290 GHz was also observed in a similar technology [146]. This gain roll-off does not appear in the simulations and can possibly be attributed to HBT model weaknesses due to the lack of reliable s-parameter measurements of the transistors at these frequencies. The input is well matched, showing S_{11} smaller than -10 dB from 150 to 325 GHz.

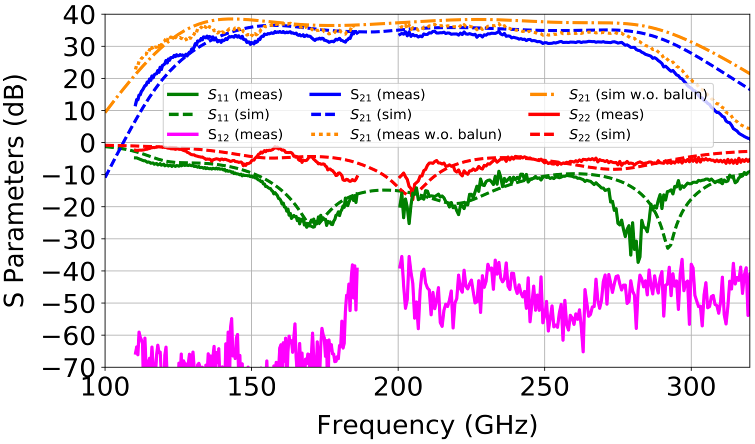

Figure 5.12: Measured and simulated LNA s-parameters.
Image after [own10] ©2023 IEEE.

Towards higher frequencies around 300 GHz, a slight frequency shift can be observed between measurement and simulation. The simulated S_{12} is around -130 dB, far exceeding the VNA's dynamic range. With the used extension modules, the VNA noise floor is limited to -50 dB (J-Band) and -70 dB (D-Band), which is at least 60 dB higher than the simulated S_{12}. For this purpose, a stability analysis calculating the k-factor out of the measured s-parameters leads to inaccurate results. Therefore, the k-factor was verified by two additional measurements gathered in Figure 5.13.

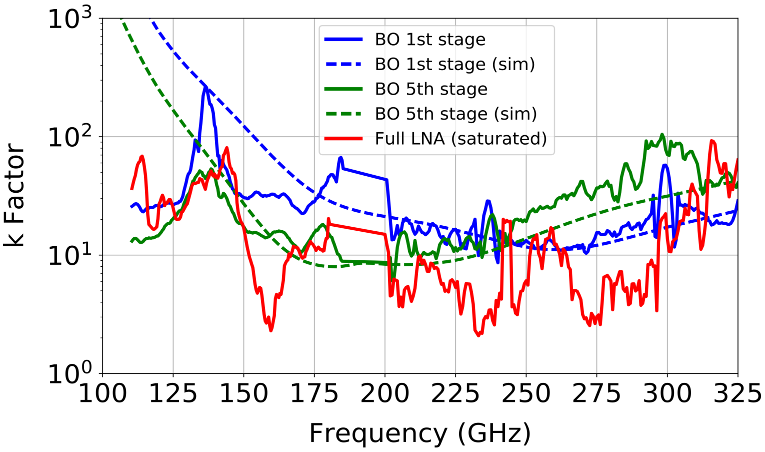

Figure 5.13: Calculated k-factors for breakouts (BO) of the first and fifth LNA stage and the LNA driven in saturation with the attenuator set to the corresponding minimum.

First, the k-factor was determined from breakout measurements of the first and last LNA stage, showing a minimum k-factor of 5. Second, the k-factor was calculated from the s-parameter measurements of the saturated LNA with the attenuator set to the corresponding minimum. With values above 2.1, the full amplifier and its single stages remain constant across the entire operating range. Further, the equivalent noise bandwidth (ENBW) was calculated from the measured gain curve based on the following equation [153] [76]

$$ENBW = \frac{[\int_0^\infty G(f)df]^2}{\int_0^\infty G(f)^2 df}, \tag{5.6}$$

where $G(f)$ is the linear amplifier power gain calculated as $10^{S_{21}/10}$ with S_{21} in dB as shown in Figure 5.12. The calculated ENBW is 151 GHz, which is close to the LNA 3 dB bandwidth of 146 GHz due to the high out-of-band gain roll-off of 150 dB per 100 GHz. This is especially important for radiometry, as a constant noise power can be assumed within the ENBW. In summary, an excellent model-to-hardware correlation was achieved within the operating bandwidth of more than 100 GHz. This validates the complex EM co-design approach.

5.6.2 Noise Figure Measurements

Before performing the noise figure measurements, it was verified that the VNA extender modules' parasitic conversion gain (CG) of the other harmonics with values less than -10 dB is sufficiently low to minimize the NF measurement error. For all measurements, the output noise floor of the corresponding VNA extension module connected to the LNA output was monitored with a Keysight E4440A PSA spectrum analyzer. All measured output noise spectral densities were corrected by the noise contribution of the corresponding VNA extension module indicated in Figure 5.14.

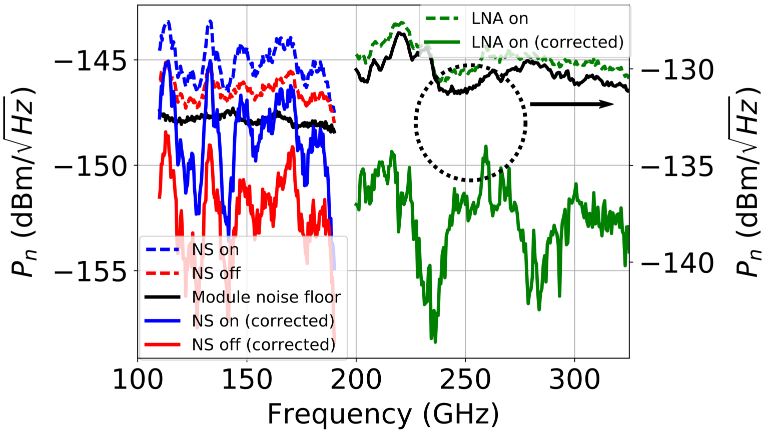

Figure 5.14: Measured noise power spectral density at the extension module output.

In the D-Band, an ELVA-1 ISSN-06 noise source with a typical ENR of 12 dB was connected to the input probe to perform the Y-factor method for NF determination as indicated in Figure 5.10 II). Based on hot and cold measurements, the following equation was used to calculate the Y-factor [154]

$$Y = \frac{P_{n,lin(on)}}{P_{n,lin(off)}}, \tag{5.7}$$

where $P_{n,lin(on)}$ and $P_{n,lin(off)}$ are the measured and corrected linear noise power values with the noise source switched on and off shown in Figure 5.14. Now, the standard equation to calculate the NF is given by [155]

$$NF = ENR_{dB} - 10 \cdot \log_{10}(Y - 1). \tag{5.8}$$

ENR is the excess noise ratio of the noise source. Equation 5.8 assumes a direct connection of the noise source to the DUT, which is not the case in the current measurement setup due to the implemented passives such as input balun, input transformer and the input probe losses in front of the LNA. The loss of the input probe reduces the applied ENR. Furthermore, the balun and transformer losses must be added to the calculated Y-factor, as they are not present in the measured $P_{n,lin(off)}$. Another factor of 3 dB has to be subtracted to determine the single sideband noise figure. Including all corrections, the following calculation was used to determine the system's NF:

$$NF = ENR_{dB} + S_{21,probe} - 10 \cdot \log_{10}(Y - 1) - S_{21,balun} - S_{21,trafo,in} - 3\,dB. \tag{5.9}$$

$S_{21,probe}$ corresponds to the input probe between the balun and noise source. Note that S_{21} of the input transformer could not be measured. Therefore, it was extracted from the full-wave EM simulation results shown in Figure 5.4 c).

In the J-Band, the input probe was terminated with a broadband 50 Ω match caused by the unavailability of a noise source. Due to the high LNA gain, the noise floor of the J-Band modules is increased by, on average, 1 dB without using an additional external LNA, as shown in Figure 5.14. The added LNA noise $P_{n,Out}$ (LNA on, corrected) at the module output was calculated by correcting for the reference noise floor. In total, the NF was determined by the following equation

$$NF = P_{n,Out} - P_{n,In} - G(f) - S_{21,probe} - CG - 3\,dB, \tag{5.10}$$

where CG is the module's conversion gain, G(f) the LNA gain, $S_{21,probe}$ the measured output probe losses, all in dB. Further, $P_{n,In}$ of -174 dBm/$\sqrt{Hz}$ is the thermal input noise power spectral density at a reference temperature of 290 K [156]. All corresponding values can be found in Figure 5.11. The measured and simulated NF is shown in Figure 5.15.

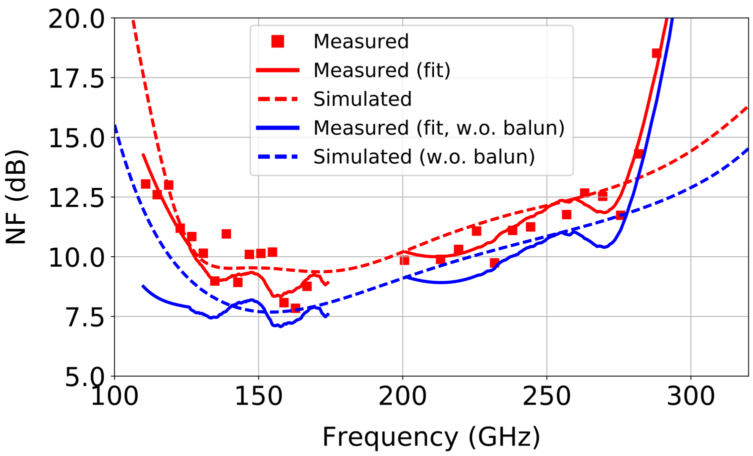

Figure 5.15: De-embedded noise figure in the D-Band and J-Band.
Image after [own10] ©2023 IEEE.

In summary, there is an excellent correlation between measurements and simulations in the frequency range from 100 to 325 GHz due to an accurate calibration and de-embedding of all relevant passives. A minimum NF of 8.4 and 7.1 dB at 155 GHz with and without the input balun de-embedded is shown that increases to 12.5 dB and 11 dB at 260 GHz. The reduced bandwidth of the NF above 280 GHz is based on a faster gain roll-off shown in the s-parameter measurements compared to the simulated values.

5.6.3 Large-Signal Measurements

To measure the LNA's large signal behavior, a pre-calibrated PM4 power meter from VDI was placed at the LNA output and the attenuator levels were varied from the corresponding maximum to minimum attenuation levels. The compression curves were calculated by de-embedding all relevant measured losses from the measured output power that are shown in Figure 5.11. The measured compression curves are illustrated in Figure 5.16 for three different frequencies. The LNA exhibits a constant OP_{1dB} from 0 to 1 dBm in an extensive frequency range from 150 to 265 GHz. With the output balun de-embedded, the OP_{1dB} increases to 1 to 2.1 dBm. However, the saturated output power was not measured because too high probe/waveguide losses of approximately 9 dB that prevented the LNA from full saturation in the J-Band with the used OML modules.

5.6.4 Variable LNA Gain

Additionally to the nominal bias conditions with 3 V V_{cc}, the LNA's small-signal behavior was investigated for several different bias voltage combinations, which can be applied to each stage individually due to access to the external base nodes provided in the breakout. A particular focus was set on possible frequency tunability. Here, only a

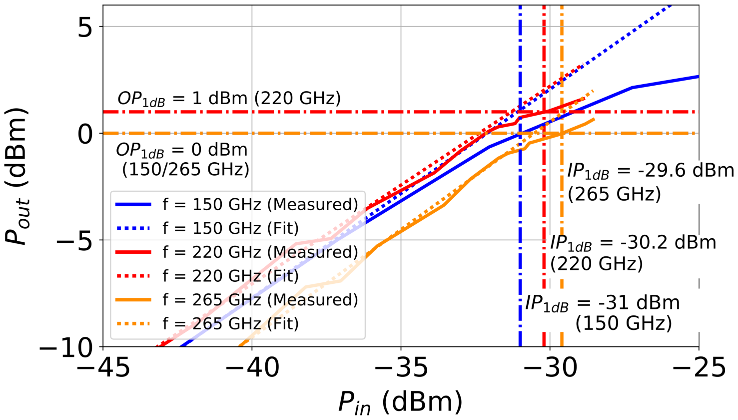

Figure 5.16: Measured LNA compression curves at 150 GHz, 220 GHz and 265 GHz. $OP1_{db}$ varies between 0 dBm and 1 dBm in the whole frequency range.
Image after [own10] ©2023 IEEE.

peak gain shift towards lower frequencies around 150 GHz was measured, resulting in a 3 dB bandwidth of 50 GHz. This was achieved with a V_{cc} of 1.5 V, thereby improving the power consumption.

Another critical aspect is shown exemplary for the last stage in Figure 5.17. By varying the base voltage of the cascode stages, the overall amplifier gain is tunable. Three curves are shown with gain values around 10 dB, 20 dB and 30 dB for the corresponding cascode V_{be} of 804 mV, 850 mV and 890 mV. The tunability is achieved when the cascodes base-emitter voltage deviates from the optimum value of 900 mV for G_{max} operation towards lower values. Then, also, the optimum output impedance trajectory changes. For this purpose, the shape of the gain curves varies and the previously described waviness increases. In total, the corresponding 3 dB bandwidth is reduced to 60 GHz centered around 210 GHz.

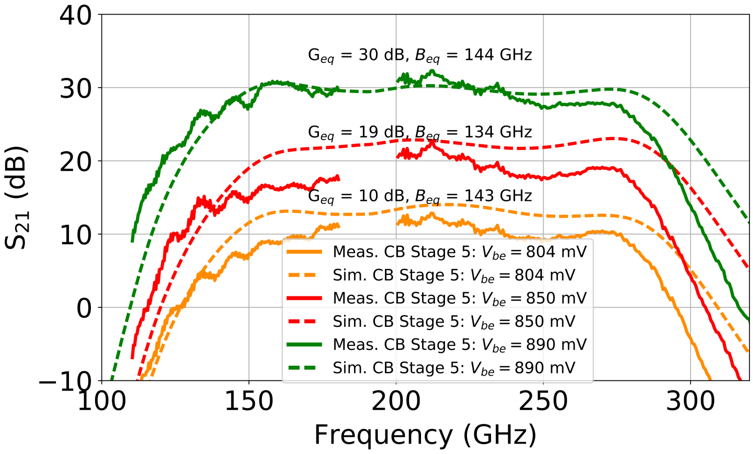

Figure 5.17: Measured LNA small-signal gain under different bias conditions at the base of the last stage's common-base transistor with $V_{cc5} = 2.0$V.

Due to the high gain values out of the 3 dB bandwidth, which are only 4 to 6 dB lower than the peak gain, the overall equivalent bandwidth of the gain curves exceeds the 3 dB bandwidth by more than a factor of two, with values reaching from 134 to 143 GHz. In other words, the usable bandwidth for passive imaging deteriorates by a small factor of 10 %. Lower gain values can be beneficial to avoid any saturation effects in the implemented radiometer detector responsivity for high object temperatures or in active imaging applications by increasing the detector's dynamic range.

5.7 Conclusion and State-of-the-Art Comparison

In this chapter, the most important design considerations for a broadband, five-stage differential cascode LNA implementation with more than 30 dB gain, 100 GHz bandwidth and a center frequency above 200 GHz for passive imaging are introduced. Key parameters are accurate device core modeling, an optimization of all capacitive and inductive core interconnections and interstage matching with novel distributed coupled-line matching transformers. The interstage matching transformer aims to realize a complex conjugate interstage matching at the upper corner frequency (280 to 300 GHz) and an appropriate gain, ensuring device stability and an approximately flat gain behavior towards lower frequencies. A broadband double-peaking gain behavior of the first three stages is achieved, including a gain dip at around 200 GHz. The last two stages realize a broad gain peak in the band center to compensate for this.

5.7.1 Comparison to the State-of-the-Art

Over the last 15 years, more than 20 silicon-integrated LNAs and PAs were developed at the IHCT for several applications. A concise summary of SiGe HBT-based amplifiers designed at the IHCT is shown in Figure 5.18 a). Not only supported by the continuous f_t/f_{max} scaling during recent years but further due to the complex EM-assisted design approach, the amplifier's gain and bandwidth increased by at least one order of magnitude during the past ten years, finally reaching a gain of 34.6 dB in a unprecedented bandwidth of more than 146 GHz centered around 204 GHz and a minimum NF of 8.4 dB at 155 GHz.

The implemented LNA further exceeds the entire current state-of-the-art indicated in Figure 5.18 b) in terms of gain and bandwidth. In more detail, it is the first silicon-integrated LNA that operates in the D-Band and J-Band with more than 100 GHz bandwidth and a small-signal gain larger than 30 dB, resulting in an excellent gain bandwidth product of 421 THz, even with the baluns not de-embedded. However, the 146 GHz large operation bandwidth and the high gain towards 300 GHz come at the cost of a relatively high 3 V V_{cc}. This results in a moderate power consumption P_{DC} of

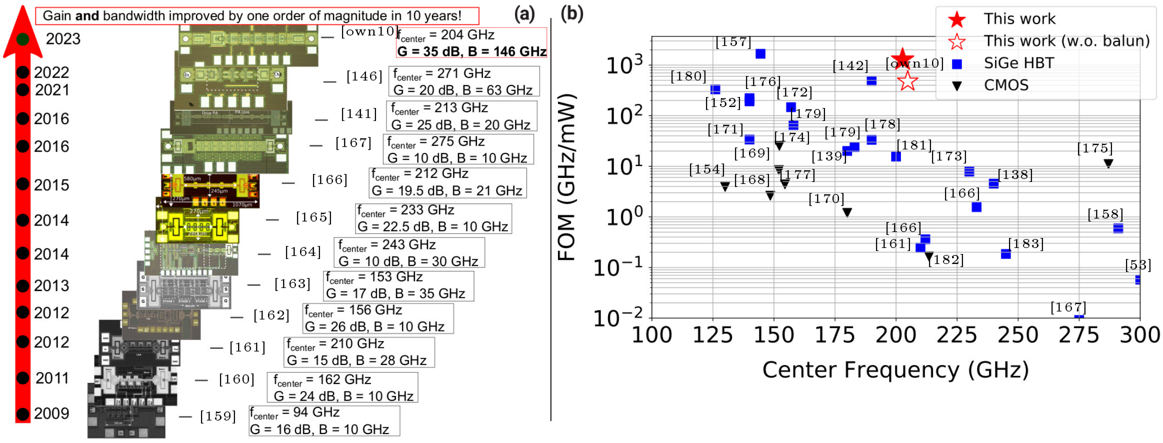

Figure 5.18: a) State-of-the-art for silicon-integrated LNAs and PAs developed at the IHCT. b) State-of-the-art (FOM) of silicon-integrated LNAs operated above 100 GHz.

152 mW and a degraded minimum noise figure in the D-Band. In the state-of-the-art, a low power consumption of 3.2 mW with devices operated in saturation [142] and a minimum NF of 4.8 dB [157] are reported with less gain and bandwidth. Simulations showed that an LNA re-biasing leads to a further NF improvement by up to 1 dB at 150 GHz at the cost of the available 3 dB bandwidth.

For a fair comparison to the state-of-the-art, all previously discussed performance metrics should be included in a global figure of merit (FOM). For this purpose, the following metric was used to evaluate the state-of-the-art [158]

$$FOM = \frac{G_{lin} \cdot BW[GHz]}{(F-1) \cdot P_{DC}[mW]}, \tag{5.11}$$

where the FOM is evaluated in [GHz/mW] and plotted in Figure 5.18 b) for state-of-the-art LNAs implemented in silicon. Typically, the FOM is applied using the peak gain and minimum measured noise factor F, which are nearly constant. It is worth mentioning that the LNAs' NF raises towards higher frequencies. This is important in broadband radiometer designs, as it deteriorates the system NETD. As a comparison basis to typical narrowband designs, the FOM for the presented LNA is calculated based on the minimum measured in-band NF. A more accurate FOM can be calculated with the equivalent noise factor determined similarly as in Equation 5.6.

The presented LNA shows the best performance among the state-of-the-art of silicon-integrated, reactively matched LNAs operating with a center frequency above 200 GHz. The calculated FOM exceeds nearly all previous designs above 150 GHz by at least one order of magnitude. Moreover, when the measured equivalent gain (G_{eq} = 33 dB), noise bandwidth (B_{eq} = 151 GHz) and minimum NF are included in Equation 2.47, a total NETD of 20 to 60 mK (depending on the minimum NF) is calculated with an assumed equivalent detector NEP of 5 $pW/\sqrt{Hz}$ and an integration time of 40 ms. These theoretical calculations indicate that the LNA is well-suitable for integration in a total power radiometer but does not account for the LNA gain variations and additional implementation losses due to the antenna to LNA and LNA to detector matching. Therefore, the overall radiometer implementation is discussed in the following chapter.

Chapter 6

Radiometer Design and Measurements

Room temperature operated, silicon-integrated total power radiometers with LNA pre-amplification are well established in the frequency range around 100 GHz with typical RF bandwidths of several tens of GHz [57], [78], [184]–[187]. Based on a narrow-band LNA NF optimization, state-of-the-art real-time NETDs approaching 100 mK in a 30 ms integration time [187] or 250 mK with a 3.125 ms integration time are reported [188]. Furthermore, most realized radiometer chipsets have only been demonstrated by on-chip measurements, not accounting for implementation losses in a fully (lens-)packaged radiometer system. Hence, for real-time imaging applications, the reported NETD performance potentially deteriorates by at least 3 dB.

To further shift the center frequency of silicon-integrated total power radiometers above 200 GHz and benefit from a higher spatial resolution, in the following, the design of a radiometer based on the previously described LNA and direct detector blocks is studied. The most challenging design aspects are maintaining the LNA gain of more than 30 dB and bandwidth of more than 100 GHz when implemented with an antenna and a direct detector under a close-to-optimum noise match. With the characteristic NF increase towards higher frequencies, a bandwidth above 100 GHz is of special importance as it improves the overall system NETD and counteracts the antenna implementation losses. Another optimization aspect is the coverage of a second orthogonal linear polarization path, which improves the total radiometer NETD by a factor of at least $\sqrt{2}$ as indicated in Chapter 4. With the designed radiometer, the main challenges for real-time passive imaging, namely output signal drifts, are analyzed to finally characterize the system NETD and demonstrate the first passive THz images recorded with an uncooled, silicon-integrated, LNA-coupled radiometer operating above 200 GHz.

6.1 Radiometer Implementation

The block diagram and the micrograph of the implemented dual-polarized radiometer are shown in Figure 6.1. The radiometer consists of a dual-polarized antenna, a 5-stage LNA with several modifications in each polarization path and a differential common-base detector circuit, implemented in the x2 device size (A_e = 2x0.96x0.1 µm^2), at each LNAs' output. The main challenge of the radiometer design is to provide a comparable system bandwidth, gain and NF, including all different building blocks to the standalone LNA.

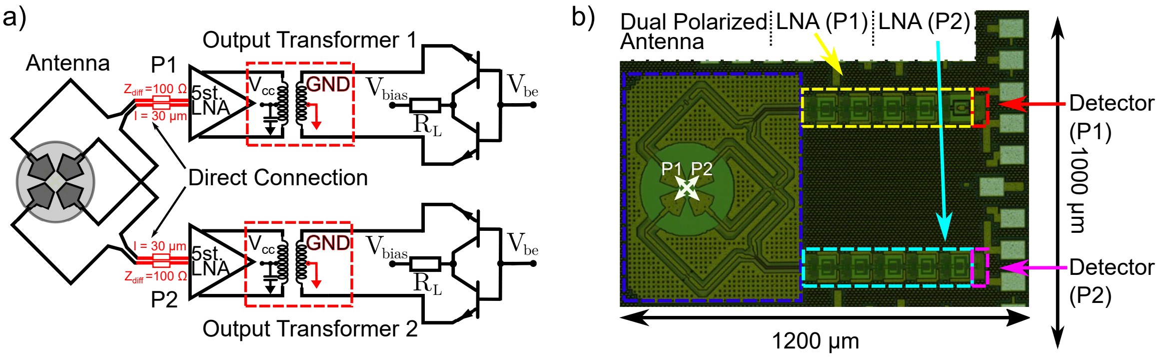

Figure 6.1: a) Radiometer schematic consisting of a dual-polarized antenna, a 5-stage LNA for each polarization path with differently tuned output matching transformers and a CB detector circuit implemented with x2 devices (A_e = 2x0.96x0.1 µm^2). b) Chip micrograph and dimensions of the dual-polarized radiometer.

The main differences of the radiometer LNA compared to the in Chapter 5 presented LNA breakout can be attributed to the input and output matching networks and are marked in red in Figure 6.1 a). Considering the input, the LNA of each polarization path is directly connected to the approximately pure real 100 Ω dual-polarized antenna through 100 Ω differential transmission lines without the input matching transformer of the LNA breakout. Regarding the output, two different output matching transformers were implemented, resulting in a separate LNA detector interstage matching for a slightly different frequency tuning of each polarization path. Furthermore, the detector ground path was provided through the center tap of the output matching transformer. Here, the input matching network and antenna combination directly influence the LNA NF. The output matching network is essential as it sets the radiometer thermal sensitivity and thus defines how much the detector output noise deteriorates the overall system performance. Due to the importance of both design tasks, they are further analyzed in detail in the subsequent sections.

6.1.1 Dual-Polarized Antenna

The implemented antenna is based on a previously published slot antenna [16], [189] ported to IHP's SG13G3 device technology. Here, minor modifications were included by removing parts of the fill structures to enhance the antenna radiation efficiency. The antenna is designed to illuminate a 9 mm (1.4 mm extension) hyper-hemispherical silicon lens through the backside of a silicon die. Similarly to the previous direct detector-coupled antenna versions, the radiator is implemented in the 12 µm thick BEOL stack on top of the 150 µm silicon substrate and stays DRC compliant.

The main radiating slot has two polarization paths (P1, P2). Each slot is excited by a pair of patch probes, located perpendicular to the slot perimeter, as shown in Figure 6.2 a). An additional ground plane is placed underneath each probe's feed lines. By differential antenna operation, only odd azimuthal modes along a circular slot are excited and a virtual RF short is created along perpendicular polarizations, allowing their independent function. A large fractional bandwidth is reached by exploiting the mutual coupling of all probes, an appropriate choice of probe spacing, edge length and the depth of the ground plane. The radiator probes are connected with two differential 900 µm long transmission lines, providing a mode conversion from the microstrip line configuration at the radiator to a grounded co-planar stripline connected to the differential input of the LNA.

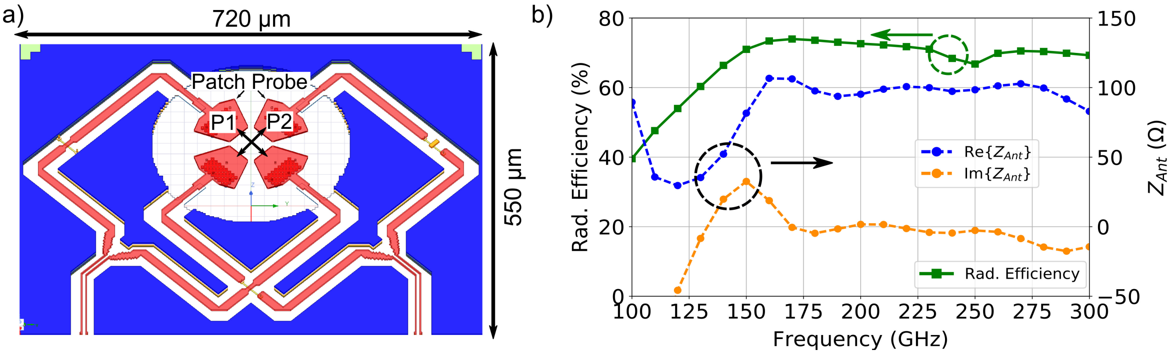

Figure 6.2: a) HFSS model and dimensions of the implemented dual-polarized antenna. b) Simulated antenna input impedance and radiation efficiency.

The simulated antenna radiation efficiency of the dual-polarized antenna on a silicon half-space radiating through the lossy silicon substrate and the simulated antenna input impedance are shown in Figure 6.2 b). The radiation efficiency is between 67 and 74 % in the frequency range of 150 to 300 GHz, while the input impedance ranges from (85 + j33) Ω at 150 GHz to (110 - j14) Ω at 300 GHz. As the variations in both polarizations are negligible, only the results for P1 are shown.

6.1.2 Input Matching Network

The LNA noise temperature T_{LNA} is one of the most critical design parameters for a total power radiometer as it is directly proportional to the system's NETD derived in Equation 2.47. Contrary to the LNA breakout, the radiometer input matching now depends on the realized antenna impedance shown in Figure 6.2. Furthermore, the realized NF is highly sensitive to the losses of the input matching network, which in the investigated breakout was implemented by the input matching transformer. Here, a direct antenna-LNA input matching co-design without an additional matching network might improve the system performance, avoiding the losses of a sophisticated input matching network.

To emphasize the choice of a proper input matching network, both Z_{Ant} and the output impedance of the breakout implemented input transformer when terminated with the antenna impedance ($Z_{Out,Trafo+Ant}$) are included in Figure 6.3 a) together with the LNA's 1 dB noise circles evaluated at 150 and 280 GHz. The impedance

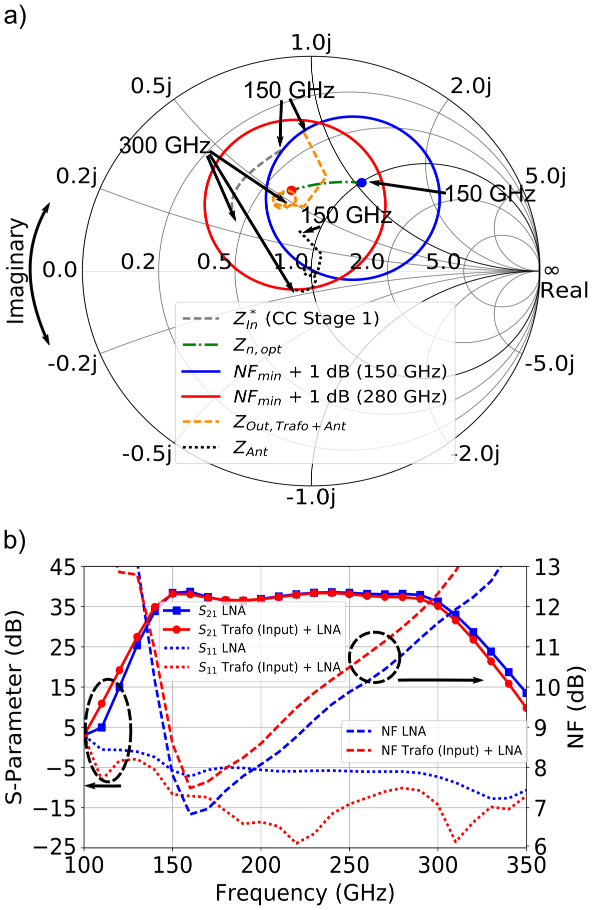

Figure 6.3: a) Simulated optimum LNA impedance conditions for minimum noise ($Z_{n,opt}$) and maximum gain ($Z^*_{In,CC1}$), including the realized antenna impedance Z_{Ant} trajectory without and with input transformer ($Z_{Out,Trafo+Ant}$).
b) Simulated LNA S_{11}, S_{21} and NF with and without input transformer (loaded with the antenna impedance).

trajectory $Z_{Out,Trafo+Ant}$ is close to the optimum noise impedance $Z_{n,opt}$ across the whole bandwidth. However, the ideal simulations do not account for implementation losses. Simulations considering these are gathered in Figure 6.3 b).

The input matching transformer provides an excellent input match with S_{11} below 10 dB from 150 to 350 GHz. Still, with 1.5 to 2 dB implementation losses from 111 to 283 GHz, the overall LNA gain, when loaded with 100 Ω differential output impedance, is comparable to the gain of the LNA connected to the antenna through a 30 µm long differential transmission line (Z_{diff} = 100 Ω). Furthermore, the minimum LNA NF improves by roughly 0.8 dB in the latter case, which converts in a theoretical system NETD improvement by 20 % according to Equation 2.47 without gain variations. For this purpose, the input matching transformer was not implemented in the radiometer system.

6.1.3 LNA Detector Matching

The detector to LNA interstage matching is crucial for the radiometer operation as it may limit the overall system bandwidth and maximum radiometer responsivity. Both LNA polarizations are intended to provide a slightly different frequency tuning to potentially analyze a black body's emitted frequency content. To realize this, two separate output impedance matching transformers, denoted as transformer P1 and P2, were designed for detector interstage matching by full-wave EM simulations and are shown in Figure 6.4 a). A central feature of both transformers is the supply of the detector DC ground path to the emitter nodes, as an additional RF choke would reduce the overall system bandwidth. This was implemented through common mode center taps at the transformer output metal layers to minimize the influence on the broadband differential LNA gain.

Transformer P1 is the same transformer already implemented in the LNA breakout and analyzed in Section 5.3.5. Compared to transformer P1, transformer P2 is implemented in the higher metal layers Metal 4 and Top Metal 2. This results in a weaker capacitive line coupling in the 150 to 300 GHz band and thus, an on-average two times increased imaginary part from 70 to 160 Ω at the LNA output node, which provides the detector input termination. At the same time, the real part increases by around 10 %. This is beneficial, as due to the high parallel output load of the cascode stage, including the core described in Section 5.2 a), a nearly constant pure real LNA output impedance approaching 100 Ω was not achievable, which is not necessarily requested for optimum detector operation. To ensure a broadband detector responsivity, the transformer-based LNA output impedances were designed with the help of constant detector responsivity contours for several detector bias points. These contours were

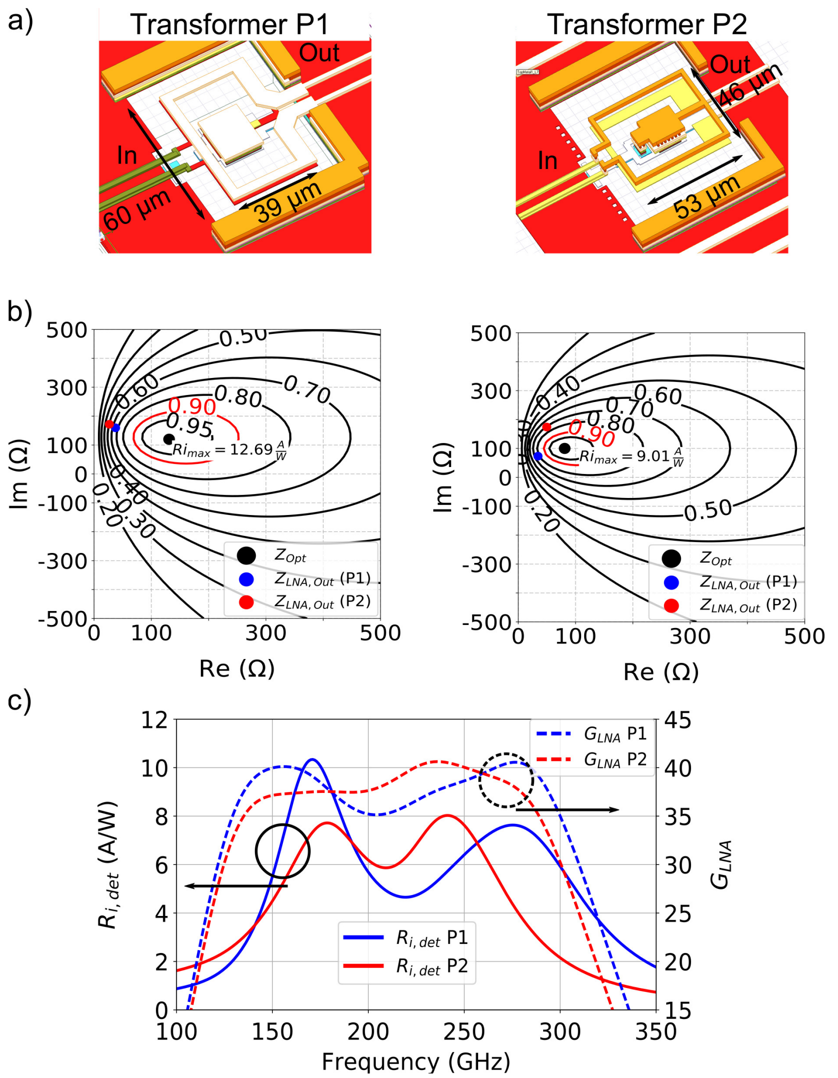

Figure 6.4: a) HFSS model view of the output transformers implemented in the radiometer polarization paths P1 and P2.
b) Constant responsivity contours for the implemented x2 detector biased in the forward-active region with V_{be} of 780 mV, including the HFSS core model and corresponding values for the realized LNA output impedances.
c) Simulated G_{LNA} with the LNA loaded by the differential detector input impedance and $R_{i,det}$ for the detector input terminated with the polarization-dependent LNA output impedance.

introduced in Section 3.5.4 and are exemplarily shown for the detector operated in the forward-active region with a $V_{be,det}$ of 780 mV in Figure 6.4 b) at 160 and 260 GHz. All contour simulations include the fully 3D-EM modeled detector core with proximity to the output matching transformer provided by 100 Ω differential transmission lines of around 10 µm length.

Restricted by the cascode core and its high Q output node, the realized LNA output impedances for both polarization paths lie above the 50 % maximum responsivity contour from 160 to 270 GHz. The realized simulated detector current responsivity

$R_{i,det}$, when loaded with the LNA output impedance for the whole bandwidth, is further shown in Figure 6.4 c), emphasizing a large 3 dB detector bandwidth from 140 to 280 GHz for polarization path P2 and 147 to 306 GHz for polarization path P1. Furthermore, the LNA gain with the output differentially terminated by the detector input impedance is gathered, approaching 40 dB for both polarization paths. By overlapping $R_{i,det}$ and G_{LNA}, it can be observed that the radiometer responsivity will peak at around 160 GHz in the first and 240 GHz in the second polarization path. Notably, the overlapping linear multiplication of both curves only indicates the maximum system responsivity, i.e., common mode terminations are not considered.

6.2 CW Measurement Setup

The verification of the LNA NEP and responsivity was done in a similar free-space measurement setup and procedure as introduced in Section 4.1 and shown in Figure 4.2. Minor modifications are discussed below. The dual-polarized radiometer chipset was glued to a 9 mm hyper-hemispherical silicon lens with an extension of 1.4 mm. To cover the frequency range between 110 and 325 GHz, the WR-6 and WR-3 VNA extension modules, described in Section 5.6, were included in the characterization setup, leading to a gap in the preceding measurement results between 180 and 200 GHz. Furthermore, the modules were coupled to waveguide attenuators and the free-space measurement distance was set to 50 cm to avoid system saturation due to too high input power levels.

Simulations for both polarizations proved the input power levels necessary for a linear operation. Corresponding results are shown in Figure 6.5 a) and indicate a system responsivity drop starting at power levels of -60 dBm at the LNA input. To allow enough headroom, a maximum input power at the lens surface P_{Lens} of -70 dBm was targeted by adjusting the waveguide attenuator levels. With the values set accordingly, P_{Lens} was calculated by the Friis transmission equation after de-embedding the measured antenna directivity, which is in between 21.7 dBi at 137 GHz and 24.1 dBi at 280 GHz and the attenuator losses from the PM4-calibrated output power of the VNA extension modules. The calculated P_{Lens} is frequency dependent and in the range of -85 to -70 dBm in the D-Band and -75 to -65 dBm in the J-Band as shown in Figure 6.5 b). The radiometer responsivity was de-embedded with Equation 4.1. Contrary to the previous detector measurements, the detectors implemented in the radiometer are operated only in the forward-active region, as the detector power consumption with bias currents less than 1 mA does not significantly contribute to the total radiometer power consumption. For this purpose, the detector was loaded with the same 1.83 kΩ load at the collector output as in the previous detector measurements. A more detailed description of the measurement setup is provided in Section 4.1.

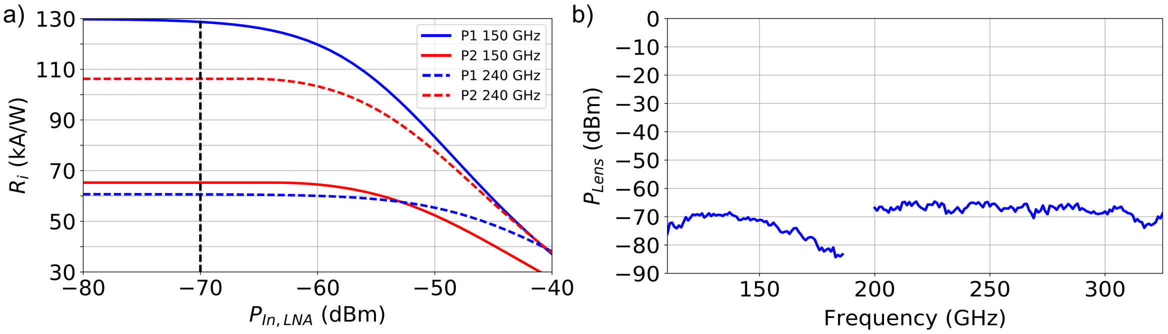

Figure 6.5: a) Simulated radiometer R_i vs. LNA input power at 150 and 240 GHz.
b) Calculated power at the lens aperture for the radiometer operated in the free-space setup with r = 50 cm.

6.2.1 Noise Measurements

Determining the radiometer NEP requires an accurate experimental characterization of all introduced noise components. This is necessary, as the noise self-mixing process cannot be simulated by Harmonic Balance simulations. This effect can only be simulated in the time-domain. Due to the complex LNA core and passive modeling, including several s-parameter file re-imports into the circuit simulator, time-domain simulations lack the required accuracy and are very time-consuming. Therefore, the measured detector output voltage noise spectral density is presented in Figure 6.6 a) for both polarization paths vs. detector bias point and b) vs. (chopping) frequency. Most important to note is that the radiometer noise floor with values around 1.25 to $1.5\,\mu V/\sqrt{Hz}$ at 780 mV $V_{be,det}$ is at least a factor of 20 higher than the noise floor of the standalone detector. Thus, v_n is mainly determined by the LNA. An increasing v_n with $V_{be,det}$ (at 300 Hz) is observed in Figure 6.6 a), due to its linear dependence to the detector responsivity $R_{v,det}$ as indicated in Equation 2.43.

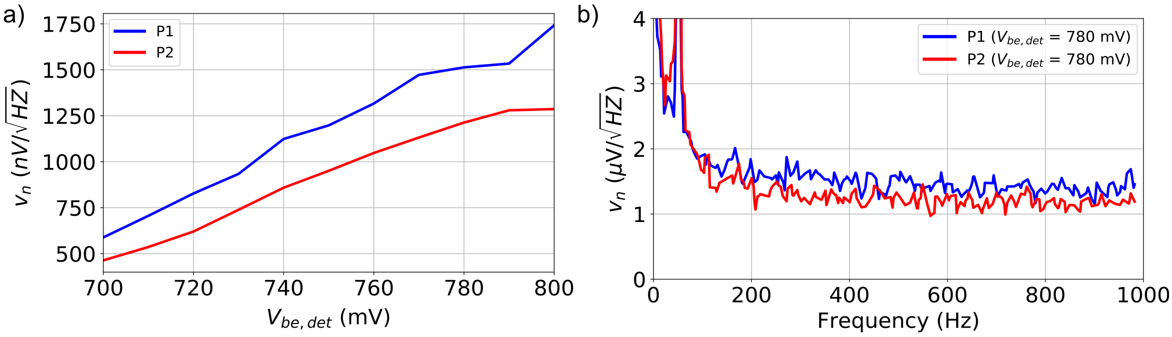

Figure 6.6: a) Evolution of the measured radiometer output noise voltage spectral density v_n for different detector bias points in the forward-active region ($V_{ce,det} = 1$ V).
b) v_n vs. chopping frequency with $V_{be,det} = 780$ mV.

The flattened curve towards 800 mV $V_{be,det}$ can be explained by the complex interstage matching impedances that cause a lower LNA gain at these bias points. Another important observation can be made regarding the spectral trend of v_n shown in Figure 6.6 b) for a selected detector bias of 780 mV. Here, it becomes visible that the radiometer noise floor is white with a very low 1/f noise corner frequency in the range of 100 Hz. Nevertheless, the low-frequency noise may be mainly influenced by the bias network, showing a strong 50 Hz peak.

6.2.2 CW Measurement Results

To evaluate the radiometer performance towards passive imaging, the frequency- dependent NEP and responsivity trends were investigated for several detector bias points spanning from 700 to 800 mV $V_{be,det}$. The evolution of the measured and simulated radiometer responsivity and the corresponding measured NEP are shown in Figure 6.7 a) and b) for a selected detector bias point of $V_{be,det} = 780$ mV. Regarding the radiometer voltage responsivity $R_v(f)$, a good measurement-simulation correlation can be noted with typical deviations in the range of 3 dB, mainly defined by the lower measured LNA gain shown in the previous LNA measurement Section 5.6.1. A maximum radiometer responsivity of 62 MV/W at 149 GHz and 54 MV/W at 249 GHz was measured for polarization P1 and P2 with corresponding minimum NEP values ranging from 25 to $22 fW/\sqrt{Hz}$, respectively. With a nearly identical maximum responsivity, the difference in NEP for P1 and P2 can be attributed to different LNA NF in both polarization paths, as for the measurements, two different chip samples, one for P1 and another one for P2, were used.

The system NETD depends on the equivalent system NEP and its evaluated equivalent bandwidth B_{eq} according to Equation 2.33 or equivalently on the thermal responsivity $R_v(T)$ as shown in Equation 2.29. Therefore, the previously mentioned equations were used to estimate the radiometer NETD and $R_v(T)$ based on the measured CW frequency trends as indicated in Figure 6.7 a). The calculated equivalent radiometer bandwidth is 147 GHz (P1) and 134 GHz (P2) for the chosen $V_{be,det}$ of 780 mV. The corresponding calculated NETD measured in a 1 Hz bandwidth is shown in Figure 6.7 c). With values of 23 mK for P1 at 150 GHz and 19 mK for P2 at 230 GHz, a minimum NETD smaller than 25 mK is indicated for both polarizations, which is almost constant across the detector operating point. This behavior underlines that the LNA parameters gain, NF and bandwidth define the radiometer sensitivity. In this case, the last term of Equation 2.47 can be omitted for NETD calculation. To estimate the real-time NETD, an integration time of $\tau_I = 25$ ms, equivalent to 40 fps was assumed. According to Equation 2.47, the NETD calculated in a 1 Hz bandwidth has to be multiplied by a factor of 4.47 $(1/\sqrt{2\tau_I})$, resulting in a calculated real-time NETD of 85 mK (P2) and 103 mK (P1). The calculated thermal responsivity depends on the detector responsivity and increases with $V_{be,det}$. $R_v(T)$ values above 60 $\mu V/K$ were calculated for both polarizations.

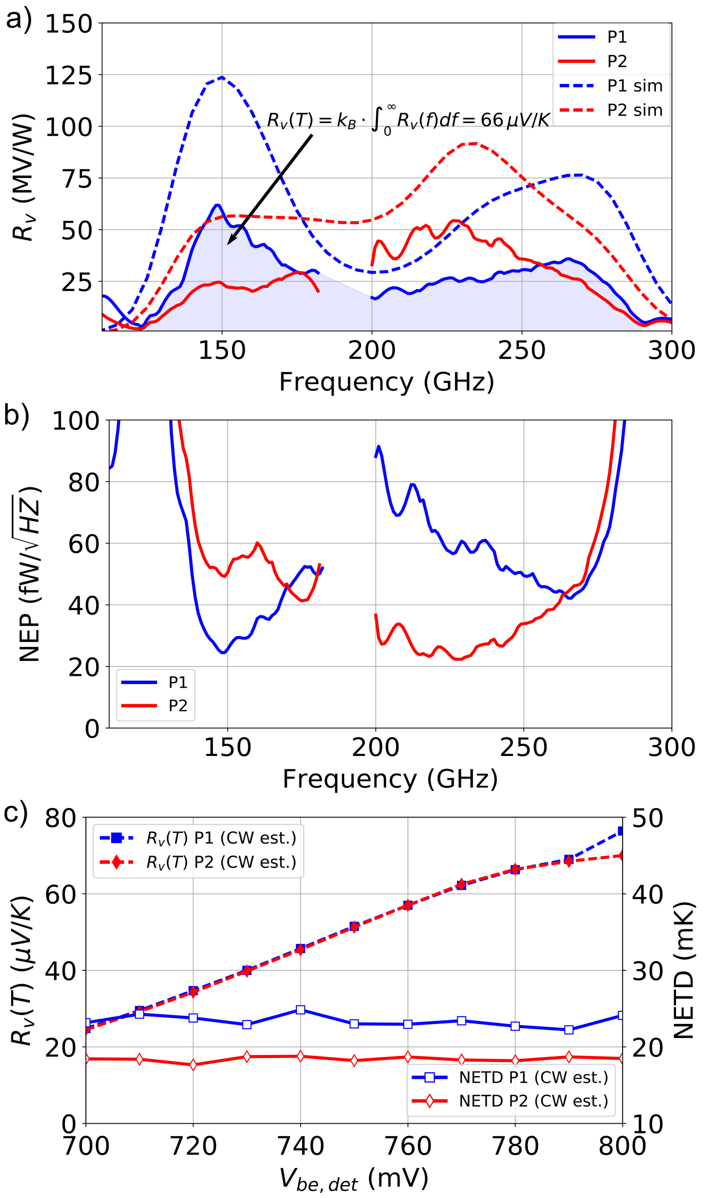

Figure 6.7: a) Measured radiometer voltage responsivity R_v.
b) Measured radiometer NEP.
c) Calculated thermal responsivity and NETD in a 1 Hz readout bandwidth.
A detector bias point of 780 mV $V_{be,det}$ was chosen in the forward active region.

The estimated system NETD based on the CW measurements only indicates the maximum possible system performance under ideal conditions. Especially the attenuator de-embedding and the directivity calculations are prone to errors. Therefore, the radiometer NETD was characterized in a real-time measurement setup and the measured NETD is compared to the CW-measurement-based estimations.

6.3 NETD Characterization

A real-time NETD characterization of a system with a theoretical NETD of around 100 mK is challenging due to the high system complexity with possible drifts in several NETD-relevant system parameters that influence the system's 1/f noise. These drifts are analyzed in the following to clarify if an accurate NETD characterization is possible without an external optical chopper relying only on DC measurements. This would be the case when the occurring drifts show a very slow time variation in the order of several tens of seconds or a repetitive frequency pattern. Then, the radiometer can be re-calibrated, pointing to a stable reference temperature in a given period.

6.3.1 Measurement Challenges

To measure all parasitic drifts of the radiometer output signals in the time- and frequency domain, for the following analysis, a 16-bit National Instruments USB 6366 analog to digital converter (ADC) with a maximum sampling rate of 2 mega samples per second (MS/s) and an input impedance of 100 GΩ was connected to the radiometer output instead of the amplifier-coupled spectrum analyzer. Due to the large estimated thermal responsivity above 60 $\mu V/K$, the external voltage amplifier at the system output was removed, as it deteriorates the output SNR. With a theoretically calculated real-time NETD around 100 mK, several additional interdependent factors need to be accounted for in real-time measurements. Crucial are gain variations or temperature drifts as they influence the long-term radiometer stability and directly affect the measurable NETD.

These factors and their influence on the NETD measurements are emphasized by time-domain, frequency-domain and temperature measurements of the lens-coupled radiometer chipset with the input signal determined by the laboratory temperature. All measurement results are gathered in Figure 6.8. A long and short-term measurement of the radiometer output voltage V_{Out} were performed for the frequency- and time-domain analysis. In the short-term measurement, 2 million samples were captured with a sampling rate of 100 kilo samples per second (kS/s) and a resolution bandwidth of 100 mHz. For the long-term measurement, a sampling rate of 40 S/s (fps) was chosen, and 2^{21} samples were recorded for 14 hours and 33 min, resulting in an approximately 20 Hz frequency resolution. The measurements were performed with polarization P1 and the detector biased in the forward-active region supplied by a V_{ce} of 543 mV and a V_{be} of 760 mV, with 3 V LNA V_{cc}.

- **I - Radiometer (Gain) Drift and Detector RTS Noise**: Radiometer output signal drifts can be easily observed in the long-term time-domain measurement focusing on the minute time scale. In Figure 6.8 I a), a 60 min extraction of the

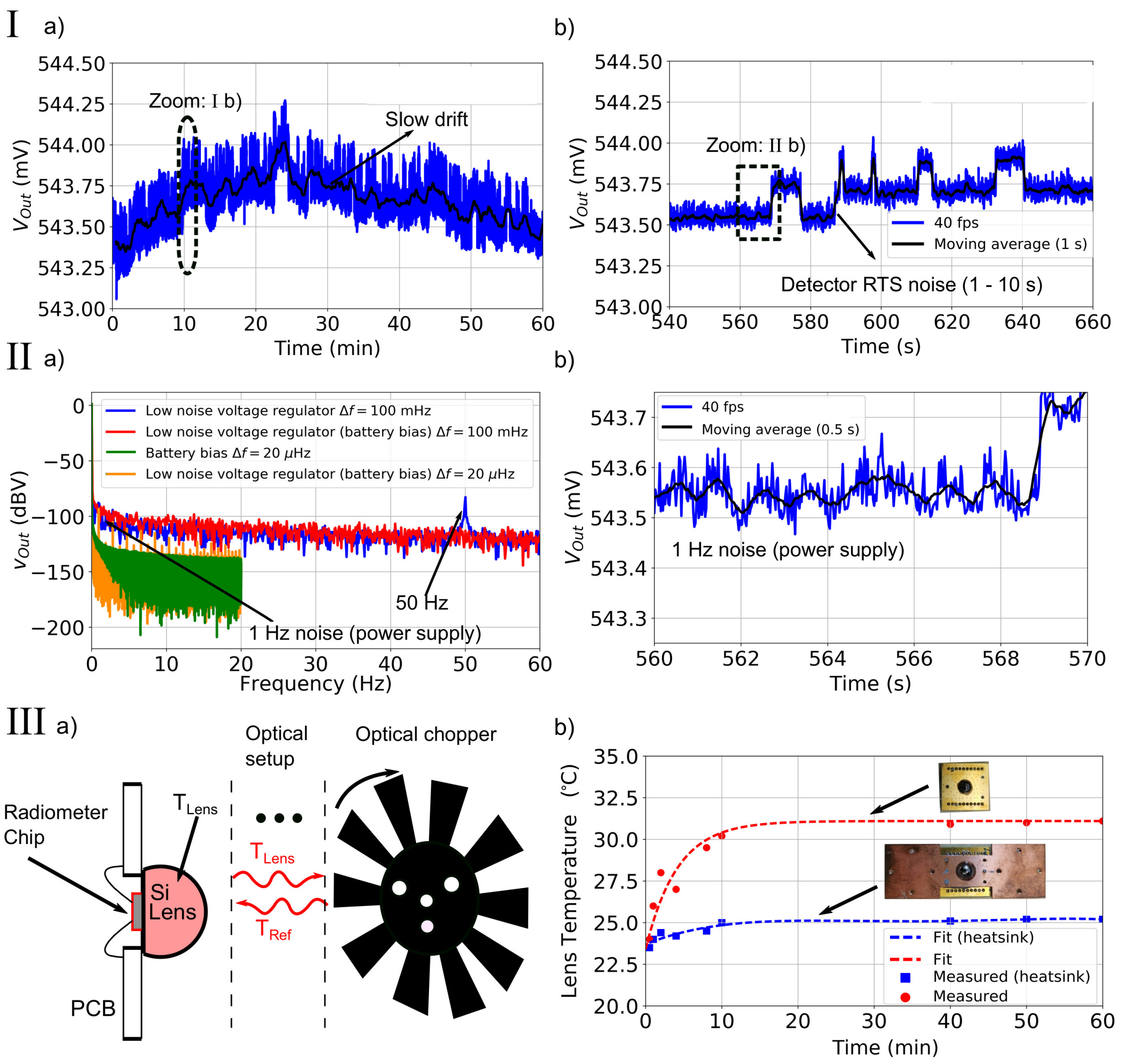

Figure 6.8: Challenges for real-time radiometric characterization.
I Influence of the bias network.
a) Frequency domain (long+short-term). b) Time domain (short-term).
II Slow signal drift and detector RTS noise in the time domain.
a) Short-term. b) Long-term.
III Thermal heating of the lens aperture.
a) Temperature measurement. b) Reflection of T_{Ref} in the optical setup.

long-term time-domain measurement is shown. The moving average indicates a slow output signal drift of around 100 µV per 10 minutes, which can be easily calibrated if the radiometer pinpoints to a stable temperature reference, i.e., each 30 s. However, this long-term drift is overlayed by short signal pulses in a time-frame of typically around 1 to 10 seconds. These short pulses have a nearly constant peak-to-peak amplitude of around 200 µV and randomly appear in the time-domain output signal. Therefore, they cannot be overcome by a simple calibration method. Further measurements of the standalone detector with the unbiased LNA showed similar output voltage fluctuations. Thus, their origin was found in the detector circuit. Such behavior is comparable to the reported random telegraph noise (RTS) for SiGe HBTs [190], which for the investigated technology appears within several milliseconds and is caused by slight variations of the detector base-emitter voltage [100].

The main drawback from the system perspective is that small changes in the base-emitter voltage directly affect the radiometer responsivity. They can be equivalently seen as gain variations ΔG introduced in Equation 2.47. Unfortunately, these variations propagate multiplicatively through all radiometer system parts, contrary to the usually observed additive noise at single LNA stages [86]. In other words, the contributions of the detector responsivity variations are equally critical as the additionally appearing LNA gain variations. Further, they cannot be suppressed by LNA designs with an increased total gain. In summary, a signal difference of 200 µV introduced by the detector RTS noise is equivalent to a temperature difference of 3 K, which is not tolerable with an estimated NETD around 100 mK and cannot easily be compensated. A possible method of minimizing this effect is fast optical chopping with the radiometer pointing to a temperature reference in a time-frame of several milliseconds.

- **II - Bias Network**: Another possible reason for radiometer signal drifts is based on slow LNA or detector bias point variations caused by bias network instabilities or the presence of a parasitic 50 Hz signal amplitude coupled through the global power supply network [191] to the DC power supply. This 50 Hz signal causes errors when measuring low signal levels close to the ADC resolution or using optical chopping frequencies below 100 Hz. This effect is highlighted by the blue curve corresponding to the measured short-term frequency spectrum shown in Figure 6.8 II a). It could be overcome using battery-biased, low dropout linear voltage regulators LT3042 from Analog Devices combined with an 11-element external LC low-pass filter for LNA and detector biasing (red curve). This filter provides a simulated cut-off frequency of 15 Hz for low impedance input and detector output load conditions. However, the frequency spectrum corresponding to the long-term measurements with the battery-biased voltage regulator indicates the appearance of 1 Hz peaks in the voltage regulator output spectrum, which should not be interchanged with radiometer 1/f noise. A spurious free output spectrum could only be achieved with a fully battery-biased detector circuit. This is an unfeasible option due to the constant battery discharge during the measurement period, contributing to radiometer signal drifts.
- **III - Radiometer Lens and Reference Temperature**: Slow radiometer output signal drifts are often referred to ambient or system temperature variations. The LNA power consumption above 160 mW increases the radiometer chip tem-

perature and further results in parasitic heating of the connected silicon lens, influencing the minimum detectable object temperature. This effect is present in the black body characterization setup with an optical chopper located close to the source, shown in Figure 4.11 and indicated in Figure 6.8 III a). The optical chopper metal blades reflect the radiated lens temperature through the mirror setup. In other words, the reference temperature T_{ref} depends on T_{Lens}, when it is higher than the ambient room temperature. Furthermore, also the chopping blades may heat up and result in a shift in reference temperature.

To quantify the parasitic lens heat effects, T_{Lens} was recorded with a FLIR T450sc IR camera over a 60 min time-span, with first only a single polarization path biased. The corresponding results are shown in Figure 6.8 III b). The sample was investigated with a lens connection to a copper heatsink which minimizes the parasitic lens heat. In total, the copper heatsink reduces the lens temperature T_{Lens} by more than 5 to 25 °C, which is above the ambient room temperature of approximately 23 °C. To avoid the lens heating effects, especially if both polarizations are used, a Peltier cooling system was mounted on the heatsink to regulate the lens temperature externally.

All previous effects have to be considered when the radiometer is implemented in a real-time measurement setup. Primarily due to the high LNA gain and system responsivity in the range of 50 MV/W across the whole bandwidth, small signal drifts result in detector signal variations that are comparable to 1 K temperature drifts, making the following NETD measurements with the black body source extremely sensitive and underline the need for an optical chopped system.

6.3.2 Broadband Black Body Characterization

To characterize the radiometer NETD, the same focused mirror setup with a tunable black body source was used as described in detail in Section 4.2 and shown in Figure 4.11 a). Only the differences to the previously described setup are introduced in the following. Due to the high LNA gain and the bandwidth between 100 GHz and 300 GHz, no IR filter was included in the optical path. A minimum black body aperture of 22.2 mm resulted in a nearly homogeneous lens illumination with black body radiation. However, the signal levels at the lens border decreased by roughly 0.5 dBV. By integrating across the whole lens aperture, a lens fill factor of 97 % was found that was de-embedded from the consecutive measurements. All measurements were performed with a mechanical chopping of the black body emission and the chopping factor of $\sqrt{2}/\pi$ was de-embedded. 30 and 300 Hz were used as chopping frequencies, both showing the same measured $R_v(T)$ values.

To de-embed $R_v(T)$, the output radiometer voltage slope was measured with increasing black body temperature from 50 to 500 °C for different detector base-emitter voltages $V_{be,det}$ in the forward-active region. Corresponding results for both polarizations are shown in Figure 6.9 a) and b) for two chosen detector bias points of 720 and 780 mV.

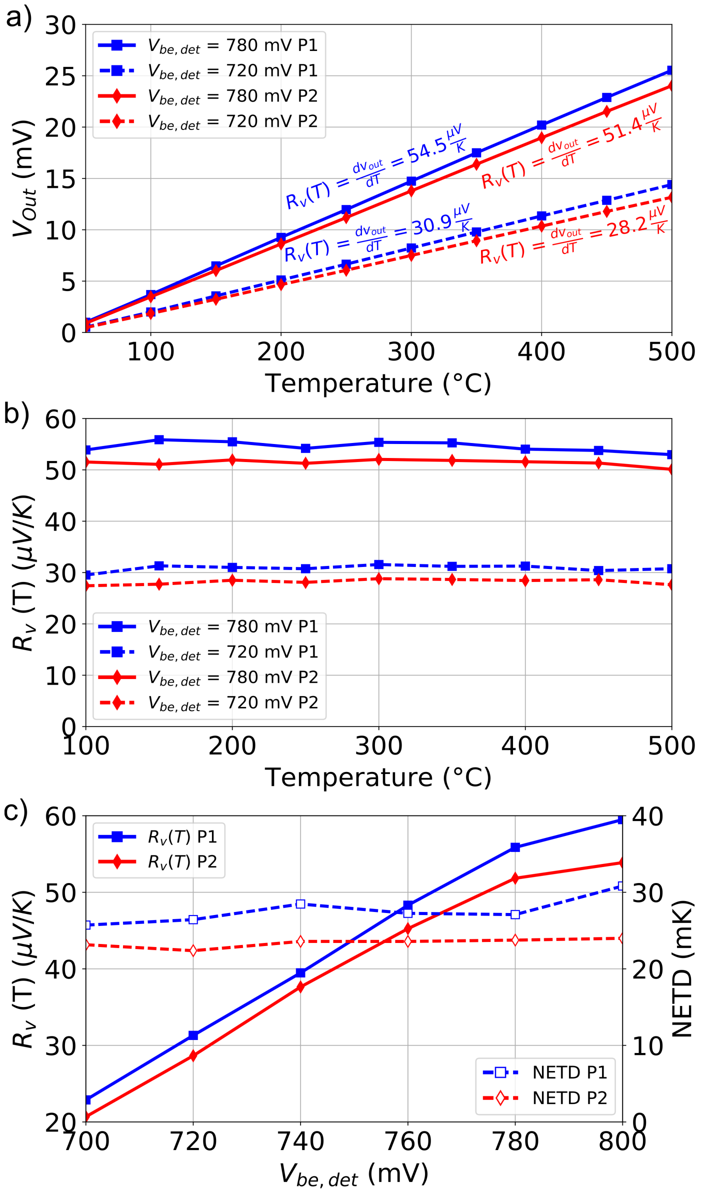

Figure 6.9: a) Measured radiometer output voltage vs. black body temperature.
b) Calculated radiometer $R_v(T)$ deviations vs. black body temperature.
c) Calculated $R_v(T)$ and NETD in a 1 Hz readout bandwidth vs. $V_{be,det}$.
The detector was biased in the forward-active region.

For temperatures approaching 100 °C, signal levels around 4 mV were measured without an external amplifier. Another important aspect is highlighted in Figure 6.9 b) showing a constant $R_v(T)$ in the whole temperature range for both polarizations with a deviation of roughly 5 % among each other. This, firstly, indicates that the radiometer is not driven into saturation up to temperatures of 500 °C. Secondly, it stresses that the parasitic heat due to the IR part of the black body spectrum is sufficiently dissipated among the used copper heatsink. In total, a lens temperature increase of around 1 K was measured during the black body temperature sweep. Small variations in the curve are based on the temperature accuracy of the black body source specified to be ±0.5 K.

Finally, Figure 6.9 c) shows the measured $R_v(T)$ and NETD in a 1 Hz readout bandwidth depending on $V_{be,det}$. In general, the same trends as calculated based on the CW measurements shown in Figure 6.7 c) can be observed. The de-embedded $R_v(T)$ measured in the black body setup is 10 to 15 % smaller. This is mainly based on the attenuator de-embedding procedure and the 180 to 200 GHz frequency band, which could not be measured with the available VNA extension modules and were linearly interpolated for the estimation of $R_v(T)$. With less than 1 dB deviation, both procedures correlate very well in de-embedding the radiometer thermal responsivity. In total, the measured NETD is constant across detector base-emitter voltage and ranges from 23 mK for P2 and 27 mK for P1 in a 1 Hz bandwidth, translating to an excellent real-time NETD of 102 to 120 mK for a frame rate of 40 fps.

6.4 Real-Time Passive Imaging

Previously, it was derived that chopping is necessary for the radiometer operation with optimum NETD performance. However, hot objects with a temperature difference causing higher output signals than the equivalent RTS noise amplitudes and signal drift values in the ±200 µV range can still be detected in a simple DC measurement setup without chopping. To demonstrate real-time passive imaging, first, a human finger with a temperature T_{Finger} of approximately 35 °C was constantly moved in a line directly in front of the radiometer to avoid any spillover losses of the mirror system. The corresponding output signal was recorded with an ADC sampling rate of 100 kS/s in a time-frame of 10 s and is shown in Figure 6.10.

The emitted radiation of the finger in the radiometer bandwidth results in a signal drop of roughly 800 µV, which well corresponds to a temperature difference of roughly 14 K to the ambient room temperature according to Figure 6.9 a) assuming an emissivity above 95 % [192]. This signal drop is only visible with averaging applied. In the presented plot, a number of consecutive samples were averaged, resulting in a reduction of the overall sampling rate and thus a reduced rms noise voltage $v_{n,rms}$. This technique is equivalent to an increase in integration time. When comparing the radiometer output signal without averaging, $v_{n,rms}$ is 940 µV, which divided by $R_v(T)$ corresponds to a NETD of approximately 17 K. With an average of 10000, 10 S/s are recorded and $v_{n,rms}$ drops to 24 µV with a corresponding NETD of 440 mK. This is roughly eight times higher than the previously calculated values, as $v_{n,rms}$ contains the

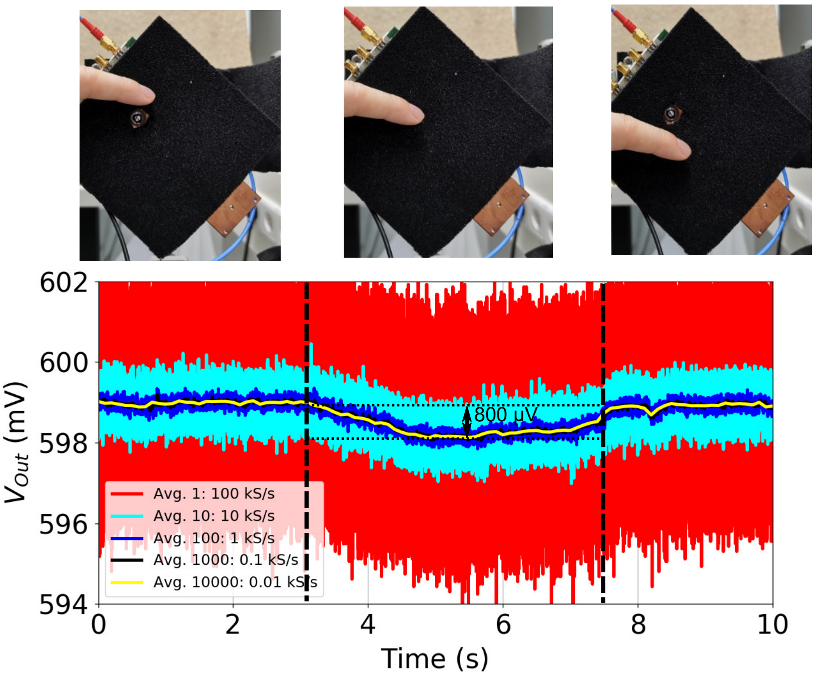

Figure 6.10: Measured radiometer output voltage in the time-domain with and without averaging. A human finger with a temperature of approximately 35 °C was linearly moved in front of the radiometer.

influence of all 1/f noise components, when evaluated without chopping. Nevertheless, as the blue, black and yellow curves demonstrate, a human finger is clearly visible within a DC readout and 100 to 1 ms integration time (10 to 1000 S/s).

For a further demonstration of passive imaging under ideal operating conditions, the finger was positioned on a 3D motorized xyz translation stage in the optical mirror setup placed at the optimum black body position and then raster-scanned with a chopping frequency of 300 Hz applied. A scan window size of 50 mm and a scan resolution of 2.5 mm, which is well below the lens aperture size that has to be filled entirely with black body radiation for minimum NETD operation, were chosen. The chopped signal was read out at each position after a fast Fourier Transformation (FFT) with a sampling rate of 2 MS/s. 131072 samples were captured per data point. After applying a flat-top window function, the signal amplitude was further read-out, resulting in a 57 Hz equivalent noise bandwidth. The system-defined real-time data-point acquisition takes approximately 65 ms, theoretically leading to a total image acquisition time of 28 s. Due to the limited motor speed with a point-to-point movement time larger than 1 s, the total raster-scanning time was approximately 10 min. The recorded passive THz images of the finger are shown in Figure 6.11. Two images were captured, with and without covering by a cardbox of 1 mm thickness. For comparison, visible and IR images of the finger are included in this figure.

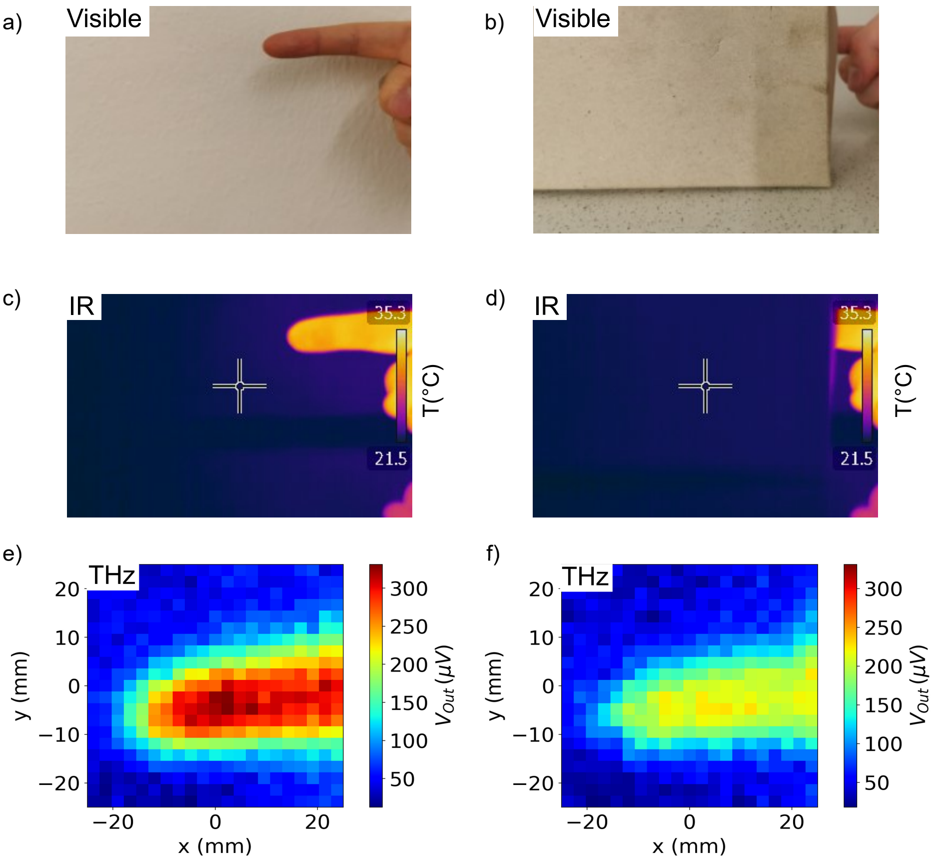

Figure 6.11: Visible, IR, and passive THz images of a human finger ($T_{Finger} \approx 35°C$).
a) Visible image.
b) Visible image of the cardbox-covered finger.
c) IR image.
d) IR image of the cardbox-covered finger.
e) Passive THz image.
f) Passive THz image of the cardbox-covered finger showing a 30 % signal drop. The cardbox thickness is 1.0 mm.

Most important to note is the maximum linear SNR of 26.5 in the THz image of the uncovered finger. The maximum signal amplitude of 720 µV with the chopping factor de-embedded further corresponds to a measured temperature difference of roughly 13.2 K to the ambient room temperature, when divided by the thermal radiometer sensitivity that was presented in Figure 6.9 c). With cardbox covering, the amplitude reduces only by 30 %, indicating an at least 50 % lower cardbox signal attenuation in the 100 to 300 GHz band than previously shown in the passive THz images with direct detector operating above 300 GHz in Section 4.2.4. In summary, an excellent ability for detecting concealed objects, i.e., under clothing in a real-time scenario, is indicated.

6.5 Summary, Conclusion and State-of-the-Art

This chapter introduces the design and measurement challenges of a dual-polarized radiometer with more than 100 GHz RF bandwidth. The previously described LNA and common-base detector circuits are utilized for the design. With the major building blocks available, the critical design parameters are the radiometer input and output matching networks. Based on the analysis of the LNA noise circles and the detector constant responsivity contours, it is shown that a direct transmission line coupling of the broadband 100 Ω dual-polarized antenna results in a 0.5 dB improved NF without using the input matching transformer utilized in the LNA breakout. For output matching, two different output matching transformers were designed in both polarization paths, realizing a slight frequency tuning. Furthermore, an analysis of the contours of constant detector responsivity showed that the output impedance of both transformers already allows a broadband detector LNA matching with less than 3 dB R_v losses across the whole operation band simulated from 130 to 280 GHz.

To evaluate the radiometer NETD, it was packaged with a 9 mm hyper-hemispherical silicon lens, characterized in a free-space measurement and a focused 2f mirror setup with a black body temperature source. In total, a minimum NEP of 25 and 22 fW/$\sqrt{Hz}$ and a maximum responsivity of 62 MV/W were measured in the free-space measurement setup for polarizations P1 and P2 with corresponding equivalent RF bandwidths of 147 GHz and 134 GHz centered around 200 GHz in a 1 Hz noise bandwidth. An extensive radiometer noise analysis was performed in the time- and frequency-domain to emphasize the challenges of real-time passive imaging. The primary outcome of this analysis is that the radiometer signal drifts based on temperature, gain and bias variations, as well as detector RTS noise prevent sub-Kelvin NETD resolutions, even when the radiometer pinpoints to a stable reference in a minute timescale. This can be overcome with optical chopping. However, the in-built optical chopper metal blades do not serve as a stable temperature reference, as they not only heat up while rotating but further reflect the THz radiation caused by the parasitic lens heating due to the chip power consumption of more than 160 mW. A copper heatsink and an optional Peltier element were implemented to minimize this effect.

With this knowledge, the radiometer NETD and thermal responsivity were measured for different detector bias points in the forward-active region by temperature sweeps of the black body source applied from 50 to 500 °C with a chopping frequency of 300 Hz. In total, a minimum NETD of 27 mK for P1 and 23 mK for P2 was measured in a 1 Hz bandwidth, as well as a thermal responsivity of up to 60 µV/K for P1 and 54 µV/K for P2. By scaling with a factor of $1/(\sqrt{2\tau_I})$, an excellent real-time NETD of 120 mK for P1 and 103 mK for P2 is achieved. The NETD values stay constant across the detector base-emitter bias voltage and indicate that the LNA gain, NF and RF bandwidth mainly define the minimum radiometer NETD. The NETD was further calculated as an integration of the measured RF voltage responsivity curves and shows only a deviation of roughly 15 to 20 %, which can be attributed to a gap in the CW measurements and the de-embedding of the attenuators necessary to avoid radiometer saturation in the free-space CW measurements.

The state-of-the-art of silicon-integrated radiometers is further shown in Table 6.1. The implemented radiometer circuit is the first silicon-integrated radiometer that achieves a bandwidth of more than 100 GHz and a center frequency above 200 GHz. Based on the large bandwidth that compensates for the LNA NF increase towards higher frequencies above 200 GHz, it is the first antenna-integrated, fully-packaged radiometer that achieves a calculated real-time NETD of down to 100 mK in a 25 ms integration time in the investigated frequency band.

Finally, passive images of a human finger were recorded by motorized raster-scanning of the packaged radiometer with a sampling rate of 15 fps. Additionally, the same measurement was performed through a conventional cardbox with a thickness of 1 mm, resulting in only 30 % signal drop. This way, the radiometer's excellent suitability for passive detection of concealed objects in a real-time environment is demonstrated. Currently, the image acquisition time is only limited by the movement time of the used stepper motors.

Table 6.1: State-of-the-art of silicon-integrated radiometers with LNA pre-amplification in the mmWave and THz frequency range

f_{center} [GHz]	B [GHz]	$R_{v,sys}$ MV/W	Min. NEP_{sys} [fW/$\sqrt{Hz}$]	G_{LNA} [dB]	NF_{LNA} [dB]	P_{DC} [mW]	τ_I [ms]	NETD [K]	Antenna Integration	Reference
56	6	61	3.2	28	5.3	42.5	-	-	No	[83]
86	10	16	7.6	35	8.9	102	20	1	No	[184]
90	18	0.666	36	36	6	110	30	1.1	No	[185]
91	8	166	1.9	40	7.6	28.5	30	0.21	No	[186]
91.5	15	5	21	23	8	34.8	30	0.83	No	[78]
92.5	35	59	4.8	34.5	6.2	23.9	30	0.1	No	[187]
94	15	0.77	430	16.9	5	10	30	0.47	No	[57]
94	26	43	10	30	9.7	200	30	0.4	No	[88]
100	-	-	-	32	6.9	196	20	0.43	Yes	[55]
115	40	6.4	7.1	29	6.1	25	30	0.12	No	[56]
130	51.4	688	9.3	33	4.8	33.8	30	0.13	No	[193]
136	11.8	52	1.4	36	7.38	47.2	3.125	0.25	No	[188]
140	21	0.6	53	31	8.8	152	30	1.5	No	[194]
165	10	28	14	$\geq$35	8.24	95	3.125	0.25	No	[76]
206.5	**147**	**62**	**25**	$\geq 34^{\dagger}$	$\geq 7.1^{\dagger}$	$\geq 160^{\dagger}$	**500/25**	**0.027/0.120**	**Yes**	**This Work P1**
204.5	**134**	**54**	**22**	$\geq 34^{\dagger}$	$\geq 7.1^{\dagger}$	$\geq 160^{\dagger}$	**500/25**	**0.023/0.103**	**Yes**	**This Work P2**

† Estimated from LNA measurements.

Chapter 7

Conclusions and Outlook

7.1 Conclusion

This thesis describes the design, analysis and measurement of uncooled, silicon-integrated direct detection receivers for passive imaging in the THz frequency range. It focuses on two approaches: I) Antenna-coupled direct detectors with and II) without LNA pre-amplification. Although passive imaging has already been demonstrated in this frequency range, especially above 200 GHz, most systems rely either on bulky III-V components or are implemented based on microbolometers with cryogenic cooling. However, silicon technologies offer a practical, low-cost integration of radiometer systems, including mixed-signal capabilities towards miniaturized systems-on-chip for applications in security screening or radio astronomy. These applications further benefit from the inherent see-through capabilities of THz radiation. Thus, commercially available passive imaging cameras operating in the IR region can be potentially outperformed by silicon-integrated circuits operating in the THz frequency range.

To understand the design challenges of passive THz imaging systems in silicon, first, its theoretical fundamentals are derived in this dissertation starting from the well-known Planck's law, resulting in system design objectives allowing a NETD smaller than 1 K in both approaches. The focus is set on the development and analysis of broadband THz direct detectors, LNAs and a total power radiometer operating above 200 GHz in advanced SiGe HBT technologies with f_t/f_{max} of 350/550 and 450/670 GHz, to achieve these challenging design objectives. The major outcomes of this dissertation are highlighted below.

Direct Detector: Based on a nonlinear equivalent model, the theoretical bandwidth and sensitivity limitations, as well as the optimum bias and matching conditions for THz direct detectors consisting of differential common-base detector circuits, were investigated. The gained knowledge was used for the co-design of five different single- and dual-polarized, antenna-coupled direct detectors, packaged with a 3 mm diameter, hyper-hemispherical silicon lens and fully characterized in the 200 GHz to 1 THz frequency range. All detectors achieve a state-of-the-art performance with a maximum voltage responsivity of up to 13 kV/W and a minimum NEP down to 1.9 pW/$\sqrt{Hz}$, which equals a constant equivalent NEP of 3.7 pW/$\sqrt{Hz}$ within a 500 GHz operation bandwidth spanning from approximately 300 to 800 GHz.

Broadband LNA: Funded in an accurate device model, including the full-wave EM simulation of the transistor core and the used distributed coupled-line matching structures, a 5-stage differential amplifier was designed for integration in a total power radiometer and characterized by on-wafer measurements. The LNA provides a maximum gain of 34.6 dB and a 3 dB bandwidth of 146 GHz with an operating frequency range from 131 to 277 GHz with a NF of 8.4 dB at 155 GHz that increases to 12.5 dB at 260 GHz including the losses of the connecting baluns. With this performance, the implemented LNA exceeds the current state-of-the-art of silicon-integrated LNAs in terms of gain and bandwidth, potentially allowing a real-time NETD of 20 to 60 mK.

Total Power Radiometer: Funded in the detector and LNA performance analysis, a dual-polarized radiometer was designed that specifically focused on preserving the large bandwidth, high gain and minimum NF operation, combining the LNA and detector implementations with a dual-polarized antenna. The designed radiometer was packaged with a 9 mm hyper-hemispherical silicon lens and evaluated in a freespace measurement setup from 100 to 300 GHz. In total, the radiometer achieves a maximum responsivity of 62 MV/W at 150 GHz in the first polarization path and a minimum NEP of 22 fW/$\sqrt{Hz}$ at 230 GHz in the second polarization path and an equivalent bandwidth of up to 147 GHz. It is the first silicon-integrated total power radiometer that operates above 200 GHz and provides a bandwidth of more than 100 GHz.

All presented integrated and packaged circuits currently provide a state-of-the-art performance.

The radiometer and direct detector thermal responsivity and NETD have been further investigated in an optical measurement setup with a black body source. Here, a NETD below 1 K has been demonstrated with SiGe HBT direct detectors and an integration time of 500 ms for the first time. In the radiometer implementation, an excellent state-of-the-art NETD approaching 100 mK was calculated in an integration time of 25 ms, allowing real-time passive imaging. Due to the single-pixel implementations, passive imaging has been demonstrated by raster-scanning of several objects, where the motor movement speed mainly limits the image acquisition time. Passive images of a 100 °C hot resistor have been recorded with direct detectors, while a human finger has been imaged with the radiometer. In both cases, the images were taken with and without covering by a conventional cardbox item. As the cardbox blocks only up to 50 % of the THz signal, the advantages on traditional IR radiation for passive imaging, which is entirely blocked by the cardbox, are emphasized.

7.2 Outlook

This thesis demonstrates the theoretical feasibility of real-time room-temperature passive imaging with a silicon-integrated total power radiometer and silicon-integrated THz direct detectors. In the demonstrated single-pixel implementations, the image acquisition is based on a continuous or raster-scanned detector movement. Each image pixel is recorded at a different detector or radiometer position. Thus, the scanning time is drastically enlarged and limited by the motor movement speed. However, passive imaging in a day life application such as security screening requires a true real-time capability. This can only be provided by large-scale focal plane standalone detector or radiometer arrays without using additional bulky optics such as rotating mirrors. Due to the low output noise for direct detectors, a dedicated readout circuit has to be developed, enabling a simultaneous individual pixel readout not deteriorating the standalone detector NEP. Several issues have to be addressed for imaging arrays consisting of the radiometer circuit, which are challenging to achieve as they trade-off with system performance characteristics such as gain, NF and bandwidth. First, the power consumption of more than 160 mW has to be reduced to minimize the chip heat and allow a room-temperature operation of the multipixel array. Second, the radiometer chipset has to be reduced in size to lower the overall cost and footprint of the multipixel array. A real-time video camera for passive THz imaging can be realized if these changes are implemented with only a small multipixel sensitivity deterioration.

Bibliography

Own Publications

[own1] J. Grzyb, P. Rodríguez-Vázquez, S. Malz, M. Andree, and U. R. Pfeiffer, “A SiGe HBT 215–240 GHz DCA IQ TX/RX Chipset With Built-In Test of USB/LSB RF Asymmetry for 100+ Gb/s Data Rates,” *IEEE Transactions on Microwave Theory and Techniques*, vol. 70, no. 3, pp. 1696–1714, 2022.

[own2] P. Hillger, M. v. Delden, U. Thanthrige, *et al.*, “Toward Mobile Integrated Electronic Systems at THz Frequencies,” *Journal of Infrared, Millimeter, and Terahertz Waves*, vol. 41, 846–869, 2020.

[own3] M. Andree, V. Jagtap, J. Grzyb, and U. R. Pfeiffer, “A Broadband Dual-Polarized Low-NEP SiGe HBT Terahertz Direct Detector for Polarization-Sensitive Imaging,” in *2023 48th International Conference on Infrared, Millimeter, and Terahertz Waves (IRMMW-THz)*, 2023, pp. 1–2.

[own4] M. Andree, V. Jagtap, J. Grzyb, and U. R. Pfeiffer, “Enabling Polarization Terahertz Imaging using Broadband Dual-polarized SiGe HBT Detectors,” in *SPIE conference on Millimetre Wave and Terahertz Sensors and Technology XIV*, 2023, pp. 1–2.

[own5] M. Andree, J. Grzyb, R. Jain, B. Heinemann, and U. R. Pfeiffer, “Broadband Modeling, Analysis, and Characterization of SiGe HBT Terahertz Direct Detectors,” *IEEE Transactions on Microwave Theory and Techniques*, vol. 70, no. 2, pp. 1314–1333, 2022.

[own6] M. Andree, J. Grzyb, R. Jain, B. Heinemann, and U. R. Pfeiffer, “A Broadband Antenna-Coupled Terahertz Direct Detector in a 0.13-μm SiGe HBT Technology,” in *Proc. 14th European Microwave Integrated Circuits Conf.*, Paris, France, Sep. 2019, pp. 168–171.

[own7] M. Andree, J. Grzyb, R. Jain, B. Heinemann, and U. Pfeiffer, “A Broadband Dual-Polarized Terahertz Direct Detector in a 0.13-μm SiGe HBT Technology,” in *Proc. IEEE Int. Microwave Symp. Conf.*, Boston, MA, USA, Jun. 2019.

[own8] J. Grzyb, M. Andree, R. Jain, B. Heinemann, and U. R. Pfeiffer, “Low-NEP Room-Temperature Broadband THz Direct Detection with a 0.13-µm SiGe HBT Device,” in *2020 45th International Conference on Infrared, Millimeter, and Terahertz Waves (IRMMW-THz)*, 2020, pp. 1–2.

[own9] J. Grzyb, M. Andree, R. Jain, B. Heinemann, and U. R. Pfeiffer, “A Lens-Coupled On-Chip Antenna for Dual-Polarization SiGe HBT THz Direct Detector,” *IEEE Antennas and Wireless Propagation Letters*, vol. 18, no. 11, pp. 2404–2408, 2019.

[own10] M. Andree, J. Grzyb, B. Heinemann, and U. R. Pfeiffer, “A D-Band to J-Band Low-Noise Amplifier with High Gain-Bandwidth Product in an Advanced 130 nm SiGe BiCMOS Technology,” in *2023 IEEE Radio Frequency Integrated Circuits Symposium (RFIC)*, San Diego, CA, USA, Jun. 2023, pp. 1–2.

[own11] J. Grzyb, M. Andree, P. Hillger, T. Bücher, and U. Pfeiffer, “A Balun-Integrated On-Chip Differential Pad for Full/Multi-Band mmWave/THz Measurements,” in *Proc. IEEE Int. Microwave Symp. Conf.*, San Diego, CA, USA, Jun. 2023.

Cited References

[1] L. Wei, L. Yu, H. Jiaoqi, H. Guorong, Z. Yang, and F. Weiling, “Application of Terahertz Spectroscopy in Biomolecule Detection,” *Frontiers in Laboratory Medicine*, vol. 2, no. 4, pp. 127–133, Dec. 2018.

[2] P. Siegel, “Terahertz Technology,” *IEEE Transactions on Microwave Theory and Techniques*, vol. 50, no. 3, pp. 910–928, 2002.

[3] S. Okano and K. Ikushima, “Single Photon Detection of Terahertz Waves on an Integrated-Circuit Resonator,” in *2016 Progress in Electromagnetic Research Symposium (PIERS)*, 2016, pp. 3344–3344.

[4] S. Paul, A. Saikia, V. Majhi, and V. K. Pandey, *Introduction to Biomedical Instrumentation and Its Applications*. Amsterdam, Boston: Academic Press, 2022.

[5] T. S. Rappaport, Y. Xing, O. Kanhere, S. Ju, A. Madanayake, S. Mandal, A. Alkhateeb, and G. C. Trichopoulos, “Wireless Communications and Applications Above 100 GHz: Opportunities and Challenges for 6G and Beyond,” *IEEE Access*, vol. 7, pp. 78 729–78 757, 2019.

[6] P. Rodriguez-Vazquez, J. Grzyb, B. Heinemann, and U. R. Pfeiffer, “A QPSK 110-Gb/s Polarization-Diversity MIMO Wireless Link With a 220–255 GHz Tunable LO in a SiGe HBT Technology,” *IEEE Transactions on Microwave Theory and Techniques*, vol. 68, no. 9, pp. 3834–3851, 2020.

[7] C. S. Joseph, A. N. Yaroslavsky, V. A. Neel, T. M. Goyette, and R. H. Giles, “Continuous Wave Terahertz Transmission Imaging of Nonmelanoma Skin Cancers,” *Lasers in Surgery and Medicine*, vol. 43, no. 6, pp. 457–462, 2011.

[8] S. Gui, Y. Yang, J. Li, F. Zuo, and Y. Pi, “THz Radar Security Screening Method for Walking Human Torso With Multi-Angle Synthetic Aperture,” *IEEE Sensors Journal*, vol. 21, no. 16, pp. 17 962–17 972, 2021.

[9] T. Trafela, M. Mizuno, K. Fukunaga, and M. Strlič, “THz Spectroscopy and Chemometrics for Quantitative Determination of Chemical Properties and Dating of Historic Paper,” in *35th International Conference on Infrared, Millimeter, and Terahertz Waves*, 2010, pp. 1–2.

[10] R. H. Jacobsen, D. M. Mittleman, and M. C. Nuss, “Chemical Recognition of Gases and Gas Mixtures with Terahertz Waves,” *Opt. Lett.*, vol. 21, no. 24, pp. 2011–2013, 1996.

[11] R. Appleby and H. B. Wallace, “Standoff Detection of Weapons and Contraband in the 100 GHz to 1 THz Region,” *IEEE Transactions on Antennas and Propagation*, vol. 55, no. 11, pp. 2944–2956, 2007.

[12] P. Hillger, J. Grzyb, R. Jain, and U. R. Pfeiffer, “Terahertz Imaging and Sensing Applications With Silicon-Based Technologies,” *IEEE Transactions on Terahertz Science and Technology*, vol. 9, no. 1, pp. 1–19, 2019.

[13] A. Svecic, J. Francoeur, G. Soulez, F. Monet, R. Kashyap, and S. Kadoury, “Shape and Flow Sensing in Arterial Image Guidance From UV Exposed Optical Fibers Based on Spatio-Temporal Networks,” *IEEE Transactions on Biomedical Engineering*, vol. 70, no. 5, pp. 1692–1703, 2023.

[14] R. Perez-Siguas, E. Matta-Solis, A. Remuzgo-Artezano, H. Matta-Solis, H. Matta-Perez, and L. Perez-Siguas, “Hand X-ray Image Processing System for the Early Detection of Rheumatoid Arthritis,” in *2023 Third International Conference on Advances in Electrical, Computing, Communication and Sustainable Technologies (ICAECT)*, 2023, pp. 1–4.

[15] C. Mangiavillano, A. Kaineder, K. Aufinger, and A. Stelzer, “A 1.42-mm2 0.45–0.49 THz Monostatic FMCW Radar Transceiver in 90-nm SiGe BiCMOS,” *IEEE Transactions on Terahertz Science and Technology*, vol. 12, no. 6, pp. 592–602, 2022.

[16] J. Grzyb, K. Statnikov, N. Sarmah, B. Heinemann, and U. Pfeiffer, “A 210–270-GHz Circularly Polarized FMCW Radar With a Single-Lens-Coupled SiGe HBT Chip,” *IEEE Transactions on Terahertz Science and Technology*, vol. PP, Sep. 2016.

[17] G. P. Kniffin and L. M. Zurk, “Model-Based Material Parameter Estimation for Terahertz Reflection Spectroscopy,” *IEEE Transactions on Terahertz Science and Technology*, vol. 2, no. 2, pp. 231–241, 2012.

[18] V. A. Revkova, I. V. Ilina, S. A. Gurova, R. O. Shatalova, M. A. Konoplyannikov, V. A. Kalsin, V. P. Baklaushev, and D. S. Sitnikov, “Effects of High Intensity Non-Ionizing Pulses of Terahertz Radiation on Human Skin Fibroblasts,” in *Advances in Terahertz Biomedical Imaging and Spectroscopy*, K. I. Zaytsev, D. S. Ponomarev, and M. Skorobogatiy, Eds., International Society for Optics and Photonics, vol. 11975, SPIE, 2022, p. 1 197 504.

[19] L. Yu, L. Hao, T. Meiqiong, *et al.*, “The Medical Application of Terahertz Technology in Non-Invasive Detection of Cells and Tissues: Opportunities and Challenges,” *RSC Adv.*, vol. 9, pp. 9354–9363, 17 2019.

[20] H. Chen, W.-J. Lee, H.-Y. Huang, *et al.*, “Performance of THz Fiber-Scanning Near-Field Microscopy to Diagnose Breast Tumors,” *Optics Express*, vol. 19, no. 20, pp. 19 523–19 531, 2011.

[21] Y. Zou, Q. Liu, X. Yang, *et al.*, “Label-free Monitoring of Cell Death Induced by Oxidative Stress in Living Human Cells using Terahertz ATR Spectroscopy,” *Biomed. Opt. Express*, vol. 9, no. 1, pp. 14–24, 2018.

[22] Y. Uzawa, Y. Fujii, M. Kroug, *et al.*, “Development of Superconducting THz Receivers for Radio Astronomy,” in *2016 41st International Conference on Infrared, Millimeter, and Terahertz waves (IRMMW-THz)*, 2016, pp. 1–3.

[23] C. Guo, W. Xu, M. Cai, S. Duan, J. Fu, and X. Zhang, “A Review: Application of Terahertz Nondestructive Testing Technology in Electrical Insulation Materials,” *IEEE Access*, vol. 10, pp. 121 547–121 560, 2022.

[24] N. C. van der Valk, W. A. van der Marel, and P. C. Planken, “Terahertz Polarization Imaging,” *Opt. Lett.*, vol. 30, no. 20, pp. 2802–2804, 2005.

[25] Z. Thacker and P. J. Pinhero, “Terahertz Spectroscopy of Candidate Oxides in MIM Diodes for Terahertz Detection,” *IEEE Transactions on Terahertz Science and Technology*, vol. 6, no. 3, pp. 414–419, 2016.

[26] C. Sirtori, "Bridge for the Terahertz Gap," *Nature*, vol. 417, pp. 132–3, Jun. 2002.

[27] S. H. Naghavi, M. T. Taba, R. Han, M. A. Aseeri, A. Cathelin, and E. Afshari, "Filling the Gap With Sand: When CMOS Reaches THz," *IEEE Solid-State Circuits Magazine*, vol. 11, no. 3, pp. 33–42, 2019.

[28] B. Heinemann, H. Rucker, R. Barth, *et al.*, "SiGe HBT with f_T/f_{max} of 505 GHz /720 GHz," in *IEEE Int. Electron Devices Meeting*, San Francisco, CA, USA, 2016, pp. 3.1.1–3.1.4.

[29] M. Urteaga, Z. Griffith, M. Seo, J. Hacker, and M. J. W. Rodwell, "InP HBT Technologies for THz Integrated Circuits," *Proceedings of the IEEE*, vol. 105, no. 6, pp. 1051–1067, 2017.

[30] X. Mei, W. Yoshida, M. Lange, *et al.*, "First Demonstration of Amplification at 1 THz Using 25-nm InP High Electron Mobility Transistor Process," *IEEE Electron Device Letters*, vol. 36, no. 4, pp. 327–329, 2015.

[31] R. Al Hadi, H. Sherry, J. Grzyb, *et al.*, "A 1 k-Pixel Video Camera for 0.7–1.1 Terahertz Imaging Applications in 65-nm CMOS," *IEEE Journal of Solid-State Circuits*, vol. 47, no. 12, pp. 2999–3012, 2012.

[32] S. Yokoyama, M. Ikebe, Y. Kanazawa, *et al.*, "5.8 A 32×32-Pixel 0.9THz Imager with Pixel-Parallel 12b VCO-Based ADC in 0.18 µm CMOS," in *2019 IEEE International Solid- State Circuits Conference - (ISSCC)*, 2019, pp. 108–110.

[33] K. Statnikov, J. Grzyb, B. Heinemann, and U. R. Pfeiffer, "160-GHz to 1-THz Multi-Color Active Imaging With a Lens-Coupled SiGe HBT Chip-Set," *IEEE Transactions on Microwave Theory and Techniques*, vol. 63, no. 2, pp. 520–532, 2015.

[34] C.-H. Li, C.-L. Ko, M.-C. Kuo, and D.-C. Chang, "A 340-GHz Heterodyne Receiver Front End in 40-nm CMOS for THz Biomedical Imaging Applications," *IEEE Transactions on Terahertz Science and Technology*, vol. 6, no. 4, pp. 625–636, 2016.

[35] P. Hillger, J. Grzyb, S. Malz, B. Heinemann, and U. Pfeiffer, "A Lens-Integrated 430 GHz SiGe HBT Source with up to -6.3 dBm Radiated Power," in *2017 IEEE Radio Frequency Integrated Circuits Symposium (RFIC)*, 2017, pp. 160–163.

[36] R. Jain, P. Hillger, E. Ashna, J. Grzyb, and U. R. Pfeiffer, "A 64-Pixel 0.42-THz Source SoC With Spatial Modulation Diversity for Computational Imaging," *IEEE Journal of Solid-State Circuits*, vol. 55, no. 12, pp. 3281–3293, 2020.

[37] P. Hillger, R. Jain, J. Grzyb, *et al.*, "A 128-Pixel System-on-a-Chip for Real-Time Super-Resolution Terahertz Near-Field Imaging," *IEEE Journal of Solid-State Circuits*, vol. 53, no. 12, pp. 3599–3612, 2018.

[38] P. Hillger, A. Schlüter, R. Jain, S. Malz, J. Grzyb, and U. Pfeiffer, "Low-Cost 0.5 THz Computed Tomography Based on Silicon Components," in *2017 42nd International Conference on Infrared, Millimeter, and Terahertz Waves (IRMMW-THz)*, 2017, pp. 1–2.

[39] A. Tang, T. Reck, R. Shu, *et al.*, "A W-Band 65nm CMOS/InP-hybrid Radiometer & Passive Imager," in *2016 IEEE MTT-S International Microwave Symposium (IMS)*, 2016, pp. 1–3.

[40] E. Heinz, T. May, D. Born, *et al.*, "Passive Submillimeter-wave Stand-off Video Camera for Security Applications," *Journal of Infrared, Millimeter, and Terahertz Waves*, vol. 31, no. 11, pp. 1355–1369, Sep. 2010.

[41] A. Timofeev, J. Luomahaara, L. Gronberg, *et al.*, “Optical and Electrical Characterization of a Large Kinetic Inductance Bolometer Focal Plane Array,” *IEEE Transactions on Terahertz Science and Technology*, vol. 7, no. 2, pp. 218–224, Mar. 2017.

[42] M. Kowalski and M. Kastek, “Comparative Studies of Passive Imaging in Terahertz and Mid-Wavelength Infrared Ranges for Object Detection,” *IEEE Transactions on Information Forensics and Security*, vol. 11, no. 9, pp. 2028–2035, 2016.

[43] S. Gunapala, D. Ting, A. Soibel, *et al.*, “High Dynamic Range Infrared Sensors for Remote Sensing Applications,” in *IGARSS 2018 - 2018 IEEE International Geoscience and Remote Sensing Symposium*, 2018, pp. 6342–6345.

[44] C. Marshall, T. Parker, and T. White, “Infrared Sensor Technology,” in *Proceedings of 17th International Conference of the Engineering in Medicine and Biology Society*, vol. 2, 1995, 1715–1716 vol.2.

[45] B. Dupont, A. Dupret, S. Becker, A. Hamelin, F. Guellec, P. Imperinetti, and W. Rabaud, “A [10°C; 70°C] 640×480 17 μm Pixel Pitch TEC-less IR Bolometer Imager with Below 50mK and Below 4V Power Supply,” in *2013 IEEE International Solid-State Circuits Conference Digest of Technical Papers*, 2013, pp. 394–395.

[46] Teledyne FLIR LLC, *Https://www.flir.com/*, accessed 20-June-2023 [Online].

[47] Thruvision Ltd., *Https://thruvision.com/*, accessed 20-June-2023 [Online].

[48] Y. Meng, A. Qing, C. Lin, Z. Jiefeng, Y. Zhao, and C. Zhang, “Passive Millimeter Wave Imaging System Based on Helical Scanning,” *Scientific Reports*, vol. 8, May 2018.

[49] M. Tekbaş and G. Çakır, “A Compact W-Band Low-Noise Radiometry Sensor for a Single-Pixel Passive Millimeter-Wave Imager,” *Electronics*, vol. 12, no. 10, 2023.

[50] A. Fournol, J. Blond, J. Meilhan, A. Aliane, H. Kaya, and L. Dussopt, “Cooled Bolometer Design for High-Sensitivity THz Passive Imaging,” in *2022 47th International Conference on Infrared, Millimeter and Terahertz Waves (IRMMW-THz)*, 2022, pp. 1–2.

[51] E. N. Grossman, K. Leong, X. Mei, and W. Deal, “Low-Frequency Noise and Passive Imaging With 670 GHz HEMT Low-Noise Amplifiers,” *IEEE Transactions on Terahertz Science and Technology*, vol. 4, no. 6, pp. 749–752, 2014.

[52] M. Aoki, S. R. Tripathi, M. Takeda, and N. Hiromoto, “Passive Imaging Using a 4K-cryocooled THz Photoconductive Detector System with Background-Limited Performance,” in *2011 International Conference on Infrared, Millimeter, and Terahertz Waves*, 2011, pp. 1–2.

[53] S. P. Singh, T. Rahkonen, M. E. Leinonen, and A. Pärssinen, “Design Aspects of Single-Ended and Differential SiGe Low-Noise Amplifiers Operating Above $f_{max}/2$ in Sub-THz/THz Frequencies,” *IEEE Journal of Solid-State Circuits*, pp. 1–11, 2023.

[54] F. Caster II, L. Gilreath, S. Pan, Z. Wang, F. Capolino, and P. Heydari, “Design and Analysis of a W-band 9-Element Imaging Array Receiver Using Spatial-Overlapping Super-Pixels in Silicon,” *IEEE Journal of Solid-State Circuits*, vol. 49, no. 6, pp. 1317–1332, 2014.

[55] A. Tang, Y. Kim, and Q. J. Gu, “25.4 A 0.43K-noise-equivalent-Δ T 100GHz Dicke-Free Radiometer with 100% Time Efficiency in 65nm CMOS,” in *2016 IEEE International Solid-State Circuits Conference (ISSCC)*, 2016, pp. 430–431.

[56] R. B. Yishay and D. Elad, “A 95–135 GHz Low Power Dicke Radiometer in SiGe BiCMOS Technology,” in *2020 15th European Microwave Integrated Circuits Conference (EuMIC)*, 2021, pp. 133–136.

[57] B. Ustundag, E. Turkmen, A. Burak, *et al.*, “Front-End Blocks of a W-Band Dicke Radiometer in SiGe BiCMOS Technology,” *IEEE Transactions on Circuits and Systems II: Express Briefs*, vol. 67, no. 11, pp. 2417–2421, 2020.

[58] S. Malz, R. Jain, and U. R. Pfeiffer, “Towards Passive Imaging with CMOS THz Cameras,” 2016, pp. 1–2.

[59] D. Čibiraitė, V. Krozer, H. Roskos, A. Lisauskas, K. Ikamas, and T. Lisauskas, “Passive Detection and Imaging of Human Body Radiation Using an Uncooled Field-Effect Transistor-Based THz Detector,” *Sensors*, vol. 20, p. 4087, Jul. 2020.

[60] S. van Berkel, O. Yurduseven, A. Freni, A. Neto, and N. Llombart, “THz Imaging Using Uncooled Wideband Direct Detection Focal Plane Arrays,” *IEEE Trans. THz Sci. Techn.*, vol. 7, no. 5, pp. 481–492, 2017.

[61] M. Planck and M. Masius, *The Theory of Heat Radiation*. Blakiston’s Son and Co, 1914, p. xi.

[62] A. Luukanen, A. Miller, and E. Grossman, “Passive Hyperspectral Terahertz Imagery for Security Screening using A Cryogenic Microbolometer,” *Proc SPIE*, May 2005.

[63] C. Dietlein, A. Luukanen, F. Meyer, Z. Popovic, and E. Grossman, “Phenomenology of Passive Broadband Terahertz Images,” Jan. 2006.

[64] M. Planck, *On the Theory of the Energy Distribution Law of the Normal Spectrum*. Verhandl. Dtsch. phys. Ges., 1900.

[65] M. F. Modest, *Radiative Heat Transfer*. Elsevier, 2013, p. 9.

[66] M. Kaviany, *Principles of Heat Transfer*. John Wiley & Sons, 2002, p. 380.

[67] F. Kreith, R. Manglik, and M. Bohn, *Principles of Heat Transfer*. CL Engineering, 2010, p. 21.

[68] T. Bergman, A. Lavine, F. Incropera, and D. Dewitt, *Fundamentals of Heat and Mass Transfer*. John Wiley & Sons, 2011, p. 862.

[69] R. Han, Y. Zhang, Y. Kim, D. Y. Kim, H. Shichijo, E. Afshari, and K. K. O, “Active Terahertz Imaging Using Schottky Diodes in CMOS: Array and 860-GHz Pixel,” *IEEE J. Solid-State Circuits*, vol. 48, no. 10, pp. 2296–2308, Oct. 2013.

[70] D. Yoon, J. Kim, J. Yun, M. Kaynak, B. Tillack, and J.-S. Rieh, “300-GHz Direct and Heterodyne Active Imagers Based on 0.13-μm SiGe HBT Technology,” *IEEE Trans. THz Sci. Techn.*, vol. 7, no. 5, pp. 536–545, Sep. 2017.

[71] H. Sherry, R. Al Hadi, J. Grzyb, E. Ojefors, A. Cathelin, A. Kaiser, and U. R. Pfeiffer, “Lens-integrated THz imaging arrays in 65nm CMOS technologies,” in *Proc. IEEE Radio Frequency Integrated Circuits Symp.*, Baltimore, MD, USA, Jun. 2011, pp. 1–4.

[72] R. Al Hadi, J. Grzyb, B. Heinemann, and U. Pfeiffer, “A Terahertz Detector Array in a SiGe HBT Technology,” *IEEE J. Solid-State Circuits*, vol. 48, no. 9, pp. 2002–2010, Sep. 2013.

[73] M. Tiuri, “Radio Astronomy Receivers,” *IEEE Transactions on Antennas and Propagation*, vol. 12, no. 7, pp. 930–938, 1964.

[74] H. Haus, “The Noise Figure of Optical Amplifiers,” *IEEE Photonics Technology Letters*, vol. 10, no. 11, pp. 1602–1604, 1998.

[75] C. A. Balanis, “Antenna Theory: Analysis and Design,” p. 93, 2005.

[76] E. Dacquay, A. Tomkins, K. H. K. Yau, E. Laskin, P. Chevalier, A. Chantre, B. Sautreuil, and S. P. Voinigescu, “D -Band Total Power Radiometer Performance Optimization in an SiGe HBT Technology,” *IEEE Transactions on Microwave Theory and Techniques*, vol. 60, no. 3, pp. 813–826, 2012.

[77] J. J. Lynch, H. P. Moyer, J. H. Schaffner, Y. Royter, M. Sokolich, B. Hughes, Y. J. Yoon, and J. N. Schulman, “Passive Millimeter-Wave Imaging Module With Preamplified Zero-Bias Detection,” *IEEE Transactions on Microwave Theory and Techniques*, vol. 56, no. 7, pp. 1592–1600, 2008.

[78] J. W. May and G. M. Rebeiz, “Design and Characterization of W-Band SiGe RFICs for Passive Millimeter-Wave Imaging,” *IEEE Transactions on Microwave Theory and Techniques*, vol. 58, no. 5, pp. 1420–1430, 2010.

[79] M. Fivash, “Calculating the Square Law Detector Signal-to-Noise Output,” *Microwaves & RF*, vol. 26, p. 133, Jun. 1987.

[80] C. Miller, W. Daywitt, and M. Arthur, “Noise Standards, Measurements, and Receiver Noise Definitions,” *Proceedings of the IEEE*, vol. 55, no. 6, pp. 865–877, 1967.

[81] C. A. Blackwell and R. S. Simpson, “The Convolution Theorem in Modern Analysis,” *IEEE Transactions on Education*, vol. 9, no. 1, pp. 29–32, 1966.

[82] J. Nanzer, *Microwave and Millimeter-wave Remote Sensing for Security Applications* (Artech House antennas and propagation series), en. Norwood, MA: Artech House, 2012.

[83] S. Malotaux, M. Babaie, and M. Spirito, “A Total-Power Radiometer Front End in a 0.25- μm BiCMOS Technology With Low $1/f$ -Corner,” *IEEE Journal of Solid-State Circuits*, vol. 52, no. 9, pp. 2256–2266, 2017.

[84] J. Park, “White Noise and the Delta Function,” *Proceedings of the IEEE*, vol. 56, no. 1, pp. 114–115, 1968.

[85] D. Walter, A. Bülau, and A. Zimmermann, “Review on Excess Noise Measurements of Resistors,” *Sensors*, vol. 23, no. 3, 2023.

[86] A. Tang, “Overview of CMOS Technology for Radiometry and Passive Imaging,” in *Micro- and Nanotechnology Sensors, Systems, and Applications IX*, T. George, A. K. Dutta, and M. S. Islam, Eds., International Society for Optics and Photonics, vol. 10194, SPIE, 2017, 101942P.

[87] R. H. Dicke, “The Measurement of Thermal Radiation at Microwave Frequencies,” *Review of Scientific Instruments*, vol. 17, no. 7, pp. 268–275, Jul. 1946.

[88] L. Gilreath, V. Jain, and P. Heydari, “Design and Analysis of a W-Band SiGe Direct-Detection-Based Passive Imaging Receiver,” *IEEE Journal of Solid-State Circuits*, vol. 46, no. 10, pp. 2240–2252, 2011.

[89] E. Javadi, D. B. But, K. Ikamas, J. Zdanevičius, W. Knap, and A. Lisauskas, “Sensitivity of field-effect transistor-based terahertz detectors,” *Sensors*, vol. 21, no. 9, 2021.

[90] M. Schroeter, A. Pawlak, and A. Mukherjee, “HICUM/L2— A Geometry Scalable Physics-Based Compact Bipolar Transistor Model,” 2017.

[91] W.Shockley, “The Theory of p-n Junctions in Semiconductors and p-n Junction Transistors,” *The Bell System Technical Journal*, vol. 28, no. 3, pp. 435–489, 1949.

[92] H. K. Gummel and H. C. Poon, “An Integral Charge Control Model of Bipolar Transistors,” *The Bell System Technical Journal*, vol. 49, no. 5, pp. 827–852, 1970.

[93] G Niu, “Noise in SiGe HBT RF Technology: Physics, Modeling, and Circuit Implications,” *Proc. IEEE*, vol. 93, no. 9, pp. 1583–1597, 2005.

[94] S. P. O. Bruce, L. K. J. Vandamme, and A Rydberg, “Measurement of Low Frequency Base and Collector Current Noise and Coherence in SiGe Heterojunction Bipolar Transistors Using Transimpedance Apmplifiers,” *IEEE Trans. Electron Devices*, vol. 46, no. 5, pp. 993–1000, 1999.

[95] J. D. Cressler, “SiGe HBT Technology: A New Contender for Si-Based RF and Microwave Circuit Applications,” *IEEE Trans. Microw. Theory Tech.*, vol. 26, no. 5, pp. 572–589, May 1998.

[96] M. Seif et. al., “Study of Low Frequency Noise in Advanced SiGe:C Heterojunction Bipolar Transistors,” in *Proc. IEEE Europ. Solid State Dev. Res. Conf.*, Venice, Italy, 2014, pp. 373–376.

[97] M Bouhouche, S Latreche, and C Gontrand, “Low Frequency Noise in SiGe Bipolar Transistor: Effect of Extrinsic Base Implantation Traps,” *Int. J. Computer Applications*, vol. 33, no. 6, pp. 59–64, 2011.

[98] J. Tang et. al., “Modeling and Characterization of SiGe HBT Low-Frequency Noise Figures-of-Merit for RFIC Applications,” *IEEE Trans. Microw. Theory Tech.*, vol. 50, no. 11, pp. 2467–2473, 2002.

[99] Ch. Mukherjee et. al., “Low-Frequency Noise in Advanced SiGe:C HBTs–Part I: Analysis,” *IEEE Trans. Electron Devices*, vol. 63, no. 9, pp. 3649–3656, 2016.

[100] M. von Haartman, M. Sandén, M. Östling, and G. Bosman, “Random Telegraph Signal Noise in SiGe Heterojunction Bipolar Transistors,” *Journal of Applied Physics*, vol. 92, no. 8, pp. 4414–4421, Oct. 2002.

[101] R. Wang, S. Guo, Z. Zhang, J. Zou, D. Mao, and R. Huang, “Complex Random Telegraph Noise (RTN): What Do We Understand?” In *2018 IEEE International Symposium on the Physical and Failure Analysis of Integrated Circuits (IPFA)*, 2018, pp. 1–7.

[102] Ch. Mukherjee et. al., “Low-Frequency Noise in Advanced SiGe:C HBTs–Part II: Correlation and Modeling,” *IEEE Trans. Electron Devices*, vol. 63, no. 9, pp. 3657–3662, 2016.

[103] J Tang, J. A. Babcock, T. L. Krakowski, L Smith, and C. G, “Characterization and Modeling of SiGe HBT Low-Frequency Noise in Inverse Operating Condition,” in *Proc. IEEE Bipolar/BiCMOS Circuits and Techn. Meet.*, Atlanta, GA, USA, 2011, pp. 174–177.

[104] J. T. et. al., “Impact of Reverse EB Stress and Mixed-Mode Stress on Low-Frequency Noise for SiGe HBTs in Forward and Inverse Modes,” in *Proc. IEEE Bipolar/BiCMOS Circuits and Techn. Meet.*, Bordeaux, France, 2013, pp. 163–166.

[105] E. Zhao, “Low-Frequency Noise in SiGe HBTs and Lateral BJTs,” Ph.D. dissertation, Georgia Institute of Technology, 2006.

[106] J. M. Lopez-Gonzalez, P Sakalas, and M Schröter, “Analytical Modelling of 200 GHz SiGe HBT High-Frequency Noise Paramaters,” *Semicond. Sci. Technol.*, no. 25, 2010.

[107] N. Rinaldi and M. Schroeter, *Silicon-Germanium Heterojunction Bipolar Transistors for mm-Wave Systems: Technology, Modeling and Circuit Applications.* River Publisher, 2018, pp. 1098–1113.

[108] M. Schroeter and A. Chakravorty, *Compact Hierarchical Bipolar Transistor Modeling With HiCUM.* Int. Ser. on Advances in Solid State Electronics and Tech., 2010.

[109] M. Schroeter, A. Pawlak, and A. Mukherjee, *HICUM/L2: A Geometry Scalable Physics-based Compact Bipolar Transistor Model.* 2015.

[110] D. Etor, L. E. Dodd, D. Wood, and C. Balocco, "Impedance Matching at THz Frequencies: Optimizing Power Transfer in Rectennas," in *2015 40th International Conference on Infrared, Millimeter, and Terahertz waves (IRMMW-THz)*, 2015, pp. 1–2.

[111] J. Grzyb, H. Sherry, Y. Zhao, R. A. Hadi, A. Cathelin, A. Kaiser, and U. Pfeiffer, "Real-time video rate imaging with a 1k-pixel THz CMOS focal plane array," in *Proc. SPIE*, vol. 8362, May 2012, pp. 86 –97.

[112] J. Grzyb, R. Al Hadi, and U. R. Pfeiffer, "Lens-integrated on-chip antennas for THz direct detectors in SiGe HBT technology," in *Proc. IEEE Antennas and Propag. Soc. Int. Symp.*, Orlanda, FL, USAS, 2013, pp. 2265–2266.

[113] J. Grzyb and U. Pfeiffer, "THz Direct Detector and Heterodyne Receiver Arrays in Silicon Nanoscale Technologies," *J. Infrared Millim.*, vol. 36, no. 10, pp. 998 –1032, Jun. 2015.

[114] D. Filipovic, S. Gearhart, and G. Rebeiz, "Double-slot Antennas on Extended Hemispherical and Elliptical Silicon Dielectric Lenses," *IEEE Transactions on Microwave Theory and Techniques*, vol. 41, no. 10, pp. 1738–1749, 1993.

[115] K. T. Selvan and R. Janaswamy, "Fraunhofer and Fresnel Distances: Unified Derivation for Aperture Antennas," *IEEE Antennas and Propagation Magazine*, vol. 59, no. 4, pp. 12–15, 2017.

[116] R. Jain, R. Zatta, J. Grzyb, D. Harame, and U. R. Pfeiffer, "A Terahertz Direct Detector in 22nm FD-SOI CMOS," in *2018 13th European Microwave Integrated Circuits Conference (EuMIC)*, 2018, pp. 25–28.

[117] H. Friis, "A Note on a Simple Transmission Formula," *Proceedings of the IRE*, vol. 34, no. 5, pp. 254–256, 1946.

[118] C. Tong and R. Blundell, "An Annular Slot Antenna on a Dielectric Half-space," *IEEE Transactions on Antennas and Propagation*, vol. 42, no. 7, pp. 967–974, 1994.

[119] L. Li, J. Yang, X. Chen, X. Zhang, R. Ma, and W. Zhang, "Ultra-Wideband Differential Wide-Slot Antenna With Improved Radiation Patterns and Gain," *IEEE Transactions on Antennas and Propagation*, vol. 60, no. 12, pp. 6013–6018, 2012.

[120] T. Kleinpenning, "Location of Low-frequency Noise Sources in Submicrometer Bipolar Transistors," *IEEE Transactions on Electron Devices*, vol. 39, no. 6, pp. 1501–1506, 1992.

[121] D. Filipovic, G. Gauthier, S. Raman, and G. Rebeiz, "Off-Axis Properties of Silicon and Quartz Dielectric Lens Antennas," *IEEE Transactions on Antennas and Propagation*, vol. 45, no. 5, pp. 760–766, 1997.

[122] E. Öjefors, A. Lisauskas, D. Glaab, H. G. Roskos, and U. R. Pfeiffer, "Terahertz Imaging Detectors in CMOS Technology," English, *Journal of Infrared, Millimeter, and Terahertz Waves*, vol. 30, no. 12, pp. 1269–1280, 2009.

[123] U. R. Pfeiffer and E. Ojefors, “A 600-GHz CMOS Focal-plane Array for Terahertz Imaging Applications,” in *ESSCIRC 2008 - 34th European Solid-State Circuits Conference*, 2008, pp. 110–113.

[124] R. Al Hadi, H. Sherry, J. Grzyb, *et al.*, “A Broadband 0.6 to 1 THz CMOS Imaging Detector with an Integrated Lens,” in *2011 IEEE MTT-S International Microwave Symposium*, 2011, pp. 1–4.

[125] U. R. Pfeiffer, J. Grzyb, H. Sherry, A. Cathelin, and A. Kaiser, “Toward Low-NEP Room-temperature THz MOSFET Direct Detectors in CMOS Technology,” in *2013 38th International Conference on Infrared, Millimeter, and Terahertz Waves (IRMMW-THz)*, 2013, pp. 1–2.

[126] R. Jain, P. Hillger, J. Grzyb, E. Ashna, V. Jagtap, R. Zatta, and U. R. Pfeiffer, “34.3 A 32×32 Pixel 0.46-to-0.75THz Light-Field Camera SoC in 0.13µ m CMOS,” in *2021 IEEE International Solid- State Circuits Conference (ISSCC)*, vol. 64, 2021, pp. 484–486.

[127] K. Sengupta, D. Seo, L. Yang, and A. Hajimiri, “Silicon Integrated 280 GHz Imaging Chipset with 4×4 SiGe Receiver Array and CMOS Source,” *IEEE Trans. THz Sci. Techn.*, vol. 5, no. 3, pp. 427–437, May 2015.

[128] R. Han, Y. Zhang, Y. Kim, D. Y. Kim, H. Shichijo, E. Afshari, and K. K. O, “Active Terahertz Imaging Using Schottky Diodes in CMOS: Array and 860-GHz Pixel,” *IEEE J. Solid-State Circuits*, vol. 48, no. 10, pp. 2296–2308, Oct. 2013.

[129] M. Uzunkol, O. D. Gurbuz, F. Golcuk, and G. M. Rebeiz, “A 0.32 THz SiGe 4x4 Imaging Array Using High-Efficiency On-Chip Antennas,” *IEEE J. Solid-State Circuits*, vol. 48, no. 9, pp. 2056–2066, Sep. 2013.

[130] G. Karolyi, D. Gergelyi, and P. Foldesy, “Sub-THz Sensor Array With Embedded Signal Processing in 90 nm CMOS Technology,” *IEEE Sens. J.*, vol. 14, no. 8, pp. 2432–2441, Aug. 2014.

[131] S. Boppel, A. Lisauskas, M. Mundt, *et al.*, “CMOS Integrated Antenna-Coupled Field-Effect Transistors for the Detection of Radiation From 0.2 to 4.3 THz,” *IEEE Trans. Microw. Theory Tech.*, vol. 60, no. 12, pp. 3834–3843, Dec. 2012.

[132] A. Boukhayma, A. Dupret, J.-P. Rostaing, and C. Enz, “A Low-Noise CMOS THz Imager Based on Source Modulation and an In-Pixel High-Q Passive Switched-Capacitor N-Path Filter.,” *Sensors*, vol. 16, no. 3, Mar. 2016.

[133] R. Jain, H. Rucker, and U. R. Pfeiffer, “Zero Gate-bias Terahertz Detection with an Asymmetric NMOS Transistor,” in *Proc. Int. Conf. on Infrared, Millim., and Terahertz Waves*, Copenhagen, Denmark, Sep. 2016, pp. 1–2.

[134] Z. Ahmad and K. K. O, “THz Detection Using p+/n-Well Diodes Fabricated in 45-nm CMOS,” *IEEE Trans. Electron Devices*, vol. 37, no. 7, pp. 823–826, Jul. 2016.

[135] D. Y. Kim, S. Park, and R. Han, “Design and Demonstration of 820-GHz Array Using Diode-connected NMOS Transistors in 130-nm CMOS for Active Imaging,” *IEEE Trans. THz Sci. Techn.*, vol. 6, no. 2, pp. 306–317, Mar. 2016.

[136] Z.-y. Liu, L.-y. Liu, J. Yang, and N.-j. Wu, “A CMOS Fully Integrated 860-GHz Terahertz Sensor,” *IEEE Trans. THz Sci. Techn.*, vol. 7, no. 4, pp. 455–465, Jul. 2017.

[137] C. S. Guenzer, “Chopping Factors for Circular and Square Apertures,” *Applied Optics*, vol. 15, no. 1, p. 80, Jan. 1976.

[138] M. Najmussadat, R. Ahamed, M. Varonen, D. Parveg, Y. Tawfik, and K. A. I. Halonen, “Design of a 240-GHz LNA in 0.13 µm SiGe BiCMOS Technology,” in *2020 15th European Microwave Integrated Circuits Conference (EuMIC)*, 2021, pp. 17–20.

[139] Y. Mehta, S. Thomas, and A. Babakhani, “A 140–220-GHz Low-Noise Amplifier With 6-dB Minimum Noise Figure and 80-GHz Bandwidth in 130-nm SiGe BiCMOS,” *IEEE Microwave and Wireless Technology Letters*, vol. 33, no. 2, pp. 200–203, 2023.

[140] P. V. Testa, C. Carta, B. Klein, R. Hahnel, D. Plettemeier, and F. Ellinger, “A 210-GHz SiGe Balanced Amplifier for Ultrawideband and Low-Voltage Applications,” *IEEE Microwave and Wireless Components Letters*, vol. 27, no. 3, pp. 287–289, 2017.

[141] N. Sarmah, K. Aufinger, R. Lachner, and U. R. Pfeiffer, “A 200–225 GHz SiGe Power Amplifier with peak Psat of 9.6 dBm using wideband power combination,” in *ESSCIRC Conference 2016: 42nd European Solid-State Circuits Conference*, 2016, pp. 193–196.

[142] Y. Zhang, W. Liang, X. Jin, M. Krattenmacher, S. Falk, P. Sakalas, B. Heinemann, and M. Schröter, “3.2-mW Ultra-Low-Power 173–207-GHz Amplifier With 130-nm SiGe HBTs Operating in Saturation,” *IEEE Journal of Solid-State Circuits*, vol. 55, no. 6, pp. 1471–1481, 2020.

[143] H. Li, J. Chen, D. Hou, *et al.*, “A 250-GHz Differential SiGe Amplifier With 21.5-dB Gain for Sub-THz Transmitters,” *IEEE Transactions on Terahertz Science and Technology*, vol. 10, no. 6, pp. 624–633, 2020.

[144] D. M. Pozar, *Microwave Engineering; 3rd Ed.* Wiley, 2005.

[145] H. Friis, “Noise Figures of Radio Receivers,” *Proceedings of the IRE*, vol. 32, no. 7, pp. 419–422, 1944.

[146] T. Bücher, J. Grzyb, P. Hillger, H. Rücker, B. Heinemann, and U. R. Pfeiffer, “A Broadband 300 GHz Power Amplifier in a 130 nm SiGe BiCMOS Technology for Communication Applications,” *IEEE Journal of Solid-State Circuits*, vol. 57, no. 7, pp. 2024–2034, 2022.

[147] M. H. Eissa and D. Kissinger, “4.5 A 13.5dBm Fully Integrated 200-to-255GHz Power Amplifier with a 4-Way Power Combiner in SiGe:C BiCMOS,” in *2019 IEEE International Solid- State Circuits Conference - (ISSCC)*, 2019, pp. 82–84.

[148] X. Li, W. Chen, P. Zhou, Y. Wang, F. Huang, S. Li, J. Chen, and Z. Feng, “A 250–310 GHz Power Amplifier With 15-dB Peak Gain in 130-nm SiGe BiCMOS Process for Terahertz Wireless System,” *IEEE Transactions on Terahertz Science and Technology*, vol. 12, no. 1, pp. 1–12, 2022.

[149] P. Neininger, L. John, F. Thome, C. Friesicke, P. Bruckner, R. Quay, and T. Zwick, “Limitations and Implementation Strategies of Interstage Matching in a 6-W, 28-38-GHz GaN Power Amplifier MMIC,” *IEEE Transactions on Microwave Theory and Techniques*, vol. 69, no. 5, pp. 2541–2553, May 2021.

[150] R. Fano, “Theoretical Limitations on the Broadband Matching of Arbitrary Impedances,” *Journal of the Franklin Institute*, vol. 249, no. 1, pp. 57–83, Jan. 1950.

[151] H. W. Bode, *Network Analysis and Feedback Amplifier Design.* Van Nostrand, 1945.

[152] A. Moradinia, S. G. Rao, and J. D. Cressler, “A SiGe HBT D-Band LNA Utilizing Asymmetric Broadside Coupled Lines,” *IEEE Microwave and Wireless Technology Letters*, vol. 33, no. 6, pp. 707–710, Jun. 2023.

[153] B. Ustundag, E. Turkmen, B. Cetindogan, A. Guner, M. Kaynak, and Y. Gurbuz, "Low-Noise Amplifiers for W-Band and D-Band Passive Imaging Systems in SiGe BiCMOS Technology," in *2018 Asia-Pacific Microwave Conference (APMC)*, 2018, pp. 651–653.

[154] P. Hetterle, A. Engelmann, F. Probst, R. Weigel, and M. Dietz, "Design of a Low Voltage D-band LNA in 22 nm FDSOI," in *2022 17th European Microwave Integrated Circuits Conference (EuMIC)*, 2022, pp. 252–255.

[155] Y.-C. Chang, S.-G. Lin, H.-K. Chiou, D.-C. Chang, and Y.-Z. Juang, "On-Wafer Noise Figure Measurements of Millimeter-Wave LNA and Mixer," in *2010 Asia-Pacific Microwave Conference*, 2010, pp. 1424–1427.

[156] A. Hati, D. Howe, F. Walls, and D. Walker, "Noise Figure vs. PM Noise Measurements: A Study at Microwave Frequencies," in *IEEE International Frequency Control Symposium and PDA Exhibition Jointly with the 17th European Frequency and Time Forum, 2003. Proceedings of the 2003*, 2003, pp. 516–520.

[157] E. Turkmen, A. Burak, A. Guner, I. Kalyoncu, M. Kaynak, and Y. Gurbuz, "A SiGe HBT *D* -Band LNA With Butterworth Response and Noise Reduction Technique," *IEEE Microwave and Wireless Components Letters*, vol. 28, no. 6, pp. 524–526, 2018.

[158] A. Gadallah, M. H. Eissa, T. Mausolf, D. Kissinger, and A. Malignaggi, "A 300-GHz Low-Noise Amplifier in 130-nm SiGe SG13G3 Technology," *IEEE Microwave and Wireless Components Letters*, vol. 32, no. 4, pp. 331–334, 2022.

[159] E. Öjefors, J. Borngräber, F. Korndörfer, and U. Pfeiffer, "A Aubharmonic Front-end in SiGe:C Technology for 94-GHz Imaging Arrays," *International Journal of Microwave and Wireless Technologies*, vol. 1, no. 4, pp. 361–368, Jun. 2009.

[160] E. Öjefors, F. Pourchon, P. Chevalier, and U. R. Pfeiffer, "A 160-GHz Low-noise Downconversion Receiver Front-end in a SiGe HBT Technology," *International Journal of Microwave and Wireless Technologies*, vol. 3, no. 3, pp. 347–353, Mar. 2011.

[161] E. Ojefors, B. Heinemann, and U. R. Pfeiffer, "Subharmonic 220- and 320-GHz SiGe HBT Receiver Front-Ends," *IEEE Transactions on Microwave Theory and Techniques*, vol. 60, no. 5, pp. 1397–1404, May 2012.

[162] Y. Zhao, E. Ojefors, K. Aufinger, T. F. Meister, and U. R. Pfeiffer, "A 160-GHz Subharmonic Transmitter and Receiver Chipset in an SiGe HBT Technology," *IEEE Transactions on Microwave Theory and Techniques*, vol. 60, no. 10, pp. 3286–3299, Oct. 2012.

[163] N. Sarmah, B. Heinemann, and U. R. Pfeiffer, "A 135 - 170 GHz Power Amplifier in an Advanced Sige HBT Technology," in *2013 IEEE Radio Frequency Integrated Circuits Symposium (RFIC)*, IEEE, Jun. 2013.

[164] N. Sarmah, B. Heinemann, and U. R. Pfeiffer, "235 - 275 GHz (x16) Frequency Multiplier Chains with up to 0 dBm Peak Output Power and low DC Power Consumption," in *2014 IEEE Radio Frequency Integrated Circuits Symposium*, IEEE, Jun. 2014.

[165] S. Malz, B. Heinemann, and U. R. Pfeiffer, "A 233-GHz low noise amplifier with 22.5dB gain in 0.13 μm SiGe," in *2014 9th European Microwave Integrated Circuit Conference*, IEEE, Oct. 2014.

[166] S. Malz, B. Heinemann, R. Lachner, and U. R. Pfeiffer, "J-band Amplifier Design using Gain-enhanced Cascodes in 0.13 μm SiGe," *International Journal of Microwave and Wireless Technologies*, vol. 7, pp. 339 –347, 2015.

[167] S. Malz, P. Hillger, B. Heinemann, and U. R. Pfeiffer, "A 275 GHz Amplifier in 0.13 μm SiGe," in *2016 11th European Microwave Integrated Circuits Conference (EuMIC)*, IEEE, Oct. 2016.

[168] I. Kim, W. Kim, and S. Hong, "A D-band Variable-Gain LNA with Triple-inductive Coupling Gm-boosting," in *2022 IEEE International Symposium on Radio-Frequency Integration Technology (RFIT)*, IEEE, Aug. 2022.

[169] P. J. Artz, P. Scholz, T. Mausolf, and F. Gerfers, "A Fully-Differential 146.6-157.4 GHz LNA Utilizing Back Gate Control to Adjust Gain in 22 nm FDSOI," in *2022 IEEE/MTT-S International Microwave Symposium - IMS 2022*, IEEE, Jun. 2022.

[170] H.-S. Chen and J. Y.-C. Liu, "A 180-GHz Low-Noise Amplifier With Recursive Z-Embedding Technique in 40-nm CMOS," *IEEE Transactions on Circuits and Systems II: Express Briefs*, vol. 69, no. 12, pp. 4649–4653, Dec. 2022.

[171] İ. K. Aksoyak, M. Möck, and A. Ç. Ulusoy, "A Differential D-Band Low-Noise Amplifier in 0.13 μm SiGe," *IEEE Microwave and Wireless Components Letters*, vol. 32, no. 8, pp. 979–982, Aug. 2022.

[172] T. Maiwald, J. Potschka, K. Kolb, M. Dietz, K. Aufinger, A. Visweswaran, and R. Weigel, "A Full D-Band Low Noise Amplifier in 130 nm SiGe BiCMOS using Zero-Ohm Transmission Lines," in *2020 15th European Microwave Integrated Circuits Conference (EuMIC)*, 2021, pp. 13–16.

[173] H. Li, J. Chen, D. Hou, Z. Li, P. Zhou, and W. Hong, "A 230-GHz SiGe Amplifier With 21.8-dB Gain and 3-dBm Output Power for Sub-THz Receivers," *IEEE Microwave and Wireless Components Letters*, vol. 31, no. 8, pp. 1004–1007, Aug. 2021.

[174] D.-W. Park, D. R. Utomo, B. Yun, H. U. Mahmood, and S.-G. Lee, "A D-Band Power Amplifier in 65-nm CMOS by Adopting Simultaneous Output Power-and Gain-Matched Gmax-Core," *IEEE Access*, vol. 9, pp. 99 039–99 049, 2021.

[175] K. K. Tokgoz, I. Abdo, T. Fujimura, *et al.*, "A 273–301-GHz Amplifier With 21-dB Peak Gain in 65-nm Standard Bulk CMOS," *IEEE Microwave and Wireless Components Letters*, vol. 29, no. 5, pp. 342–344, May 2019.

[176] E. Aguilar, A. Hagelauer, D. Kissinger, and R. Weigel, "A Low-Power Wideband D-band LNA in a 130 nm BiCMOS Technology for Imaging Applications," in *2018 IEEE 18th Topical Meeting on Silicon Monolithic Integrated Circuits in RF Systems (SiRF)*, 2018, pp. 27–29.

[177] D. Parveg, M. Varonen, D. Karaca, A. Vahdati, M. Kantanen, and K. A. I. Halonen, "Design of a D-Band CMOS Amplifier Utilizing Coupled Slow-Wave Coplanar Waveguides," *IEEE Transactions on Microwave Theory and Techniques*, vol. 66, no. 3, pp. 1359–1373, Mar. 2018.

[178] P. Starke, D. Fritsche, C. Carta, and F. Ellinger, "A 24.7 dB Low Noise Amplifier with Variable Gain and Tunable Matching in 130 nm SiGe at 200 GHz," in *2017 12th European Microwave Integrated Circuits Conference (EuMIC)*, IEEE, Oct. 2017.

[179] C. T. Coen, A. C. Ulusoy, P. Song, A. Ildefonso, M. Kaynak, B. Tillack, and J. D. Cressler, “Design and On-Wafer Characterization of G -Band SiGe HBT Low-Noise Amplifiers,” *IEEE Transactions on Microwave Theory and Techniques*, vol. 64, no. 11, pp. 3631–3642, Nov. 2016.

[180] A. C. Ulusoy, P. Song, W. T. Khan, M. Kaynak, B. Tillack, J. Papapolymerou, and J. D. Cressler, “A SiGe D-Band Low-Noise Amplifier Utilizing Gain-Boosting Technique,” *IEEE Microwave and Wireless Components Letters*, vol. 25, no. 1, pp. 61–63, Jan. 2015.

[181] D. Fritsche, C. Carta, and F. Ellinger, “A Broadband 200 GHz Amplifier with 17 dB Gain and 18 mW DC-Power Consumption in 0.13 μm SiGe BiCMOS,” *IEEE Microwave and Wireless Components Letters*, vol. 24, no. 11, pp. 790–792, Nov. 2014.

[182] C.-L. Ko, C.-H. Li, C.-N. Kuo, M.-C. Kuo, and D.-C. Chang, “A 210-GHz Amplifier in 40-nm Digital CMOS Technology,” *IEEE Transactions on Microwave Theory and Techniques*, vol. 61, no. 6, pp. 2438–2446, Jun. 2013.

[183] K. Schmalz, J. Borngraber, Y. Mao, H. Rucker, and R. Weber, “A 245 GHz LNA in SiGe Technology,” *IEEE Microwave and Wireless Components Letters*, vol. 22, no. 10, pp. 533–535, Oct. 2012.

[184] L. Zhou, C.-C. Wang, Z. Chen, and P. Heydari, “A W-band CMOS Receiver Chipset for Millimeter-Wave Radiometer Systems,” *IEEE Journal of Solid-State Circuits*, vol. 46, no. 2, pp. 378–391, 2011.

[185] A. Tomkins, P. Garcia, and S. P. Voinigescu, “A Passive W-Band Imaging Receiver in 65-nm Bulk CMOS,” *IEEE Journal of Solid-State Circuits*, vol. 45, no. 10, pp. 1981–1991, 2010.

[186] X. Bi, M. A. Arasu, Y. Zhu, and M. Je, “A Low Switching-Loss W-Band Radiometer Utilizing a Single-Pole-Double-Throw Distributed Amplifier in 0.13-μm SiGe BiCMOS,” *IEEE Transactions on Microwave Theory and Techniques*, vol. 64, no. 1, pp. 226–238, 2016.

[187] R. B. Yishay and D. Elad, “Low Power 75–110 GHz SiGe Dicke Radiometer Front-End,” in *2021 IEEE MTT-S International Microwave Symposium (IMS)*, 2021, pp. 885–887.

[188] T. Kanar and G. M. Rebeiz, “A Low-Power 136-GHz SiGe Total Power Radiometer With NETD of 0.25 K,” *IEEE Transactions on Microwave Theory and Techniques*, vol. 64, no. 3, pp. 906–914, 2016.

[189] J. Grzyb, K. Statnikov, N. Sarmah, and U. Pfeiffer, “A Broadband 240 GHz Lens-Integrated Polarization-Diversity On-Chip Circular Slot Antenna for a power source module in SiGe technology,” in *2015 European Microwave Conference (EuMC)*, 2015, pp. 570–573.

[190] C. Mukherjee, T. Jacquet, T. Zimmer, C. Maneux, A. Chakravorty, J. Boeck, and K. Aufinger, “Comprehensive Study of Random Telegraph Noise in Base and Collector of Advanced SiGe HBT: Bias, Geometry and Trap Locations,” in *2016 46th European Solid-State Device Research Conference (ESSDERC)*, 2016, pp. 260–263.

[191] G. Neidhöfer, “50-Hz Frequency [History],” *IEEE Power and Energy Magazine*, vol. 9, no. 4, pp. 66–81, 2011.

[192] M. Charlton, S. A. Stanley, Z. Whitman, V. Wenn, T. J. Coats, M. Sims, and J. P. Thompson, “The Effect of Constitutive Pigmentation on the Measured Emissivity of Human Skin,” *PLOS ONE*, vol. 15, no. 11, F. Li, Ed., e0241843, Nov. 2020.

[193] E. Turkmen, B. Cetindogan, M. Yazici, and Y. Gurbuz, “Design and Characterization of a D-Band SiGe HBT Front-End for Dicke Radiometers,” *IEEE Sensors Journal*, vol. 20, no. 9, pp. 4694–4703, 2020.

[194] Q. J. Gu, Z. Xu, A. Tang, and M.-C. Frank Chang, “A D-Band Passive Imager in 65 nm CMOS,” *IEEE Microwave and Wireless Components Letters*, vol. 22, no. 5, pp. 263–265, 2012.